

An appeal to President Ahmadinejad

The conviction of two Iranian AIDS physicians violates international norms of justice and threatens to undermine collaborations between Iranian scientists and their colleagues elsewhere.

“Iran now has one of the best prison programmes for HIV in not just the region, but in the world,” exclaimed Hamid Setayesh, the UNAIDS coordinator for the country, in 2006. “They’re passing out condoms and syringes in prisons. This is unbelievable. In the whole world, there aren’t more than six or seven countries doing that.”

Perhaps just as unbelievable is the fact that two of the physicians who helped pioneer Iran’s progressive AIDS-prevention programme are now behind bars themselves. Tehran’s Revolutionary Court last week sentenced the brothers Kamiar and Arash Alaei to, respectively, three- and six-year jail terms in the city’s notorious Evin prison on charges of being US stooges bent on fomenting a velvet revolution to overthrow the state (see page 517).

One of the acts that apparently attracted suspicion was the brothers’ participation alongside US government officials in two US–Iranian health-diplomacy round tables held in the United States in 2006 and 2007. The meetings were run by the Aspen Institute, a non-governmental organization founded in 1950 to provide an impartial international forum on major policy issues. The chair of one of the sessions introduced it proudly as one of the “first formal dialogues for almost 25 years” between Iran and the United States.

Human-rights organizations who have examined the brothers’ cases say that their detention, which began in June last year, and their convictions on 31 December in a dosed trial lasting barely half a day, both fell far short of the minimum international legal norms for a fair and equitable procedure.

An especially puzzling aspect of the case is that Iran’s president, Mahmoud Ahmadinejad, has publicly supported international

collaboration in science. Speaking at Columbia University in New York in September 2007, Ahmadinejad described researchers as “shining torches who shed light in order to remove darkness and the ambiguities around us in guiding humanity out of ignorance and perplexity”, and he invited Columbia faculty members and students to work with their counterparts in Iran. “You’re officially invited,” he said.

Such dialogue — ‘smart power’ — should be encouraged by all sides, because cooperation in the relatively apolitical areas of medicine and science keeps open rare avenues of back-channel diplomacy. Unfortunately, ‘dumb power’ is currently prevailing. The action of the Iranian judiciary in this case can have only a chilling effect on such activities, and there have been ill-considered moves elsewhere. Prime examples are the shortsighted visa policies being pursued by nations such as France, which unjustly discriminate against Iranian researchers (see *Nature* 456, 680–681; 2008), and the Bush administration’s declaration that the United States is seeking regime change in Iran by supporting ‘pro-democracy’ elements there. Academics in Iran who desire reform, but by self-determination, say that such covert US policies have left them vulnerable to the same charges faced by the Alaei brothers. More smart power is needed all round.

President Ahmadinejad. Your country’s HIV-prevention programme has won respect in the Muslim world and beyond. As you said at Columbia University, the open scientific and medical dialogue needed to progress in issues such as the fight against AIDS must be above the contemporary realpolitik of broader political issues. We urge you today to request the appropriate authorities to review the cases of Arash and Kamiar Alaei so that the truth may prevail. ■

Science restored

Obama’s pledge to set US science in its rightful place requires a dose of reality from researchers.

Scientists as far away as the Royal Society in London cheered on 20 January when US President Barack Obama promised in his inaugural address to “restore science to its rightful place”. In the US federal science agencies, where staffers were holding inaugural parties of their own, many were elated at his words.

The eight-year Republican administration of outgoing President George W. Bush is regarded by many, if not most, researchers as a dark time for scientific openness in the United States. It was a time in which politically appointed officials censored technical reports that conflicted with the administration’s conservative agenda, and ignored scientific advice on issues ranging from contraception to stem cells to climate change. With just six words, Obama had dedared that era at an end.

But researchers need to remember that the task of restoring science is not down to the new president alone — they too have some work to do. The acrimonious tone of the Bush years has drawn scientists of all stripes into the political sphere, if only to defend their research from partisan attack. During the election campaign, moreover, many US scientists actively supported Obama against his Republican rival John McCain. But those same scientists must now take a step back to ensure that their newfound political activism does not compromise their scientific integrity.

This does not mean that scientists should diminish their involvement in political life. Quite the opposite: policy debates on issues such as climate change and energy independence depend so heavily on scientific input that scientists can hardly escape being involved. Nor should they: if responsible researchers do not offer their opinions on policy, others will — as happened during the 1990s when a group of scientifically marginal sceptics tried to dominate the policy debate on climate change.

The many scientists who now view Obama in almost messianic terms

should try to be more realistic and sceptical about his administration; the new team will make mistakes, too, and should hear about them when it does. And researchers should remember that political winds can change. The Republicans will at some point be in the majority again, and lines of communication need to be kept open.

Perhaps most importantly, scientists must not fall into the trap of believing that their research necessarily supports a single course of action — partisan or otherwise. Scientists can tell policy-makers what the consequences might be if, say, atmospheric concentrations of carbon dioxide were to stabilize at 400 or 600 or 1,000 parts per million. But they cannot tell policy-makers what level the world should work towards, because that depends on what consequences people are prepared to accept — especially when weighed against economic or energy needs. Such a decision is a political matter. So when scientists are acting as advisers, they must be willing and able to

“Scientists who now view Obama in almost messianic terms should try to be more realistic and sceptical about his administration.”

set their personal preferences aside and examine a range of possible outcomes. And when they are speaking on their own behalf — as is their right as citizens — they must convey such an endorsement as opinion, not as a scientific finding.

As a corollary, researchers must also continue to speak out against politicians who pick and choose data to support their preconceived conclusions, as the Bush administration was accused of doing when it systematically played down evidence for climate change, or for the ineffectiveness of abstinence-based sex education. Wise policy, like good science, is possible only when decision-makers look at all the facts — and understand all the uncertainties in those facts.

For thousands of researchers in the United States and abroad, Obama's words promise a new era of openness and an elevation of science in political life. Science may be restored to its rightful place, but it will be up to scientists to ensure that it stays there. ■

A responsibility index

How to evaluate a nation's scientific integrity.

If there was one word that resonated above all at this week's Global Competitiveness Forum in Riyadh, Saudi Arabia, it was 'trust'. Given the context of the meeting — a disastrous meltdown of the world financial system — the assembled chief executives of international companies and institutions might have found this something of a sick joke. But Saudi Arabia has set itself the goal of strong international competitiveness, and in the past year has dimbed the rankings of competitiveness as measured by the World Economic Forum from 35th to 27th position. It also wants to promote a national climate and international perception of good corporate behaviour — a goal in which trust is essential.

Like many emerging countries, Saudi Arabia measures itself by indices, and has developed its own index for 'responsible competitiveness', based on a number of metrics (see www.rci.org.sa). But fostering strong science-based innovation requires its own metrics of inputs and achievement. So here, for any country concerned about the reputation and integrity of its research base, are some metrics that might be developed into an index for responsible scientific competitiveness.

One set of metrics relates to misconduct such as fraud, fabrication and plagiarism, which can gravely damage a country's reputation and destroy that of any researcher caught in its immediate wake, let alone the perpetrators. Two responsibility metrics would therefore relate to the infrastructures in place for the prevention and to the investigation, punishment and open declaration of misconduct. The latter metric, in turn, would look at the investigatory mechanisms in place at both the national funding-agency level, and the local level of publicly funded universities and government labs.

Less headline-grabbing misbehaviour is also important. As discussions about scientifically developed countries in this publication have shown, human nature and pressures to deliver results lead to worrying levels of discreet sleaze — the selection or cleaning up of data, the

addition or removal of names from author lists and the like. This can only be treated in culture, by the education of young researchers in good practice, by the reward of good mentoring, by the scrutiny and preservation of lab notebooks, and the insistent emphasis of guidelines. Such institutional encouragement of good practice is easy to document as a metric, albeit in short supply in most countries.

A second set of metrics would measure the transparency and objectivity of a nation's systems of evaluation, funding, staff appointments and promotion. A system that discriminates against researchers on the grounds of gender, ethnicity, age or cronyism is short-sighted and will gravely undermine the scientific potential of any nation.

A third set would evaluate a nation's framework for science policy, and the extent to which it allows talented scientists to follow their noses in the pursuit of what makes the world tick while also giving societal values and economic needs their due priority.

And a final set would measure the elusive concept of 'openness' — a key corollary of trust. Openness implies a receptivity to the ideas and practices of researchers in other countries, especially valuable given the evidence that international collaborations are more powerful generators of strong science than those that are intra-national. But openness is also expressed as a willingness to have ideas and conclusions publicly criticized — a culture essential to science itself, but also to the successful pursuit of a robust strategic policy and hence to international confidence.

Taken together, these qualitative metrics would amount to an index of responsible science for any country, whatever its stage of scientific development. They could be measured by the documentation of structures and practices and by independent surveys of scientists. A study of the state of openness and development in Arab countries (N. Fergany *Nature* **444**, 33–34; 2006) showed that Saudi Arabia in 2005 was starting from a low base. Since then, support for education, uptake by women of tertiary education and support for science have experienced significant growth. We leave it to the Saudis and to researchers and policy-makers in other ambitious technological powers to reflect on just how well their countries measure up across these metrics of responsible scientific competitiveness. ■

RESEARCH HIGHLIGHTS

Waning woods

Science **323**, 521–524 (2009)

Trees in western North America are dying more quickly than they used to, but there is no corresponding increase in the number of new seedling trees. Mortality rates, which are currently of the order of 1% a year, have in many cases doubled in just a couple of decades.

The trend was picked out by a group led by Phillip van Mantgem and Nathan Stephenson, both then based at the US Geological Survey Western Ecological Research Center in Three Rivers, California. The increased mortality correlates with climate change in the region, which has warmed by an average of between 0.3 and 0.4°C per decade since the 1970s.



N. STEPHENSON

ENVIRONMENT

The case for clean air

N. Engl. J. Med. **360**, 376–386 (2009)

Dirty air really can shorten your life. A drop of just 10 micrograms per cubic metre in the concentration of airborne particulate matter less than 2.5 micrometres in diameter extends human life by an average of almost 7.5 months, according to a team led by Arden Pope of Brigham Young University in Provo, Utah.

Comparing data from surveys carried out in 1979–1983 and 1999–2000, the researchers charted improvements in pollution levels in 51 US cities. They then correlated that data with changes in life expectancy over the same period, using census and health survey data to factor out other variables such as population density, income and smoking.

BIOGEOGRAPHY

On jaws and geography

Proc. R. Soc. B. doi:10.1098/rspb.2008.1785 (2009)

Two conflicting theories explain the heritage of New Zealand's current flora and fauna.

Sea levels rose 25 million–22 million years ago, and some believe that the landmass was completely submerged during this time and then repopulated later by transoceanic voyagers. Others hold that the land was only ever partly submerged, and that the ancestors of some of today's resident species have been there since New Zealand separated from other continents, 82 million–60 million years ago.

Marc Jones of University College London and his colleagues identified fossil jaw bones and teeth (pictured right) of a rhynchocephalian reptile, a relative of the extant New Zealand tuatara. Given the fossil's age — 19 million–16 million years — these

lizard-like creatures would have had less time to repopulate the landmass than had previously been thought, suggesting that New Zealand was never fully underwater and has been home to the tuatara's ancestors since the time of the dinosaurs.

OCEANOGRAPHY

Rogue waves

Geophys. Res. Lett. doi:10.1029/2008GL036280 (2009)

In June 2008, a Japanese fishing boat, the *Suwa-Maru No. 58*, capsized in the Pacific in apparently moderate seas, killing 17 of the 20 crew members. The investigators conjectured that it was hit by sudden big waves.

Hitoshi Tamura and his colleagues at the Japan Agency for Marine–Earth Science and Technology in Yokohama have reconstructed the wind and sea conditions at the time of the event in a computer model to offer a plausible account of how hitherto mysterious freak waves can form. They say that the low- and

high-frequency components of ordinary ocean waves interacted to channel their energy into a narrow frequency band, creating very large-amplitude waves.

ANALYTICAL CHEMISTRY

A cheap nose for TNT

J. Am. Chem. Soc. doi:10.1021/ja809104h (2009)

Despite recent advances, detecting trace explosives in a simple, portable and low-cost manner is a challenge. Jinghong Li of Tsinghua University in Beijing, Nongjian Tao of Arizona State University in Tempe and their colleagues have now created an effective sensing platform.

Their device uses an ionic liquid to pre-concentrate the explosives, electrochemical reactions to generate reaction products that absorb in the visible spectrum, and colorimetric methods to detect them. The authors tested the platform's power in detecting compounds such as TNT or picric acid down to a few tens of parts per trillion. The platform can distinguish these from potential red herrings such as vapour-producing household chemicals and personal care products.

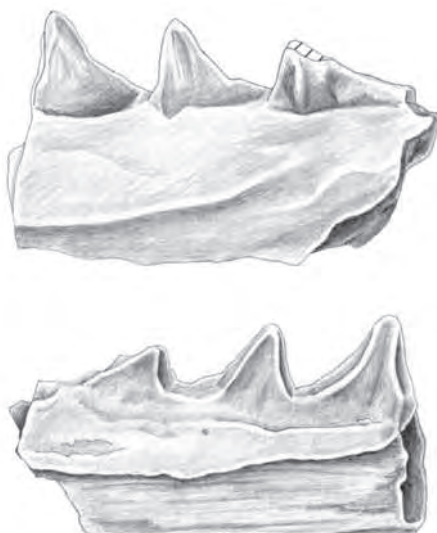
ATMOSPHERIC SCIENCE

Dust devilry

Geophys. Res. Lett. doi:10.1029/2008GL035846 (2009)

Desert dust, kicked up from the Sahara of northern Africa, may make small cumulus clouds less likely to release their raindrops, according to Cynthia Twohy of Oregon State University in Corvallis and her colleagues.

The researchers measured the nucleation particles around which cloud droplets form, over the eastern North Atlantic Ocean. They



© 2009 Macmillan Publishers Limited. All rights reserved

found that a surprisingly high percentage of the particles were Saharan dust. The tiny dust particles can lead to higher droplet concentrations but smaller droplet sizes — which may make precipitation less likely. This could create a cycle whereby dust leads to drought, and drought leads to more dust.

QUANTUM PHYSICS

Beam Yb up

Science **323**, 486–489 (2009)

Real-world teleportation takes a particle's fuzzy quantum state and transposes it onto a neighbour. It's a tricky business because direct handling of quantum information can destroy it.

Steven Olmschenk of the University of Maryland, College Park, and his colleagues solve that problem using ytterbium ions (Yb^+) and a trick of the light. The researchers begin with two ions: one in a quantum state and the second, a 'blank', placed about a metre away. They stimulated each ion to release a photon and then use the photons to quantum mechanically entangle the two ions together. Several circumspect measurements then transpose the state of the original Yb^+ onto its blank partner.

The team's technique may someday allow long-distance quantum communication.

BEHAVIOUR

Marmo-what?

Am. J. Primatol. doi:10.1002/ajp.20657 (2009)

The first evidence of within-species dialects among neotropical primates has been revealed.

Stella de la Torre at the University of San Francisco Quito, Ecuador, and Charles Snowdon at the University of Wisconsin, Madison, recorded the vocal patterns of adult pygmy marmosets (*Callithrix pygmaea*; pictured right) from 14 groups found in five geographically distinct regions of northeastern Ecuador. Although variation among the calls of adults from the same region was common, they discovered consistent structural differences in calls between regions.

The authors suggest that social factors, genetic drift and habitat acoustics — with different sounds being needed to best transmit information through different forest habitats — could explain the differences.

ANIMAL ACOUSTICS

This whale goes to 11

J. Acoust. Soc. Am. doi:10.1121/1.3040028 (2009)

Killer whales (*Orcinus orca*; pictured below) are a boisterous bunch, keeping track of each other in the underwater gloom by calling. Many whales, such as those resident in Puget Sound, near Seattle, Washington, have to contend with a great deal of noise made by motorized boats.

Marla Holt of the Northwest Fisheries Science Center in Seattle and her colleagues measured the calls of Puget Sound whales with a series of omnidirectional hydrophones. The whales pumped up the amplitude by one decibel for every extra decibel of background

noise. The authors speculate that the increased effort may cost more energy, and that the noise may stress the whales or even disrupt their communications.



FLIP NICKLIN/FLIPA

GEOSCIENCE

Tell-tale ooze

Earth Planet. Sci. Lett. **227**, 156–165 (2009)

Ancient ooze from the bottom of the Pacific provides evidence that the deep ocean sucked up vast amounts of carbon dioxide during the last ice age, thus cooling the planet.

In making this argument, Samuel Jaccard of the Swiss Federal Institute of Technology in Zurich and his colleagues resurrected a hypothesis first proposed 20 years ago. The idea had been discounted, but the team obtained new data from trace elements locked in ice-age ooze, collected from the ocean bottom by a drillship. That evidence, along with a revised understanding of nutrient dynamics in the ocean, suggests deep Pacific waters held less oxygen and stored much more carbon dioxide than previously thought, say the researchers.



N. GORDON/NATUREPL.COM

JOURNAL CLUB

Sue Gibson

Imperial College London, UK

An organic chemist highlights an ingenious way to make radiotracers.

In diagnostic medicine, radiotracers are used to image molecules in the body by methods such as positron emission tomography. Radionuclides such as carbon-11, nitrogen-13 or fluorine-18 are incorporated into molecules normally used by the body, such as glucose, or into designer organic molecules that bind to receptor sites within the body and provide valuable information about how they function. But the short half-lives of these radionuclides — 20, 10 and 110 minutes respectively — mean that the chemical reactions used to make the tracers must be speedy.

One step that is often time-consuming is separating out synthesized radiotracers from the large quantities of unreacted precursor molecules used to ensure efficient use of the radionuclide.

A new approach to this problem has been reported that exploits fluororous solid-phase extraction, a technique that separates molecules on the basis of their fluorine content (R. Bejot *et al.* *Angew. Chem. Int. Edn* **48**, 586–589; 2009). Veronique Gouverneur at the University of Oxford, UK, and her team designed heavily fluorinated precursor molecules — typically containing 13–25 fluorine atoms — that release their fluorine-rich section on reaction with a radionuclide. This generates a mixture of the desired defluorinated radiotracer and undesired fluorine-rich molecules. The mixture is then passed through a bed of fluorinated silica, which retains the heavily fluorinated compounds, leaving the radiotracer to emerge free of contaminants and ready for clinical use.

Gouverneur's work opens the door to the development of a plethora of new synthetic chemistry methods and the creation of new radiotracers for use in areas including tumour imaging and neuroimaging.

Discuss this paper at <http://blogs.nature.com/nature/journalclub>

NEWS

Stem cells ready for prime time

US regulatory agency gives the go-ahead for first clinical trials of a human embryonic stem-cell treatment.

It was a triumph of science, not politics. Yet the approval for the world's first clinical trial of a therapy generated by human embryonic stem cells, announced on 23 January, certainly seemed to be deeply political.

It was just three days into US President Barack Obama's term of office when Geron, based in Menlo Park, California, told the world that the US Food and Drug Administration (FDA) had agreed to its phase I safety study of a stem-cell-derived therapy for spinal-cord injury.

But supporters say that the significance of the approval lies not in the ideology of the new administration, but in the considerable scientific hurdles that were overcome in reaching this milestone.

"There was a lot of scepticism as to whether we could reliably reproduce these manufactured products at levels of purity and identity sufficient to even allow the FDA to allow a phase I clinical trial," says Michael West, who founded Geron in 1990 and is now chief executive of BioTime in Alameda, California.

Geron, he says, "has convinced the FDA that those cells could be manufactured reliably enough for at least the first clinical trials. That is a milestone. A lot of the critics said it would be 30–50 years before we got there."

Financial benefit

The announcement boosted the price of shares in the company, which has an extensive patent portfolio relating to embryonic stem-cell research. As of 26 January, they were trading at US\$8.15 a share — up 56% from the day before the announcement.

In the trial, up to ten individuals who have been left paralysed after spinal-cord injury will be injected at the point of injury with stem-cell-derived precursors of oligodendrocytes, which are key supportive cells in the central nervous system. The treatments will start within 7–14 days of their injury. The company hopes that the cells will lay down sheaths of myelin — an insulator essential for conducting nerve impulses — around injured neurons, as well as stimulating nerve cells to regenerate. The cells have demonstrated both capabilities in animals (H. Keirstead *et al.* *J. Neurosci.* **25**, 4694–4705; 2005).

Geron says that it expects to begin enrolment early this summer at up to seven US

medical centres. In a conference call with analysts and reporters, the firm's president and chief executive Thomas Okarma said that the trial "marks the dawn of a new era in medical therapeutics. This approach is one that reaches beyond pills and scalpels to achieve a new level of healing."

Geron's 22,000-page FDA application was first submitted in March 2008, at a time when President George W. Bush had placed tight restrictions on federal funding for embryonic stem-cell research. Although Obama has promised to reverse those restrictions, the company and the FDA deny that any politics were at play in the timing of the announcement.

"Science drives our decision-making," says Karen Riley, an FDA spokeswoman. "Political considerations have no role in this process." Riley adds that the process was prolonged by the time it took Geron to respond to additional questions the FDA asked the company last spring after receiving the application. Okarma says that the application included data from more than 24 studies, involving nearly 2,000 animals with injured spinal cords and requiring the production and injection of more than 5 billion cells.

Indeed, the Geron cells come from one of

a score of lines approved for federal funding under the Bush policy.

Groups opposing such research say that the trial's risks include the growth of tumours. "The ethical concerns include both using human embryos for the experiment as the source material, but also concern for the patient," says David Prentice, senior fellow for life sciences at the Family Research Council, a Christian advocacy group in Washington DC. "This is not a life-threatening condition," he says. "Are you actually going to be shortening the patient's life?" He cites a 2006 study in which some neural support cells — derived from human embryonic stem cells — reverted to undifferentiated growth when injected in rat models of Parkinson's disease (N. S. Roy *et al.* *Nature Med.* **12**, 1259–1268; 2006).

Not perfect, but timely

Supporters of stem-cell research have praised the FDA approval, saying that there is no 'perfect' trial with which to begin. "What I care about, what investors care about, what people who are debilitated care about, is something that can happen in the near future — not a perfect product two generations from now," says Steve Brozak, president of investment company WBB Securities in Westfield, New Jersey. Brozak has tracked stem-cell research since James Thomson, a researcher at the University of Wisconsin in Madison, published his work on the first successful isolation of human embryonic stem-cell lines in 1998.

Other advocates say the trial should not become a test case on which the fortunes of the entire field rise or fall. "This is a trial of one particular application, not a trial of all embryonic stem cells," says Sean Tipton, immediate past-president of the Coalition for the Advancement of Medical Research in Washington DC.

Geron is a big fish in what is currently a very small pond. The other high-profile company in the field, Advanced Cell Technology in Los Angeles, California, was recently on the brink of bankruptcy. And Novocell in San Diego, is working to develop human embryonic stem cells into pancreatic β -cells, which produce insulin. Although diabetes provides a huge treatment target, Novocell's project is daunting because of the technical challenges involved in producing β -cells that safely mediate blood-sugar levels.

Meredith Wadman



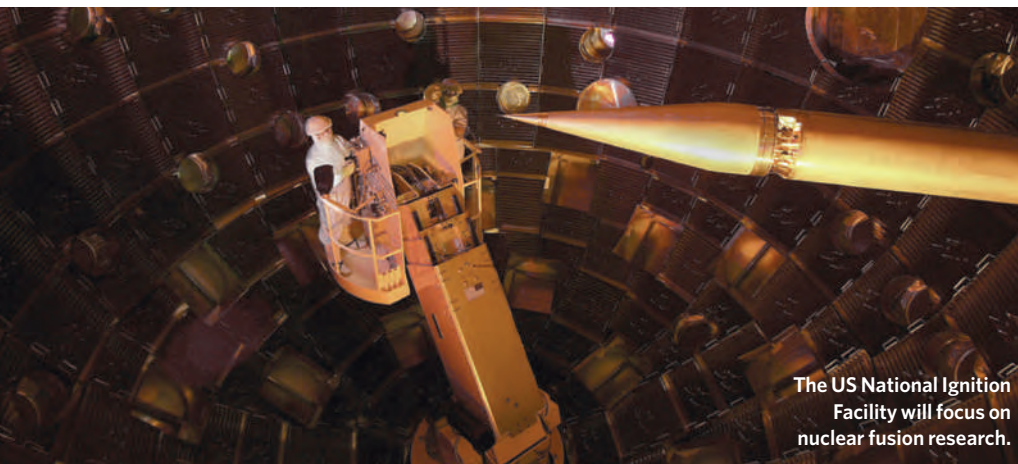
Thomas Okarma is keen to start Geron's stem-cell trial.

J. JACOBSON/AP PHOTO

**HAVE YOUR SAY**

Comment on any of our News stories, online.

www.nature.com/news



The US National Ignition Facility will focus on nuclear fusion research.

Laser facility flickers into life

The US National Ignition Facility (NIF) in Livermore, California, is almost ready to fire up its 192 laser beams to recreate the Sun's fusion burn.

The last of the project's 6,206 optics units — the mostly glass and crystal components that focus the lasers onto a tiny target — was installed on 26 January. It marked the end of the US\$3.5-billion facility's construction ahead of a federal deadline of 31 March.

After years of delay and hundreds of millions of dollars in overrun costs, "the project is, for all intents and purposes, completed", says NIF director Edward Moses. He will now focus on

ramping up the 'shots' of laser light. On hitting the target, the shots create temperatures of more than 100 million degrees and pressures that are thousands of times greater than at Earth's core, which scientists hope will trigger nuclear fusion. Although smaller lasers have achieved petawatt (10^{15} W) powers in femtosecond (10^{-15} s) bursts, NIF's total energy will exceed that of any current facility. Its goal is to reach 1.8 million joules, far greater than the 40,000 joules generated by the current leader: OMEGA at the University of Rochester, New York. It is likely to remain at the top until a similar facility, the Laser Mégajoule near Bordeaux, France, is completed in 2010.

Experiments have already begun towards NIF's primary mission: finding other ways to certify the safety and reliability of decades-old thermonuclear weapons rather than testing them underground. However, some critics have questioned whether this research will contribute much towards 'stockpile stewardship' (see *Nature* 407, 129–130; 2000).

Still, there are other reasons for NIF. This year, scientists will use the machine to explore astrophysical questions, such as how the implosion of a massive, dying star leads to supernova explosions. And Raymond Jeanloz, a geophysicist at the University of California at Berkeley, wants to probe the conditions expected inside giant exoplanets: "There's a regime at these high pressures where the chemistry is wonderfully and totally different," he says, "and it has never been accessed experimentally."

As NIF's shots reach full strength, perhaps as early as 2010, a third community will be feeling excited: those who hope to use nuclear fusion as a potential source of energy. A competing technique, used by fusion projects such as ITER in Cadarache, France, traps hydrogen fuel in magnetic fields while heating it to temperatures far greater than that of the Sun. Although both laser- and magnetic-fusion machines have achieved bursts of energy from fusion, none has achieved the conditions necessary for self-sustained fusion power. NIF's proponents think they have a chance. "We've been waiting for this since the 1960s," says Moses. ■

Eric Hand

Iranian AIDS doctors' trial draws condemnation

Iran has sentenced two of the country's HIV researchers to prison for communicating with an "enemy government" and plotting to overthrow the state. Arash and Kamiar Alaei, who are brothers, underwent a half-day trial on 31 December in Tehran's Revolutionary Court. Kamiar was sentenced to three years in prison, and Arash to six.

The Iranian authorities notified the physicians' lawyer, Masoud Shafie, of the verdicts on 20 January. He has 20 days to appeal and intends to do so; the brothers say they are innocent.

The Alaeis were arrested last June, and their detention and trial were "unfair even by the draconian standards of Iran's penal code", says Jonathan Hutson, a spokesman for Physicians for Human Rights, based in Cambridge, Massachusetts.

Hutson points out that the six-month detention itself breached human rights, as Iran failed to meet its international legal

obligations to explain the arrests, or to allow the men access to lawyers or the right to contest their detention before a judge.

And although Iranian law prohibits anyone from being detained for more than four months without charge, the state filed the charge of communicating with an "enemy government" only in December. Moreover, at the trial the prosecution indicted the men on new secret charges, now known to be the plot charges, denying them the right to defend themselves against these accusations and their right to due process.

The Iranian authorities claimed that the brothers had collaborated with scientists around the world, attended international AIDS conferences, and met with non-governmental AIDS organizations. "Those are not crimes — that's good medicine," says Hutson, arguing that the verdicts will have a chilling effect on academic collaboration between Iran and the rest of the world.

Julio Frenk, dean of the Harvard School of Public Health, echoed this concern on 15 January. The brothers' rights must be respected, he said, "so that they may continue their important work and so that all Iranian scientists and their international colleagues may feel secure about working together to solve the shared public health challenges of the world".

Last week, the state-run Islamic Republic News Agency cited an Iranian counter-intelligence official as saying that the brothers and two other unnamed individuals had confessed to working on behalf of the United States to overthrow the state, and that these statements would be televised. "Given interrogation techniques and duress known to exist in other cases like this one in Iran, any purported confession must be viewed as tainted and unreliable," says Hutson. ■

Declan Butler

See Editorial, page 511.

SPECIAL REPORT

Cutting out the chemicals

The international treaty drawn up to tackle ozone-destroying substances is gearing up to curb greenhouse gases. **Jeff Tollefson** reports.

Ozone experts are exploring ways to curb powerful greenhouse gases of their own making under the Montreal Protocol, arguing that direct regulation would be faster and cheaper than using carbon markets under a global climate treaty.

The Montreal Protocol set a strong precedent for such an approach, having almost eliminated production of the once-ubiquitous chlorofluorocarbons (CFCs) that eat away at stratospheric ozone. Used in refrigerants, propellants and solvents, CFCs were initially replaced with hydrochlorofluorocarbons (HCFCs); now, chemical manufacturers have moved on to a third-generation replacement, hydrofluorocarbons (HFCs; see graphic). HFCs are cheap and perform well, but are also powerful greenhouse gases. Although in this respect many are less potent than their predecessors, their ability to trap heat can be thousands of times that of carbon dioxide.

Because HFCs do not affect ozone, they are not covered by the Montreal Protocol. As greenhouse gases, they are covered under the Kyoto Protocol, but many believe that they could be eliminated much faster — and at a fraction of the cost — if Montreal were expanded to include them. The Montreal agreement has broad international support, a network of experts worldwide and a 20-year track record of handling these types of chemicals.

"We created these chemicals, and we can get rid of them," says Durwood Zaelke, president of the Institute for Governance & Sustainable

Development, an advocacy group in Washington DC. "We have the technology. We have the chemicals. We have the wherewithal within the treaty. It's just an administrative issue."

The idea has been bouncing around in the environmental community for years, but Argentina, the United States and others garnered support to formally explore the idea during the annual Montreal Protocol conference last November in Doha, Qatar. The treaty's technical advisory team is now working on an assessment of the issue, and government delegates have invited climate negotiators to attend a workshop on the topic in Geneva, Switzerland, in July. A second workshop will focus on ways to collect and destroy ozone-depleting substances from 'banks' of old refrigerators and other such equipment.

Tackling HFCs would represent the most explicit foray yet into the global-warming arena by a body that has to a large extent accomplished its work. The ozone layer, which Montreal was set up to protect, may only now be starting to recover. Emissions of some ozone-depleting chemicals will continue for some time, and even in 2100 long-lived CFCs will remain the dominant ozone destroyers. But schedules are in place to phase out most of the remaining chemicals of concern. "The ozone story is winding to a close," says David Fahey, a physicist at the US National Oceanic and Atmospheric Administration's Earth System Research Laboratory in Boulder, Colorado. But now, he adds, climate change is expanding the

Booming demand for refrigerators is boosting greenhouse-gas production.

Montreal Protocol's horizons.

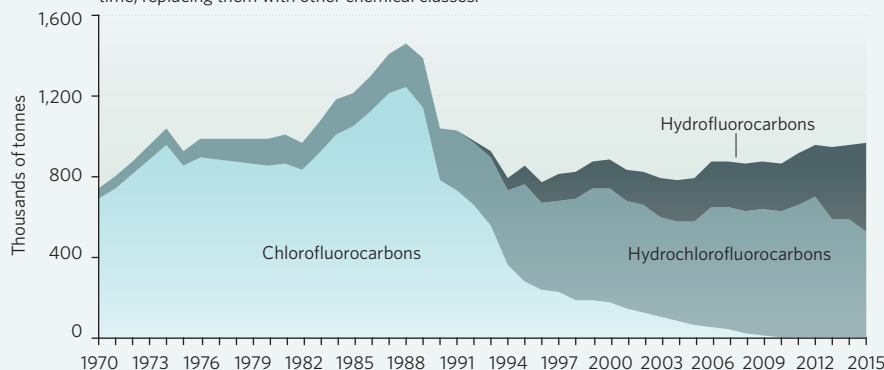
In fact, the Montreal treaty's links to global warming go all the way back to its preamble, which specifically states that "potential climatic effects" should be considered when analysing chemicals. And Fahey says Montreal's experts have performed well on that account. He co-authored a 2007 paper estimating that, by 2010, the Montreal treaty will have locked in the equivalent of roughly 11 billion tonnes of CO₂ emissions reductions annually — compared with an estimated 2 billion tonnes of reductions per year for the Kyoto Protocol (G. J. M. Velders *et al. Proc. Natl Acad. Sci. USA* **104**, 4814–4819; 2007). The team, led by Guus Velders at the Netherlands Environmental Assessment Agency in Bilthoven, expects to release another analysis of HFCs in advance of the Geneva workshop this summer.

In September 2007, that paper became a focal point in the discussion when Montreal delegates agreed to accelerate the phase-out of HCFCs by a decade, to 2030, explicitly citing the potential to further reduce greenhouse-gas emissions. The US Environmental Protection Agency says that the resulting greenhouse-gas reductions could equate to around 2.6 billion tonnes of CO₂, akin to taking more than 68 million vehicles off the road for 30 years, depending on which chemicals fill the void.

This is largely why the Montreal parties decided to weigh in on HFCs now. Although they represent less than 1% of the greenhouse-gas forcing, HFC emissions are rising by about 15% per year, largely as demand for air conditioning and refrigerators grows in countries

ESTIMATED GLOBAL FLUORO-CHEMICAL CONSUMPTION

The Montreal Protocol has phased out ozone-destroying substances over time, replacing them with other chemical classes.





Radioactive surprise
Old plutonium, vintage 1946, discovered in dump.
www.nature.com/news

legislation introduced in the US Senate last year proposed a stricter phase-down for HFCs than for other greenhouse gases, but under separate regulations. Compliance would cost just \$2 to \$3 per unit, DuPont estimates, meaning only a \$4 to \$6 bump in consumer prices.

Even such a small price signal is sufficient to spur recycling, better industrial processes and, ultimately, the development of new, more climate-friendly chemicals, says McFarland. "We're willing to step forward and do our part." By shifting HFCs into the Montreal Protocol, these same practices can then be exported to the developing world. "It's just a perfect fit," he says.

And many see opportunities to take the Montreal Protocol even further, by applying either the treaty itself or its framework to other powerful greenhouse gases such as perfluorocarbons (PFCs) and sulphur hexafluoride (SF₆), both of which are covered under the Kyoto agreement. Emissions of both gases are limited to relatively small and specialized industrial sectors, which lend themselves to the kinds of rapid technical assessment and technology transfer that Montreal can do.

In Poznań, the Group of 77 developing nations and China proposed a framework for the transfer and financing of climate technologies that is based largely on the Montreal Protocol. The proposal sets up the same kind of governing board, with equal membership representing developed and developing nations, to oversee decisions about which technologies to deploy. They also proposed that developing nations put an eye-popping 0.5–1% of their gross national product into a climate fund to support these and other actions each year.

Wara says that such numbers are well beyond what most governments are going to be willing to fund, which is why markets will be needed to generate the kind of money necessary to realign the global energy system. Some say such an approach could be deployed alongside a cap-and-trade system to pay for demonstration projects or readily deployable technologies, or even to provide direct support for energy efficiency projects.

Steve Rayner, director of the James Martin Institute for Science and Civilization at the University of Oxford, UK, says the idea has merit. He worries that the carbon market will be too slow to spur the kind of technological transformations that will be necessary to avoid the worst that global warming has to offer. "The more we can simplify and make the direct connections between the investments we are going to make and the installation of technology, the better off we are."

such as China. Left unchecked, that figure will increase rapidly as developing countries begin shifting from HCFCs to HFCs.

"If we don't do it now, the problem will be much bigger later," says Madhava Sarma, former executive secretary for the Montreal Protocol, and now a consultant in Chennai, India. The treaty, ratified by 193 nations at the outset, has already been amended five times. Ratifying the treaty a sixth time to cover HFCs should be doable, he says.

HFCs could also be dealt with in a global carbon market; the problem is that, because many are thousands of times more potent than CO₂, they fetch a price on the market that greatly exceeds the cost of controlling them. In a particularly controversial example, industrialized countries have been offsetting their emissions by paying companies in the developing world to incinerate the chemical HFC-23, which is 11,700 times more potent than CO₂ as a greenhouse gas (M. Wara *Nature* **445**, 595–596; 2007). "In the end, they are going to transfer several billion dollars, but it could have been done for tens of millions," says Washington DC-based David Doniger, a policy director for the Natural Resources Defense Council.

Michael Wara, a researcher at Stanford University in California, is less convinced that HFCs need be addressed under the Montreal Protocol. He says that an alternative pricing structure could be set up within the Kyoto Protocol and the United Nations Framework Convention on Climate Change (UNFCCC) to avoid having to pay the full market value for HFCs. "It makes much more sense in my mind

to deal with this head-on in the UNFCCC," he says.

Even those who support bringing HFCs under the Montreal umbrella realize that the community is not entirely on board yet. This week, the US Department of State is co-hosting a stakeholder meeting with scientists, environmentalists and business representatives to talk about the implications. "There's an education process to go through," says Daniel Reifsnnyder, who handles ozone issues at the State Department. He acknowledges that when he and others floated the idea at the UN climate meeting in Poland last month, they got a cool reception. "In Poznań, there was quite a bit of concern, and I would say even some suspicion, about what people were doing and why," he says.

But the idea does have some powerful backers. The chemical giant DuPont, based in Wilmington, Delaware, is more concerned about industrial HFC refrigerants than incidental HFC by-products, for which the company is already phasing in voluntary controls. Mack McFarland, global environmental manager for DuPont's fluorochemicals business, says policy-makers are beginning to recognize the problems created when HFCs are wrapped into the carbon market.

He illustrates with the following scenario: a US\$25-per-tonne price on carbon equates to \$150 for the cost of the HFCs that go into an average home air conditioner, which translates into a \$450 to \$600 price bump for consumers. By contrast, the Lieberman–Warner climate

"We created these chemicals, and we can get rid of them."

Pfizer to buy Wyeth in \$68-billion deal

One of the world's biggest pharmaceutical companies is set to get even larger. Pfizer announced on 26 January that it intends to acquire Wyeth, a company with a strong reputation in biologics and vaccines.

The combined company — united under the name Pfizer — would be a behemoth, with nearly 130,000 employees and more than US\$71 billion in revenue. Pfizer will pay about \$68 billion for Wyeth, based in Madison, New Jersey, an unusually large deal given the current financial crisis. The acquisition, expected to close late this year, will draw on Pfizer's cash and stock resources, along with a loan of \$22.5 billion, backed by a syndicate of five banks, some of which recently received bailout funds from the US government.

The deal comes as Pfizer nears the expiry dates of its patents on several key drugs, including atorvastatin (Lipitor), a cholesterol medication that is the best-selling drug in the world.

Over the past two years, Pfizer has shed 16,000 employees, closed 15 manufacturing sites, and culled research programmes (see *Nature* 456, 6–7; 2008). The company now says it intends to cut 19,500 more jobs, losing 15% of its workforce. This includes 8,000 job losses announced before the Wyeth purchase.

Both Wyeth and Pfizer have strong research



J. CHRISTENSEN/REUTERS

Pfizer's headquarters in New York, where Pfizer and Wyeth announced that they would merge.

programmes in diseases of the central nervous system, such as Alzheimer's disease, and in animal health-care products. But Pfizer chief executive Jeffrey Kindler says that the Wyeth acquisition will diversify Pfizer's pipeline, particularly in vaccines and in biologics — drugs comprised of complex biological molecules.

In the short term, Wyeth can bolster Pfizer's portfolio with two top-selling products. The pneumococcal conjugate vaccine (Prevnar) against meningitis in infants and children is the world's best-selling vaccine, and etanercept (Enbrel) — an arthritis and psoriasis therapy that Wyeth markets with Amgen of Thousand

Ocean fertilization: dead in the water?

The theory that adding iron to the oceans can help suck up atmospheric carbon dioxide cheaply and efficiently has received a further blow. A study¹ published in this week's issue of *Nature* (see page 577) finds that the potential of iron-induced carbon sequestration is far lower than previously estimated.

During the CROZEX experiment in 2004 and 2005, scientists on board the British vessel *RSS Discovery* observed the impact of natural iron fertilization on algal growth and carbon export near the Crozet Islands, an archipelago some 2,000 kilometres southeast of South Africa. The team found that, relative to one unit of added iron, the amount of carbon sequestered to 200 metres' depth, where it will stay for a couple of decades, was almost 80 times smaller than the amount that scientists had determined during a similar study in the nearby Kerguelen region².

"Ecosystem response and carbon export seem to vary very substantially from region to region," says Ulrich Bathmann, a biological

oceanographer at the Alfred Wegener Institute (AWI) for Polar and Marine Research in Bremerhaven, Germany, who was not involved in the new study. "And the closer you look, the more complex the story gets."

Separately, on 26 January, the German science ministry gave the green light to LOHAFEX, an Indo-German ocean-fertilization experiment that has been waiting to get going in the Southern Ocean. Responding to environmental and political concerns, the ministry had ruled on 13 January that an independent assessment be carried out before the experiment could start³. From aboard the German vessel *RV Polarstern*, the LOHAFEX team plans to dump 20 tonnes of iron sulphate into a 300-square-kilometre area between Argentina and the Antarctic Peninsula.

The CROZEX study, led by Raymond Pollard of the National Oceanography Centre in Southampton, UK, looked instead at natural ocean fertilization, in which iron-rich dust blowing off the Crozet Islands settles on the

waters. The team observed that some 270 tonnes of iron triggered a two- to threefold increase in biological productivity over an area the size of Ireland. But sediment probes revealed that the export of carbon to the deep ocean was nowhere near as massive as the Kerguelen study, and lab experiments, had suggested.

Although the study design allowed for only a rough estimate of carbon sequestration, the findings are sobering. Previously, scientists had cautioned that removing 30% of the carbon released every year as a result of human activity would require treating an ocean area ten times larger than the entire Southern Ocean, the most fertile waters for iron seeding⁴. Scaled up, the CROZEX results imply that even if the world's total ocean surface had a craving for iron, satisfying that would not have a large effect on the levels of atmospheric CO₂.

"You might get a different response if you shock the system by dumping a lot of iron all at once," says Pollard. "The effect will still be much



GOT A NEWS TIP?

Send any article ideas for Nature's News section to newstips@nature.com

K. CAMPBELL/GETTY

Oaks, California — is the world's best-selling biologic. Wyeth's expertise in developing and manufacturing biologics is particularly enticing: biologics can bring in large revenues and are more difficult to copy as generic drugs. As a result, pharmaceutical companies that have traditionally relied on small-molecule drugs are now trying to bolster their expertise in biologics.

But in the past, Pfizer's large acquisitions were blamed for slowing productivity and damaging employee morale. 'Mega-mergers' between large, mature pharmaceutical companies have an uneven track record, says Gary Pisano, a professor at the Harvard Business School in Boston, Massachusetts. "It's hard to think of how a merger of two companies that have been struggling with their pipeline performance will lead to a more innovative company," he says. "The data are pretty clear that when companies go through that, often innovative performance declines."

At a press conference on 26 January, Kindler acknowledged this legacy, but maintained that Pfizer is a very different company now. Recent restructuring has created smaller, more focused research units and streamlined management, both of which may guard against the organizational chaos that resulted from past acquisitions, he says. "We obviously have learned a lot from our prior acquisitions," he says. "This is very, very different from prior large pharmaceutical mergers."

Heidi Ledford



RV *Polarstern*: ready to fertilize the ocean.

smaller than some geoengineers would wish."

Some think it is game over. "Ocean iron fertilization is simply no longer to be taken as a viable option for mitigation of the CO₂ problem," says Hein de Baar, an oceanographer at the Royal Netherlands Institute for Sea Research in Texel. ■ Quirin Schiermeier

1. Pollard, R. T. *et al. Nature* **457**, 577–580 (2009).
2. Blain S. *et al. Nature* **446**, 1070–1074 (2007).
3. *Nature* **457**, 243 (2009).
4. Buesseler, K. O. & Boyd, P. W. *Science* **300**, 67–68 (2003).

Science adviser should show his independence, says report

The UK government's chief scientific adviser has hit back at members of parliament who slammed him last week for what they see as his failure to adequately defend the use of science in policy-making.

In a report published on 20 January, the House of Commons committee for innovation, universities, science and skills criticized John Beddington, a population biologist who took up his post on 1 January 2008, for "defending government policy" when he should "champion evidence-based science within government".

Responding to the criticisms, Beddington told *Nature*: "I am surprised and disappointed about the committee's comments. I think their comments are unfair and unbalanced." But he says he intends to raise his public profile this year, by instigating a comparison of science-policy advice used by President Barack Obama and by the European Commission. "I am more than happy to challenge the government where it is appropriate," he says, "but I also need to work within government to influence policy."

In particular, the report expressed concern that Beddington has not challenged the government over its decision to provide homeopathic medicine free through the National Health Service. In contrast, David King, Beddington's predecessor, openly attacked the government's policy on homeopathy, warning that it could put patients' health at risk. Beddington says he made it "crystal clear" in oral and written evidence to the committee that he "saw no credible scientific evidence" that homeopathy is effective at treating medical conditions beyond having a placebo effect.

Phil Willis, chairman of the Commons committee that produced the report, says his group will continue to scrutinize Beddington. "It is very important that he is seen as independent," Willis says. "If the chief scientific adviser is part of the establishment and does not use his position to challenge the government in its use of science, then no one else can do it."

Nick Dusic, director of the Campaign



John Beddington, UK chief scientific adviser.

for Science & Engineering in the UK, says "there is a general worry" among the science community that Beddington does not have as high a profile as previous science advisers, such as King and Robert May, who held the post from 1995 to 2000. "Challenging the government on its use of science in policy-making is the key job of the chief scientific adviser," says Dusic. "He may be doing this inside government, but as outsiders we are not seeing it."

Beddington "is a tough character and very good at what he does, but more of a low-key character than I was", says May. "As chief scientific adviser you have to operate in the culture of the civil service but must also be and be seen as an independent voice. I have no doubt he is an independent voice — I don't know if he was conveying this."

The committee's report also has harsh words for the Department for Innovation, Universities and Skills, which was set up in June 2007 and is responsible for science funding. Willis told *Nature* that the department had produced an "appalling" annual report, making it difficult for the committee to judge how well the department is working. "The jury is still out about the department. But it was hard to find anyone who thought it was working effectively," he says.

A spokesman for the department noted that its annual report had been produced in early 2008, when the department was less than a year old. He says it "will respond fully in due course". ■

Natasha Gilbert

IMPERIAL COLLEGE LONDON

China targets top talent from overseas

China has announced a nationwide plan that promises top salaries and attractive funding to elite researchers who are working overseas and willing to return to the country. The plan, known as the one-thousand-talents scheme, aims to boost China's innovation capability. But critics say that its success will depend on whether domestic talent gets similar support, and whether the country's science infrastructure can be reformed.

"The scheme sends a strong signal that the Chinese government values talented people from overseas and welcomes their contribution in key areas of research development," says Zhanqing Li, an atmospheric scientist at the University of Maryland in College Park.

The plan, announced this month by the country's top personnel administration, targets people with full professorships or the equivalent in developed countries. It offers a relocation package of 1 million renminbi (US\$146,000) per person, with salaries and research funding left to universities and institutes to sort out.

Previous approaches — such as the Chinese Academy of Sciences' one-hundred-talents scheme and the education ministry's Yangtze River Scholar Scheme — have lured more than 4,000 researchers, mostly at postdoctoral or assistant-professor levels, back to the country in the past fifteen years.

Time for change

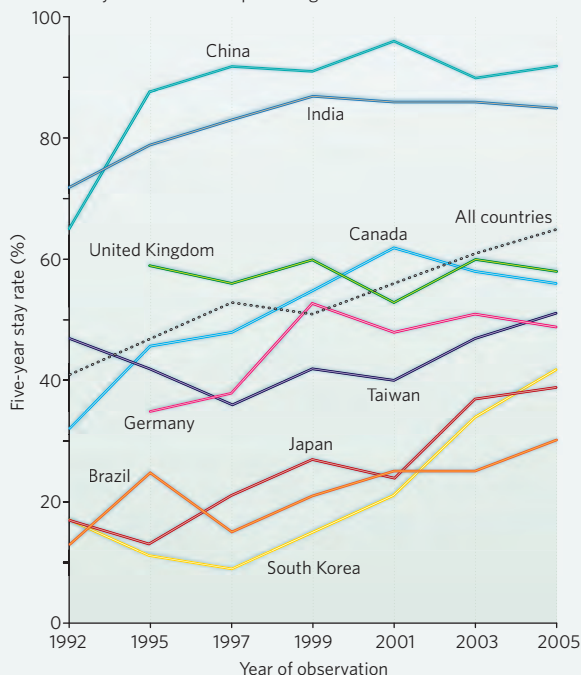
The new scheme "wouldn't have worked just a few years ago", says Muming Poo, a neuroscientist at the University of California, Berkeley, and director of the academy's Institute of Neuroscience in Shanghai. But given pressures on funding in the developed world, China can offer researchers comparable, if not better, support.

Researchers of non-Chinese origins will also be considered, says a source in the personnel and education bureau at the Chinese Academy of Sciences' headquarters in Beijing, who did not want to be identified without official permission to speak. In contrast to the current regulations, the new scheme means that non-Chinese nationals

"Without a long-term commitment to creating such an environment, any talent schemes would be futile."

STAYING IN THE UNITED STATES

Chinese students who receive their doctoral degrees in the United States are more likely than students from any other country to stay there. China is implementing a new scheme to try to lure the most promising ones back home.



SOURCE: Finn, M. Stay Rates of Foreign Doctorate Recipients from US Universities: 2005 (Oak Ridge Institute for Science and Education, 2007).

will be eligible for positions as principal investigators on major national projects.

Details have not yet been released on how much the science and education ministries will contribute. But Poo says that the Chinese Academy of Sciences, a ministry-level organization, alone will provide up to 20 million renminbi for top-level scientists as a one-off, start-up package over five years, including annual salaries of up to 1 million renminbi. The number of recruits over the next five years will depend on the balance of demand and supply, and is likely to be in the hundreds.

"The details of how the scheme will be operated will be important," says Rao Yi, dean of the life-sciences school at Peking University. Rao warns that the selection process should focus on a candidate's potential as well as his or her past academic record. "Some assistant or associate professors may have more potential than full professors," says Wei Jia, a biochemist at the University of North Carolina in Greensboro. "This should be dealt with on an individual

basis." The widely differing criteria for professorship between universities and countries should also be a factor.

Jia says that institutes and universities should develop long-term strategic plans before starting to recruit. In the past, some organizations were more preoccupied with meeting targets than ensuring that the skills and research areas of the recruits were appropriate. "This has led to talented people moving to another organization or even leaving the country," says Jia, who returned to the United States last year after nearly a decade in China.

Domestic discontent

The generous package of the new talent scheme, especially the salaries, is likely to cause resentment in researchers already in China. Last year, the 1.7-million-renminbi salary of Shi Yigong, whom the Beijing-based Tsinghua University recruited from Princeton University in New Jersey, was leaked and caused an outcry among principal investigators in China, who have an average annual salary of 150,000 renminbi.

Top-range salaries and funding are necessary for attracting the overseas elite, but the resentment of their

domestic peers should not be ignored, say critics. "It is important that researchers recruited to China at a junior stage should be able to compete for the same level of support," says Rao. "There should be a matching talent scheme for domestic scientists."

Still, some doubt whether overseas professors will jump to the call. "Money is important for practical issues," says Li. "But the determinant factor is whether we would be able to be as productive in China as we are in the United States." Some elite researchers may be put off by the scientific culture and policies in China, which historically has neither encouraged critical thinking and intellectual exchange nor ensured fair competition.

"We have a proverb in China: it takes a decade to grow a strong tree and a century to create a nourishing environment in which talents could flourish," says Jia. "Without a long-term commitment to creating such an environment, any talent schemes would be futile." Poo agrees: "Talent schemes and science-infrastructure reform must go hand in hand."

Jane Qiu

Obama swiftly reverses Bush orders

US President Barack Obama began his first week in office with a series of executive orders, including one repealing a ban on US funding to international aid groups that perform or offer advice on abortions.

First instituted in 1984 by Ronald Reagan, the 'global gag rule' was repealed by Bill Clinton in 1993 and then reinstated by George W. Bush in 2001.

Although Obama has halted all pending rules and regulations, several controversial policies from the Bush administration's last days have already taken effect, including one that allows agencies to bypass federal wildlife biologists when reviewing projects under the Endangered Species Act.

And on 26 January, Obama announced plans to strengthen federal fuel-efficiency standards for vehicles and to review a decision by the Bush administration that would stop California and other states from adopting stricter standards of their own.

Greenhouse-gas satellite heads into orbit

Japan successfully launched its Greenhouse Gases Observing Satellite (GOSAT) on 23 January, to monitor levels of methane, water vapour, ozone and carbon dioxide. The Japan Aerospace Exploration Agency says that data from the satellite will provide details about the global distribution and seasonal variations of these gases, helping to refine climate-change predictions.

On 23 February, GOSAT will be joined by NASA's Orbiting Carbon Observatory, which will generate complementary data on the sources of carbon dioxide emissions (see *Nature* 450, 785–786; 2007).



Japan's GOSAT heads for the heavens.

Tanzanian toad makes a colourful debut

The South Nguru Mountains in eastern Tanzania are home to this ornate toad (pictured), a still-unnamed member of the genus *Nectophrynoides* reported last month (M. Menegon *et al. Acta Herpetologica* 3, 107–127; 2008). It was among 15 amphibian species new to science that were discovered between 2004 and 2006 during surveys by a team led by Nisha Owen of the Frontier Tanzania Forest Research Program in Dar es Salaam.

The palm-sized toad's distinctive orange protuberances are glands, which may also be yellow and green or red. The glands' secretions are as yet unknown, but related amphibians exude noxious compounds to put off would-be predators.



P. WHITEHORN/FRONTIER

Pig farmer infected with Ebola virus

Health officials in the Philippines confirmed last week that a worker at a pig farm has contracted the Ebola Reston subtype of Ebola virus.

The virus was found in pigs at two farms on Luzon, the largest island in the Philippines, last year (see *Nature* 457, 364–365; 2009). Fifty workers at those farms were subsequently tested for antibodies to the virus, and one has tested positive. World Health Organization officials estimate that he contracted the virus between 6 and 18 months ago, although it has not been proved that he caught it from a pig.

Direct transmission from pigs to humans would be a cause for concern because pigs are thought to act as 'mixing vessels', where viruses can mutate into more virulent forms with a greater impact on human health.

Europe's research activity lags behind its competitors'

Investment in research and development (R&D) in Europe is stagnating, according to reports from the European Commission.

The two reports, 2008 *Innovation Scoreboard* and 2008 *Science, Technology and Competitiveness*, reveal that Europe's research intensity — the percentage of gross domestic product (GDP) spent on R&D — languished at about 1.8% of GDP between 2000 and 2006. This leaves the European Union unlikely to reach the target of 3% by 2010 set by European heads of state at a summit in Barcelona in 2002.

The reports single out poor R&D investment by business as a key problem, especially in France, Italy, the United

Kingdom and Germany, which together account for 69% of the European Union's R&D spend.

Over the same period, R&D intensity rose from 3.04% to 3.39% in Japan and from 0.90% to 1.42% in China; it fell from 2.74% to 2.61% in the United States.

For a longer version of this story, see <http://tinyurl.com/d48sgj>.

US agencies under scrutiny over high-risk programmes

A US congressional watchdog has added programmes at the Food and Drug Administration (FDA) and the Environmental Protection Agency (EPA) to its list of government operations that require special oversight or reform.

To help Congress set its agenda every two years, the Government Accountability Office identifies high-risk programmes that need to be either overhauled or guarded against "waste, fraud, abuse, and mismanagement". The report, released on 22 January, says that the FDA should, for instance, increase its inspections of foreign drug and medical-device manufacturers. The FDA plans to expand its oversight abroad, and has opened offices in China and India in the past six months.

The report also says that the EPA should speed up its evaluations of chemical risks and have the power to demand more safety information from chemical companies.

Correction

The graphic in the biosecurity section of the News Feature '43 by the numbers' (*Nature* 457, 252–253; 2009) incorrectly displayed the proportion of money spent at the end of the Clinton administration. The html version of this article has been corrected, and a corrected PDF can be downloaded from <http://tinyurl.com/bezwcy>.



MAKING CONNECTIONS

By turning neurons technicolour, Jeff Lichtman exposed the brain's wiring. **Jonah Lehrer** meets the 'unapologetic cell biologist' with ambitions to map every connection in the human brain.

At first glance, Jeff Lichtman seems to be hanging long strips of sticky tape from the walls of his Harvard lab. The tape flutters in the breeze from the air-conditioner. But closer inspection reveals that this is not tape: it is the brain of a mouse, rendered into one long, delicate strip of tissue and fixed onto a plastic film. When the film is tilted to the light, the tissue becomes visible, like the smear of a greasy fingerprint.

These smudges are the creation of a new brain-slicing machine invented by Lichtman, a molecular and cellular biologist at Harvard University, along with Kenneth Hayworth, a graduate student at the University of Southern California, Los Angeles. Called the automatic tape-collecting lathe ultramicrotome (ATLUM), the machine resembles an old-fashioned film projector with two large reels. At its centre is a fixed diamond blade that cuts continuously into a rotating mouse brain, much like an apple parer. The end

result is a seamless sliver of tissue, less than 10 nanometres thick and around 5 metres long, that is deposited on the plastic film spinning around the spools.

Although Lichtman appreciates the technical precision of the ATLUM — "That's a real diamond!" he says — he is most excited about its scientific potential. Researchers in his lab are starting to put these slices under an electron microscope to visualize the intricate web of connections between neighbouring neurons.

Lichtman eventually hopes to have a 'farm' of several dozen such microscopes scanning tissue around the clock. Even then it would take months, if not years, to capture all the connections in the strip from a

single brain. "When you cut the brain this thin, there's just such a massive amount to see," he says. "It does require us to think about imaging on a different scale."

Lichtman likes to think on a different scale. In recent years, he has become a leading

proponent of a new field that is working to create a connectome, a complete map of neural wiring in the mammalian brain. Currently, such a map exists only for the nematode *Caenorhabditis elegans*, which has 302 neurons. The adult human brain, in contrast, contains 100 billion neurons and several trillion synaptic connections. "I know the goal sounds daunting," Lichtman says. He insists that such a wiring diagram is an essential undertaking, because it will allow scientists to see, for the first time, the path that information takes as it is shuttled from cell to cell, and how all these cells and the information they transmit weave together to create a conscious brain.

All in the wiring

As Francis Crick and Edward James wrote in a *Nature* Commentary¹ in 1993, "It is intolerable that we do not have [a connection map of] the human brain. Without it there is little hope of understanding how our brains work except in the crudest way." Thomas Insel, the director of the National Institute of Mental Health in Bethesda, Maryland, notes that many of the most common mental illnesses, from autism

"You can learn a tremendous amount, and generate some interesting theories, just by staring at pictures of the brain."

— Jeff Lichtman

C. SENTER/AP



to schizophrenia, seem to be diseases of “faulty wiring”, in which the brain has a set of aberrant connections. “The brain needs a connectome, just as modern genetics needed a genome,” says Insel. “That’s the only way we’re going to understand how the brain works at a detailed level, and also what happens when something goes wrong.”

As yet, Lichtman, Insel and others have not proposed a formal connectome project — and Lichtman declines to even give a rough estimate of such a project’s cost, saying only that it would be a “scary number”. But a debate is under way about whether such an undertaking would be worthwhile. Studies have shown that a majority of synaptic connections — some estimates run as high as 80% — are extremely weak and transmit few electrical signals. If that’s the case, then a map of structural connections might actually misrepresent the brain’s functional organization. “Only a very small proportion of connections seem to drive network activity,” says John Isaac, who studies synaptic plasticity at the National Institutes of Health (NIH) in Bethesda, Maryland. “How do you know which connections are important? A wiring diagram won’t tell you that.” It is also unclear if the connectomes of different individuals could be readily compared in the same way that their genomes can be. Whereas

bioinformatics can easily identify two similar genes in different genetic sequences, it is not yet clear what comparable tools will serve for identifying functionally equivalent neurons in two brains — if they even exist — or in a diseased brain versus a healthy one.

Leading connectomics scientists are not deterred by these problems, saying that they will be solved only once the research is under way. “The point is that you don’t even know what’s important until you see the system in its entirety,” says Winfried Denk, director of biomedical optics at the Max Planck Institute for Medical Research in Heidelberg, Germany, and a pioneer of advanced microscopy. “There is a tremendous virtue in completeness.”

Lichtman says the criticisms of the connectome are similar to those put forward at the start of the Human Genome Project — and he expects them to die down once the data start coming through. Indeed, Lichtman is so convinced of the connectome’s value that he hopes it could transform the way that neuroscientists study the brain. He says that the typical experimental process, in which a scientist sets out to test a specific hypothesis, is simply incapable of deciphering something as complex as the human mind. “History has shown that it’s rather tough to come up with good hypotheses about how the brain works,” he says. He thinks that scientists should rely more on inductive reasoning — the staple of nineteenth-century scientists — in which hypotheses are generated only after careful observation. “We need to rediscover the power of looking,” he says. “You can learn a tremendous amount, and generate some interesting theories, just by staring at pictures of the brain.”

Lichtman is perhaps best known for pictures generated by Brainbow, a technique unveiled in November 2007, with which his team engineered individual neurons to emit more than 90 different shades of fluorescent light, from cerulean blue to heather grey, rendering mouse brains as Impressionist landscapes². Lichtman is proud of the images — “People always ask me for screensavers and stuff” — but he says that the beauty of the Brainbow is actually a side effect of the biology. “The prettiness is just the structure of the brain,” he says. “All I did was make the structure visible.”

Because each neuron is labelled with a different hue, Lichtman and others could start

to untangle the knot of neural connections in the mouse brain. In this sense, the Brainbow represents an important milestone, as it promises to advance a scientific goal that was first outlined in the 1880s, when the Spanish physiologist Santiago Ramón y Cajal set out to trace the microscopic structure of the nervous system. He used a technique developed by Camillo Golgi that darkly stained a few cells in brain tissue with silver chromate salt. Although Ramón y Cajal was able to decipher the layout of individual cells — he compared its shape to the branches of a tree — the monochromatic pictures made it difficult to parse the connections between two neurons that were identically labelled. Where did one cell end and the other begin?

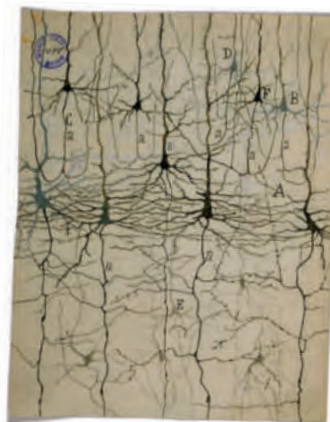
Context is everything

Lichtman argues that the difficulty of this parsing problem has led neuroscientists to neglect neuronal connections and circuits

ever since, and instead fixate on the electrophysiological activity of individual cells and the biochemistry of synapses. “We’ve developed all these powerful tools that let us see what one neuron is doing,” Lichtman says. But in his view, a brain cell by itself can’t do anything; it is defined by its web. This is why, he says, it is so essential to develop tools that allow scientists to visualize neural cells and their connections on a massive scale.

In 1970, neuroscientist Paul Redfern at the University of Liverpool, UK, described a peculiar aspect of the nervous

system³. He measured the electrical signals that stimulate muscles in a newborn rat, and watched how they changed in the first 2–3 weeks of its life. Based on these data, he proposed that when a rat is newborn, each muscle fibre makes connections with a few dozen neurons that grow out from the spinal cord. Then a period of competition ensues until, within a few weeks, most of these connections disappear, leaving only one victorious neuron synapsed to each fibre. Redfern’s idea challenged the widespread assumption that the wiring of the nervous system is predetermined and precisely choreographed. And Lichtman, who came across the paper a few years later as an MD–PhD student already interested in the brain, at Washington University in St Louis, was captivated by the question of how the nervous system figured out which neuron would pair with which muscle fibre. “I remember



Santiago Ramón y Cajal drew the microscopic structure of neurons.

CAJAL INSTITUTE, CSIC, MADRID, SPAIN

reading that Redfern paper and thinking that that was just the most interesting problem," he says. "I wanted to understand the rules of the game."

Lichtman soon discovered why such a basic question remained unanswered: it was virtually impossible to visualize and track individual neurons over time. Although light microscopy had advanced radically since Ramón y Cajal, and scientists had found fluorescent dyes and other new staining techniques, most of these still rendered every neuron the same colour and so were unable to distinguish which cell connected to which. Think of the tangle of cables running from an overloaded socket: if the wires are all black, it's difficult to know which wire connects to which appliance. But if each wire is painted a distinct colour, it's suddenly possible to find the one to disconnect. The insight, which Lichtman began working on as a young assistant professor at Washington University, was that the easiest way to distinguish these cells was with a splash of colour.

His first attempt, published in 1985, involved electrically stimulating axons so that they took up various fluorescent probes⁴. The experiment was successful — each neuron was a unique colour — but painstaking, because the neurons had to be stimulated one at a time. Lichtman knew he would need to take a different tack to study neurons en masse, and the development of green fluorescent protein in the 1990s, followed by its many-coloured spin-offs, gave him the tools he needed.

In 2000, Lichtman collaborated with Joshua Sanes, a professor of molecular biology who was then at Washington University but who moved to Harvard University in 2004, the same time as Lichtman. They began generating lines

of mice that expressed different fluorescent proteins in some cells of their nervous system, so that some mice had neon-blue neurons whereas others had cells of red, green or yellow. The results were extremely variable, with some mouse strains expressing a fluorescent gene everywhere and others showing fluorescence in only a small percentage of cells. Sanes and Lichtman began crossing these different lines of mice, so that a strain expressing a few blue-labelled cells would be mated with a 'yellow' line with many labelled cells. The end result was mouse brains with neurons expressing three different shades: blue, yellow and green⁵. "That's when I started to get excited," Lichtman remembers. "We still couldn't see that much, but I began to appreciate how powerful these fluorescent cells could be, if only we could engineer more colours."

In 2002, Jean Livet joined the Lichtman lab as a postdoc and immediately began working on the problem. "Jeff would always say to me, 'More colours! We need more colours!'" says Livet, now at the Vision Institute in Paris. "The idea of a fluorescent brain became like an obsession." Livet's elegant solution, which he devised after several weeks of "doodling in the lab notebook", was to use a DNA-engineering system called *Cre/lox*. Cre is an enzyme that deletes or inverts any section of DNA flanked by *lox* sequences. (The *Cre/lox* system is often used to delete genes from specific tissues and create knockout mouse strains.) Livet realized

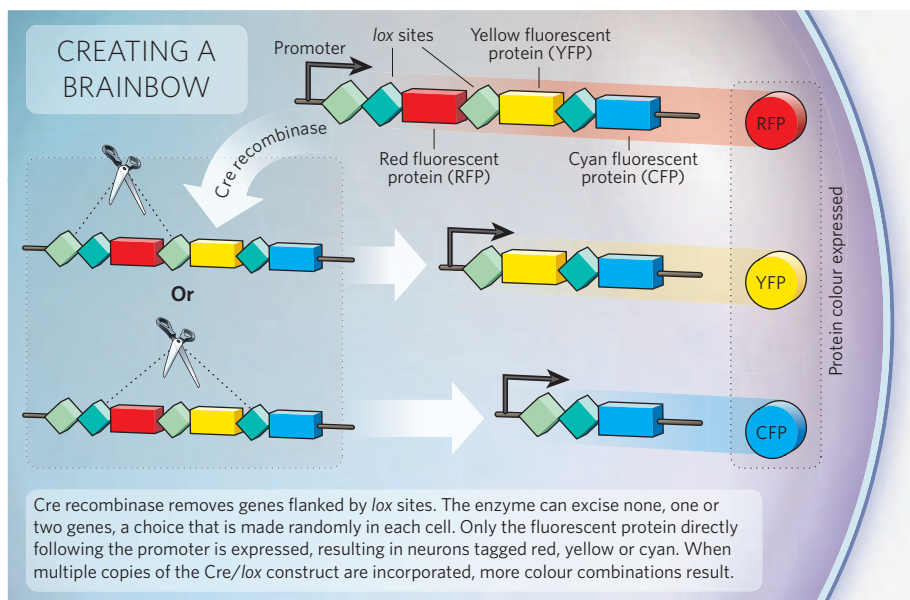
Brainbow-coloured nerve cells in the brainstem (main picture), in the dentate gyrus of the hippocampus (inset, top) and in a peripheral nerve.

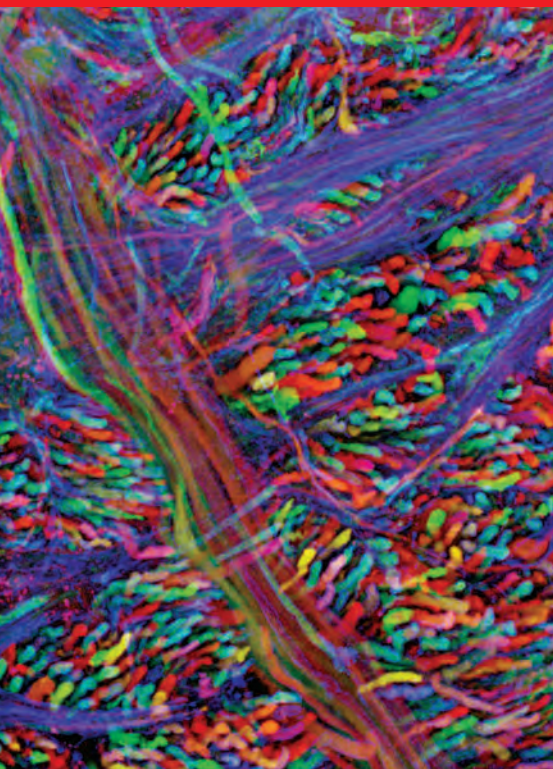
that if he could build a genetic construct that contained multiple fluorescent proteins flanked by *lox* sites — he chose red, blue and yellow — he could force the Cre enzyme to randomly 'choose' which colours to erase and which to leave (see 'Creating a Brainbow'). "It would be like rolling the dice in each cell," says Livet, "so you never know what colour you will get."

At the end of the Brainbow

The reality, however, far exceeded their optimistic imagination. Because the mice incorporated multiple copies of the genetic construct carrying red, blue and yellow proteins, the Cre enzyme mixed up a far more extensive colour palette. "We thought we would just get cells expressing a single fluorescent colour, such as blue or yellow," says Lichtman, "but instead we got cells expressing blue-blue-blue-yellow, or blue-yellow-yellow-yellow, and so on. It was a staggering result, to see a brain expressing 80 or 100 distinct colours." Other scientists immediately recognized the potential of the Brainbow (a name that Lichtman devised, and with which he is dearly pleased), and have begun applying the technique to visualize the nervous systems in a variety of lab animals, including zebrafish and fruitflies. "It's an incredibly exciting technique," says Insel. "We've had such a crude map of connections for so long, and this is one of those advances that allows us to really think about how the brain is wired at a cellular level."

With his fluorescently tagged mice, Lichtman finally had a way to solve the problem that had fascinated him since reading Redfern's paper about 25 years earlier. By making maps





of blood vessels and other landmarks visible under the microscope, he could return again and again to precisely the same spot of a neuromuscular junction in a newborn mouse's neck, and know from the neuron's colours exactly which cells remained and which were pruned back⁶. Researchers had mostly assumed that the pruning process followed the classic Hebbian model — “cells that fire together, wire together” — and that the cell with the most synapses on the target muscle, and so transmitting the most electrical impulses, would always gain control. But by observing the process, Lichtman has found that this isn't the case. “Sometimes, the cell with only 20% of the synaptic territory takes over,” he says. “The underdog wins.”

Lichtman says that neurons that are simultaneously competing to form synapses with several muscle fibres will deploy resources depending on the outcome of all those competitions. A cell that has yet to win a synaptic competition will be able to send more resources to its remaining synapses. (As Lichtman puts it, “being a loser makes you more likely to win somewhere else”.) The end result is an exquisitely organized circuit, in which every neuromuscular junction is properly plugged into the nervous system. “The Brainbow allows you to watch this competition in real time,” says Lichtman, who hopes to image similar competitions in the brains of mice. “You can see the purple cell win, or watch the turquoise cell retreat. It might seem disorderly, but this is how a brain is built, one competition at a time.”

Even as the Brainbow has been illuminating aspects of brain building, Lichtman has

been working on refining the method in his pursuit of the connectome. One of his priorities is to visualize the fine-grained branches of the neuropil, the web of dendrites and axons that protrude from either end of a neuron and form synapses with neighbouring cells. The neuropil is too thin to discern with ordinary light microscopes, whose resolution is fundamentally limited by the wavelength of light. This means that objects smaller than 200 nanometres can't be reliably detected. (A typical synaptic cleft, for instance, is between 20 and 40 nanometres, making it all but impossible to see.)

In the past five years, several teams have come up with methods to improve this resolution, allowing fluorescent light microscopy to approach the resolution of electron microscopy. Lichtman is now working to image the neuropil with Xiaowei Zhuang, a professor of chemistry at Harvard University who developed one such high-resolution technique called stochastic optical reconstruction microscopy (STORM). The advantage of this method over electron microscopy is that it can be readily combined with the spectral information of the Brainbow, so that the dendritic arbors of each cell are properly identified. Lichtman refers to this project as “BrainSTORM”. The challenge, however, is turning STORM — a labour-intensive method in which each image requires extensive computer processing — into an automated method capable of capturing image after image through the entire brain of a living mouse.

Gathering resources

Lichtman knows that mapping the brain is an epic and expensive undertaking, and it is not one that he can complete alone or with a single method. Some neural connections

will be best imaged with the Brainbow, BrainSTORM and other sophisticated microscopy techniques, whereas others — perhaps those buried too deep in the brain to be seen by fluorescence imaging — will be better viewed with ATLUM and electron microscopy. Gathering and processing

these images for just one brain will require a new level of standardization and industrialization, something he is working towards with the electron-microscope farm and automated BrainSTORM. “The sheer quantity of connections means that all of these techniques need to be extremely scalable, so that we can construct and analyse massive data sets,” he says.

Lichtman is starting to collect the resources he will need to work on this scale, and is leading a ‘connectome consortium’ that includes Zhuang and Sanes. Last November, the group



Jeff Lichtman's microtome turns mouse brains into a single strip of tissue, fixed to a plastic film.

won a US\$10-million grant from the Howard Hughes Medical Institute to show that a high-throughput version of BrainSTORM is feasible. The NIH is funding the development of the next generation of Brainbow mice, and Microsoft Research is assisting with some of the complex computational aspects of the project. Given the resources, Lichtman is confident that the connectome will be completed. He cites recent large-scale neuroscientific projects, such as the gene-expression map created for the Allen Brain Atlas, as proof that such an ambitious endeavour is possible.

And in the meantime, Lichtman takes solace in the beauty of his Brainbow images. If other neuroscientists can appreciate their full potential, he thinks, it could change the way they think about the brain. They will see the organ not as a mass of discrete anatomical areas, or as a collection of chemical ingredients, but as a vast loom of connected cells.

“This is what we are,” Lichtman says. “Lots and lots of connections.” ■

Jonah Lehrer is a freelance writer based in Boston, Massachusetts.

1. Crick, F. & Jones, E. *Nature* **361**, 109–110 (1993).
2. Livet, J. *et al.* *Nature* **450**, 56–62 (2007).
3. Redfern, P. A. *J. Physiol. (Lond.)* **209**, 701–709 (1970).
4. Lichtman, J. W., Wilkinson, R. S. & Rich, M. M. *Nature* **314**, 357–359 (1985).
5. Feng, G. *et al.* *Neuron* **28**, 41–51 (2000).
6. Walsh, M. K. & Lichtman, J. W. *Neuron* **37**, 67–73 (2003).

“This is one of those advances that allows us to really think about how the brain is wired at a cellular level.”

— Thomas Insel



SECRET SIGNALS

Are people's interactions driven by a primitive, non-linguistic type of communication? **Mark Buchanan** looks at how modern technology can reveal the basis of our powers of persuasion.

You answer the telephone and hear a perky voice: "Hello, this is Michelle from Brown's computers. I wonder if you have a few moments to talk about some of our new products?"

Sales call! Your first impulse is to slam the receiver down. But — well, at least the woman is polite. And knowledgeable. And...

Fifteen minutes later, as you give the ever-cheerful Michelle your credit-card number to purchase a new Super Zippy hard drive, you tell yourself what a good deal it is, and how much you've been needing the thing.

Or do you? Computer scientist Alex Pentland from the media lab at the Massachusetts Institute of Technology (MIT) in Cambridge would argue that your decision had very little to do with what the saleswoman said, and everything to do with how she said it — her intonation, say, or the fluctuating pace and amplitude of her voice. The sale was probably made within the first few seconds, he says, guided by signals you did not even perceive.

"Human behaviour is much more predictable than is generally thought," says Pentland. A person's responses can often be explained by "non-linguistic behaviours of other people and

simple instincts for social display and response, without any recourse to conscious cognition".

This 'second channel' of human communication acts in parallel with that based on rational thinking and verbal communication, and it is much more important in human affairs than most people like to think, says Pentland. Yet evidence for it has been accumulating in the laboratory for decades. And now modern technology has made it possible to monitor these social signals in spontaneous, natural settings on a scale that was not possible before.

"Collecting this kind of spontaneous data is extremely hard," says neuroscientist Anna Esposito of the International Institute for Advanced Scientific Studies in Vietri sul Mare, Italy. "But Alex has found a way to do it."

Indeed, over the past decade Pentland and his team have developed a range of wearable devices that include electronic badges, modified personal digital assistants (PDAs) and specially configured mobile phones. These instruments can track not only a person's location, but also his or her behavioural details — such as intonation and upper-body movements. The resulting data can then be analysed for patterns of meaningful social signals.

Pentland and his colleagues have already done multiple experiments with this technology at call centres and elsewhere, and are now moving into sites such as banks and hospitals, where they collect data on hundreds of people over many months to reveal the hidden communications in organizations. The potential reward, Pentland says, is a richer, more complete and more objective view of human interaction — with our inherent bias toward what's conscious and verbal taken out of the equation.

Out of control

"It is difficult for people to accept," says psychologist John Bargh of Yale University in New Haven, Connecticut, a pioneer in the study of subliminal influences on human behaviour, but much of a person's everyday life "is determined not by their conscious intentions and deliberate choices, but by mental processes put into motion by their environment".

"A gazillion experiments show that I can flash something at you so fast you don't see it, yet the information does bias you towards one decision as opposed to another," says cognitive psychologist Michael Gazzaniga of

ILLUSTRATIONS BY J. MAGEE

the University of California at Santa Barbara. Moreover, he says, the literature is full of experiments showing that conscious explanations for our behaviour are often just rationalizations invented after the fact. He cites the example of a patient whose corpus callosum had been severed as a treatment for epilepsy, making it impossible for one side of the brain to communicate with the other. Gazzaniga and his colleagues presented the word 'walk' to the patient's left visual field, which corresponds to the right side of the brain. When the patient stood up and began walking, they asked him why; the right side of the patient's brain had been shown to lack the ability to process language. His left brain, which never received the walk command, but which handles language processing, quickly invented a logical explanation: "I wanted to go get a Coke."

Analogous effects have been found many times in healthy people. In the early 1990s, for example, psychologists Robert Rosenthal of the University of California, Riverside, and Nalini Ambady of Tufts University in Medford, Massachusetts, asked college students to give reasons for liking or disliking their instructors. The students tended to mention the instructors' friendliness or the clarity of their lectures, attributing their rating to conscious assessment. But Rosenthal and Ambady found that most of this is simply rationalization. The researchers could predict how around 70% of the students would rate an instructor just by analysing the instructor's body language in 30 seconds of soundless video (N. Ambady and R. Rosenthal, *J. Pers. Soc. Psychol.* **64**, 431–441; 1993).

Pentland's efforts to track such phenomena in the wild, so to speak, date back to the early 2000s. In one experiment, the group took data over a period of several months in 2005, as operators at a call centre in the United Kingdom tried to make sales over the telephone. The operators were fitted with small electronic devices that measured variations in their tone and pitch, but not the specific words they used. Yet the researchers were able to devise an algorithm that could predict whether a call would result in a sale from only a few seconds of data. Successful operators, it turned out, spoke little and listened more. And when they did speak, their voices fluctuated strongly in amplitude and pitch, suggesting interest and responsiveness.

"If operators do it right," says Pentland, "they are almost certain to be successful." Indeed, the call centre now uses this new understanding to train its operators to sell more effectively, and to recruit people who have the right speech patterns. Other experiments suggest that such measures could improve sales success by as much as 20%, says Pentland, which is worth millions to large industries.

And in a new experiment involving a 45-minute mock salary negotiation between students in a business school, Pentland says that by combining several display signals from the first 5 minutes of the negotiation, his team could predict who would come out on top with 87% accuracy.

"Human behaviour is much more predictable than is generally thought."
— Alex Pentland

As a result of such experiments, the MIT group has identified a handful of common social signals that predict the outcomes of sales pitches, the success of bluffing in poker, even subjective judgements of trust. These signals include the 'activity level', effectively the fraction of time the person speaks; their 'engagement' or how much a person drives the conversation; and 'mirroring', which occurs when one participant subconsciously copies another's prosody and gesture.

Pentland is well aware that not everyone has embraced this vision of a hidden, pervasive 'second channel' in human affairs. Although the idea is reasonably well accepted for other animals, Pentland says that the reluctance to accept it in humans lies in part because of an inherent bias in how science looks at human behaviour versus that of other species. "If our data were collected from ape troops," he says, "and we altered the semantically loaded labels a bit, talked about 'forage' instead of 'work', 'food access' instead of 'salary', they would feel entirely unsurprising."

Keep it simple

Behavioural science, as he sees it, ought to seek the simplest explanation for human behaviour first, looking to simple social signals, before constructing more complicated explanations based on language and conscious reasoning. Indeed, he says, humans lived in social groups long before language evolved, and the language function presumably exists on top of a more archaic brain system for non-linguistic social signalling.

The behaviour of non-human primates supports this idea, says primatologist Frans de Waal of Emory University in Atlanta, Georgia. Apes, chimpanzees and other primates — our close evolutionary cousins — lack anything like our facility for language, yet still lead sophisticated social lives through displays of power, meaningful noises and facial expressions.

So it is "incredibly naive," he says, to take conscious verbal communication as the primary way that people respond to each other.

In the future, Pentland hopes, the type of work he and his colleagues have been doing can be expanded to look in much more detail at human social interactions in larger groups. In an ongoing experiment at a large German bank, for example, they are using their sensors to focus on personal characteristics that are thought to be linked to group creativity. According to recent work on creativity, says computer scientist Peter Gloor, who studies collaborative innovation networks at MIT's



Alex Pentland (seated) and his team have come up with wearable devices that record speech patterns and movement.

Sloan School of Management and who has collaborated with Pentland, creative people tend to be more open and agreeable, and less neurotic than others, and they tend to fluctuate more between extroversion and introversion. These traits can be assessed with standard psychological questionnaires, but Pentland's group thinks the sensors can do the job more effectively, giving managers more reliable ways to identify patterns of human behaviour, and thereby to assemble the best possible creative teams.

The group had 22 bank employees wear data-collecting badges for one month, and studied how the data revealed personal characteristics relevant to creativity. For example, from the sensor data, the team was able to construct a 'contribution index' for each person that measured, roughly speaking, their pro-activeness in interpersonal interactions. Someone with contribution index of 1 looks frequently at other people. Someone with an index of -1 is only ever looked at, he or she never looks another actor squarely in the face. The group then compared this measure with descriptors of each individual as assessed in a standard psychological test, judging variables such as the person's 'openness' towards fantasy, aesthetics, feelings and new ideas, or their 'extroversion', spontaneous warmth, gregariousness, assertiveness and activity.

High values of the index, they found, correlated very strongly with the psychological assessment of extroversion. "The more one person looks at others," says Pentland, "the more of an extrovert they seem to be."

Neural networking

Pentland's team also looked at the social networks in which the employees took part. In particular, the data showed that individuals who scored more highly on the 'openness' variables were much more likely than others to shift their network position from day to day, or even within a day. Part of the time they might act as a central hub in the social network of a creative team; at other times they would have much less interaction and sit on the periphery. People who are more open to new ideas, says Gloor, "change network position frequently, being highly central at one time and less central at others".

These techniques, he suggests, offer a fundamentally new way to look at organizations, as they give specific, quantitative measures of human traits and behaviour. One possible objection to such studies is as old as social science: people may change their behaviour

when they're observed. But Pentland and his colleagues think this worry is overblown. In this particular experiment, they point out, the employees knew only that their behaviour was being monitored, and were not aware of specifically what was being recorded or all the ways in which the data would be analysed. Moreover, the measurements went on for a full month. While people can take on particular roles in the short term, says Gloor, research suggests that it is harder to do so over long periods of time. Pentland is planning experiments over the next few years that could settle this question.

But psychologist Bernard Rimé of the Catholic University of Louvain in Belgium has other reservations. Some of Pentland's findings, he says, have been known since the study of non-verbal communication first took off back in the 1960s. Back then, Rimé recalls, call-centre operators "were trained to smile when talking, because smiling indeed influences the vocal signal, communicating warmth and positive affect". He acknowledges that the new technology makes this research more powerful, but wonders whether it will really help to tackle the toughest challenges of the field. In particular, he says that the relative simplicity of predicting some kinds of human behaviour may paint a false picture due to the formidable diversity and contextual variety of human signalling. The

link between environmental cues and displayed responses is sometimes simple, as in the call-centre experiments. But more frequently, Rimé suggests, many other factors interfere, such as past experiences, personal habits, inherited traits, intellectual abilities and shared knowledge about the situation. "In this case," he says, "predicting people's behaviour becomes quite a challenging task, if possible at all."

Pentland agrees that this is the key challenge, but suggests that the sensors are orders of magnitude more powerful than what was used to study human non-verbal interactions in the past. "People used to measure mostly short-term features such as nods or smiles, whereas we can make continuous, quantitative measurements over much longer times," he says. "We can also examine precise details of frequency and amplitude, something you can't do easily without automated tools."

The earlier work, he suggests, was akin to trying to understand written text by looking just at individual letters, ignoring words or sentences. Moreover, he suggests, almost all previous work was done in the lab, and quantification was all but impossible in anthropological-style field work.

"In contrast," Pentland says, "we are taking people in real situations, in day-to-day work settings over months, and finding lots of reliable and directly predictive relationships."

One thing he does admit is that experiments of this sort raise the spectre of Big-Brother-style intrusiveness. Pentland hopes that corporations won't look at the technology as just another way to spy on employees, which would almost guarantee resentment and loss of morale. He says that many of the problems could be addressed if the companies followed the protocol used in his own group's experiments: the data were first stored locally on each subject's machine, so that at the end of the day, he or she could review what had been collected and decide whether it would be shared or permanently deleted. Pentland also says that employees should be given the ability to turn off the device if they wish.

If these kinds of protections are respected, he says, then the devices could lead to fundamentally better science, including a deeper knowledge of that second channel of human social interaction. "People have been studying this kind of stuff for a long time," says Gazzaniga, "but Alex is raising it up to another level. It is very clever stuff."

Mark Buchanan is a science writer based in the United Kingdom. He is author of *The Social Atom*.

"Collecting this kind of spontaneous data is extremely hard. But Alex has found a way to do it."

— Anna Esposito



CORRESPONDENCE

These letters respond to the Commentary 'Towards responsible use of cognitive-enhancing drugs by the healthy' by Henry Greely and colleagues (*Nature* **456**, 702–705; 2008).

Risks and benefits may turn out to be finely balanced

SIR — This Commentary is the latest in a series of expert-led deliberations on the prospects and implications of cognitive-enhancing drugs (see, for example, refs 1–3). Much of the debate on enhancement, as illustrated by the Commentary, is highly speculative and rests on assumptions that are not well grounded in evidence or experience. There are three key problematic areas.

First, efficacy — the claimed and assumed benefits are often exaggerated. Careful analysis of trial data suggests that any cognitive-enhancing effects of these drugs in healthy humans are at best modest and mixed, and at worst little better than placebo.

Second, safety — very few drugs are completely without adverse effects, especially when used chronically. In the absence of data on the long-term safety implications of these drugs, it is premature to be helping society "accept the benefits of enhancement" when the balance between risk and benefit might be much narrower than assumed.

Third, demand — there is little empirical evidence that large numbers of people will use (or are interested in using) enhancers on a routine basis. There is partial or anecdotal evidence of use in specific situations (for example, examinations), but equally, other partial or anecdotal evidence suggests considerable resistance to chronic use among the general public.

If enough positive assumptions are made about these key issues, then almost any technology can look attractive or inevitable. The speculation offered in the Commentary may be of interest to academic debates in philosophy.

But what is needed is realism, based on a more sober evidence-based assessment that does not create unrealistic expectations about either the potential benefits, or the threats, to individuals and society.

Simon J. Williams Department of Sociology, University of Warwick, Coventry CV4 7AL, UK
e-mail: s.j.williams@warwick.ac.uk
Paul Martin Institute for Science and Society, University of Nottingham, University Park, Nottingham NG7 2RD, UK

1. Academy of Medical Sciences *Brain Science, Addiction and Drugs* (AMS, 2008).
2. British Medical Association *Boosting Your Brain Power: Ethical Aspects of Cognitive Enhancements* (BMA, 2007).
3. Foresight *Drugs Futures 2025?* (UK Department of Trade and Industry, 2005).

Much ado about cognitive enhancement

SIR — Henry Greely and colleagues call for answers to several controversial questions regarding the use of drugs by healthy people to boost cognitive performance. The most important scientific and ethical concern they raise is safety, not least because the pressure that leads people to enhance their performance might also be a crucial trigger to mental disorder. This is particularly likely when combined with sleep deprivation and anxiety caused by aggressive competition, as we have already learned from the indiscriminate use of amphetamines.

However, it would not be surprising if the repurposing of these drugs has less of an impact than expected by some and feared by others. Myriad personality traits are just as important as memory or 'intelligence' in the overall scheme of a successful life. Studies of gifted or 'savant'

children show that self-confidence, discipline, focus, drive, resilience and social skills are highly complex personality traits, often found in successful people (see, for example, E. Winner *Gifted Children: Myths and Realities*; Basic Books, 1996).

Using medications to improve cognitive performance might be relevant in the short term. But a fully successful future will always depend on two very singular human features: eagerness to excel and setting a high standard of achievement.

João Ricardo Oliveira Neuropsychiatry Department and Keizo Asami Laboratory, Federal University of Pernambuco, 50670-901, Recife-PE, Brazil

A medical view of potential adverse effects

SIR — Most seasoned physicians have had the sobering experience of prescribing medications that, despite good intentions, caused bad outcomes. They would call for

louder notes of caution than those expressed in this Commentary when considering the safety of 'cognitive-enhancing' drugs such as Ritalin and Adderall.

The authors do not mention the US Food and Drug Administration warning on the packets of both of these drugs. Printed in capitals in a black box, it includes phrases such as: "amphetamines have a high potential for abuse. Administration of amphetamines for prolonged periods of time may lead to drug dependence ... Misuse of amphetamine may cause sudden death and serious cardiovascular adverse effects."

This warning does not cover other rare but serious side effects, such as Stevens-Johnson syndrome (a serious skin reaction) or toxic psychosis. Furthermore, the incidence of serious cardiac arrhythmias is likely to be higher in older people with incipient cardiovascular disease — likely consumers of 'healthy' enhancement.

Further reason for caution in advocating neuroenhancers is the disproportionate advantage the



Early scientific visitors found mammalian fossils awaiting discovery in apothecary shops

Xu Xing on the discovery of the Peking Man fossils, page 538

drugs, if effective, would confer on the wealthy. The authors' acknowledgment of existing disturbing inequities does not mean that we should add more.

A responsible position would be to call for a moratorium on the use of enhancers until enforceable policies to minimize socioeconomic disparities are in place, research into the use and impact of these drugs is completed, information on risks and benefits is broadly disseminated — and physicians, educators and regulators have articulated professional normative positions.

Anjan Chatterjee Department of Neurology and Center for Cognitive Neuroscience, University of Pennsylvania, Philadelphia, Pennsylvania 19104, USA
e-mail: anjan@mail.med.upenn.edu

Recall of learned information may rely on taking drug again

SIR — Henry Greely and colleagues identify critical areas of public discussion about perceptions and use of drugs that are alleged or expected to improve cognition.

Stimulants and other drugs proposed as potential cognitive enhancers are known to create profound state dependence, a phenomenon in which information or associations learned while 'under the influence' of a drug will later be remembered or used only when the learner has again taken the drug. Thus, individuals who use amphetamines to improve their learning of new information may indeed learn slightly faster or with less effort than those who do not use such drugs. Later, however, they may not remember or use the learned information unless they take amphetamines or related drugs again.

How and when state dependence occurs has been studied extensively in humans and other animals, in well-controlled learning tasks in laboratory

settings. State dependency of cognitive enhancers would dramatically influence drug use, the permanence of learning and the ability to use information in new conditions. Indeed, state dependence can complicate clinical use of pharmacotherapies for such disorders as anxiety and attention-deficit hyperactivity disorder.

Greely and colleagues note critical research and policy questions that societies must consider to shape expectations about putative cognitive enhancers. We urge that the discussion includes the known and profound state-dependent effects of these agents.

Alice M. Young Department of Pharmacology and Neuroscience, Texas Tech University Health Sciences Center, 3601 4th Street, STOP 6592, Lubbock, Texas 79430, USA
e-mail: alice.young@ttuhsc.edu
Francis C. Colpaert Institut de Recherche Pierre Fabre, 3, rue des Satellites, BP 94244, 31432 Toulouse Cedex 4, France

Patterns of drug use have varied throughout history

SIR — Current issues are assessed by Henry Greely and colleagues, but their Commentary contains a bias consistent with current Western culture. The use of these drugs is probably older than recorded history. They have often been used regardless of social convention or rules — and have had impacts on societies.

In the 1960s, 'mind-altering drugs' had a different connotation from the present, exemplified by Timothy Leary's "Turn on, tune in and drop out" philosophy. Drugs such as marijuana and LSD were said to enhance individual thinking and creativity, but research both on the mental effects of these drugs and on their use has decreased. Since then, the use of mind-altering drugs has shifted towards

enhancing performance, usually with amphetamine analogues. It seems that these are becoming acceptable when used for the goal of efficient production in standardized ways.

Don Burnap 11 Oakland Street, Rapid City, South Dakota 57701, USA

The five preceding letters are a selection of many comments on this Commentary that were submitted to Correspondence. Many other reactions from readers have been posted in a long and lively online discussion forum at Nature Network, including the following anonymous contributions.

Careful use helps me do better research, and society benefits

SIR — I commend the authors of this Commentary on what I think is a fair and insightful piece. I suspect many of the negative commenters are guilty of default outrage without careful thought.

I find that my own occasional, metered use of these drugs can make astounding increases in my ability as a researcher — which results in tangible benefit to society. It's not a competition, I'm not taking an exam. I'm doing research; research that I hope may one day improve the lives of many. I exercise, sleep, eat well and I drink coffee. Yet sometimes that significant extra boost allows me to spend 12 hours successfully working through mathematics that for weeks I was previously unequal to solving. Why is this the act of a social criminal?

Current attitudes towards such drugs seem to be that they are good if you need them to become equal, but wrong if you want to become more than equal. Can we really be so quick to condemn a striving to better ourselves? Should we tell brighter students to hold back to the median? I think not. This issue is not black and white; it requires the careful grey-scale considerations

the Commentary authors recommend.

It is true that many physicians and biomedical researchers have placed themselves in quite a tangled conflict-of-interest web, and that this compromise can be dangerous.

Some of the authors of this Commentary may have some conflict of interest, which thankfully *Nature* requires authors to disclose. However, that possible conflict of interest does not release you, the reader, from your obligation to rationally and carefully consider their argument. They are not wrong just because some of them consult for pharmaceutical companies.

Enhancement means a broader role for physicians

SIR — This Commentary raises a wider issue of perceived responsibility. The traditional role of physician as healer does not sit with the category of enhancement. Plastic surgery serves as a good analogy here, with views remaining varied on the ultimate responsibility. But with planned, novel, pharmacological intervention, physicians must surely be party to the cause, and thus a broadening of their role would be necessary.

Ultimately, the call for risk-benefit research and a fuller understanding of mechanisms is therefore welcome, but the real beneficiaries, at least in the short term, are likely to be dominated by the genuinely needy — neurological and psychiatric patients. These groups have had their needs for cognitive enhancement unmet for far too long.

Further discussion of the Commentary and these Correspondence contributions is welcome at Nature Network. Please visit <http://tinyurl.com/6nyu29> to have your say.

COMMENTARY

Pruning the regulatory tree

For human-subjects research, maximum regulation does not mean maximum protection.

Stop regulating minimal risk research, say **Scott Kim, Peter Ubel and Raymond De Vries**.

The rapid improvement of the US system to protect research subjects is an important human-rights achievement, but it has grown in ways that require careful cultivation and, at times, cutting back.

Consider a much-discussed study in which Peter Pronovost, a critical-care researcher at the Johns Hopkins University in Baltimore, Maryland, tested how using a simple checklist of scientifically proven steps, such as hand washing, might reduce catheter-induced infections. The study enlisted 108 intensive-care units in Michigan and over the course of 18 months it saved an estimated 1,500 lives and US\$175 million through shorter hospital stays. But not long after the results were published, the Office for Human Research Protections (OHRP) at the US Department of Health and Human Services ordered the hospitals to halt data collection on the study.

Although the OHRP agreed that the study was minimal risk and did not need informed consent, it concluded¹ that Johns Hopkins University had incorrectly deemed the study exempt from review by institutional review boards (IRBs). Without this exemption, the study would have taken longer, cost more and resulted in greater variation between procedures at different study sites (given the involvement of dozens of IRBs). This is not a case of abuse or even misinterpretation of current regulations. Rather, it illustrates a serious flaw in the regulations: the requirement of extensive and expensive protocol reviews that yield no ethical benefit.

Many are frustrated with the current system for protecting research subjects: some find it too flimsy, others see it as too overbearing². This tension paralyzes reform efforts. We propose a way around the stalemate through a simple regulatory change that is far-reaching, equitable and yet low risk: exempt minimal-risk research from IRB review.

Low-risk research protocols are common in several disciplines including health-services research, education research, history and the social sciences. The US Federal regulations define minimal-risk research as that in which "the probability and magnitude of harm or discomfort anticipated in the research are not greater in and of themselves than those ordinarily encountered in daily life or during the

performance of routine physical or psychological examinations or tests."³ Review boards routinely use the concept in making decisions, but current oversight is complex and extensive (see table).

We propose that institutions streamline oversight of minimal-risk research by requiring investigators to complete a brief application describing research procedures, risks, burdens and the potential loss of otherwise expected benefits to the subjects. An institution-designated person reviews the application, and exempted protocols would not be subject to further IRB review. The application becomes the project's registration and serves as an accountability document. Note that our proposal is not meant to apply to minimal-risk

research involving direct interactions with people who are incapable of informed consent, because research with such people raises special ethical concerns.

How would our proposal affect subject safety? Since only those studies with minimal chance of minimal harm are exempted, the effect on subject welfare would be minimal. What about the effect on informed consent and subject autonomy? Consider studies that require direct interaction with subjects. Informal voluntary consent should still be given by subjects. This is the prevailing practice for low-risk interpersonal interactions of everyday life in a liberal democratic society, and should suffice for minimal-risk research interactions too. Indeed, formal consent is

contrary to the implicit, intuitive norms of communication and can even cause mistrust⁴.

Current regulations justify exceptions to formal informed consent mainly by appealing to minimal risk. They allow verbal consent rather than the usual written consent largely based on minimal-risk considerations⁵. Informed consent itself can be waived if the study is minimal risk and other conditions are met³. We believe that the minimal-risk criterion serves as the sole ethical justification of these waivers; other regulatory conditions (such as the requirement that the research would not be 'practicable' without the waiver) provide no additional ethical justification.

The burdens of oversight

Although the ethical benefits of regulating minimal-risk research are negligible, the costs are not. The IRB system is widely recognized as being underfunded² yet a 2005 study⁵ found that 41% of all new protocols reviewed by US academic medical centre IRBs are expedited (and thus minimal risk). The median annual cost for a medical-centre IRB was \$750,000. Because expedited reviews cost about the same as full reviews⁵, the median cost of expedited reviews is approximately \$300,000 per year. And because 43% of IRBs surveyed do not pay their review-board members (who are generally highly remunerated professionals), these costs represent an underestimate of true costs. Moreover, minimal-risk-research reviews are likely to be more common at non-medical centre IRBs. At our institution (a major research university with a medical centre),

"At least half of institutional-review-board costs are devoted to evaluating minimal-risk research."

EXISTING REVIEW PROCESSES FOR MINIMAL-RISK RESEARCH

Current exemption process ³	Current expedited review process ³
Researcher submits application — type varies by institution.	Researcher submits a full IRB application.
Institution-designated person determines study is minimal risk according to de facto standard ¹² .	IRB designee determines whether the study is minimal risk.
The protocol must also meet one of six criteria for exemption.	The protocol must also meet one of nine criteria for expedited review. The IRB designee reviews protocol.
Some IRBs do not allow exemptions, regardless of federal criteria.	If informed consent is required, review board and investigator will exchange drafts of the consent form.
	If waiver/alteration of informed consent, or its documentation, is requested, further review is needed.
	Changes to the protocol require amendment applications to the IRB. Annual review is required.

IRB = institutional review board



WOODCUT BY D. PUDLES

56% of new IRB approvals are expedited, with additional 23% that are exempted⁶. Non-medical centre, low-volume IRBs (which review a disproportionate number of minimal-risk-research protocols) do not enjoy economies of scale⁷. Thus, at least half (and probably much more) of all direct IRB costs are devoted to expensive reviews of minimal-risk studies — resources that could be used to improve the oversight of riskier studies.

There are also significant financial and scientific costs to researchers and sponsors. Even expedited reviews can take several weeks for approval, and those few weeks in the brief life of a single sponsored project add up to a substantial amount when extrapolated to the thousands of such projects. Minor revisions to protocol can add weeks of delay and, when pressed for time, researchers sometimes accept sub-optimal science in order to comply with the rules.

Patients are affected because of lack of quality-improvement research. A report⁸ by an interdisciplinary study group notes that the current system has “generated disincentives to engage in quality improvement” and produces “inconsistent decisions, increases costs, retards improvement, and undermines respect for research review”. Quality-improvement research has tremendous implications for public health. Provonost’s study, for example, addresses

a problem responsible for 28,000 deaths and billions of dollars per year in the United States¹. There is considerable concern that the OHRP actions in this case will have a chilling effect on quality-improvement research.

Unnecessary oversight also generates other costs. Some researchers, when asked to conform to a system they believe is ethically unnecessary, may decide to violate the procedures⁹. Such behaviour can become culturally entrenched and passed on from mentor to trainee. We do not condone such behaviour, but it is counter-productive to knowingly support a regulatory system that undermines the very intent of those regulations. Researchers are also increasingly concerned that some types of human-subject regulation are a form of censorship and an infringement of academic freedom¹⁰.

Institutions have a tendency to impose on themselves requirements that are even more stringent than those required by law. But a new regulation that exempts minimal-risk research from IRB review would send a clear and unambiguous message that the government’s priority is not on intense oversight of low-risk research.

Can minimal-risk research determinations be made reliably and validly? Some may point to the debates over minimal risk in the paediatric literature as evidence that ‘minimal risk’

is a contested concept¹¹. But that literature is constrained by the special situation in paediatric research — whether a study is minimal risk can determine whether it is allowed at all. The situation is very different in our proposal, in which a determination of greater than minimal risk simply means that a protocol is non-exempt and in need of the usual institutional review.

Who would make the judgement that a protocol is minimal risk? The system already determines, routinely, which protocols are minimal risk. Although no policy is self-interpreting, most disagreements that arise will be about fuzzy boundaries rather than about the large domain of protocols that are clearly minimal risk. Such boundary disagreements can be conservatively handled without the danger of riskier research falling through the gaps. Even if the new line were drawn so conservatively (which we do not recommend) that only 50% of currently expedited protocols were made exempt, substantial resources would be freed for better uses. There will no doubt be an evolution in the interpretation of the concept when it is used to exempt rather than expedite a protocol review.

It is unethical to support a system that creates a significant financial, scientific, clinical and ethical burden with virtually no counterbalancing good. The maturation of any system involves trimming unnecessary parts, and redoubling the focus on areas that need further attention. Minimal-risk-research oversight should be pruned from the federal regulations and made exempt. Such pruning is necessary for the long-term health of the whole by freeing up scarce resources to where they are most needed. ■

Scott Kim and **Raymond De Vries** are at the Bioethics Program and **Peter Ubel** is at the Center for Behavioral and Decision Sciences in Medicine at the University of Michigan, 300 North Ingalls Street, Ann Arbor, MI 48109, USA.
e-mail: scottkim@med.umich.edu

1. Kuehn, B. M. *J. Am. Med. Assoc.* **299**, 1005–1006 (2008).
2. Emanuel, E. J. *et al. Ann. Intern. Med.* **141**, 282–291 (2004).
3. *Code of Federal Regulations Title 45: Public Welfare, Part 46: Protection of Human Subjects* (Department of Health and Human Services, 2005).
4. Singer, E., Hippler, H. J. & Schwarz, N. *Int. J. Public Opin. Res.* **4**, 256–268 (1992).
5. Sugarman, J. *et al. New Engl. J. Med.* **352**, 1825–1827 (2005).
6. www.research.umich.edu/hrpp/index.html
7. Wagner, T. H., Bhandari, A., Chadwick, G. L. & Nelson, D. K. *Acad. Med.* **78**, 638–644 (2003).
8. Lynn, J. *et al. Ann. Intern. Med.* **146**, 666–673 (2007).
9. Martinson, B. C., Anderson, M. S. & de Vries, R. *Nature* **435**, 737–738 (2005).
10. Hamburger, P. *Supreme Court Rev.* 271–354 (2004).
11. Wendler, D., Belsky, L., Thompson, K. M. & Emanuel, E. J. *J. Am. Med. Assoc.* **294**, 826–832 (2005).
12. Prentice, E. & Oki, G. in *Institutional Review Board: Management and Function* (eds Arndur, R. J. & Bankert, E.) 111–113 (Jones and Bartlett, 2002).

Discuss this article at <http://tinyurl.com/cnmq9s>.

ESSAY

Accelerating production of medical isotopes

The global problem of a safe and reliable supply of radioactive isotopes for use in critical hospital procedures can be solved with accelerators, not nuclear reactors, says **Thomas Ruth**.

Physicians and patients around the world are increasingly anxious about the shortage of nuclear isotopes used in medical imaging. A single radionuclide — technetium-99m (^{99m}Tc) — is used in four-fifths of all such imaging procedures worldwide. Yet its supply is remarkably fragile. In 2007, the unanticipated closure of a single nuclear-reactor facility in Canada slashed isotope stocks in North American hospitals by about 80%, causing much panic and the cancellation of 50,000 medical procedures over five weeks. Some patients went into surgery without the scans their doctors usually rely on. The medical-isotope supply came back online, but the fragility of the system did not improve. In 2008, isotope shortages struck again.

Shockingly, there are no dear plans in place for how to tackle this problem. My colleagues and I see viable mid-term and long-term solutions. Each relies on a very different plan. But both involve accelerators, rather than reactors.

Nuclear medicine, developed following the Second World War, relies on the injection of a radioactive compound into the bloodstream, and instruments that can then detect and map, in three dimensions, the distribution of the injected radioactivity and its decay products. It is used primarily to locate tumours in the body, monitor cardiac function following heart attacks, map blood flow in the brain, and guide surgery. About 70,000 diagnostic images are taken each day, worldwide.

Some 85% of the ^{99m}Tc used in Europe and North America comes from the decay of molybdenum-99 (^{99}Mo) made at just two reactor facilities: the High Flux Reactor in Petten, the Netherlands, and the National Research Universal reactor in Chalk River, Ontario, Canada. Supplies are shipped continuously to hospitals. Stockpiling the ^{99}Mo radioisotope for more than a couple of days is

impossible, as it has a half-life of just 66 hours.

In November 2007, the Chalk River facility was closed for one month owing to a regulatory dispute over its maintenance. The shutdown and subsequent isotope shortage became the subject of such a public outcry that the Canadian government ordered the reactor to restart; the president of the national Nuclear Safety Commission, who had ordered

for unrelated reasons. The press latched on to a comment that this was a 'perfect storm' for isotope availability. In December 2008, the Chalk River reactor was again shut for a few days for routine maintenance, but unexpected difficulties kept it down for longer than expected. This again put a pinch on supplies. Meanwhile, the reactor in Petten is not expected to reopen until February 2009 (recent reports indicate that it may even be later in the year).

Both reactors are relatively old, and it's not clear how long they might last. There are plans to replace the Petten reactor in 2015. The Chalk River facility's licence to operate ends in 2011, with an expected renewal to 2016; anything beyond that date is uncertain. The problem is critical. Earlier this month, the Union of Concerned Scientists issued a call for more medical-isotope production capacity in the United States to help secure supplies.

Unfortunately, there are no near-term or even long-term solutions being implemented that could provide a reliable and adequate supply for Europe and North America. The operator of the Chalk River facility was helping to build two dedicated radionuclide-producing replacement reactors, called the MAPLE reactors, which would have had the capacity to meet the entire world's supply needs. But in June 2008, the project was cancelled following extended technical difficulties that had delayed full operation for more than eight years. A new project in Australia might be able to make up 10–20% of North America's requirement within a few years of its anticipated opening this year. And there are plans to retrofit the Missouri University Research Reactor to produce ^{99}Mo , but a fully successful upgrade within the next five years will probably result in the reactor having the capacity to meet only half of North America's needs. This is not enough.



Canada's ageing Chalk River nuclear reactor (top) is prone to unexpected closures; supplies of medical isotopes for diagnoses (bottom) remain critical.

the shutdown, was removed from her position in the process. Then in August 2008, the reactor in Petten was closed because of a leak in the coolant system. There couldn't have been a worse time: the four next-largest facilities, including Chalk River, were already offline

ZUMA-NEWS/COM

BSIP, RAGUET/SPL

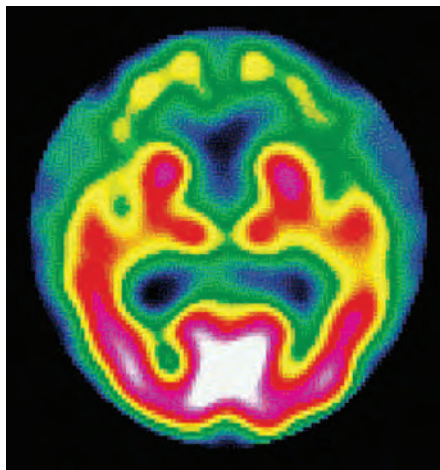
Complicating the scene further is the issue of using highly enriched uranium, containing about 93% of the nuclear isotope uranium-235 (^{235}U), in these reactors. Such reactors may use highly enriched uranium, as a fuel source and as a source material from which to create ^{99}Mo . The International Atomic Energy Agency and the US National Nuclear Security Administration have for years been involved in converting reactors to operate with low-enriched uranium fuel, so as to lower the risks associated with terrorists getting access to highly enriched material. But a problem remains with the target material. All major reactors currently in use bombard ^{235}U with neutrons to initiate fission and produce ^{99}Mo .

Future fission

There is, however, an alternative. Instead of using a reactor to fire neutrons at ^{235}U , an accelerator can fire photons at the relatively stable uranium isotope, uranium-238. This also spurs the needed fission process. The production rate of ^{99}Mo is several orders of magnitude lower, but this is outweighed by the advantage of using safer materials.

The challenge, then, is to generate a high-intensity beam of photons to produce commercially practical yields equivalent to those that can be generated by existing reactors. The science and engineering of high-intensity electron machines has advanced significantly over the past few years (led by DESY, the German electron synchrotron physics lab in Hamburg). Accelerator physicists believe that it is now possible to build a machine that fits the bill by converting accelerated electrons into light.

The Canadian government is interested enough in alternatives to reactor-produced ^{99}Mo that the Department of Natural Resources sponsored a workshop in October 2008, co-hosted by TRIUMF — Canada's national laboratory for particle and nuclear physics — where I work, to explore the possibility of designing and building such an electron linear accelerator. This workshop concluded that these accelerators could in principle be built and routinely operated, and that several research projects should be initiated to verify that. If an accelerator were given the green light to proceed by the Canadian government, perhaps within the next five years, it would take about three years and between US\$50 million and \$125 million to build. If our calculations are borne out, it would be capable of producing enough ^{99}Mo to meet Canada's needs (about 10% of North America's needs or 5% of world demand). So several machines would be required to replace the existing reactors. But these accelerators



A SPECT scan shows blood flow in the brain.

would be cheaper than reactors, which on average cost between US\$500 million and \$1 billion, as one does not need to worry about the same level of nuclear containment. Also, decommissioning of an accelerator facility is less complicated than for a reactor. Once feasibility is proven, they could be easily cranked out in high numbers.

Shifting picture

In the long term, accelerators of a different type will surely play a growing role in medical imaging. Although $^{99\text{m}}\text{Tc}$ is the dominant medical isotope, that picture is changing.

The type of scan that $^{99\text{m}}\text{Tc}$ is used for is called single photon emission computed tomography (SPECT). But an alternative type of scan, called positron emission tomography (PET), is coming to the fore. Both techniques make use of biologically active molecules tagged with radionuclides, but the radionuclides decay differently.

PET allows users to see fine details more clearly, largely thanks to the fact that it relies on a radio nuclide that emits two decay products in opposing directions at the same time. Tracing these decay products allows a PET system to define more precisely where the radiation has come from within the body, and how strong the radiation is at that point. The tracer used in SPECT, by contrast, emits only one decay product. Thus a SPECT system has a harder time tracing where that radiation came from, and cannot tell if a smaller signal is the result of less-intense radiation, or because that radiation travelled out from deeper within the body. The result is a blurrier picture.

In addition, the tracers used for PET are easier to attach to small molecules that bind to specific factors within the body, such as a

certain hormone. This can be very useful in making diagnoses.

PET uses isotopes that are made in an accelerator, not a reactor. But the half-lives of these radioisotopes are even shorter than those used for SPECT, so hospitals must be equipped with their own cyclotrons, or have access to a regional facility. The most versatile radionuclide for PET imaging, carbon-11, has a half-life of just 20 minutes, and the most commonly used PET tracer for oncology, fluorine-18, has a half-life of 110 minutes. This makes PET, for now, a more expensive proposition than SPECT.

Today, only 2,000 of the 12,500 nuclear medicine installations in the United States have PET scanners, and access to the needed radioisotopes is still limited. During the shortage at the end of 2007, a number of centres with access to PET successfully used this as an alternative to SPECT for cancer diagnoses. Ideally, every hospital would be equipped in this way. For this to become a reality, cyclotrons and PET scanners will have to become more affordable, and governments will have to provide incentives. In China, the government has almost leapfrogged SPECT and is investing directly in PET. Prices for PET scanners are dropping rapidly, and cyclotrons are becoming more affordable with time; but it will be a decade before PET can outcompete SPECT.

Time for action

Meanwhile, the major markets in the United States and Europe will continue to need $^{99}\text{Mo}/^{99\text{m}}\text{Tc}$. Decisions must be made quickly to determine whether the accelerator approach is viable and preferable to reactors while the replacement facilities can still be completed in a timely fashion.

At the time of writing, the Chalk River reactor has developed a leak that will require a significant shutdown for its repair. Both the Petten and Chalk River reactors are ageing, and such leaks are not unexpected. How much longer can these devices be kept in safe and efficient operation?

The Canadian government has an opportunity to continue its legacy of being the leader in the nuclear field. Although the production and delivery of radioisotopes for medicine has been in the private sector, the well-being of the citizens of the world requires significant involvement of both the private sector and governments at all levels. Action is required before it is too late.

Thomas Ruth is a research scientist at TRIUMF and a senior scientist at the British Columbia Cancer Agency, both in Vancouver, Canada. e-mail: truth@triumf.ca

"The problem is critical."

BOOKS & ARTS

Old bones unearth a new passion

Palaeontology in China has been invigorated by highly organized efforts to dig up bones for use in traditional Chinese medicine, explains **Xu Xing**.

**The People's Peking Man:
Popular Science and Human Identity in
Twentieth-Century China**

by Sigrid Schmalzer

University of Chicago Press: 2008.

368 pp. \$85

Participation in scientific discovery is generally restricted to academic elites, and the specialized character of many scientific fields can make them seem impenetrable to the public. However, many non-specialists find evolutionary science attractive because of the appeal of basic questions that ask who we are and where we came from. Evolutionary science also enjoys a broad social impact because of its tendency to become intertwined with religion, politics and culture. This is especially true in China, which, in spite of rapid progress, still lags behind western countries in most scientific disciplines. However, palaeontology and palaeoanthropology have emerged as exceptions because China's rich fossil resources both contribute to scientific advances in these fields and stimulate wide public interest in them.

The connections between palaeoanthropological discoveries, the public understanding of science in twentieth-century China, and broader issues of cultural transformation and national identity are the main themes of *The People's Peking Man*, a highly original book by US historian Sigrid Schmalzer. Schmalzer spent a year visiting the Institute of Vertebrate Paleontology and Paleoanthropology in Beijing, where many leading students of Chinese fossil hominids, such as Peking Man (skull reconstruction pictured, right), have been based over the years. In preparing her book, Schmalzer interviewed many active and retired Chinese scientists, as well as amateur enthusiasts and even the son of Pei Wenzhong, the palaeoanthropologist who in 1929 discovered the first skullcap of Peking Man.

Schmalzer focuses on social and intellectual history, and does not dwell on either the strictly scientific impact of the Peking Man fossils — now known to be of the early human species *Homo erectus* — or the frequently recounted story of their discovery. However, Schmalzer



China's rich availability of early human remains has inspired its citizens to get involved in fossil hunting.

does an excellent job of putting the finds in their proper historical and cultural context. For example, she emphasizes that non-specialists play a significant part in fossil discovery in China because many of them have long experience of collecting bones for medicinal use, and may know the fossil sites of a given area better than any qualified researcher.

The discovery of the legendary Peking Man fossils was greatly facilitated by this unique tradition, as Schmalzer explains. Early scientific visitors found mammalian fossils awaiting discovery in apothecary shops, and it was lay knowledge of where to find abundant 'dragon bones' that led scientists to the limestone fissure that eventually produced the Peking Man skullcaps. Although the practice of digging for bones to sell in apothecary shops is not as common today, commercial digging has increased in China owing to the expanding market for fossils as collector's items. Although such operations create their share of problems for the science of palaeontology,

they have brought large numbers of people into the search for fossils and have therefore resulted in the discovery of more specimens. Some significant recent advances in Chinese palaeontology could not have taken place without this commercial digging.

The contributions of non-specialists to science in China are not restricted to field activity, and the various forms of public participation in science represent one of Schmalzer's main interests. The state has long been interested in popularizing science for various purposes, including the eradication of superstition and its replacement with the principles of what it calls rational socialism. Chinese citizens, particularly in Mao Zedong's era, benefited from a good system of popular-science education and, in some cases, even had the opportunity to get directly involved in scientific activities. This emphasis on science dissemination and mass participation in science continues to have a considerable effect on modern Chinese society. One result is that technology and agriculture are better developed in China than the basic sciences, partly because the former are more easily understood and accessible to the general public. However, government efforts to bring science to the Chinese masses sometimes crossed over



STR/AFP/GETTY IMAGES

P. GOETHEL/ELUCK/SPL

into counterproductive attacks on scientific 'elitism', particularly during the Cultural Revolution of the late 1960s and early 1970s.

As a scientific discipline with profound implications for the origin and diversification of humans, palaeoanthropology has inevitably contributed to shaping human identity. In this regard, Schmalzer makes a strong case for the key role of palaeoanthropology in the intellectual history of modern China. Her book draws on a wide range of academic and popular sources to show how scientific ideas about human evolution have influenced political and ideological currents in Chinese society, and

how ideology has influenced — most scientists would probably say distorted — the scientific interpretations in return.

The People's Peking Man is not a primer on the fossil record of Chinese hominids or the latest interpretations of human evolution. In one or two places, Schmalzer even seems to flirt with postmodernist scepticism about the empirical validity of science, asserting that "the boundary between science and non-science is blurry, contested and constructed". However, Schmalzer's book finds a great deal to say about issues as diverse as the historical significance of Chinese fossil humans, the search for yetis (called *yeren*,

or 'wild people' in China), changing concepts of human identity, and the conflict between top-down science dissemination and bottom-up mass participation in Chinese science. She also explores other diverse issues that include the connections among science, politics, religion and culture, and the relationship between professional scientists and the general public. Schmalzer presents all these topics in a lively, accessible and thought-provoking way. ■

Xu Xing is a professor at the Institute of Vertebrate Paleontology and Paleoanthropology, Chinese Academy of Sciences, Beijing 100044, China. e-mail: xu.xing@ivpp.ac.cn

Thinking outside the box

Supersizing the Mind: Embodiment, Action, and Cognitive Extension

by Andy Clark

Oxford University Press: 2008. 320 pp. \$35

In *Supersizing the Mind*, philosopher Andy Clark makes the compelling argument that the mind extends beyond the body to include the tools, symbols and other artefacts we deploy to engage the world. According to Clark and other proponents of the 'extended mind' hypothesis, the laptop on which I am writing this review is coupled to my brain and has become part of my mind. Manipulating sentences on the screen can prompt new insights and new ways of conveying ideas, a reiterative cognitive process that would be difficult to achieve without such a tool. The same argument applies to my BlackBerry, to the white board in my office, and even to the conversations I might have with my colleagues. Cognition, Clark argues, is not 'brain-bound' but a dynamic interaction between the neural circuits inside our skulls, our bodies and the objects and events in the outside world.

For researchers who study the control of movement, this idea has resonance. Perhaps it is for this reason that Clark begins by explaining how the production of fluid movements, such as walking or running, is a joint product of control systems in the brain and the dynamics of the limbs — the elasticity, viscosity and mass of the muscles, the connection of tendons to the joints, and the physical contact between the limbs and the environment. Clark uses this familiar example as an entry point

to the more contentious idea that cognitive activity similarly extends beyond the brain, skull and body to the external world.

The book develops the seminal ideas set out in a 1998 paper, 'The Extended Mind', co-authored by Clark and fellow philosopher David Chalmers. Over the past ten years, that paper has emerged as the key reference among philosophers, neuroscientists and psychologists who are interested in embodied cognition. The paper has naturally engendered criticism, particularly from those who see the mind and cognitive activity as brain-bound. In *Supersizing the Mind*, for which Chalmers has written a thoughtful and challenging foreword, Clark deals directly with many of these critiques, and in doing so, strengthens the major tenets of the extended mind hypothesis while offering a more nuanced discussion of the implications of this idea.

Clark explores in detail the consequences of embodied and extended cognition for our conscious perception of the world. He acknowledges that the "intimacy of brain, body, world,

and action" must have implications for our perceptual experience, but ultimately rejects the idea of enactive perception championed by philosopher Alva Noë, in which our experience is seen as nothing more than the sensorimotor routines that we use to interact with the world. For Clark, perception is shaped by the way in which we explore this world. But at the same time, he argues, our conscious experience of objects and events is not bound to the details of the sensorimotor routines that mediate that exploration. These routines, he suggests, are controlled by encapsulated systems with operating characteristics that are not privy to conscious, or even unconscious, scrutiny and whose activity is removed from the information they convey. In rejecting Noë's sensorimotor model, Clark argues that conscious perception does not depend on a "common sensorimotor currency" but arises from a subtle interplay between brain, body and environment, "replete with special-purpose streaming and with multiple, quasi-independent forms of internal, and external, representation and processing".

Supersizing the Mind is a treat to read. It is brimming with remarkable ideas, novel insights and amusing language. But it also challenges those of us who study cognitive processes. If

Clark is right, and I think he is, then simply studying what goes on in the brain will tell us only part of what happens as cognitive activity unfolds. To capture the richness of thought, we have to step outside the box and embrace the world beyond the skull. ■

Melvyn Goodale holds the Canada Research Chair in Visual Neuroscience at the University of Western Ontario, London, Ontario N6A 3K7, Canada. He is co-author (with David Milner) of *Sight Unseen: An Exploration of Conscious and Unconscious Vision*.

e-mail: mgoodale@uwo.ca



Does the mind extend past the brain and body to our external interactions?

Can robots have a conscience?

**Moral Machines:
Teaching Robots Right from Wrong**
by Wendell Wallach and Colin Allen
Oxford University Press: 2008.
288 pp. \$29.95

Artificial moral agents do not exist but are easily imagined: driverless trains that choose to turn away from a track on which five engineers are working, or autonomous armed drone aircraft that can distinguish between legitimate and unsanctioned targets. In *Moral Machines*, ethicist Wendell Wallach and philosopher Colin Allen pose three questions: “Does the world need artificial moral agents? Do people want computers making moral decisions? And how should engineers and philosophers proceed to design such agents?”

In contrast to Hollywood’s fantasies of intelligent but malignant doom machines and researchers’ speculations about machine-based transcendence, *Moral Machines* is modest, accurate and informative. The authors provide clear accounts of the basic ethical and philosophical issues, presupposing no technical background. To ask whether non-conscious machines can be real moral agents, they focus on ‘functional morality’: “Moral agents monitor and regulate their behaviour in light of the harms their actions may cause or the duties they may neglect.” The book covers a wide range of approaches, organizing current research into top-down application of traditional ethical theories, bottom-up evolutionary or learning strategies, and work on implementing emotions in computers.

As no robot is close to realizing functional morality, the book’s discussion may seem premature. The authors argue for an early start. But there is a risk that such early framing of issues can become powerfully salient; witness the influence of Isaac Asimov’s Three Laws of Robotics, an example of a hierarchical, rule-based morality for robots. The authors’ stated goal is to frame discussion in a way that guides the engineering task of designing artificial moral agents. But there are three main problems about the way they frame the topic.

First, the authors stretch their case, both in terms of the need

for moral evaluations and the systems they analyse. In answer to the question of whether the world needs these artificial moral agents, they use the example of the power blackout in the northeastern United States in 2003, in which “software agents and control systems at... power plants activated shutdown procedures, leaving almost no time for human intervention”. Consequently, they argue that “there is a need for autonomous systems to weigh risks against values”. The example is surprising: large-scale networked electricity infrastructure is a long way from the robot vacuum cleaners and nurses that might need a functional morality. Although the book focuses mainly on physical robots and the software simulations used to design them, the authors deliberately increase the scope of their topic to include software agents, or bots. But they do not discuss the related ethical issues, such as privacy, raised by programs such as “data-mining bots that roam the Web”. Asking people whether they would want computers making moral decisions may yield different answers than if you asked them the same about physical robots, in which issues of control and responsibility are simpler because robots are local.

Second, the focus on autonomy in the authors’ definition of robot, by stressing “independence from direct human oversight”, forecloses the important alternative option

of remotely controlled robots. An example of this type of technology is robotic surgery, which promises great benefits but raises far fewer philosophical and ethical issues than other applications. Similarly, remotely piloted Predator drone aircraft raise no new ethical issues. In these cases, one could simply insist on and develop better technologies for remote human oversight and control. For example, following the commuter-train wreck in Los Angeles, California, in September 2008, it was proposed that surveillance cameras in train cabs — instead of extra moral education for the drivers — could alleviate the failures of human autonomy; in this case, the driver reportedly being distracted by texting. Thus, autonomy should not be stressed in the definition of the target technologies: “Should a good autonomous agent alert a human overseer if it cannot take action without causing some harm to humans? (If so, it is sufficiently autonomous?)”

Third, the book advocates implementing human morality, as it is the only one we know about. This choice is not so obvious. For the foreseeable future, robots will be inferior to humans in their moral decision-making capacity. So Asimov’s hierarchical morality has appeal, compared with a human-based morality that stresses the equality of all moral agents. The morality of dogs would be a good alternative. Similar to dogs, robots will vary in their ability to make morally appropriate judgments. My family has had well-trained dogs that we trusted off-leash, others that could be trusted only when temptations such as squirrels or cats were absent, and some that needed leashes and even muzzles. All were pack animals, focused on a leader and unlike all our cats in this respect. A worthy goal for near-term robot ethics would be machines that we could classify in this way, so that we could give each the level of trust and control that lets them serve us well.

Moral Machines looks well in advance at robot ethics, but the jury is out on whether this book will set the agenda or if it is too premature to be influential. ■

Peter Danielson is Mary and Maurice Young Professor of Applied Ethics at the Centre for Applied Ethics, University of British Columbia, Vancouver, British Columbia V6T 1Z2, Canada. He is author of *Artificial Morality* and editor of *Modeling Rationality, Morality, and Evolution*. e-mail: pad@ethics.ubc.ca



Robots could be given varying levels of morality depending on their role.

A. WYANT/GETTY IMAGES



Annie Cattrell's flock of birds was inspired by the extraordinary biology underlying commonplace creatures.

The art of laboratory design

Can visual arts stimulate creativity in the science laboratory? A new biochemistry building for the University of Oxford might provide the answer, finds **Georgina Ferry**.

"The lab is a major building type, yet we have come to expect little of it," lamented art historian Martin Kemp in this journal more than a decade ago (see *Nature* 395, 849; 1998). The new biochemistry laboratory that opened at the University of Oxford, UK, in December 2008 refutes Kemp's charge that such buildings are graceless and functional.

The innovative design, by London-based architects Hawkins\Brown, ensures that the 300 researchers working there communicate as much as possible. The traditional layout is reversed: here, labs are on the outside, divided by clear glass walls from the write-up areas, which are open to a vast, five-storey atrium. Everyone is visible. Open staircases clad in warm wood fly across the atrium at odd angles, and each floor hosts a duster of inviting squashy leather chairs and coffee tables, giving the impression of an upmarket hotel.

What sets this laboratory apart from other 'statement' science buildings is the degree to which visual artists were involved in the project from its inception. Seven large-scale works were commissioned from four contemporary artists: of the total £49-million (US\$71-million) budget, around £750,000 was spent on art. To those that grumble that this sum might have been better

spent on science, Jonathan Hodgkin, professor of genetics and one of two departmental coordinators of the art project, points out that the money has come from designated arts grants from the Calouste Gulbenkian Foundation, the UK Wellcome Trust's public engagement fund and the Arts Council of England. "Part of our aim is to humanize the image of science for the public," Hodgkin explains.

All four of the artists developed their work after spending time with researchers in their labs. The entire L-shaped facade around the entrance displays Nicky Hirst's *Glass Menagerie*. Her multiple life-like forms based on the Rorschach inkblot test, screen-printed onto the glass panes, raise questions about how we organize and view the world around us.

Fine-art photographer Peter Fraser followed the demolition of the department's old buildings and the construction of the new. "He is documenting a process of physical change and 'capturing the intermediates', which is what we do as scientists," says Hodgkin. Meanwhile, digital artist Tim Head found common ground in Mark Sansom's Structural Bioinformatics and Computational Biochemistry group. "The point of the residency was not to illustrate the science," says Sansom. "But if you have

a greater degree of visual literacy, you reflect more on both the way you represent things, and also the way that may limit the way you think about them."

In the atrium, artist Annie Cattrell has suspended a flock of more than 150 bird forms cast in resin. Commenting on the success of the art-science collaboration, she noted each side's respect for the professionalism of the other, and the "lovely sense of trust" she felt in working with Sansom and Hodgkin. Her piece was inspired by learning about Hodgkin's work on nematode genetics, and understanding that "you can find something extraordinary in something so prosaic".

The prime purpose of the art project is to create a stunning physical environment for research. "The senior people [in the university] grasped that if you are trying to recruit the best people in the world, walking them through a building that is dark and dingy is not the best way to get them," says Sansom. Time will tell if money spent on art gives a significant return in scientific discovery.

Georgina Ferry is a writer based in Oxford, UK.

For a 360° view of the building and artwork, see <http://tinyurl.com/95ctgy>.

K. COLLIE/HAWKINS BROWN

EVOLUTIONARY GENOMICS

A positive becomes a negative

Laurence D. Hurst

Which human genes have been hotspots for positive selection? Analyses of the top candidates reveal, not genes subject to such selection, but genes that have probably been subject to biased DNA repair.

To find out what makes us humans unique, we can look for genes, and ours alone, in which Darwinian positive selection has occurred. In principle, genes thought to be hotspots for positive selection can be discovered by genome scans that pinpoint especially fast evolutionary change in DNA sequences^{1–3}. Work by Berglund *et al.*⁴ and Galtier *et al.*⁵, however, undermines the assumed connection between fast evolution and pervasive positive selection. Instead, it seems that hotspots have probably accelerated evolution by means of a biased DNA repair process, not because the changes were good for us. Indeed, many changes are probably detrimental.

To infer human-specific changes, the two groups compared human genes with those of the chimpanzee and other primates. Every observed difference was a mutation that was initially rare but became common, maybe — but not necessarily — because of positive selection. Standard tests for positive selection assume that mutations become common either through conferring an advantage on the organism (positive selection) or through chance (drift). The two groups used the same methods for finding hotspots of positive selection as were used in previous studies^{1–3}. All of these approaches identify DNA sequence for which the rate of evolution is higher than expected, but they differ in how the expected is defined.

The first method identifies sequence that is evolving at superfast rates in humans compared with other primates (Fig. 1). Berglund *et al.*⁴ applied two further methods, both of which compare the rate of evolution of a protein with the rate of evolution of sites in the protein's gene where mutations do not affect it (synonymous sites). The first of these methods asks if the ratio of the two rates (K_a/K_s) is unusually high in humans. The second asks if, after controlling for the variation seen between humans, the between-species value of this ratio is unusually high.

Berglund *et al.* report that the three methods typically pinpoint different candidates for positive selection. However, one regularity does appear. Any position in a gene is occupied by one of four nucleotides, A, T, C or G, combinations of which code for amino

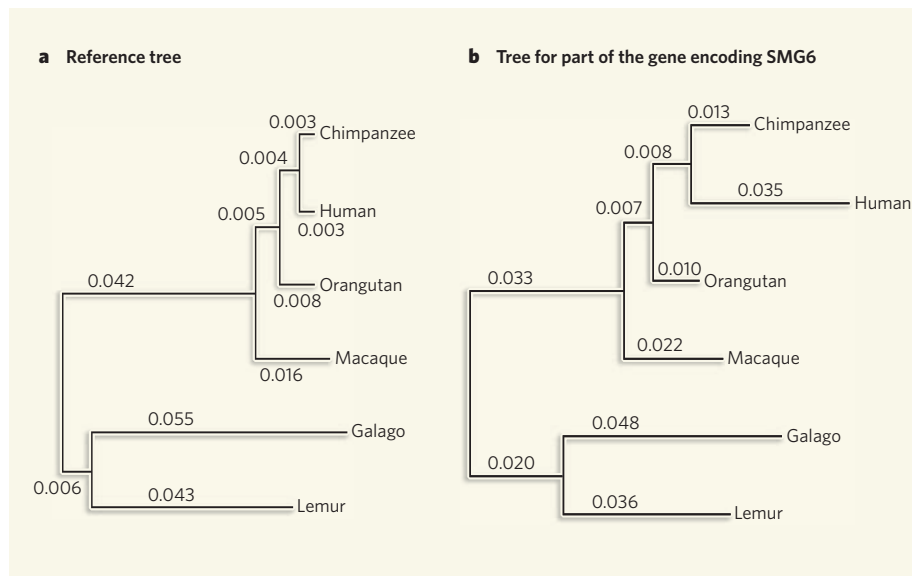


Figure 1 | Identification of a gene segment showing unusually rapid evolution. This example comes from the study by Galtier *et al.*⁵, who identified human-specific accelerated change in DNA sequence by comparing the proportional number of changes seen in a given gene segment (or gene) with that of a reference set drawn from 1,000 genes. Considering that 0.003 changes have occurred in the human-specific lineage, compared with the sum of all branch lengths across the tree (0.185), we conclude that only 1.6% of all sequence change happened after the split between humans and chimps in the human lineage. **b**, Tree resulting from sequence data for part of the gene encoding the SMG6 protein. Here, 15% of all the sequence change has occurred in the human lineage, implying human-specific acceleration of rates. Of 29 changes, 25 are AT→GC, implicating biased gene conversion as the cause. Numbers indicate the average number of amino-acid changes per site. (Figure adapted from ref. 5.)

acids — the building blocks of proteins. Curiously, the top candidates for positive selection show a great excess of nucleotide changes that were ancestrally either A or T but became G or C. Galtier *et al.*⁵ find the same effect, and also show that it applies to hotspots in non-human primates.

Why should this be? Positive selection operating on the choice of amino acids should not so consistently prefer a change of AT to GC. Moreover, the bias, although highly localized within genes, is not unique to the protein-coding parts of the gene, but is seen in the intervening noncoding parts as well^{4,5}. Both groups conclude that the hotspot genes are not under positive selection at the protein level.

Assuming that some force is driving the

transformation of AT to GC, the reasonable inference is that speedy evolutionary change is giving a false signal of positive selection. Both groups also show that a force promoting AT to GC changes can lead to sequences that not only have accelerated rates of change but also have a K_a/K_s ratio that exceeds one, the common acid-test of positive selection. If this were to be the case, it would require that accelerated evolution is especially concentrated at sites in the gene that, if changed, alter the protein. That is especially likely if, ancestrally, the gene's synonymous (non-amino-acid-specifying) sites were GC rich but sites that specified an amino acid were not: the GC biasing force would cause an excess of protein-changing substitutions compared with the

relatively unaffected synonymous sites, these always being GC rich⁴.

What might the biasing force be? Changing nucleotides at synonymous sites modulates expression of a gene⁶. But why then would the changes be highly localized within genes, and why is the bias also in noncoding sequence? A simpler explanation than positive selection on either proteins or expression rate, and one that anticipated⁷ the new results, invokes a biased DNA repair process.

During the manufacture of sex cells, a cell with two copies of each of our 23 chromosomes divides to produce cells with just one set of each. During this process, chromosomes can swap DNA (recombination); this involves a break in one chromosome that exposes a single strand of the normally double-stranded DNA. The single strand then finds a complementary strand in its partner chromosome. The two strands pair up to make a new double-stranded bit of DNA. The sequence of the two strands may not, however, be perfectly complementary and might break the rules of DNA pairing (G should pair with C, and A with T). Mismatch repair enzymes then correct rule violations. Imagine a C mismatched with an A. There are two choices for repair: replace C with T or replace A with G. Importantly, the system is biased⁸ and more commonly replaces A with G. More generally, it favours Gs and Cs over As or Ts. The repair bias may be an evolved property to cope with a high mutation rate of C to T.

Biased gene conversion⁹ (BGC), as the process is termed, explains a general trend towards higher rates of evolution in chromosome domains that commonly undergo recombination¹⁰, and correctly predicts the high rates of recombination in the superfast hotspots^{4,5}. Many such sites lie towards the ends of chromosomes, where recombination is common. Moreover, as gene conversion also happens between physically adjacent duplicated genes, BGC explains why chromosomally neighbouring duplicates have similar GC-rich sequence¹¹. A suggestive finding is that two top hotspots are a pair of adjacent duplicate genes (those encoding the olfactory receptors OL3A3 and OL3A2).

Importantly, BGC can drive mutations that are deleterious⁵. This may explain why hotspots can occur in genes that, in species other than ourselves, are under strong selection not to change, and hence are not obvious candidates for positive selection. Given that BGC can force deleterious mutations to spread through a population, part of the high rate of evolution in the hotspots could be because of the subsequent spread of compensatory mutations⁵.

There remains one mechanistic oddity. It has been observed that the correlation between evolutionary rate and recombination rate holds only for the recombination rate seen in males (see, for example, refs 10 and 12). This is evidence against a role for recombination's

randomizing effects (a shuffling of which mutations sit next to each other), which form the underpinnings of a potential alternative explanation. Why the effect is male-specific is not known.

The results of Berglund *et al.*⁴ and Galtier *et al.*⁵ accord with the view of BGC as a driver of sequence evolution, potentially explaining the occurrence of large spans of approximately homogeneous nucleotide content (isochores) in our genome¹³. More disturbingly, the results bring into question the usefulness of the standard tool kit for identifying hotspots of changes that are beneficial to organisms. Convincing demonstration of positive selection now requires both evidence that the changes were not caused by BGC and scrutiny of the impact of the amino-acid changes. ■

Laurence D. Hurst is in the Department of Biology and Biochemistry, University of Bath, Bath BA2 7AY, UK.

e-mail: l.d.hurst@bath.ac.uk

1. Pollard, K. S. *et al. Nature* **443**, 167–172 (2006).
2. Bustamante, C. D. *et al. Nature* **437**, 1153–1157 (2005).
3. Clark, A. G. *et al. Science* **302**, 1960–1963 (2003).
4. Berglund, J., Pollard, K. S. & Webster, M. T. *PLoS Biol.* **7**, e1000026 (2009).
5. Galtier, N., Duret, L., Glémin, S. & Ranwez, V. *Trends Genet.* **25**, 1–5 (2009).
6. Kudla, G., Lipinski, L., Caffin, F., Helwak, A. & Zylicz, M. *PLoS Biol.* **4**, 933–942 (2006).
7. Galtier, N. & Duret, L. *Trends Genet.* **23**, 273–277 (2007).
8. Brown, T. C. & Jiricny, J. *Cell* **54**, 705–711 (1988).
9. Marais, G. *Trends Genet.* **19**, 330–338 (2003).
10. Duret, L. & Arndt, P. F. *PLoS Genet.* **4**, e1000071 (2008).
11. Galtier, N. *Trends Genet.* **19**, 65–68 (2003).
12. Dreszer, T. R. *et al. Genome Res.* **17**, 1420–1430 (2007).
13. Eyre-Walker, A. & Hurst, L. D. *Nature Rev. Genet.* **2**, 549–555 (2001).

IMMUNOLOGY

Natural killer cells remember

Sophie Ugolini and Eric Vivier

Cells of the adaptive immune system hold a grudge: on re-encountering a pathogen, they show a robust protective response. It seems that natural killer cells of the innate immune system might also have this ability.

Learning, a hallmark of life, produces adaptation to new information. The immune system, like the nervous system, has this ability to learn from previous experience — such as a single encounter with the many pathogens that exist. The result is immunological memory that confers long-lasting protection. For instance, once exposed to the measles virus in childhood, humans are immune to the disease for up to 75 years¹. Until now, immunological memory was thought to be a feature of the adaptive immune system, specifically, of immune cells called T and B cells. In this issue, however, Sun *et al.*² (page 557) shed light on an unexpected player in the persistence of immunity: natural killer cells, which have traditionally been considered to be part of the innate immune system.

Adaptive immunity appeared in vertebrates around 500 million years ago³. In the more complex vertebrates, each clone of T and B cells expresses a unique cell-surface receptor, which preferentially recognizes a specific antigen and so, potentially, a specific invading pathogen. The ensemble of antigen-specific T- and B-cell receptors is called the immune repertoire. When these receptors recognize and bind an antigen, the clones of T or B cells on which the receptors are expressed expand dramatically in number, and the cells acquire effector functions — for example, T cells acquire the ability to kill the offending antigen-containing cells and B cells secrete antibodies. Once the immune response is over, a 'contraction' phase occurs, and only a small fraction of the expanded T- or B-cell population survives. These long-

lived memory cells are central to maintaining long-term immunity after infection or vaccination. T and B cells are thus said to be adaptive, because their repertoire depends on an individual's antigenic history.

Natural killer cells are classified as part of the innate immune system. Through many receptors, they recognize a vast array of molecules, the expression of which is indicative of a particular situation, such as microbial infection, tumour formation or DNA damage⁴. Sun *et al.*² now show that natural killer cells also have properties previously ascribed only to T and B cells.

In mice, a subset of natural killer cells, which express the Ly49H receptor on their surface (Ly49H⁺ cells), specifically recognize a protein produced by some strains of mouse cytomegalovirus (MCMV)^{5,6}. The specific recognition of these cells, an ability also shared by cells of the adaptive immune system^{5,6}, allows Ly49H⁺ natural killer cells to limit MCMV infection at an early stage. But before infection, the number of Ly49H⁺ natural killer cells is much higher than the number of antigen-specific T cells (around half of all natural killer cells are Ly49H⁺, compared with between 1 in 10⁴ and 1 in 10⁸ T cells for a given T-cell clone before infection).

Previous work⁷ has shown that MCMV infection results in a two- to tenfold increase in the number of natural killer cells. To compare this response under conditions similar to that of a T-cell response, Sun *et al.* experimentally reduced the initial number of Ly49H⁺ natural

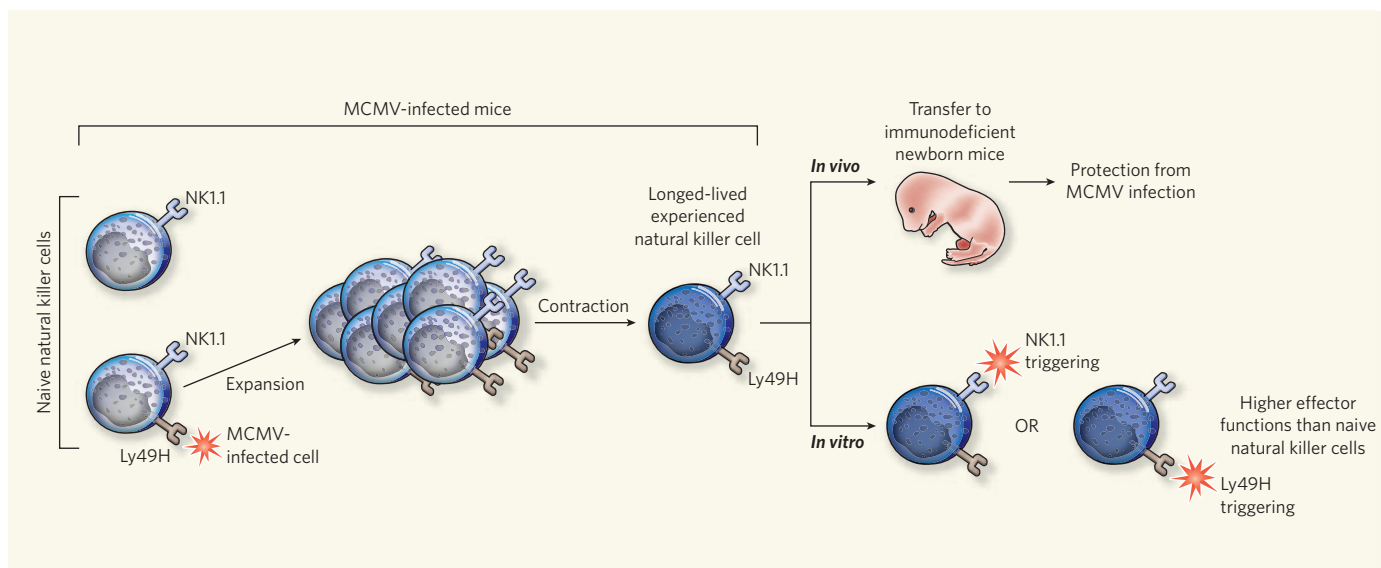


Figure 1 | Natural killer cells and virus exposure. To distinguish between target cells and non-target cells, natural killer cells have many surface receptors⁴. On first encounter with a target, such as mouse cells infected with cytomegalovirus (MCMV), which are recognized by the Ly49H receptor on the natural killer cell surface, mouse natural killer cells start to divide and proliferate. Sun *et al.*² find that this expansion phase is followed by a contraction phase that leaves a few virus-experienced cells.

On subsequent exposure, these latter cells are more protective against MCMV infection when transferred to immunodeficient mice than are cells from mice not previously infected. They are also more efficient in their *in vitro* response not only to molecules that activate their Ly49H receptor but also to those that activate another receptor on their surface, NK1.1. Experienced natural killer cells might therefore have a type of memory that ensures a broad crossreactivity.

killer cells. They found that these cells can proliferate extensively (up to 900-fold expansion), specifically in response to MCMV. Once the infection had peaked, a contraction phase followed, with a subset of the 'virus-experienced' Ly49H⁺ natural killer cells surviving and maintaining the characteristics of an effector cell. What's more, when the authors transferred these virus-experienced natural killer cells to newborn immunodeficient mice, the cells were tenfold more protective against MCMV infection than their counterparts from uninfected mice (Fig. 1). Protection was correlated with a greater effector function of the virus-experienced natural killer cells *in vitro*, rather than with a higher proliferation rate of these cells *in vivo*. So, as natural killer cells seem to retain information from a viral infection, Sun and colleagues' data suggest the existence of 'memory' natural killer cells.

But whether the terms memory and naive (not previously exposed to an antigen), used for T and B cells, should also be used for natural killer cells is debatable. Whereas clones of T and B cells express one antigen-specific type of receptor on their surface — providing the basis for a specific memory response — natural killer cells express an array of receptors with distinct specificities. So a natural killer cell that has been activated through one receptor could be reactivated via another receptor that recognizes an unrelated molecule. Sun *et al.* find that this is indeed the case when Ly49H⁺, virus-experienced natural killer cells are stimulated through another surface receptor, NK1.1 (Fig. 1). By contrast, memory T and B cells show a strong response only to the specific antigen that initially triggered

their expansion, or possibly to another antigen recognized by the same receptor — a cross-reactive antigen⁸.

Experienced natural killer cells therefore preserve a more general memory of their previous stimulation, and seem to show an enhanced response not just to the challenge that initially caused their expansion but also to those challenges that trigger other, unrelated receptors on their surface. So the phenomenon Sun *et al.* describe may be more related to a 'training' of natural killer cells in effector responses than to the responses of antigen-specific memory T and B cells.

Earlier studies have already indicated that natural killer cells resemble T and B cells more closely than was originally appreciated^{9,10}. In particular, they showed that these cells learn to recognize 'self'¹¹ and are primed by other immune cells such as dendritic cells¹². If Sun and colleagues' findings and these previous studies¹³ also hold true in other experimental systems, they would contribute to a blurring of the distinction between innate and adaptive immunity. The question then arises of whether this distinction is still a valid way of describing, understanding and predicting immune responses.

Furthermore, Sun *et al.* observed a high rate of natural killer cell proliferation and the occurrence of long-lived cells of this type under conditions in which the initial number of virus-specific cells was artificially lowered. Whether MCMV infection in unmanipulated mice generates long-lived natural killer cells with memory properties remains unknown. Also to be discovered is whether *in vivo* stimulation of natural killer cells with agents

other than MCMV results in the generation of long-lived experienced cells.

Nonetheless, this study² will undoubtedly prompt research into the mechanisms that allow the boosted effector function of natural killer cells to be maintained across cell divisions, in particular the epigenetic marks associated with various stages of these cells' activation. As the nature of reliable biological markers of protective immunity is still a matter of debate¹⁴, it is exciting to consider that natural killer cells might be monitored as a potential protection correlate for testing the efficiency of vaccines under development.

Sophie Ugolini and Eric Vivier are in the Centre d'Immunologie de Marseille-Luminy, Université de la Méditerranée, INSERM, CNRS, Campus de Luminy, case 906, 13288 Marseille cedex 9, France, and in the Faculté de Médecine-Timone, Marseille, France.
e-mails: ugolini@ciml.univ-mrs.fr;
vivier@ciml.univ-mrs.fr

- Gourley, T. S. *et al. Semin. Immunol.* **16**, 323–333 (2004).
- Sun, J. C., Beilke, J. N. & Lanier, L. L. *Nature* **457**, 557–561 (2009).
- Pancer, Z. & Cooper, M. D. *Annu. Rev. Immunol.* **24**, 497–518 (2006).
- Vivier, E. *et al. Nature Immunol.* **9**, 503–510 (2008).
- Smith, H. R. *et al. Proc. Natl Acad. Sci. USA* **99**, 8826–8831 (2002).
- Arase, H. *et al. Science* **296**, 1323–1326 (2002).
- Dokun, A. O. *et al. Nature Immunol.* **2**, 951–956 (2001).
- Selin, L. K. *et al. Immunol. Rev.* **211**, 164–181 (2006).
- Glas, R. *et al. J. Exp. Med.* **191**, 129–138 (2000).
- Raulet, D. H. *Nature Immunol.* **5**, 996–1002 (2004).
- Raulet, D. H. & Vance, R. E. *Nature Rev. Immunol.* **6**, 520–531 (2006).
- Lucas, M. *et al. Immunity* **26**, 503–517 (2007).
- Vivier, E. & Malissen, B. *Nature Immunol.* **6**, 17–21 (2005).
- Zinkernagel, R. M. & Hengartner, H. *Immunol. Rev.* **211**, 310–319 (2006).



50 YEARS AGO

In previous communications, the existence of a third normal, embryonic haemoglobin was reported to be present in the blood of fetuses up to five months of intra-uterine life ... By using the column chromatographic procedure described by Huisman and Prins, with some minor modifications, we were able to separate the three distinct fractions from the haemolysate of a four month old embryo ... Thus, we were able to separate not only the two haemoglobin fractions known to be present in the cord blood of full-term new-borns, but also the third, embryonic, fraction (the lowest in the chromatographic column) in the blood of small embryos ... [W]e were, for the first time, able to discover the embryonic haemoglobin fraction in the blood of two full-term new-borns who were severely malformed, whereas twenty other normal new-borns who served as controls did not show this fraction in their blood. From *Nature* 31 January 1959.

100 YEARS AGO

A striking instance of the assistance which can be rendered by wireless telegraphy in overcoming the difficulties and dangers of navigation was afforded in the case of the collision of the steamship *Florida* with the White Star liner *Republic* in the early morning of January 23. The collision occurred in a dense fog at 5.30 a.m., 175 miles east of the Ambrose lightship, New York. The *Republic* is equipped with a wireless telegraphy installation, and the captain, who was on the bridge at the time of the accident, at once had wireless messages for help sent out ... The messages were received by the liners *Baltic*, the *Lorraine*, and the *Lucania* ... The steamships proceeding to the rescue were able to transmit a wireless message to the *Republic* asking for the latitude and longitude of the collision ... Wireless telegraphy has thus been the means of averting a terrible calamity. From *Nature* 28 January 1909.

CONDENSED-MATTER PHYSICS

The pnictide code

Jan Zaanen

Hopes are that the emergent family of iron-based superconductors, the pnictides, could act as a Rosetta stone in decoding the two-decade mystery of superconductivity observed at high temperatures.

About a year ago, the announcement of the discovery¹ of a new family of superconductors made from iron-based compounds prompted an army of physicists and chemists to study these pnictides. But what caused — and is perpetuating — this frenzy? The quest for a higher transition temperature, T_c (the temperature above which no superconductivity is attained), stalled² at a meagre 56 kelvin, and the focus of the excitement has shifted: it is now hoped that the pnictides will be instrumental in deciphering the 22-year-old mystery behind high- T_c superconductivity in cuprates³ (compounds containing copper oxide). There are also compelling reasons to believe that pnictides share the main properties of cuprates. In this issue, two studies (Yuan *et al.*⁴ on page 565 and Zabolotnyy *et al.*⁵ on page 569) report observations of two features in the pnictides that further elucidate how the two families of superconductors compare.

What happens when zillions of quantum particles form a macroscopic quantum whole-ness? The electron matter that superconducts is a famous example of such 'quantum matter' that shows quantum effects on a macroscopic scale. The Bardeen–Cooper–Schrieffer (BCS) theory of superconductivity proposed in 1957 seemed to explain the phenomenon in full, but this changed with the discovery of superconductivity in the cuprates in 1986, and transition temperatures as high as 150 kelvin have subsequently been found. In some ways, the ensuing research effort has been spectacularly successful, showing that electrons in solids can form surprisingly rich quantum worlds. But the cause of their superconductivity has become even more mysterious over the years².

The key question is: how much is going on in these electron worlds? The normal (non-superconducting) state of ordinary metals such as aluminium is remarkably featureless, despite their being in the grip of the influence of quantum weirdness, which, counter-intuitively, renders things very simple. A quantum magic causes the electrons to 'forget' that they strongly interact, and the resulting 'Fermi liquid' behaves like a gas of non-interacting 'quasielectrons'. According to BCS theory, at very low temperatures the exchange of phonons (atomic lattice vibrations in the metal) leads to a weak attractive interaction between the quasielectrons, causing these to bind in Cooper pairs, which condense into a superconducting state.

But in cuprates, chemistry conspires

against the might of this quantum simplicity. Metaphorically, the cuprate electron world is like a quantized form of dense traffic on a busy highway. The electrons are subject to perpetual quantum motions, but can hinder each other's motions to such an extent that the electron 'traffic' jams completely, causing undoped cuprates to become insulating. Chemical doping can clear the way on the 'quantum highway', and at low levels of doping a quantum incarnation of stop-and-go traffic is observed⁶. At high levels of doping the quantum weirdness hits with full force — causing the electrons to forget the busy highway — and the Fermi-liquid state takes over⁷.

But both the quantized stop-and-go and the Fermi-liquid states are bad for superconductivity: the best superconducting cuprates are found at intermediate dopings, at the point at which the electron traffic starts to gather speed³.

The belief is that the electrons in pnictides might well share this 'quantum highway' behaviour. The observed transition temperatures are much too high to be explained by BCS theory, and the iron and arsenic atoms that constitute the pnictide layers create similar jamming conditions to those of copper and oxygen². Moreover, although undoped pnictides do not quite insulate, they do show a muscular antiferromagnetism — a strong sign that the electron traffic is on the verge of coming to a standstill⁸. But even though pnictides and cuprates might share the gross aspects of quantum-highway physics, in other regards they can be quite different. The hope is that by comparing both systems one can find out what really matters in high- T_c superconductivity. This is exactly what Yuan *et al.*⁴ and Zabolotnyy *et al.*⁵ try to address in their studies.

In the cuprates, one invariably finds that the electrons can move freely only in the copper-oxide planes. This led researchers to believe that superconducting electronic properties, such as the quantum-highway behaviour, were two-dimensional, and that this was a necessary prerequisite for superconductivity at high temperatures. But Yuan *et al.*⁴ now report on a demanding experiment with a simple conclusion that changes this view: despite the layered crystal structure of the pnictides, superconductivity in these materials can be three-dimensional. The implication is that, if both systems do share the secret of high- T_c superconductivity, two-dimensionality has been a red herring all along, causing theorists to look in wrong directions.

To appreciate the results of Zabolotnyy and colleagues⁵, one has to dig a bit deeper into the weird side of the quantum world. The quantity that matters most in the Fermi liquid is the Fermi surface — a boundary in the abstract space of quasielectron quantum numbers that at absolute zero temperature separates the unoccupied states from the occupied ones. Photoemission experiments, which measure the energy of electrons emitted from the metals when these are subjected to electromagnetic radiation, show sharp Fermi surfaces in cuprates in the Fermi-liquid regime at high levels of doping. At low levels of doping, where the electrons are in the stop-and-go regime and so are far from forming quasielectrons, these measurements show that there are still fuzzy remnants of these Fermi surfaces⁹. Although not at all understood, these remnants can be taken as a signal that the quantum weirdness is already in action in an attempt to simplify the electron traffic flow in the direction of the Fermi-liquid state.

Moreover, the observed, simple rounded-square shape of the single cuprate Fermi surface seems to be in accord with the predictions of the naive LDA (local density approximation) electronic-band-structure theory of metals, which completely ignores the quantum highways. But the Fermi surfaces in pnictides are more complex, and there is much more to investigate. According to the LDA, it is a semimetal-like affair of circle-shaped pockets of electrons and electron holes. Using high-resolution photoemission data, Zabolotnyy *et al.*⁵ manage to observe the pockets, but instead of the predicted circles, these look like design wheels and aircraft propellers. Does this scrambling of the LDA Fermi surfaces in the pnictides tell us about a dose victory of quantum weirdness over electron jamming⁴, or is there an alternative, more conventional explanation?

It is too early to tell. At present, it is not at all certain whether pnictides code for cuprates or just for themselves. But there is yet another excellent reason to believe in the 'pnictide code'. Temperature is the mortal enemy of quantum physics. Therefore, one anticipates that when quantum weirdness is in a tight battle with the quantum highway, the influence of temperature might be disproportionate. This is such a difficult problem that, according to some, the mathematics of string theory is needed to understand it¹⁰. But we already know what this means empirically: at temperatures well above T_c one finds cuprates in a 'bad metal' state, in which the electron matter shows extreme forms of dissipation in stark contrast to the very small friction that characterizes the Fermi-liquid state⁷. There are indications that the pnictide metals can be as 'bad' as the cuprates, and I am impatiently waiting for a concerted effort that will nail this down. ■

Jan Zaanen is at the Instituut Lorentz for Theoretical Physics, Leiden University, PO Box 9504, 2300 RA Leiden, the Netherlands. e-mail: jan@lorentz.leidenuniv.nl

1. Kamihara, Y., Watanabe, T., Hirano, M. & Hosono, H. *J. Am. Chem. Soc.* **130**, 3296–3297 (2008).
2. Grant, P. M. *Nature* **453**, 1000–1001 (2008).
3. *Nature Phys.* **2**, 133 (2006).
4. Yuan, H. Q. *et al. Nature* **457**, 565–568 (2009).
5. Zabolotnyy, V. B. *et al. Nature* **457**, 569–572 (2009).
6. Zaanen, J. *Science* **315**, 1372–1373 (2007).

7. Cooper, R. A. *et al. Science* doi:10.1126/science.1165015 (2008).
8. Kivelson, S. A. & Yao, H. *Nature Mater.* **7**, 927–928 (2008).
9. Damascelli, A., Hussain, Z. & Shen, Z.-X. *Rev. Mod. Phys.* **75**, 473–541 (2003).
10. Zaanen, J. *Nature* **448**, 1000–1001 (2007).

PLANT GENOMICS

Sorghum in sequence

Takuji Sasaki and Baltazar A. Antonio

The drought tolerance of sorghum is just one of the features that make it a valuable crop plant. There is much for agronomists to learn from the complete genome sequence of this type of grass.

It is almost four years since the genome sequence of the rice plant, *Oryza sativa*, was completed¹. Rice is the world's most important crop, and the availability of an accurate, complete, map-based sequence of a cereal genome prompted ground-breaking studies of the genetic underpinning of valuable agricultural traits, both in rice itself and in other cereals.

The genomes of more than ten plant species have since been completely sequenced, to which can now be added that of a second cereal species, *Sorghum bicolor*, as reported by Paterson *et al.* on page 551 of this issue². This constitutes another milestone in plant biology, but it won't, of course, mean that the sequencing machines will now lie idle: among commercially important crop plants, the genomes of other members of the grass family Poaceae (which includes maize, wheat and barley, as well as rice and sorghum), in addition to representatives of the Fabaceae (soybean)

and Solanaceae (tomato and potato) families, will be completed in the next few years.

Worldwide annual production of sorghum is about 60 million tonnes, less than that of the other major cereal crops. It is nonetheless a staple for both humans and livestock, and is also a potential source of biofuel. Sorghum originates from tropical Africa, which makes it highly tolerant to drought and well adapted to arid countries in northeast Africa, where it is mainly grown, as well as to dry areas in the United States and India. Most notably, sorghum provides an example of a plant that carries out the C_4 type of photosynthesis. This photosynthetic pathway, found in many plants growing in conditions of high temperature and light intensity, and low water availability, is considered to be more efficient in fixing carbon dioxide than the C_3 route that is found, for instance, in rice and wheat. Research into the genomic basis of sorghum's adaptation



In the field — sorghum under cultivation.

P. QUIRK/PHOTOLIBRARY.COM

to adverse environmental conditions and its photosynthetic efficiency should prove informative.

Another line of advance will come from comparative studies of the sorghum, rice and (in due course) other cereal genomes, to provide insights into their evolution and the generation of grass diversity. Sorghum is thought to have diverged from a common ancestor with most other grasses about 70 million years ago, and has common blocks of genome with other members of the grass family; this 'synteny', or colocalization of genes, reflects their shared ancestry³. Rice occupies the core of the 'grass circle', and as expected contains a similar quantity of euchromatin — parts of chromosomes that are especially gene-rich — to that of sorghum, and with similar gene order. The genomes of many extant plants, grasses included, arose through wholesale genome duplications, a phenomenon known as polyploidization. Maize and sorghum shared a common ancestor until about 12 million years ago, and in due course comparison of the two genomes will illuminate the processes of polyploidization and repetitive-DNA propagation.

Further on the comparative front, there are informative differences between sorghum and rice to be explored. Given the African origin of sorghum and the Asian origin of rice, comparisons will help in elucidating the genetic basis of cereal dispersion and domestication. And whereas sorghum, with biochemical and morphological features that improve net carbon assimilation at high temperatures, provides a platform for understanding tropical grasses, rice exemplifies temperate grasses with the C_3 photosynthetic system.

The true worth of plant genome information, however, lies in translating those data into an improvement of crops through various breeding strategies. The benefits of the sorghum sequence will extend to other grass species, including C_4 plants — such as sugar cane and *Miscanthus* — that are being targeted as potential resources for bioethanol production. The aim of re-engineering the rice plant to facilitate C_4 photosynthesis in this C_3 species, in order to boost yields, will also benefit from the sorghum data. In general, standard genome-sequence information is used for identifying variations in gene sequence that are useful for cloning and marker-assisted selection, both of which are now commonly incorporated in many breeding programmes involving agronomically important traits. Given the colinearity of many genes in rice and sorghum, the sorghum community could exploit the many notable findings already reported in rice in order to isolate similar genes in sorghum.

The information to be mined from a plant genome sequence is, of course, not in itself enough to enhance such traits as photosynthetic efficiency or stress tolerance. But that information constitutes the most powerful tool we have for revealing ways to increase

the amounts of food and energy provided by plants, and so to meet the demands of a world faced by an ever-increasing population and by an erratic climate. The cereal crops will play a large part in that endeavour: availability of the complete genome sequence of sorghum provides agronomists with much to be getting on with.

Takuji Sasaki and Baltazar A. Antonio are at the

National Institute of Agrobiological Sciences, 2-1-2 Kannondai, Tsukuba, Ibaraki 305-8602, Japan.

e-mails: tsasaki@nias.affrc.go.jp;

antonio@nias.affrc.go.jp

1. International Rice Genome Sequencing Project *Nature* **436**, 793–800 (2005).
2. Paterson, A. H. *et al.* *Nature* **457**, 551–556 (2009).
3. Gale, M. D. & Devos, K. M. *Science* **282**, 656–659 (1998).

ORGANIC CHEMISTRY

Chlorine lends a helping hand

D. Karl Bedke and Christopher D. Vanderwal

The development of synthetic routes to unusual and complex molecules frequently leads to surprising lessons about chemical reactivity. The first synthesis of a marine toxin provides just such a lesson.

Shellfish toxins cause illness and death in people who ingest the tainted organisms, and can affect populations of fish and other marine animals¹. Perhaps surprisingly, these compounds also have a central role in the history of organic chemistry, because their complex structures provide synthetic targets

that both stretch the limits of the field and spur the development of new reactions that go on to find use elsewhere — much as the space race spawned technologies that have found a home in many other walks of life.

In 2001, a new marine toxin was isolated² from mussels (*Mytilus galloprovincialis*) in the

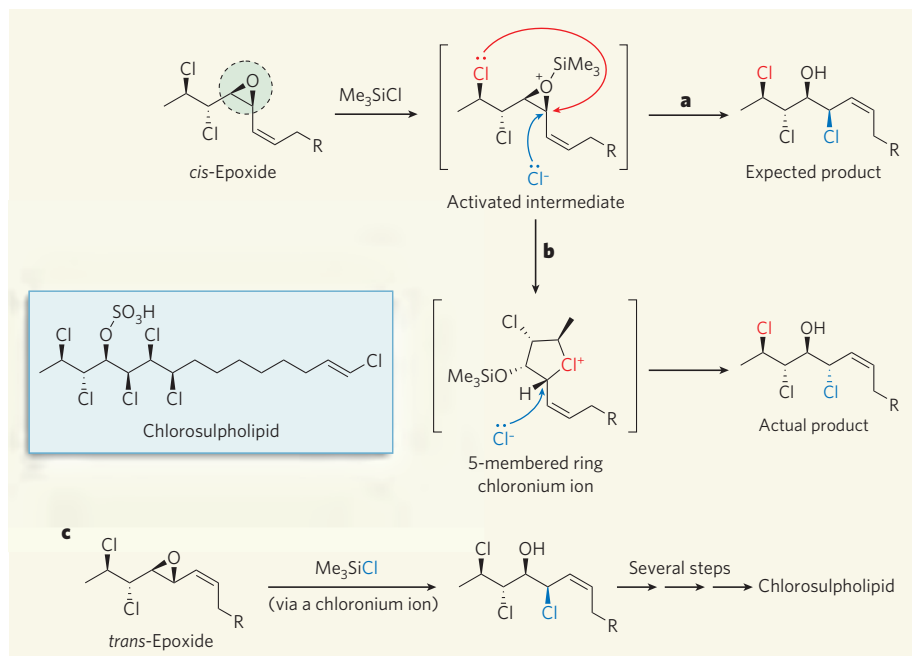


Figure 1 | Synthesis of a marine toxin involving an unexpected reaction. Nilewski *et al.*⁵ report the first complete synthesis of a chlorosulpholipid marine toxin. One of their early attempts to make the compound began from a *cis*-epoxide molecule (the epoxide group is circled), which reacts with trimethylsilyl chloride (Me_3SiCl) to form an 'activated' intermediate. **a**, The authors expected a chloride ion (Cl^- , generated from Me_3SiCl) to react with the intermediate and provide them with a product in which the newly attached chlorine atom (blue) projects above the plane of the page (indicated by showing the newly formed bond as a 'wedge'). **b**, In fact, a different product formed in which the newly attached chlorine atom projects below the plane of the page (indicated by the 'hash' bond). The authors propose that a chlorine atom (red) in the activated intermediate first attacked the epoxide group, most probably forming a 5-membered ring chloronium ion. Subsequent attack of Cl^- on the chloronium ion generated the observed product. **c**, Starting with a different reactant (a *trans*-epoxide), Nilewski *et al.* used this unexpected reaction in their successful synthesis of the chlorosulpholipid. Me is a methyl group, and R is a side group that can be converted into the right-hand side (as shown) of the final product.

Adriatic Sea. This represented a new structural class of toxin, known as chlorosulpholipids (Fig. 1). Other, structurally more complicated chlorosulpholipid toxins were later isolated from the same source^{3,4}. The molecules contain a remarkable structural element — a hydrocarbon that has several chlorine atoms attached, in which the three-dimensional, spatial arrangement (the stereochemistry) of the atoms is precisely defined. Because the compounds are available in only minute amounts from mussels, an efficient synthesis of these toxins would benefit studies of their mechanism of action and the development of methods for their detection. In this issue (page 573), Nilewski *et al.*⁵ report the first laboratory synthesis of a chlorosulpholipid. Their findings also offer a lesson in the unexpected reactivity of polychlorinated hydrocarbons.

Chlorosulpholipids might have biological roles other than as toxins. Long before their discovery in mussels, a structurally related class of lipid was isolated from the alga *Ochromonas danica*^{6,7}. These lipids are major constituents of the cell membrane of the alga, possibly replacing phospholipids (which are the usual constituents of cell membranes, but which are absent in this instance). From an evolutionary perspective, this is most unusual. Moreover, the algal lipids have a remarkable molecular structure containing polar sulphate groups both at the end of the molecule and part-way along its length (rather than having a single polar group at one end of the molecule, as do phospholipids). This feature makes it difficult to understand how the molecules could form a typical membrane bilayer, as the 'central' sulphate groups would end up buried deep within the non-polar region of the membrane — a seemingly unlikely arrangement⁷. Because the chlorosulpholipids from toxic mussels are structurally related to the algal lipids, it is likely that they also come from algae, perhaps accumulating in the filter-feeding organisms during algal blooms (which are always associated with mussel toxicity).

With so many questions about the origins, biological activity and risk to humans of chlorosulpholipids — not to mention the fact that no obvious strategy exists for making such stereochemically defined, polychlorinated compounds — there is clearly plenty of motivation to find a synthesis of these compounds. Nilewski and colleagues⁵ describe the first complete laboratory preparation of a chlorosulpholipid, in what is only the third publication to date concerning the synthesis of these fascinating compounds^{8,9}. Their strategy is simple and direct, but seems to be the result of painstaking experimentation — several other logical approaches are alluded to in the article, but all apparently failed perhaps owing to the inherent lack of reactivity of polychlorinated molecules.

The authors introduced all of the polar atoms — the chlorines and the oxygen of the sulphate — into the polychlorinated region of the molecule by adding them to carbon–carbon

double bonds (C=C bonds). Specifically, they used two alkene dichlorination reactions (in which a chlorine atom is attached to each of the two carbons of the C=C bond) and an epoxide formation/ring-opening sequence (in which an 'epoxide' intermediate is attacked by a chloride ion, yielding a product in which an oxygen is attached to one of the carbons of the C=C bond, and a chlorine atom is attached to the other; Fig. 1a).

While working on the epoxide-opening reaction, Nilewski *et al.* rediscovered an underappreciated process — the apparent formation of a reaction intermediate known as a five-membered ring chloronium ion (Fig. 1b). These ions were first described¹⁰ in 1967 (and their formation from epoxides was detailed a few years later¹¹), but they have scarcely been mentioned since. Nilewski *et al.* found that one of their epoxide-ring-opening reactions formed a product with an undesired stereochemical arrangement of chlorine atoms. This can be explained if a distal chlorine atom in the starting material attacks the epoxide, forming a five-membered ring chloronium ion as an intermediate during the reaction.

Initially troubled by this unexpected result, the authors realized that they could put it to good use: they prepared a different epoxide that contained groups arranged in different orientations from those of their original reactant, and exposed it to the same conditions as before (Fig. 1c). This time, the interference of a distal chlorine atom was helpful, and the product formed with the desired stereochemical arrangement of chlorine atoms. Once in place, these atoms controlled the subsequent addition of the remaining chlorines in the polychlorinated

portion of the molecule, so that all five chlorines adopted the desired, relative three-dimensional arrangement.

Nilewski and colleagues' synthesis⁵ could supply substantial quantities of the chlorosulpholipid for studies of its mechanism of toxicity. The availability of synthetic lipid might also allow the development of methods for detecting and analysing these toxins, to help avoid human illness. Furthermore, the authors' discovery of an unusual process in what was expected to be a routine reaction serves as a cautionary tale to other chemists, and offers a potentially useful approach for synthesizing other polychlorinated compounds. Finally, future research efforts should, with luck, reveal the role of chlorosulpholipids in algal membranes and the biosynthetic pathways used by nature to make polychlorinated molecules. ■

D. Karl Bedke and Christopher D. Vanderwal are in the Department of Chemistry, University of California, Irvine, California 92697, USA.
e-mail: cdv@uci.edu

1. Campàs, M., Prieto-Simón, B. & Marty, J.-L. *Talanta* **72**, 884–895 (2007).
2. Ciminiello, P. *et al.* *J. Org. Chem.* **66**, 578–582 (2001).
3. Ciminiello, P., Dell'Aversano, C., Fattorusso, E., Forino, M. & Magno, S. *Pure Appl. Chem.* **75**, 325–336 (2003).
4. Ciminiello, P. & Fattorusso, E. *Eur. J. Org. Chem.* 2533–2551 (2004).
5. Nilewski, C., Geisser, R. W. & Carreira, E. M. *Nature* **457**, 573–576 (2009).
6. Elovson, J. & Vagelos, P. R. *Proc. Natl Acad. Sci. USA* **62**, 957–963 (1969).
7. Haines, T. H. *Annu. Rev. Microbiol.* **27**, 403–412 (1973).
8. Shibuya, G. M., Kanady, J. S. & Vanderwal, C. D. *J. Am. Chem. Soc.* **130**, 12514–12518 (2008).
9. Yoshimitsu, T., Fukumoto, N. & Tanaka, T. *J. Org. Chem.* **74**, 696–702 (2008).
10. Peterson, P. E. *et al.* *J. Am. Chem. Soc.* **89**, 5902–5911 (1967).
11. Peterson, P. E., Indelicato, J. M. & Bonazza, B. R. *Tetrahedron Lett.* **12**, 13–16 (1971).

EVOLUTIONARY GENETICS

Origins of reproductive isolation

Edward J. Louis

A rare example of gene incompatibility between two species of budding yeast has been found. This discovery of elusive 'speciation' genes adds to other reproductive-isolation mechanisms operating in yeasts.

Reproductive isolation, leading to divergence between populations and eventually speciation, underlies the world's biodiversity. The evolutionary processes responsible for reproductive isolation have been of great theoretical and experimental interest, with new ones continually being revealed^{1–3}. For instance, in a group of related yeast *Saccharomyces* species, the process mediating reproductive isolation seems to be DNA mismatch repair acting on divergent sequences from each of the two parent species, rather than the two mechanisms that have generally been thought to mediate reproductive isolation — chromosomal

rearrangements and gene incompatibilities⁴. In fact, apart from one possible exception, chromosomal rearrangements are not a prominent mechanism of incompatibility and, although there is evidence for gene incompatibilities⁴, 'speciation' genes have not been found. Writing in *Cell*, Lee *et al.*⁵ now report incompatibility between a nuclear gene and mitochondria in two related yeast species, *S. cerevisiae* and *S. bayanus*, potentially providing the first example of speciation genes.

Hybrid lines are reproductively isolated (sterile) mainly because, after meiotic division of the first-generation (F1) hybrids, most

of the gametes formed are inviable⁶. Lee *et al.* created hybrid lines by substituting one or two *S. cerevisiae* chromosomes with the equivalent chromosomes from *S. bayanus* (Fig. 1). These substitution lines are similar to the rare, viable F2 progeny naturally produced by meiosis of the F1 hybrids between the two species. The authors then assayed both the growth rate of these lines and their ability to reproduce when mated with another hybrid of the same genetic make-up (selfing). They find that, in several cases, the substitution lines had lower fitness compared with the parent *S. cerevisiae*, indicating that these hybrids would be selected against over time — a form of reproductive barrier.

Moreover, one of these substitution lines could not maintain mitochondrial function, which is necessary for making use of non-fermentable carbon sources, meiosis and gamete production. Lee *et al.* show that this dysfunction is due to the expression of the *AEP2* gene of *S. bayanus* on the substituted chromosome 13, the protein product of which normally functions in the mitochondria: the Aep2P protein of *S. bayanus* cannot regulate the translation of *OLI1* messenger RNA encoded by the mitochondrial genome of *S. cerevisiae*. So, besides lower fitness, this complete sterility in the F2 generation owing to gene incompatibility is an additional reproductive-isolation mechanism in this hybrid; it is also the first example of gene incompatibility leading to isolation in *Saccharomyces* yeasts. The authors' interpretation is therefore that the *AEP2* and *OLI1* genes represent 'speciation' genes, and that adaptation towards use of non-fermentable carbon sources drove these genes' evolutionary divergence and thereby speciation.

Earlier studies also found gene incompatibilities to be segregating in *S. cerevisiae* populations. A prime example is the *PMS1* and *MLH1* genes, which are involved in DNA mismatch repair. The two genes' protein products interact to form a functional heterodimer⁷; however, one combination of alleles (gene copies) of these genes is non-functional, and so results in a high rate of mutations due to the lack of DNA mismatch repair. Intriguingly, this combination has not been observed in any of a number of isolates from various geographical locations⁷. Because the incompatible genotype is clearly disadvantageous, does incompatibility between these genes mean that they are examples of speciation genes?

The life history of yeast, which mainly comprises clonal growth and some sex, mostly selfing, is similar to that of the nematode worm *Caenorhabditis elegans*. Reproductive incompatibility has been reported in this species⁸ between two divergent populations. But the gene incompatibility in *C. elegans* was not interpreted as evidence for speciation genes, because the polymorphism has been maintained for a long time without speciation and seems to have moved between the populations through sexual reproduction.

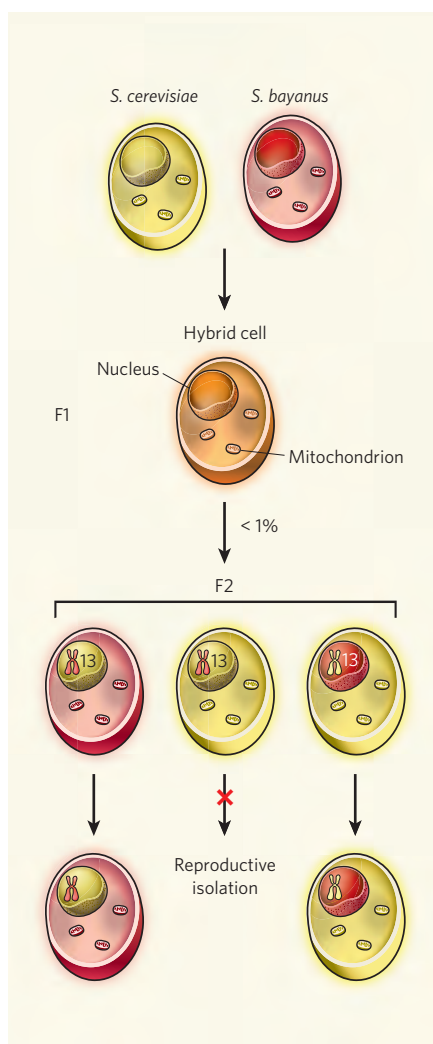


Figure 1 | Hybrid sterility due to incompatibility between nuclear and mitochondrial genomes.

When *Saccharomyces cerevisiae* and *S. bayanus* mate, the F1 generation hybrid carries a set of nuclear and mitochondrial genomes from each of the two parent yeast species. Usually, however, one mitochondrial genome is lost during growth of the F1 hybrid. The rare F2 progeny that arise from this hybrid inherit genome segments, including the mitochondrial genome, from either one or other parent — three examples are shown. So most of the reproductive isolation occurs after F1 meiosis, which can happen but yields few viable progeny. Of the rare viable F2 progeny, certain combinations of genes are incompatible, either for fitness or for subsequent meiosis. Lee *et al.*⁵ show that an *S. bayanus* gene on chromosome 13, *AEP2*, is incompatible with the processing of an *S. cerevisiae* mitochondrial gene, *OLI1*, resulting in loss of mitochondrial function and so inability of the F2 hybrid to undergo meiosis.

Moreover, reproductive isolation has been partly generated experimentally by subjecting *S. cerevisiae* populations to selection in different environments⁹. Because such isolation also seems to be due to gene incompatibilities, it could be that adaptation to different environments — perhaps different carbon sources as Lee and colleagues⁵ suggest — drives the

evolution of genes involved, potentially leading to incompatibility between divergent populations. This possibility is not unprecedented, because there is evidence for rapid evolution of the whole galactose-utilization pathway in *Saccharomyces kudriavzevii*¹⁰, with several genes in this pathway being inactivated in a single species.

The incompatibility between a nuclear gene and the expression of a mitochondrial gene that Lee *et al.* report — the first experimental example of a naturally occurring gene incompatibility resulting in reproductive isolation in *Saccharomyces* yeasts — operates at two levels: reduced fitness and loss of mitochondrial function. One question relating to this and any such finding of extant mechanisms maintaining isolation is: when did the mechanism arise? Was it part of the incipient speciation process, or is it a fixed difference post-speciation?

The gene incompatibility Lee *et al.* describe could easily have arisen after accumulated divergence and speciation. Indeed, the main reproductive barrier between hybrid species normally occurs in the F1 generation, which these authors' substitution line bypasses. What's more, *S. cerevisiae* and *S. bayanus* have readily hybridized in the past¹¹, with subsequent genome evolution. Finally, rapid evolution of pathways for use of different carbon sources has been seen in another *Saccharomyces* yeast — *S. kudriavzevii*¹⁰ — and is thought to be due to adaptation to a specific environment.

So one must be cautious in labelling gene incompatibilities as speciation genes, or at least in interpreting them as being causal in the speciation process rather than a result of divergence post-speciation. What we have now in *Saccharomyces* yeasts is the potential involvement of three post-F1 reproductive-isolation mechanisms⁴: gene incompatibilities, chromosome rearrangements and simple sequence divergence acted upon by the mismatch-repair system. Further work is needed to determine which, if any, of these mechanisms has driven the speciation process itself, and which are consequences of further adaptation and divergence of species.

Edward J. Louis is at the Institute of Genetics, Queen's Medical Centre, University of Nottingham, Nottingham NG7 2UH, UK. e-mail: ed.louis@nottingham.ac.uk

1. Coyne, J. A. *Nature* **355**, 511–515 (1992).
2. Coyne, J. A. & Orr, H. A. *Speciation* (Sinauer, 2004).
3. Dobzhansky, T. *Genetics and the Origin of Species* (Columbia Univ. Press, 1937).
4. Greig, D. *Heredity* **102**, 39–44 (2009).
5. Lee, H.-Y. *et al.* *Cell* **135**, 1065–1073 (2008).
6. Naumov, G. I. *Stud. Mycol.* **30**, 469–475 (1987).
7. Heck, J. A. *et al.* *Proc. Natl Acad. Sci. USA* **103**, 3256–3261 (2006).
8. Seidel, H. S., Rockman, M. V. & Kruglyak, L. *Science* **319**, 589–594 (2008).
9. Dettman, J. R., Sirjusingh, C., Kohn, L. M. & Anderson, J. B. *Nature* **447**, 585–588 (2007).
10. Hittinger, C. T., Rokas, A. & Carroll, S. B. *Proc. Natl Acad. Sci. USA* **101**, 14144–14149 (2004).
11. Dunn, B. & Sherlock, G. *Genome Res.* **18**, 1610–1623 (2008).

The *Sorghum bicolor* genome and the diversification of grasses

Andrew H. Paterson¹, John E. Bowers¹, Rémy Bruggmann², Inna Dubchak³, Jane Grimwood⁴, Heidrun Gundlach⁵, Georg Haberer⁵, Uffe Hellsten³, Therese Mitros⁶, Alexander Poliakov³, Jeremy Schmutz⁴, Manuel Spannagl⁵, Haibao Tang¹, Xiyin Wang^{1,7}, Thomas Wicker⁸, Arvind K. Bharti², Jarrod Chapman³, F. Alex Feltus^{1,9}, Udo Gowik¹⁰, Igor V. Grigoriev³, Eric Lyons¹¹, Christopher A. Maher¹², Mihaela Martis⁵, Apurva Narechania¹², Robert P. Otillar³, Bryan W. Penning¹³, Asaf A. Salamov³, Yu Wang⁵, Lifang Zhang¹², Nicholas C. Carpita¹⁴, Michael Freeling¹¹, Alan R. Gingle¹, C. Thomas Hash¹⁵, Beat Keller⁸, Patricia Klein¹⁶, Stephen Kresovich¹⁷, Maureen C. McCann¹³, Ray Ming¹⁸, Daniel G. Peterson^{1,19}, Mehboob-ur-Rahman^{1,20}, Doreen Ware^{12,21}, Peter Westhoff¹⁰, Klaus F. X. Mayer⁵, Joachim Messing² & Daniel S. Rokhsar^{3,4}

Sorghum, an African grass related to sugar cane and maize, is grown for food, feed, fibre and fuel. We present an initial analysis of the ~730-megabase *Sorghum bicolor* (L.) Moench genome, placing ~98% of genes in their chromosomal context using whole-genome shotgun sequence validated by genetic, physical and syntenic information. Genetic recombination is largely confined to about one-third of the sorghum genome with gene order and density similar to those of rice. Retrotransposon accumulation in recombinationally recalcitrant heterochromatin explains the ~75% larger genome size of sorghum compared with rice. Although gene and repetitive DNA distributions have been preserved since palaeopolyploidization ~70 million years ago, most duplicated gene sets lost one member before the sorghum–rice divergence. Concerted evolution makes one duplicated chromosomal segment appear to be only a few million years old. About 24% of genes are grass-specific and 7% are sorghum-specific. Recent gene and microRNA duplications may contribute to sorghum's drought tolerance.

The Saccharinae plants include some of the most efficient biomass accumulators, providing food and fuel from starch (sorghum) and sugar (sorghum and *Saccharum*, sugar cane), and have potential for use as cellulosic biofuel crops (sorghum, sugar cane, *Miscanthus*). Of singular importance to Saccharinae productivity is C₄ photosynthesis, comprising biochemical and morphological specializations that increase net carbon assimilation at high temperatures¹. Despite their common photosynthetic strategy, the Saccharinae show much morphological and genomic variation (Supplementary Fig. 1).

Its small genome (~730 Mb) makes sorghum an attractive model for functional genomics of Saccharinae and other C₄ grasses. Rice, the first fully sequenced cereal genome, is more representative of C₃ photosynthetic grasses. Drought tolerance makes sorghum especially important in dry regions such as northeast Africa (its centre of diversity) and the southern plains of the United States. Genetic variation in the partitioning of carbon into sugar stores versus cell wall mass, and in perenniality and associated features such as tillering and stalk reserve retention², make sorghum an attractive system for the study of traits important in perennial cellulosic biomass crops. Its high level of inbreeding makes it an attractive association genetics system³. Transgenic approaches to sorghum

improvement are constrained by high gene flow to weedy relatives⁴, making knowledge of its intrinsic genetic potential all the more important.

Reconstructing a repeat-rich genome from shotgun sequences

Preferred approaches to sequencing entire genomes are currently to apply shotgun sequencing⁵ either to a minimum 'tiling path' of genomic clones, or to genomic DNA directly. The latter approach, whole-genome shotgun (WGS) sequencing, is widely used for mammalian genomes, being fast, relatively economical and reducing cloning bias. However, its applicability has been questioned for repetitive DNA-rich plant genomes⁶.

Despite a repeat content of ~61%, a high-quality genome sequence was assembled from homozygous sorghum genotype BTx623 by using WGS and incorporating the following: (1) ~8.5 genome equivalents of paired-end reads⁷ from genomic libraries spanning a ~100-fold range of insert sizes (Supplementary Table 1), resolving many repetitive regions; and (2) high-quality read length averaging 723 bp, facilitating assembly. Comparison with 27 finished bacterial artificial chromosomes (BACs) showed the WGS assembly to be >98.46% complete and accurate to <1 error per 10 kb (Supplementary Note 2.5).

¹Plant Genome Mapping Laboratory, University of Georgia, Athens, Georgia 30602, USA. ²Waksman Institute for Microbiology, Rutgers University, Piscataway, New Jersey 08854, USA. ³DOE Joint Genome Institute, Walnut Creek, California 94598, USA. ⁴Stanford Human Genome Center, Stanford University, Palo Alto, California 94304, USA. ⁵MIPS/IBIS, Helmholtz Zentrum München, Ingolstaedter Landstrasse 1, 85764 Neuherberg, Germany. ⁶Center for Integrative Genomics, University of California, Berkeley, California 94720, USA. ⁷College of Sciences, Hebei Polytechnic University, Tangshan, Hebei 063000, China. ⁸Institute of Plant Biology, University of Zurich, Zollikerstrasse 107, 8008 Zurich, Switzerland. ⁹Department of Genetics and Biochemistry, Clemson University, Clemson, South Carolina 29631, USA. ¹⁰Institut für Entwicklungs- und Molekularbiologie der Pflanzen, Heinrich-Heine-Universität, Universitätsstrasse 1, D-40225 Düsseldorf, Germany. ¹¹Department of Plant and Microbial Biology, University of California, Berkeley, California 94720, USA. ¹²Cold Spring Harbor Laboratory, Cold Spring Harbor, New York 11724, USA. ¹³Department of Biological Sciences, ¹⁴Department of Botany and Plant Pathology, Purdue University, West Lafayette, Indiana 47907, USA. ¹⁵International Crops Research Institute for the Semi-Arid Tropics (ICRISAT), Patancheru 502 324, India. ¹⁶Department of Horticulture and Institute for Plant Genomics and Biotechnology, Texas A&M University, College Station, Texas 77843, USA. ¹⁷Institute for Genomic Diversity, Cornell University, Ithaca, New York 14853, USA. ¹⁸Department of Plant Biology, University of Illinois at Urbana-Champaign, Urbana, Illinois 61801, USA. ¹⁹Mississippi Genome Exploration Laboratory, Mississippi State University, Starkville, Mississippi 39762, USA. ²⁰National Institute for Biotechnology & Genetic Engineering (NIBGE), Faisalabad, Pakistan. ²¹USDA NAA Robert Holley Center for Agriculture and Health, Ithaca, New York 14853, USA.

Comparison with a high-density genetic map⁸, a 'finger-print contig' (FPC)-based physical map⁹, and the rice sequence⁶ improved the sorghum WGS assembly (Supplementary Notes 1 and 2). Among the 201 largest scaffolds (spanning 678.9 Mb, 97.3% of the assembly), 28 showed discrepancies with two or more of these lines of evidence (Supplementary Note 2.6), often near repetitive elements. After breaking the assembly at the points of discrepancy, the resulting 229 scaffolds have an N50 (number of scaffolds that collectively cover at least 50% of the assembly) of 35 and L50 (length of the shortest scaffold among those that collectively cover 50% of the assembly) of 7.0 Mb. A total of 38 (2%) of 1,869 FPC contigs⁹ were deemed erroneous, containing >5 BAC ends that fell into different sequence scaffolds.

A total of 127 scaffolds containing 625.7 Mb (89.7%) of DNA and 1,476 FPC contigs could be assigned to chromosomal locations and oriented. Fifteen out of twenty chromosome ends terminated in telomeric repeats. The other 102 scaffolds were generally smaller (53.2 Mb, 7.6%), with 85 (83%) containing far greater-than-average abundance of the Cen38 (ref. 10) centromeric repeat, and with only 374 predicted genes. These 102 scaffolds merged only 193 FPC contigs, presumably due to the greater abundance of repeats that are recalcitrant to clone-based physical mapping⁹ and may be omitted in BAC-by-BAC approaches¹¹.

Genome size evolution and its causes

The ~75% larger quantity of DNA in the genome of sorghum compared with rice is mostly heterochromatin. Alignment to genetic⁸ and cytological maps¹² suggests that sorghum and rice have similar quantities of euchromatin (252 and 309 Mb, respectively; Supplementary Table 7), accounting for 97–98% of recombination (1,025.2 cM and 1,496.5 cM, respectively) and 75.4–94.2% of genes in the respective cereals, with largely collinear gene order⁹. In contrast, sorghum heterochromatin occupies at least 460 Mb (62%), far more than in rice (63 Mb, 15%). The ~3× genome expansion in maize since its divergence from sorghum¹³ has been more dispersed—recombinogenic DNA has grown 4.5× to ~1,382 Mb, much more than can be explained by genome duplication¹⁴.

The net size expansion of the sorghum genome relative to rice largely involved long terminal repeat (LTR) retrotransposons. The

sorghum genome contains 55% retrotransposons, intermediate between the larger maize genome (79%) and smaller rice genome (26%). Sorghum more closely resembles rice in having a higher ratio of *gypsy*-like to *cop*ia-like elements (3.7 to 1 and 4.9 to 1) than maize (1.6 to 1; Supplementary Table 10).

Although recent retroelement activity is widely distributed across the sorghum genome, turnover is rapid (as in other cereals¹⁵) with pericentromeric elements persisting longer. Young LTR retrotransposon insertions (<0.01 million years (Myr) ago) appear randomly distributed along chromosomes, suggesting that they are preferentially eliminated from gene-rich regions⁹ but accumulate in gene-poor regions (Fig. 1; see also Supplementary Note 3.1). Insertion times suggest a major wave of retrotransposition <1 Myr ago, after a smaller wave 1–2 Myr ago (Supplementary Fig. 2).

CACTA-like elements, the predominant sorghum DNA transposons (4.7% of the genome), seem to relocate genes and gene fragments, as do rice 'Pack-MULEs'¹⁶ and maize helitrons¹⁷. Many sorghum CACTA elements are non-autonomous deletion derivatives in which transposon genes have been replaced with non-transposon DNA including exons from one or more cellular genes as exemplified for family *G118* (Fig. 2). Among 13,775 CACTA elements identified (Supplementary Note 3.4), 200 encode no transposon proteins but contain at least one cellular gene fragment.

In total, DNA transposons constitute 7.5% of the sorghum genome, intermediate between maize (2.7%) and rice (13.7%; Supplementary Table 10). Miniature inverted-repeat transposable elements, 1.7% of the genome, are associated with genes (Fig. 1; see also Supplementary Note 3) as in other cereals⁶. Helitrons, ~0.8% of the genome, nearly all lack helicase in sorghum as in maize¹⁷, but carry fewer gene fragments in sorghum than maize (Supplementary Note 3.5). Organellar DNA insertion has contributed only 0.085% to the sorghum nuclear genome, far less than the 0.53% of rice (Supplementary Note 2.7).

The gene complement of sorghum

Among 34,496 sorghum gene models, we found ~27,640 bona fide protein-coding genes by combining homology-based and *ab initio* gene prediction methods with expressed sequences from sorghum,

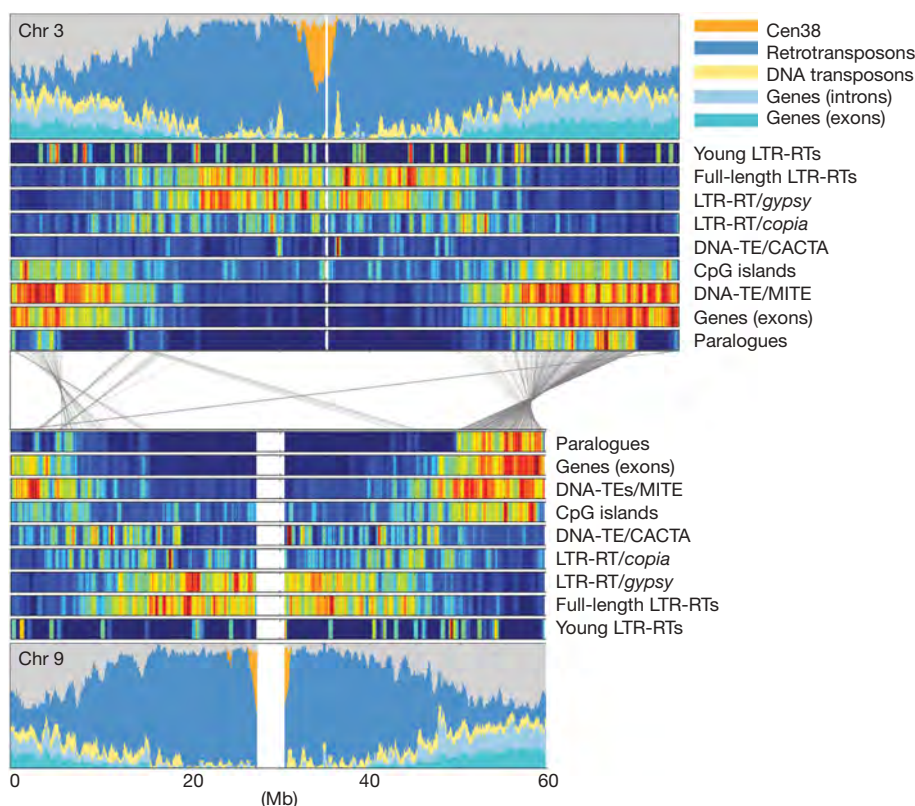


Figure 1 | Genomic landscape of sorghum chromosomes 3 and 9. Area charts quantify retrotransposons (55%), genes (6% exons, 8% introns), DNA transposons (7%) and centromeric repeats (2%). Lines between chromosomes 3 and 9 connect collinear duplicated genes. Heat-map tracks detail the distribution of selected elements. Figures for all sorghum chromosomes are in Supplementary Note 3. Cen38, sorghum-specific centromeric repeat¹⁰; RTs, retrotransposons (class I); LTR-RTs, long terminal repeat retrotransposons; DNA-TEs, DNA transposons (class II).

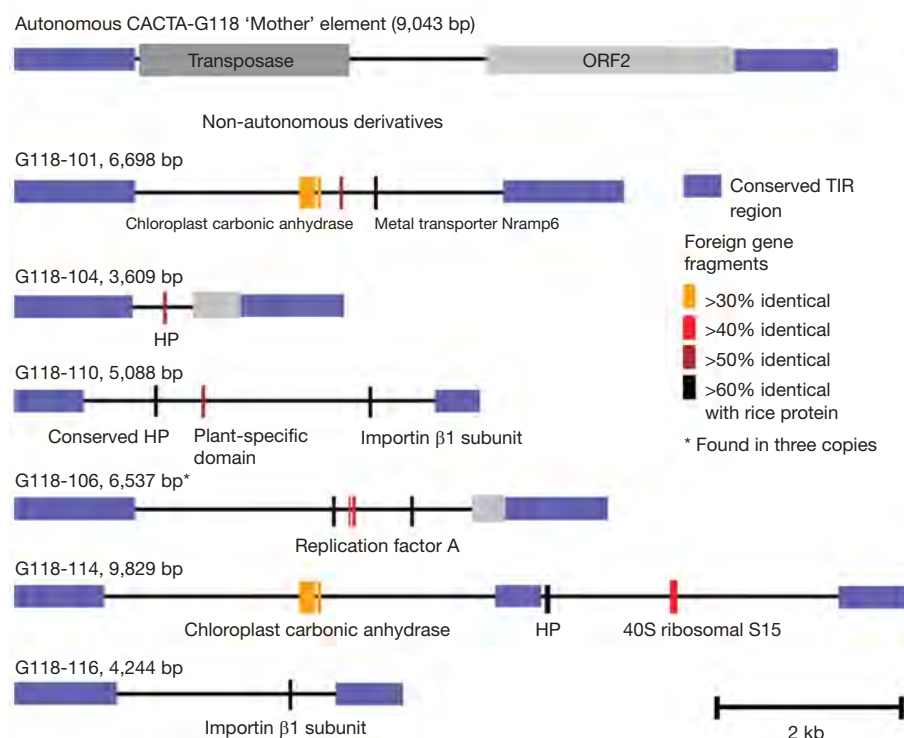


Figure 2 | CACTA element deletion derivatives that carry gene fragments. CACTA family G118 has only one complete and presumably autonomous 'mother' element. Among 18 deletion derivatives, only the terminal 500–2,500 bp are conserved, with 8 carrying gene fragments internally. One relatively homogeneous subgroup (106, 111 and 112) presumably arose recently, whereas other derivatives are unique. The locations of the hits to known rice proteins are indicated as coloured boxes. The descriptions of the foreign gene fragments are indicated underneath the boxes. HP, hypothetical protein.

maize and sugar cane (Supplementary Note 4). Evidence for alternate splicing is found in 1,491 loci.

Another 5,197 gene models are usually shorter than the bona fide genes (often <150 amino acids); have few exons (often one) and no expressed sequence tag (EST) support (compared with 85% for bona fide genes); are more diverged from rice genes; and are often found in large families with 'hypothetical', 'uncharacterized' and/or retroelement-associated annotations, despite repeat masking (Supplementary Note 4). A high concentration in pericentromeric regions where bona fide genes are scarce (Fig. 1) suggests that many of these low confidence gene models are retroelement-derived. We also identified 727 processed pseudogenes and 932 models containing domains known only from transposons.

The exon size distributions of orthologous sorghum and rice genes agree closely, and intron position and phase show >98% concordance (Supplementary Note 5). Intron size has been conserved between sorghum and rice, although it has increased in maize owing to transpositions¹⁸.

Most paralogues in sorghum are proximally duplicated, including 5,303 genes in 1,947 families of ≥ 2 genes (Supplementary Note 4.3). The longest tandem gene array is 15 cytochrome P450 genes. Other sorghum-specific tandem gene expansions include haloacid dehalogenase-like hydrolases (PF00702), FNIP repeats (PF05725), and male sterility proteins (PF03015).

We confirmed the genomic locations of 67 known sorghum microRNAs (miRNAs) and identified 82 additional miRNAs (Supplementary Note 4.4). Five clusters located within 500 bp of each other represent putative polycistronic miRNAs, similar to those in *Arabidopsis* and *Oryza*. Natural antisense miRNA precursors (nat-miRNAs) of family miR444 (ref. 19) have been identified in three copies.

Comparative gene inventories of angiosperms

The number and sizes of sorghum gene families are similar to those of *Arabidopsis*, rice and poplar (Fig. 3 and Supplementary Note 4.6). A total of 9,503 (58%) sorghum gene families were shared among all four species and 15,225 (93%) with at least one other species. Nearly 94% (25,875) of high-confidence sorghum genes have orthologues in rice, *Arabidopsis* and/or poplar, and together these gene complements define 11,502 ancestral angiosperm gene families represented

in at least one contemporary grass and rosid genome. However, 3,983 (24%) gene families have members only in the grasses sorghum and rice; 1,153 (7%) appear to be unique to sorghum.

Pfam domains that are over-represented, under-represented or even absent in sorghum relative to rice, poplar and *Arabidopsis*, may reflect biological peculiarities specific to the *Sorghum* lineage (Supplementary Table 20). Domains over-represented in sorghum are usually present in the other organisms, a notable exception being the α -kafirin domain that accounts for most seed storage protein and corresponds to maize zeins²⁰ but which is absent from rice.

Nucleotide-binding-site-leucine-rich-repeat (NBS-LRR) containing proteins associated with the plant immune system are only about half as frequent in sorghum as in rice. A search with 12 NBS domains from published rice, maize, wheat and *Arabidopsis* gene sequences revealed 211 NBS-LRR coding genes in sorghum, 410 in rice and 149 in *Arabidopsis*²¹. Sorghum NBS-LRR genes mostly encode the CC type of N-terminal domains. Only two sorghum genes (Sb02g005860 and Sb02g036630) contain the TIR domain, and neither contains an NBS domain. NBS-LRR genes are most abundant on sorghum chromosome 5 (62), and its rice homologue (chromosome 11, 106). Enrichment of NBS-LRR genes in these corresponding genomic regions suggests conservation of R gene location, in contrast to a proposal that R gene movement may be advantageous²².

Evolution of distinctive pathways and processes

The evolution of C_4 photosynthesis in the *Sorghum* lineage involved redirection of C_3 progenitor genes as well as recruitment and functional divergence of both ancient and recent gene duplicates. The sole sorghum C_4 pyruvate orthophosphate dikinase (*ppdk*) and the phosphoenolpyruvate carboxylase kinase (*ppck*) gene and its two isoforms (produced by the whole genome duplication) have only single orthologues in rice. Additional duplicates formed in maize after the sorghum–maize split (*Zmppck2* and *Zmppck3*). The C_4 NADP-dependent malic enzyme (*me*) gene has an adjacent isoform but each corresponds to a different maize homologue, suggesting tandem duplication before the sorghum–maize split. The C_4 malate dehydrogenase (*mdh*) gene and its isoform are also adjacent, but share 97% amino acid similarity and correspond to the single known maize *Mdh* gene, suggesting tandem duplication in sorghum after its split with maize. The rice *Me* and *Mdh* genes are single

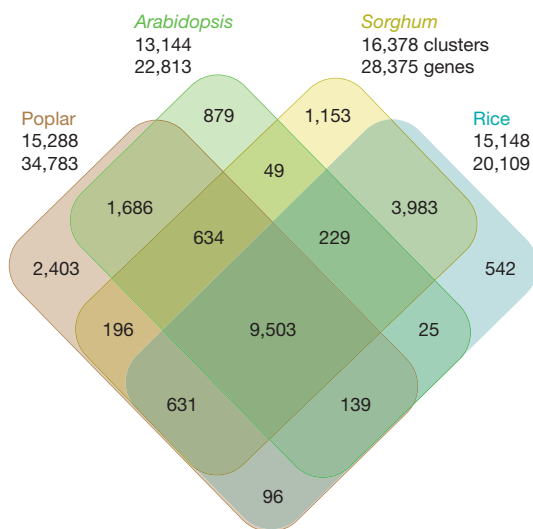


Figure 3 | Orthologous gene families between sorghum, *Arabidopsis*, rice and poplar. The numbers of gene families (clusters) and the total numbers of clustered genes are indicated for each species and species intersection.

copy, suggesting duplication and recruitment to the C_4 pathway after the Panicoideae–Oryzoideae divergence (Supplementary Note 9).

The sorghum sequence reinforces inferences previously based only on rice, about how different grass and dicotyledon gene inventories relate to their respective types of cell walls^{23,24}. In grasses, cellulose microfibrils coated with mixed-linkage (1→3),(1→4)- β -D-glucans are interlaced with glucuronoarabinoxylans and an extensive complex of phenylpropanoids²⁵. The sorghum sequence largely corroborates differences between dicotyledons and rice in the distribution of cell wall biogenesis genes (Supplementary Note 10). For example, the Cesa/Csl superfamily and callose synthases have either diverged to form new subgroups or functionally non-essential subgroups were selectively lost, such as *CslB* and *CslG* lost from the grasses, and *CslF* and *CslH* lost from species with dicotyledon-like cell walls²⁶. The previously rice-unique *CslF* and *CslH* genes are present in sorghum. *Arabidopsis* contains a single group F GT31 gene, whereas sorghum and rice contain six and ten, respectively.

The characteristic adaptation of sorghum to drought may be partly related to expansion of one miRNA and several gene families. Rice miRNA 169g, upregulated during drought stress²⁷, has five sorghum homologues (sbi-MIR169c, sbi-MIR169d, sbi-MIR169.p2, sbi-MIR169.p6 and sbi-MIR169.p7). The computationally predicted target of the sbi-MIR169 subfamily comprises members of the plant nuclear factor Y (NF-Y) B transcription factor family, linked to improved performance under drought by *Arabidopsis* and maize²⁸. Cytochrome P450 domain-containing genes, often involved in scavenging toxins such as those accumulated in response to stress, are abundant in sorghum with 326 versus 228 in rice. Expansins, enzymes that break hydrogen bonds and are responsible for a variety of growth responses that could be linked to the durability of sorghum, occur in 82 copies in sorghum versus 58 in rice and 40 each in *Arabidopsis* and poplar.

Duplication and diversification of cereal genomes

Whole-genome duplication in a common ancestor of cereals is reflected in sorghum and rice gene ‘quartets’ (Fig. 4). A total of 19,929 (57.8%) sorghum gene models were in blocks collinear with rice (Supplementary Note 6). After the shared whole-genome duplication, only one copy was retained for 13,667 (68.6%) collinear genes with 13,526 (99%) being orthologous in rice–sorghum, indicating that most gene losses predate taxon divergence. Both sorghum and rice retained both copies of 4,912 (14.2%) genes, whereas sorghum lost one copy of 1,070 (3.1%) and rice lost one copy of 634 (1.8%). These patterns are likely to be predictive of other grass genomes, as the

major grass lineages diverged from a common ancestor at about the same time²⁹ (see also Supplementary Note 7).

Although most post-duplication gene loss happened in a common cereal ancestor, some lineage-specific patterns occur. A total of 2 and 10 protein functional (Pfam) domains showed enrichment for duplicates and singletons (respectively) in sorghum but not rice (Supplementary Note 6.1). Because the sorghum–rice divergence is thought to have happened 20 Myr or more after genome duplication²⁹, this suggests that even long-term gene loss differentially affects gene functional groups.

One genomic region has been subject to a high level of concerted evolution. It was previously suggested that rice chromosomes 11 and 12 share a ~5–7-Myr-old segmental duplication^{30–32}. We found a duplicated segment in the corresponding regions of sorghum chromosomes 5 and 8 (Fig. 5). Sorghum–sorghum and rice–rice paralogues from this region show rates of synonymous DNA substitution (K_s) of 0.44 and 0.22, respectively, consistent with only 34 and 17 Myr of divergence. However, the K_s value of sorghum–rice orthologues is 0.63, similar to the respective genome-wide averages (0.81, 0.87). We hypothesize that the apparent segmental duplication actually resulted from the pan-cereal whole-genome duplication and became differentiated from the remainder of the chromosome(s) owing to concerted evolution acting independently in sorghum, rice and perhaps other cereals. Gene conversion and illegitimate recombination are more frequent in the rice 11–12 region than elsewhere in the genome³³. Physical and genetic maps suggest shared terminal segments of the corresponding chromosomes in wheat (4, 5)³⁴, foxtail millet (VII, VIII) and pearl millet (linkage groups 1, 4)³⁵.

Synthesis and implications

Comparison of the sorghum, rice and other genomes clarifies the grass gene set. Pairs of orthologous sorghum and rice genes combined with recent paralogous duplications define 19,542 conserved grass gene families, each representing one gene in the sorghum–rice common ancestor. Our sorghum gene count is similar to that in a manually curated rice annotation (RAP2)³⁶, but this similarity masks some differences. About 2,054 syntenic orthologues shared by our sorghum annotation and the TIGR5 (ref. 37) rice annotation are absent from RAP2. Conversely, ~12,000 TIGR5 annotations may be transposable elements or pseudogenes, comprising large families of hypothetical genes in both sorghum and rice RAP2, often with short exons, few introns and limited EST support. Phylogenetically incongruent cases of apparent gene loss (for example, genes shared by *Arabidopsis* and sorghum but not rice; Fig. 3) may also suggest sequence gaps or misannotations.

Grass genome architecture may reflect euchromatin-specific effects of recombination and selection, superimposed on non-adaptive processes of mutation and genetic drift that apply to all genomic regions³⁸. Patterns of gene and repetitive DNA organization remain correlated in homologous chromosomes duplicated 70 Myr ago (Fig. 1), despite extensive turnover of specific repetitive elements. Synteny is highest and retroelement abundance lowest in distal chromosomal regions. More rapid retroelement removal from gene-rich euchromatin that frequently recombines than from heterochromatin that rarely recombines supports the hypothesis that recombination may preserve gene structure, order and/or spacing by exposing new insertions to selection⁹. Less euchromatin–heterochromatin polarization in maize, where retrotransposon persistence in euchromatin seems more frequent, may reflect variation in grass genome architecture or perhaps a lingering consequence of more recent genome duplication³⁹.

Identification of conserved DNA sequences may help us to understand essential genes and binding sites that define grasses. Progress in sequencing *Brachypodium distachyon*⁴⁰ sets the stage for panicoid–oryzoid–poooid phylogenetic triangulation of genomic changes, as well as association of some such changes with phenotypes ranging from molecular (gene expression patterns) to morphological. The divergence between sorghum, rice and *Brachypodium* is sufficient to randomize

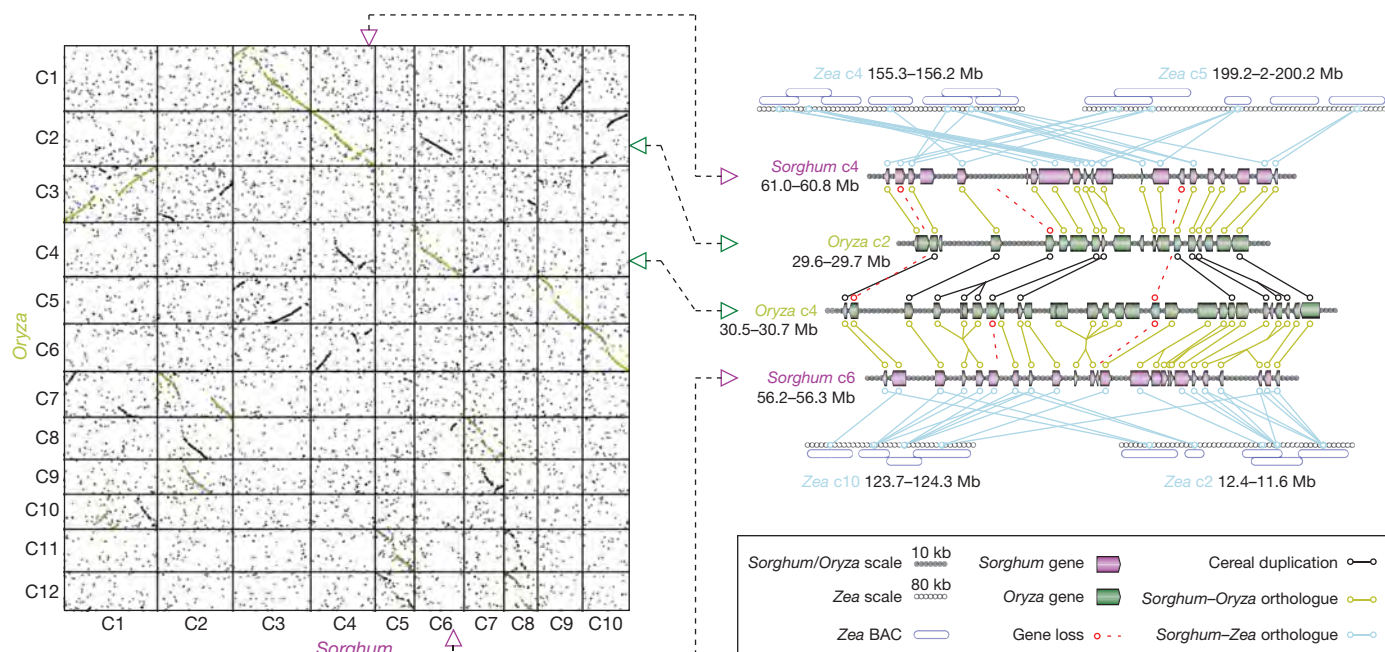


Figure 4 | Alignment of sorghum, rice and maize. Dot plots show intergenomic (gold) and intragenomic (black) alignments. One sorghum–rice quartet showing both orthologous and paralogous (duplicated) regions is magnified. Infrequent gene loss (red; see legend) after sorghum–rice divergence causes ‘special cases’ in which there are paralogues

nonfunctional sequence, facilitating conserved noncoding sequence (CNS) discovery^{41,42} (Supplementary Fig. 9). More distant comparisons to the dicotyledon *Arabidopsis* show exon conservation but no CNS (Supplementary Fig. 10). Chloridoid and arundinoid genome sequences are needed to sample the remaining grass lineages, and an outgroup such as *Ananas* (pineapple) or *Musa* (banana) would further aid in identifying genes and sequences that define grasses.

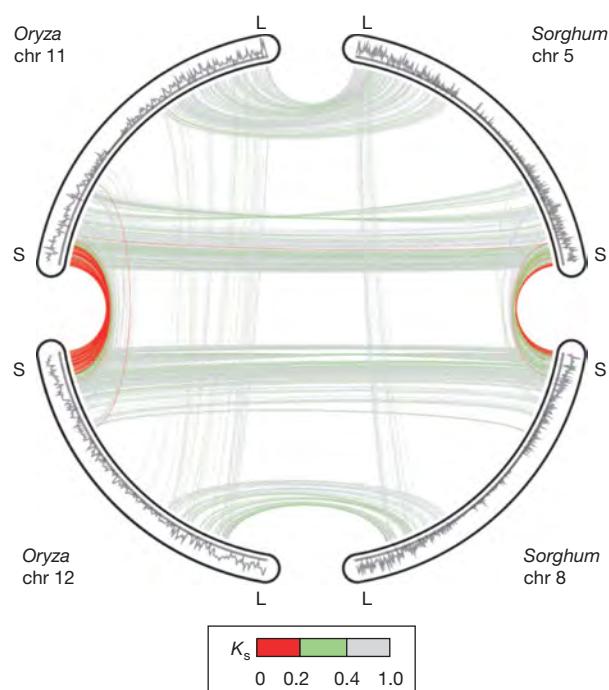


Figure 5 | Independent illegitimate recombination in corresponding regions of sorghum and rice. Four homologous rice and sorghum chromosomes (11 and 12 in rice; 5 and 8 in sorghum) are shown, with gene densities plotted. ‘L’ and ‘S’ show long and short arms, respectively. Lines show K_s between homologous gene pairs, and colours are used to show different dates of conversion events.

but no orthologues. Each sorghum region corresponds to two duplicated maize regions³⁹, with maize gene loss suggested where sorghum loci only match one of the two. Because maize BACs are mostly unfinished, sorghum loci are aligned to the centres. Note the different scale necessary for maize physical distance. Larger dot plots are in Supplementary Note 6.

The fact that the sorghum genome has not re-duplicated in ~70 Myr²⁹ makes it a valuable outgroup for deducing fates of gene pairs and CNS in grasses that have reduplicated. Single sorghum regions correspond to two regions resulting from maize-specific genome doubling³⁹—gene fractionation is evident (Fig. 4), and subfunctionalization is probable (Supplementary Fig. 10). Sorghum may prove especially valuable for unravelling genome evolution in the more closely related *Saccharum*–*Miscanthus* clade: two genome duplications since its divergence from sorghum 8–9 Myr ago⁴³ complicate sugar cane genetics⁴⁴ yet *Saccharum* BACs show substantially conserved gene order with sorghum (Supplementary Note 11).

Conservation of grass gene structure and order facilitates development of DNA markers to support crop improvement. We identified ~71,000 simple-sequence repeats (SSRs) in sorghum (Supplementary List 1); among a sampling of 212, only 9 (4.2%) map to paralogues of their source locus. Conserved-intron scanning primers (Supplementary List 2) for 6,760 genes provide DNA markers useful across many monocotyledons, particularly valuable for ‘orphan cereals’⁴⁵.

As the first sequenced plant genome of African origin, sorghum adds new dimensions to ethnobotanical research. Of particular interest will be the identification of alleles selected during the earliest stages of sorghum cultivation, which are valuable towards testing the hypothesis that convergent mutations in corresponding genes contributed to independent domestications of divergent cereals⁴⁶. Invigorated sorghum improvement would benefit regions such as the African ‘Sahel’ where drought tolerance makes sorghum a staple for human populations that are increasing by 2.8% per year. Sorghum yield improvement has lagged behind that of other grains, in Africa only gaining a total of 37% (western) to 38% (eastern) from 1961–63 to 2005–07 (Supplementary Note 12).

METHODS SUMMARY

Genome sequencing. Approximately 8.5-fold redundant paired-end shotgun sequencing was performed using standard Sanger methodologies from small (~2–3 kb) and medium (5–8 kb) insert plasmid libraries, one fosmid library (~35 kb inserts), and two BAC libraries (insert size 90 and 108 kb). (Supplementary Note 1.)

Integration of shotgun assembly with genetic and physical maps. The largest 201 scaffolds, all exceeding 39 kb, excluding ‘N’s, and collectively representing 678,902,941 bp (97.3%) of nucleotides, were checked for possible chimaeras

suggested by the sorghum genetic map, sorghum physical map, abrupt changes in gene or repeat density, rice gene order, and coverage by BAC or fosmid clones (Supplementary Note 2).

Repeat analysis. *De novo* searches for LTR retrotransposons used LTR_STRUC. *De novo* detection of CACTA-DNA transposons and MITEs used custom programs (Supplementary Note 3). Known repeats were identified by RepeatMasker (Open-3-1-8) (<http://www.repeatmasker.org>) with mips-REdat_6.2_Poaceae, a compilation of grass repeats including sorghum-specific LTR retrotransposons (<http://mips.gsf.de/proj/plant/webapp/recat/>). The insertion age of full-length LTR-retrotransposons was determined from the evolutionary distance between 5' and 3' soloLTR derived from a ClustalW alignment of the two soloLTRs.

Protein-coding gene annotation. Putative protein-coding loci were identified based on BLAST alignments of rice and *Arabidopsis* peptides and sorghum and maize ESTs. GenomeScan⁴⁷ was applied using maize-specific parameters. Predicted coding structures were merged with EST data from maize and sorghum using PASA⁴⁸.

Intergenic and intragenomic alignments. Dot plots used ColinearScan⁴⁹ and multi-alignments used MCSan⁵⁰, applied to RAP2³⁶ (mapped representative models, 29,389 loci) and the sbi1.4 annotation set (34,496 loci). Pairwise BLASTP ($E < 1 \times 10^{-5}$, top five hits), both within each genome and between the two genomes, was used to retrieve potential anchors. *Zea* BAC sequences and FPC contig coordinates were downloaded (<http://www.maizegenome.org>, release 7 January 2008). *Zea* BACs were searched for potential orthologues of *Sorghum* coding sequences using translated BLAT with a minimum score of 100.

Received 20 August; accepted 9 December 2008.

- Hatch, M. D. & Slack, C. R. Photosynthesis by sugar-cane leaves—a new carboxylation reaction and pathway of sugar formation. *Biochem. J.* **101**, 103 (1966).
- Paterson, A. H. et al. The weediness of wild plants—molecular analysis of genes influencing dispersal and persistence of johnsongrass, *Sorghum halepense* (L.) pers. *Proc. Natl Acad. Sci. USA* **92**, 6127–6131 (1995).
- Hamblin, M. T. et al. Equilibrium processes cannot explain high levels of short- and medium-range linkage disequilibrium in the domesticated grass *Sorghum bicolor*. *Genetics* **171**, 1247–1256 (2005).
- Morrell, P. L. et al. Crop-to-weed introgression has impacted allelic composition of johnsongrass populations with and without recent exposure to cultivated sorghum. *Mol. Ecol.* **14**, 2143–2154 (2005).
- Gardner, R. C. et al. The complete nucleotide sequence of an infectious clone of cauliflower mosaic virus by M13mp7 shotgun sequencing. *Nucleic Acids Res.* **9**, 2871–2888 (1981).
- Matsumoto, T. et al. The map-based sequence of the rice genome. *Nature* **436**, 793–800 (2005).
- Vieira, J. & Messing, J. The pUC plasmids, an M13mp7-derived system for insertion mutagenesis and sequencing with synthetic universal primers. *Gene* **19**, 259–268 (1982).
- Bowers, J. E. et al. A high-density genetic recombination map of sequence-tagged sites for *Sorghum*, as a framework for comparative structural and evolutionary genomics of tropical grains and grasses. *Genetics* **165**, 367–386 (2003).
- Bowers, J. E. et al. Comparative physical mapping links conservation of microsynteny to chromosome structure and recombination in grasses. *Proc. Natl Acad. Sci. USA* **102**, 13206–13211 (2005).
- Miller, J. T. et al. Cloning and characterization of a centromere-specific repetitive DNA element from *Sorghum bicolor*. *Theor. Appl. Genet.* **96**, 832–839 (1998).
- Venter, J. C. et al. Shotgun sequencing of the human genome. *Science* **280**, 1540–1542 (1998).
- Kim, J. S. et al. Chromosome identification and nomenclature of *Sorghum bicolor*. *Genetics* **169**, 1169–1173 (2005).
- Swigonova, Z. et al. Close split of sorghum and maize genome progenitors. *Genome Res.* **14**, 1916–1923 (2004).
- Swigonova, Z. et al. On the tetraploid origin of the maize genome. *Comp. Funct. Genomics* **5**, 281–284 (2004).
- Swigonova, Z., Bennetzen, J. L. & Messing, J. Structure and evolution of the *r/b* chromosomal regions in rice, maize and sorghum. *Genetics* **169**, 891–906 (2005).
- Jiang, N. et al. Pack-mule transposable elements mediate gene evolution in plants. *Nature* **431**, 569–573 (2004).
- Brunner, S. et al. Evolution of DNA sequence nonhomologies among maize inbreds. *Plant Cell* **17**, 343–360 (2005).
- Haberger, G. et al. Structure and architecture of the maize genome. *Plant Physiol.* **139**, 1612–1624 (2005).
- Lu, C. et al. Genome-wide analysis for discovery of rice microRNAs reveals natural antisense microRNAs (nat-miRNAs). *Proc. Natl Acad. Sci. USA* **105**, 4951–4956 (2008).
- Xu, J.-H. & Messing, J. Organization of the prolamin gene family provides insight into the evolution of the maize genome and gene duplications in grass species. *Proc. Natl Acad. Sci. USA* **105**, 14330–14335 (2008).
- Meyers, B. C. et al. Genome-wide analysis of NBS-LRR-encoding genes in *Arabidopsis*. *Plant Cell* **15**, 809–834 (2003).
- Leister, D. Tandem and segmental gene duplication and recombination in the evolution of plant disease resistance genes. *Trends Genet.* **20**, 116–122 (2004).
- Carpita, N. C. & Gibeaut, D. M. Structural models of primary cell walls in flowering plants—consistency of molecular structure with the physical properties of the walls during growth *Plant J.* **3**, 1–30 (1993).
- McCann, M. C. & Roberts, K. In *The Cytoskeletal Basis of Plant Growth and Form* (ed. Lloyd, C. W.) 109–129 (Academic Press, 1991).
- Carpita, N. C. Structure and biogenesis of the cell walls of grasses. *Annu. Rev. Plant Physiol. Plant Mol. Biol.* **47**, 445–476 (1996).
- Hazen, S. P. et al. Quantitative trait loci and comparative genomics of cereal cell wall composition. *Plant Physiol.* **132**, 263–271 (2003).
- Zhao, B. T. et al. Identification of drought-induced microRNAs in rice. *Biochem. Biophys. Res. Commun.* **354**, 585–590 (2007).
- Nelson, D. E. et al. Plant nuclear factor Y (NF-Y) B subunits confer drought tolerance and lead to improved corn yields on water-limited acres *Proc. Natl Acad. Sci. USA* **104**, 16450–16455 (2007).
- Paterson, A. H., Bowers, J. E. & Chapman, B. A. Ancient polyploidization predating divergence of the cereals, and its consequences for comparative genomics. *Proc. Natl Acad. Sci. USA* **101**, 9903–9908 (2004).
- Wang, X. et al. Duplication and DNA segmental loss in rice genome and their implications for diploidization. *New Phytol.* **165**, 937–946 (2005).
- Yu, J. et al. The genomes of *Oryza sativa*: A history of duplications. *PLoS Biol.* **3**, 266–281 (2005).
- The Rice Chromosomes 11 and 12 Sequencing Consortia. The sequence of rice chromosomes 11 and 12, rich in disease resistance genes and recent gene duplications. *BMC Biol.* **3**, 20 (2005).
- Wang, X. et al. Extensive concerted evolution of rice paralogs and the road to regaining independence. *Genetics* **177**, 1753–1763 (2007).
- Singh, N. K. et al. Single-copy genes define a conserved order between rice and wheat for understanding differences caused by duplication, deletion, and transposition of genes. *Funct. Integr. Genomics* **7**, 17–35 (2007).
- Devos, K. M., Pittaway, T. S., Reynolds, A. & Gale, M. D. Comparative mapping reveals a complex relationship between the pearl millet genome and those of foxtail millet and rice TAG. *Theor. Appl. Genet.* **100**, 190–198 (2000).
- Tanaka, T. et al. The rice annotation project database (RAP-DB): 2008 update. *Nucleic Acids Res.* **36**, D1028–D1033 (2008).
- Ouyang, S. et al. The TIGR rice genome annotation resource: Improvements and new features. *Nucleic Acids Res.* **35**, D883–D887 (2007).
- Lynch, M. & Conery, J. S. The origins of genome complexity. *Science* **302**, 1401–1404 (2003).
- Wei, F. et al. Physical and genetic structure of the maize genome reflects its complex evolutionary history. *PLoS Genet.* **3**, e123 (2007).
- Huo, N. et al. The nuclear genome of *Brachypodium distachyon*: Analysis of BAC end sequences. *Funct. Integr. Genomics* **8**, 135–147 (2007).
- Margulies, E. H. et al. An initial strategy for the systematic identification of functional elements in the human genome by low-redundancy comparative sequencing. *Proc. Natl Acad. Sci. USA* **102**, 4795–4800 (2005).
- Eddy, S. R. A model of the statistical power of comparative genome sequence analysis. *PLoS Biol.* **3**, 95–102 (2005).
- Jannoo, N. et al. Orthologous comparison in a gene-rich region among grasses reveals stability in the sugarcane polyploid genome. *Plant J.* **50**, 574–585 (2007).
- Ming, R. et al. Sugarcane improvement through breeding and biotechnology. *Plant Breed. Rev.* **27**, 15–118 (2005).
- Lohithaswa, H. C. et al. Leveraging the rice genome sequence for comparative genomics in monocots. *Theor. Appl. Genet.* **115**, 237–243 (2007).
- Paterson, A. H. et al. Convergent domestication of cereal crops by independent mutations at corresponding genetic loci. *Science* **269**, 1714–1718 (1995).
- Yeh, R.-F., Lim, L. P. & Burge, C. Computational inference of homologous gene structures in the human genome. *Genome Res.* **11**, 803–816 (2001).
- Haas, B. J. et al. Full-length messenger RNA sequences greatly improve genome annotation. *Genome Biol.* **3**, research0029.0021–0029.0012 (2002).
- Wang, X. Y. et al. Statistical inference of chromosomal homology based on gene colinearity and applications to *Arabidopsis* and rice. *BMC Bioinform.* **7**, 447 (2006).
- Tang, H. et al. Synteny and colinearity in plant genomes. *Science* **320**, 486–488 (2008).

Supplementary Information is linked to the online version of the paper at www.nature.com/nature.

Acknowledgements We thank the US Department of Energy Joint Genome Institute Community Sequencing Program, J. Bristow, S. Lucas and the JGI production sequencing team for sequencing sorghum; and L. Lin for contributions to Fig. 1. We appreciate funding from the US National Science Foundation (NSF DBI-9872649, 0115903; MCB-0450260), International Consortium for Sugarcane Biotechnology, National Sorghum Producers, and a John Simon Guggenheim Foundation fellowship to A.H.P.; US Department of Energy (DE-FG05-95ER20194) to J.M.; German Federal Ministry of Education GABI initiative to MIPS (0313117 and 0314000C); NSF DBI-0321467 to A.N.; and US Department of Agriculture-Agricultural Research Service to C.A.M., L.Z. and D.W.

Author Information Reprints and permissions information is available at www.nature.com/reprints. Correspondence and requests for materials should be addressed to A.H.P. (paterson@uga.edu).

Adaptive immune features of natural killer cells

Joseph C. Sun¹, Joshua N. Beilke¹ & Lewis L. Lanier¹

In an adaptive immune response, naive T cells proliferate during infection and generate long-lived memory cells that undergo secondary expansion after a repeat encounter with the same pathogen. Although natural killer (NK) cells have traditionally been classified as cells of the innate immune system, they share many similarities with cytotoxic T lymphocytes. We use a mouse model of cytomegalovirus infection to show that, like T cells, NK cells bearing the virus-specific Ly49H receptor proliferate 100-fold in the spleen and 1,000-fold in the liver after infection. After a contraction phase, Ly49H-positive NK cells reside in lymphoid and non-lymphoid organs for several months. These self-renewing 'memory' NK cells rapidly degranulate and produce cytokines on reactivation. Adoptive transfer of these NK cells into naive animals followed by viral challenge results in a robust secondary expansion and protective immunity. These findings reveal properties of NK cells that were previously attributed only to cells of the adaptive immune system.

During an infection, naive T cells proliferate in response to encounter with cognate ligand and mediate effector functions^{1–4}. This first phase of the adaptive immune response is known as the expansion phase. In many infectious models of T-cell priming *in vivo*, pathogen-specific T cells become activated and expand in number over the course of one week, undergoing more than ten divisions, and give rise to thousands of daughter cells capable of effector functions^{5–7}. In the second phase, known as 'contraction', the activated T cells undergo apoptosis; a precipitous drop in cell numbers (90–95%) is observed in all tissues^{6,8}. The third, or 'memory maintenance', phase^{3,9–11} is when stable populations of long-lived memory T cells reside in lymphoid and non-lymphoid tissues^{12,13}, patrolling against previously encountered pathogens. The fourth and last phase, the secondary or recall response, occurs when memory T cells re-encounter their cognate antigen and again robustly expand in numbers to fight the pathogen challenge¹⁴. These four phases are ascribed to cells of the adaptive immune system, and the latter two phases have not been previously documented in NK cells.

NK cells have many traits in common with CD8⁺ T cells^{14–16}. The existence of immunological memory in NK cells has recently been suggested in a model of chemical hapten-induced contact hypersensitivity¹⁷; however, the precise mechanism and identity of the antigen-specific receptors responsible for mediating the recall responses were not defined. Here, using the well-established model of mouse cytomegalovirus (MCMV) infection in which NK cells provide host protection, we show that NK cells undergo all four phases of an immune response against a pathogen.

NK-cell expansion and contraction phases

The early virus-specific immune response against MCMV in C57BL/6 (B6) mice is dominated by NK cells expressing the Ly49H receptor, which recognizes the virally encoded m157 protein on the surface of infected cells, and these NK cells confer protection against infection^{18–22}. Over the first week of MCMV infection, Ly49H⁺ NK cells undergo a twofold to threefold expansion in the spleen and a roughly tenfold increase in the liver, as described previously^{23,24} (Supplementary Fig. 1). Because Ly49H⁺ cells constitute about 50% of total NK cells in a naive B6 mouse, we proposed that a 'ceiling' for NK-cell expansion (measured at 80–90% of total NK cells) is rapidly achieved

during infection and inhibits further proliferation in a normal host. We therefore sought to investigate the proliferation potential of NK cells by experimentally decreasing the initial precursor frequency of the Ly49H⁺-cell population. We reconstituted lethally irradiated mice with 1:1 mixed bone marrow from wild-type (CD45.1⁺) and DAP12-deficient (*Tyrbp*^{−/−}) (CD45.2⁺) B6 mice (which are defective in Ly49H receptor expression and function²⁵), thus decreasing the initial frequency of fully functional, wild-type Ly49H⁺ cells in the host to about 25% of the total NK cells (Fig. 1a). After infection of mixed chimaeric mice, wild-type NK cells preferentially expanded over 7 days and became the predominant NK-cell subset in the spleen (Fig. 1a). Although the chimaeric mice contained a lower initial frequency of Ly49H⁺ NK cells than the wild-type mice, by day 7 after infection the chimaeric mice had absolute numbers of Ly49H⁺ NK cells that were comparable to those in infected wild-type mice (data not shown). The Ly49H⁺ cells within the CD45.1⁺ NK-cell fraction upregulated the expression of the maturation marker KLRG1 (Fig. 1a) and preferentially incorporated bromodeoxyuridine over 7 days after infection (Fig. 1b), confirming the proliferation of this specific NK-cell subset and excluding the possibility that DAP12-deficient NK-cell populations were diminishing. Indeed, the absolute number of DAP12-deficient NK cells increased only slightly over the course of the infection (data not shown). The percentage of Ly49H⁺ NK cells began to decline beyond day 7 after infection but continued to be elevated, compared with uninfected animals, at 15 and 28 days after infection; frequencies returned to those measured in uninfected animals by 37 days after infection (Fig. 1c). Similar expansion and contraction of Ly49H⁺ NK cells were measured in the liver and lymph nodes of chimaeric mice during infection (Supplementary Fig. 2). The Ly49H⁺ NK-cell response was specific for the m157 viral ligand because we did not observe preferential expansion of the Ly49H subset during infection with MCMV lacking m157 (Fig. 1d). In 1:5 wild-type:DAP12-deficient bone marrow chimaeric mice, in which the starting percentage of wild-type Ly49H⁺ cells was about 10% of total NK cells, the Ly49H⁺ NK cells also preferentially expanded over 7 days after infection, allowing the wild-type (CD45.1⁺) NK cells to constitute the dominant population observed at the peak of expansion (Supplementary Fig. 3a). This expansion of Ly49H⁺ NK cells after

¹Department of Microbiology and Immunology and the Cancer Research Institute, University of California, San Francisco, California 94143, USA.

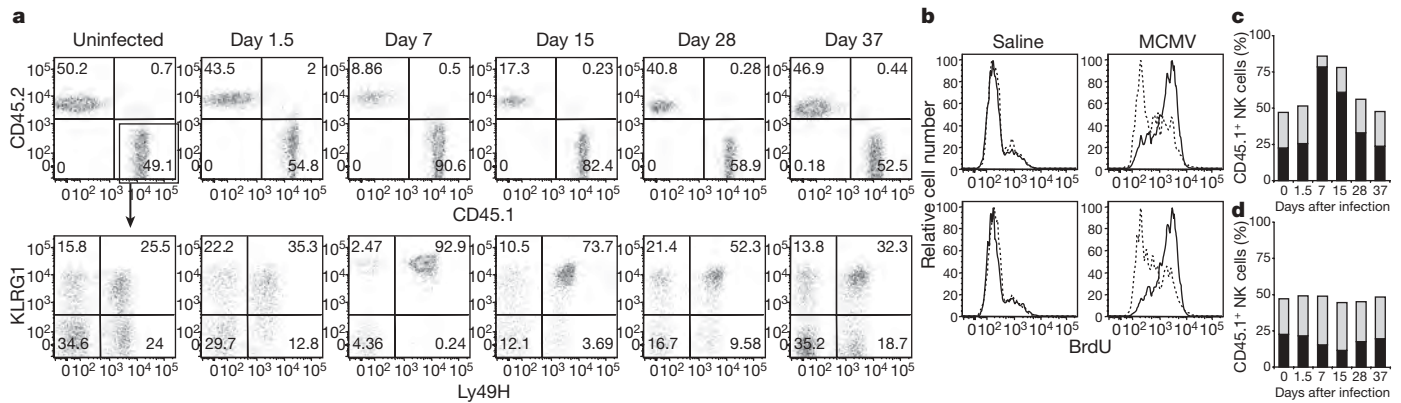


Figure 1 | Preferential expansion of wild-type, but not DAP12-deficient, NK cells during MCMV infection. Mixed-bone-marrow chimaeric mice (1:1 mixture of wild-type (CD45.1⁺) and DAP12-deficient (CD45.2⁺) cells) were infected with MCMV. **a**, Top: percentages of wild-type and DAP12-deficient NK cells (gated on CD3⁺, NK1.1⁺). Bottom: Ly49H and KLRG1 on wild-type NK cells. **b**, Top: incorporation of bromodeoxyuridine (BrdU) (day 7 after infection) of wild-type (solid lines) and DAP12-deficient (dotted lines)

infection observed in the spleen and liver was even greater than the proliferation measured in the 1:1 chimaeras (Supplementary Fig. 3b). Together, these findings highlight the ability of a small number of precursor NK cells to expand robustly into effector cells and mount a primary response against viral infection.

We next sought to address whether maximal proliferation of Ly49H⁺ NK cells could be achieved by adoptively transferring mature wild-type NK cells (CD45.1⁺) into DAP12-deficient mice (CD45.2⁺) and infecting with MCMV (Fig. 2a). Although DAP12-deficient mice have defective Ly49H⁺ NK cells, CD8⁺ T-cell responses to MCMV are normal, and mice clear infection within two weeks (data not shown). We were able to recover the transferred NK cells from recipient spleen (Fig. 2b) and thereby showed that early after infection (day 1.5 after infection), they were capable of becoming activated (CD69⁺ and NKG2D^{high}) and producing interferon (IFN)- γ (Fig. 2b). Seven days after infection, we observed a marked increase in transferred NK cell numbers, with preferential expansion in the Ly49H⁺ NK-cell subset (Fig. 2c). Adoptive transfer of carboxyfluorescein succinimidyl ester (CFSE)-labelled NK cells confirmed that only the Ly49H⁺ NK cells were dividing, fully diluting their CFSE during the 7 days after infection, whereas the Ly49H⁻ NK-cell subset remained CFSE^{high} (Fig. 2d). NK cells transferred into DAP12-deficient mice expanded as much as 100-fold in the spleen after infection (Fig. 2e). This expansion was not seen when NK cells were adoptively transferred into wild-type B6 mice, which contain competing endogenous Ly49H⁺ NK cells and thus restrict proliferation of the transferred cells (Fig. 2e). The expansion of Ly49H⁺ NK cells was not unique to DAP12-deficient recipients because we also observed robust expansion of Ly49H⁺ NK cells when they were adoptively transferred into C57BL/6 mice that do not possess the *Ly49h* gene (data not shown).

The amplitude and kinetics of the MCMV-specific NK-cell response measured in our system mirror analogous responses in primary T cells^{7,26}, as well as with adoptive transfer of T-cell antigen receptor-transgenic T cells^{5,27}. Furthermore, adoptive transfer of NK cells permits us to track the congenic CD45.1⁺ cells late after infection, allowing us to distinguish between antigen-experienced NK cells and naive NK cells that have recently left the bone marrow. Using this experimental approach, we were able to recover a long-lived 'memory' pool of NK cells that can persist in lymphoid tissues as well as non-lymphoid tissues such as the liver (Fig. 3a, b). We examined whether lowering the precursor frequency permitted a greater expansion of NK cells by measuring the amplitude of the Ly49H⁺ NK-cell response in mice after the transfer of 10⁵ or 10⁴ cells, and determined that both the

NK cells, gated on total NK cells. Bottom: incorporation of bromodeoxyuridine by Ly49H⁺ (solid lines) and Ly49H⁻ (dotted lines) wild-type NK cells, gated on CD45.1⁺ NK cells. **c**, **d**, Percentages of Ly49H⁺ cells within the wild-type NK-cell population after infection with MCMV (**c**) or MCMV- Δ m157 (**d**). Grey bars, total wild-type cells; black bars, Ly49H⁺ cells. Data are representative of three experiments with three to five mice per time point.

kinetics and fold expansion were comparable in the spleen (about 100-fold) and liver (about 1,000-fold) of MCMV-infected mice, irrespective of initial transfer numbers (Fig. 3a, b). A lower threshold therefore exists at which small numbers of precursor NK cells no longer lead to enhanced overall responses. A summary of Ly49H⁺ NK-cell fold expansion in B6 mice, the different mixed chimaeric mice and the adoptive transfer system is shown in Fig. 3c, highlighting the previously underappreciated ability of antigen-specific NK cells to undergo a profound expansion and persist after viral infection.

NK-cell memory phase

In our adoptive transfer model, the contraction phase observed during the NK-cell response to MCMV infection (Fig. 3a, b) seems to emulate the prolonged decline in effector-cell numbers observed with antigen-specific CD4 T-cell responses²⁶, rather than the rapid and more precipitous decline observed with most CD8⁺ T-cell responses⁸. After the contraction phase, we were able to detect 'memory' NK cells at 70 days after infection (Fig. 4a), and we sought to determine whether these cells were still functional. These 'memory' NK cells were indeed functional, because they produced IFN- γ *ex vivo* in response to plate-bound antibody against NK1.1 or Ly49H (Fig. 4a). In fact, their response was heightened in comparison with the response by naive NK cells, in that a greater percentage of 'memory' NK cells responded to plate-bound antibodies as well as m157-expressing target cells, and the amounts of IFN- γ produced by individual cells were higher (Fig. 4b and Supplementary Fig. 4). Degranulation by 'memory' NK cells was also enhanced, as assessed by LAMP-1 (CD107a) expression after *ex vivo* stimulation with anti-NK1.1 (Fig. 4c).

'Memory' Ly49H⁺ NK cells could be distinguished from naive Ly49H⁺ NK on the basis of several surface antigens. In particular, 'memory' NK cells expressed higher levels of the Ly49H receptor, but not other activating receptors, than naive NK cells (Fig. 4d), perhaps permitting 'memory' NK cells to have a lower threshold for activation. 'Memory' NK cells also showed a greater expression of KLRG1, CD43 and Ly6C, and a decreased expression of CD27, suggesting that they were more mature than naive NK cells (Fig. 4d). A similar phenotype was also observed on long-lived NK cells isolated from non-lymphoid tissues such as the liver (Supplementary Fig. 5). 'Memory' NK cells also constitutively expressed higher levels of *Ifng* transcripts than naive NK cells (Fig. 4e), as assessed by studies with the IFN- γ reporter Yeti mice²⁸. Taken together, these data indicate that 'memory' NK cells possess characteristics similar to those of memory T cells in both their phenotype and their ability to produce effector cytokines robustly.

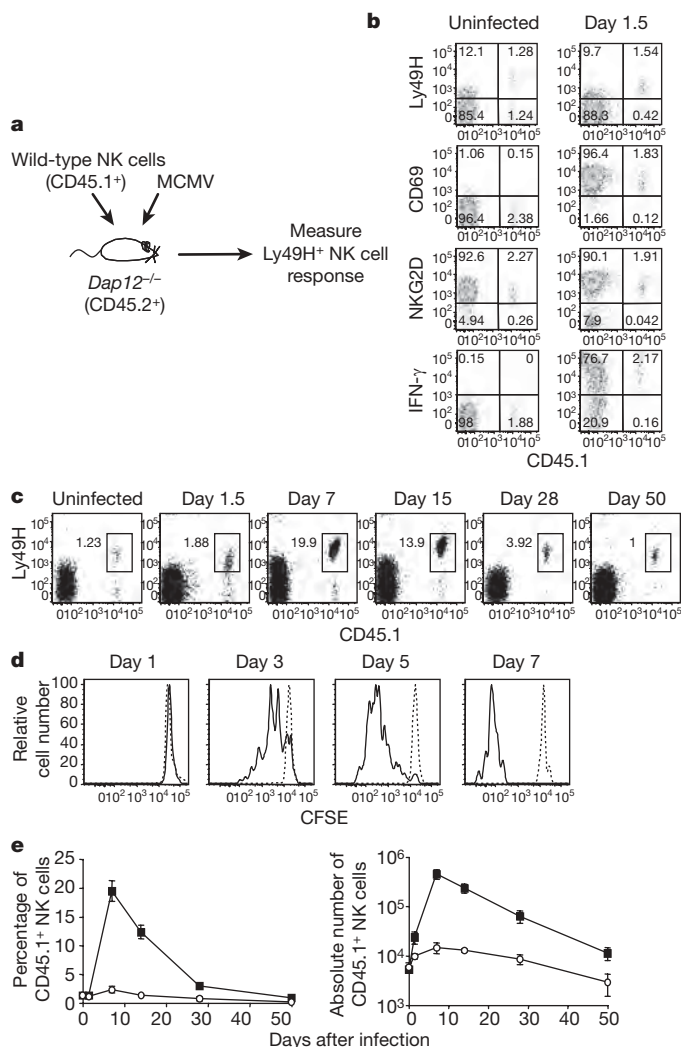


Figure 2 | Robust proliferation of adoptively transferred wild-type NK cells in DAP12-deficient mice after MCMV infection. **a**, A total of 10^5 wild-type NK cells (CD45.1⁺) were transferred into DAP12-deficient mice (CD45.2⁺) and infected with MCMV. **b**, Transferred NK cells (CD45.1⁺) within the total CD3⁺ NK1.1⁺ gated population analysed for Ly49H, CD69, NKG2D and intracellular IFN- γ . **c**, Percentages of transferred CD45.1⁺ NK cells within the total CD3⁺ NK1.1⁺ population after infection. **d**, CFSE-labelled wild-type NK cells (5×10^5) were transferred into DAP12-deficient hosts. Ly49H⁺ (solid lines) and Ly49H⁻ (dotted lines) NK cells were analysed after infection. **e**, Percentages (left graph) and absolute numbers (right graph) of transferred CD45.1⁺ NK cells in DAP12-deficient (filled squares) or wild-type B6 (open circles) recipients after infection. Error bars show s.e.m. ($n = 3-5$). Data are representative of five experiments.

NK-cell recall phase

Antigen-specific memory T cells undergo secondary expansion, and we investigated whether 'memory' NK cells also possessed this adaptive immune characteristic. Because mice previously immunized with MCMV contain neutralizing antibodies and memory cytotoxic T lymphocytes, we could not challenge directly with a second dose of virus to examine recall responses. Therefore, after the primary expansion and contraction phase in our adoptive transfer model, we enriched for 'memory' Ly49H⁺ NK cells (CD45.1⁺) at 40–50 days after infection, adoptively transferred these cells into a second DAP12-deficient mouse (CD45.2⁺) and infected it with MCMV (Fig. 5a). Although the transferred 'memory' NK cells were present in small numbers in uninfected recipients and at day 1.5 after infection, an expanded population of transferred Ly49H⁺ NK cells could be readily detected at 7 and 14 days after infection (Fig. 5b). Thus, like memory T cells, 'memory' NK cells are self-renewing, long-lived, and

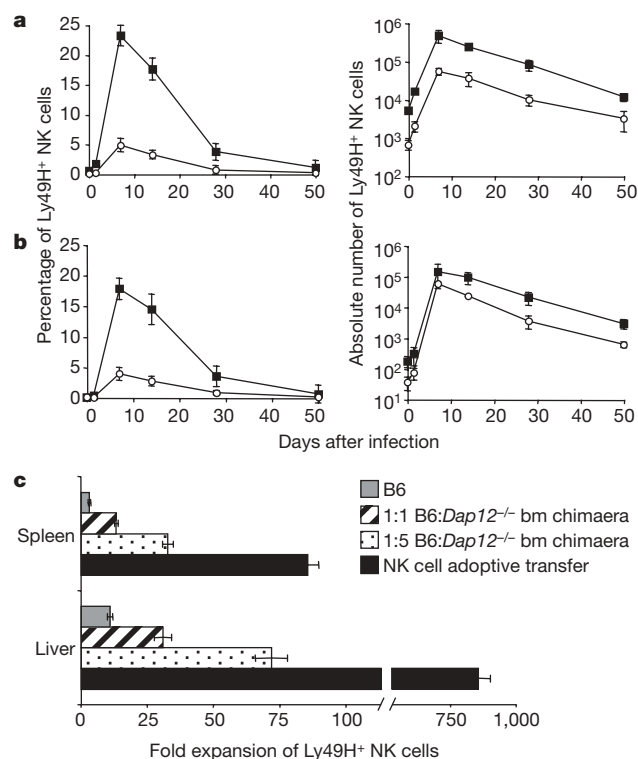


Figure 3 | Expansion and contraction of NK cells in lymphoid and non-lymphoid tissues results in 'memory' NK cells. **a**, **b**, After adoptive transfer of 10^5 (filled squares) or 10^4 (open circles) wild-type NK cells (CD45.1⁺) into DAP12-deficient mice and MCMV infection, graphs show percentages (left) and absolute numbers (right) of Ly49H⁺ NK cells in spleen (**a**) and liver (**b**). Error bars show s.e.m. ($n = 3-5$). Data are representative of three experiments. **c**, Fold expansions of Ly49H⁺ NK cells over 7 days of infection were calculated in B6 mice, in 1:1 and 1:5 wild-type:DAP12-deficient bone marrow (bm) chimaeric mice, and after adoptive transfer of wild-type NK cells into DAP12-deficient mice. Error bars show s.e.m. from three experiments in each group of mice indicated.

can mount a secondary response after viral challenge, with expansion measured at greater than 100-fold in the spleen (Fig. 5c). When CFSE-labelled naive and 'memory' NK cells were transferred into separate DAP12-deficient recipient mice and proliferation kinetics were compared after MCMV infection, we observed a similar rate of CFSE dilution at day 3 after infection and found that both groups of NK cells were CFSE-negative (indicating at least ten divisions) by day 6 after infection (Fig. 5d). Although large numbers of naive NK cells were easier to obtain and thus more cells were transferred into recipient animals than 'memory' NK cells, the kinetics and magnitude of expansion between naive and 'memory' NK-cell populations were comparable (Fig. 5d). Overall, MCMV-specific NK-cell responses after adoptive transfer of normalized naive and 'memory' NK cell numbers showed no significant differences in the expansion and contraction phases (Fig. 5e). Several careful studies of CD8⁺ T-cell responses have also revealed similarities in naive and memory T-cell proliferation rates²⁹⁻³³, indicating that the increased memory T-cell responses could be attributed to a higher precursor frequency rather than a differential rate of proliferation. Although phenotypic and functional differences exist between naive and 'memory' NK cells, it is not surprising that the kinetics of expansion between these populations do not differ, given the property of naive NK cells as 'ready-to-respond' effectors¹⁴. In fact, memory CD8⁺ T cells have often been compared to NK cells for their ability to mediate effector functions rapidly¹⁴.

Last, we wished to determine whether 'memory' NK cells are more protective than naive NK cells. We adoptively transferred equal numbers of naive and 'memory' Ly49H⁺ NK cells into newborn mice,

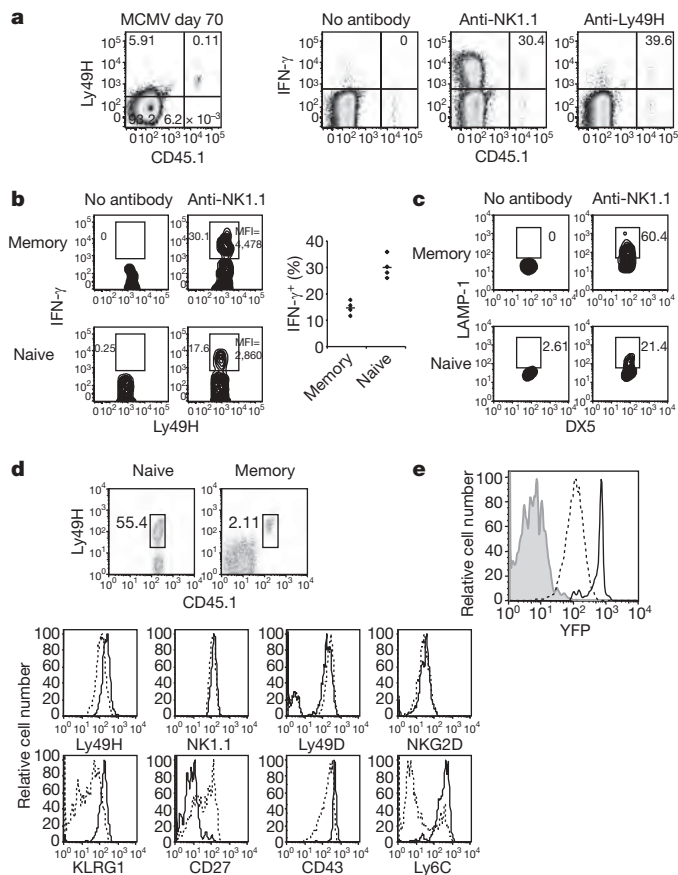


Figure 4 | Function and phenotype of 'memory' NK cells. **a**, A total of 10^5 wild-type NK cells ($CD45.1^+$) transferred into DAP12-deficient mice ($CD45.2^+$) were analysed 70 days after MCMV infection. Left: percentage of $CD45.1^+$ $Ly49H^+$ cells within the total NK-cell population. Right: percentages of $CD45.1^+$ NK cells producing IFN- γ after stimulation. **b**, 'Memory' NK cells compared with naive NK cells from uninfected mice after stimulation with anti-NK1.1. Left: percentages of $Ly49H^+$ NK cells (gated on total NK cells) producing IFN- γ . Right: percentages of $Ly49H^+$ NK cells producing IFN- γ (four mice per group; horizontal bar is mean; $P = 0.0009$). MFI, mean fluorescence intensity. **c**, LAMP-1 on 'memory' NK cells (day 55 after infection) versus naive NK cells (gated on $Ly49H^+$ NK cells) after stimulation with anti-NK1.1. **d**, Surface markers on 'memory' NK cells (day 45 after infection; solid line) versus naive NK cells (dotted lines). **e**, NK cells from day 7 MCMV-infected Yeti mice were transferred into DAP12-deficient $Rag2^{-/-}$ mice. The graph shows yellow fluorescent protein (YFP) in 'memory' $Ly49H^+$ NK cells (thick solid line) after 28 days compared with $Ly49H^+$ NK cells (dotted line) and T cells (thin solid line) in uninfected Yeti mouse.

which are susceptible to MCMV because they lack mature NK cells³⁴, challenged them with MCMV, and monitored survival. Newborn mice receiving 'memory' NK cells showed significant protection against viral infection compared with an equivalent number of naive NK cells ($P = 0.0024$; Fig. 5f). At least tenfold more naive NK cells than 'memory' NK cells were required to mediate protection against MCMV infection. When newborn recipients were treated with an antibody that blocks the $Ly49H$ receptor, protection was abrogated ($P = 0.03$; Fig. 5f). Thus, like T cells, NK cells have the ability to 'remember' previously encountered pathogens and are able to mediate more efficient protective immunity against subsequent infection.

Conclusion

Because the innate immune system is considered to be evolutionarily older than the adaptive immune system, NK cells bearing receptors that recognize major histocompatibility complex (MHC) and MHC-like molecules may have arisen as a predecessor to T cells, which express clonally selected receptors for the recognition of a limitless

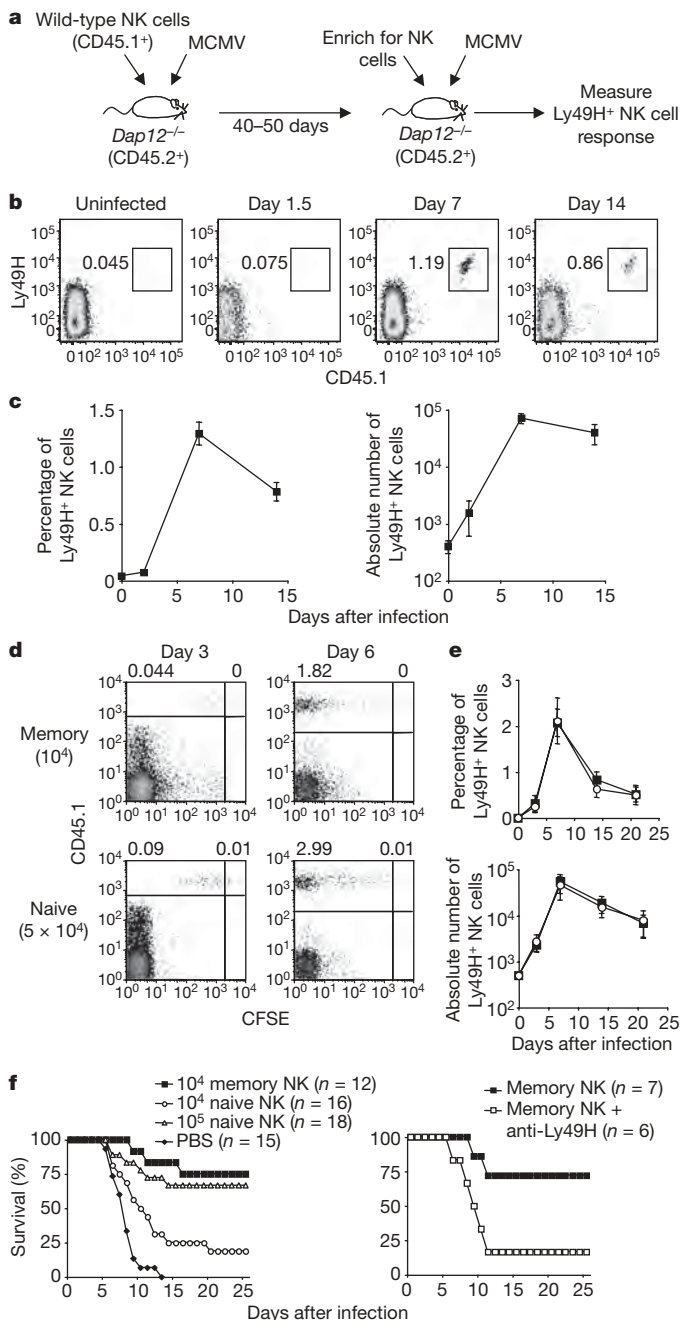


Figure 5 | Secondary expansion and protective immunity in 'memory' NK cells. **a**, A total of 10^5 wild-type NK cells ($CD45.1^+$) transferred to DAP12-deficient mice ($CD45.2^+$) were isolated 40–50 days after primary infection with MCMV and transferred into DAP12-deficient mice ($CD45.2^+$). After infection of the second host, $Ly49H^+$ NK cells were analysed. **b**, Percentages of transferred 'memory' $Ly49H^+$ NK cells in the second host. **c**, Percentages (left) and absolute numbers (right) of $Ly49H^+$ NK cells within the total NK-cell population in the second host. Error bars show s.e.m. ($n = 3$ –5). Data are representative of five experiments. **d**, Analysis of CFSE-labelled 'memory' and naive NK cells transferred into DAP12-deficient recipient mice (days 3 and 6 after infection). **e**, Expansion and contraction of 'memory' (filled squares) and naive (open circles) NK cells (10^4 input) shown as percentages (top) and absolute numbers (bottom) of $Ly49H^+$ NK cells within the total NK-cell population. Error bars show s.e.m. ($n = 3$ –5). Data are representative of three experiments. **f**, Survival of DAP12-deficient neonatal mice receiving 10^4 or 10^5 naive NK cells, or 10^4 'memory' NK cells (or PBS as control) followed by MCMV infection, with or without anti- $Ly49H$ blocking. Data were pooled from three experiments.

antigen repertoire in the context of MHC. Alternatively, NK cells may have co-evolved with T cells. As an evolutionary bridge, NK cells might conceivably possess attributes of both innate and adaptive immunity, and we are only beginning to unearth characteristics of the latter. The categorization of NK cells within the immune system is beginning to undergo a paradigm shift, which will have major implications for our approach to vaccination strategies for the generation of immunological memory against pathogens.

METHODS SUMMARY

Mice and infections. C57BL/6 and congenic CD45.1⁺ mice were purchased from the National Cancer Institute. DAP12-deficient mice²⁵, backcrossed 13 generations onto C57BL/6, were bred and maintained in accordance with the guidelines of the Institutional Animal Care and Use Committee. R. Locksley provided Yeti mice²⁸. Mixed-bone-marrow chimaeric mice were generated as described³⁵. Mice were infected by intraperitoneal injections of Smith strain MCMV (5×10^4 plaque-forming units (p.f.u.)) and MCMV- Δ m157 (10^5 p.f.u.) (provided by U. Koszinowski)³⁶. Newborn mice were infected with 2×10^3 p.f.u. of MCMV.

NK-cell enrichment and adoptive transfer. NK cells were isolated with an NK-cell Isolation Kit (Miltenyi Biotec) and injected intravenously into adult recipients or intraperitoneally into neonatal recipients one day before viral infection. Newborn mice were given 50 μ g of anti-Ly49H monoclonal antibody (mAb) 3D10 one day before infection.

Ex vivo stimulation of NK cells. Tissue culture plates treated with N-(1-(2,3-dioleoyloxy)propyl)-N,N,N-trimethylammonium methylsulphate (Sigma) were coated with anti-NK1.1 or anti-Ly49H (provided by W. Yokoyama) and cells were incubated for 5 h at 37 °C in the presence of Golgiplug (BD Pharmingen), followed by staining for intracellular cytokines. NK cells were co-cultured with Ba/F3 cells or m157-transduced Ba/F3 (ref. 18) before intracellular cytokine staining.

Flow cytometry. Fc receptors were blocked with 2.4G2 mAb before surface staining with indicated antibodies or isotype-matched control immunoglobulin (BD or eBiosciences). Staining with bromodeoxyuridine was performed with a BrdU Flow Kit (BD). Labelling of cells with CFSE was performed in accordance with the manufacturer's instructions (Invitrogen). Samples were acquired on an LSRII (BD) and analysed with FlowJo software (TreeStar).

Statistical methods. The Mann-Whitney nonparametric U-test was used to compare survival between groups of mice. A value of 25 days was assigned to survivors living more than 25 days after MCMV infection. Student's t-test was used to compare groups in *ex vivo* stimulation experiments.

Received 23 October; accepted 24 November 2008.

Published online 11 January 2009.

- Harty, J. T. & Badovinac, V. P. Shaping and reshaping CD8⁺ T-cell memory. *Nature Rev. Immunol.* **8**, 107–119 (2008).
- Kaech, S. M., Wherry, E. J. & Ahmed, R. Effector and memory T-cell differentiation: implications for vaccine development. *Nature Rev. Immunol.* **2**, 251–262 (2002).
- Sprent, J. & Surh, C. D. T cell memory. *Annu. Rev. Immunol.* **20**, 551–579 (2002).
- Williams, M. A. & Bevan, M. J. Effector and memory CTL differentiation. *Annu. Rev. Immunol.* **25**, 171–192 (2007).
- Butz, E. A. & Bevan, M. J. Massive expansion of antigen-specific CD8⁺ T cells during an acute virus infection. *Immunity* **8**, 167–175 (1998).
- Goldrath, A. W. & Bevan, M. J. Selecting and maintaining a diverse T-cell repertoire. *Nature* **402**, 255–262 (1999).
- Murali-Krishna, K. et al. Counting antigen-specific CD8 T cells: a reevaluation of bystander activation during viral infection. *Immunity* **8**, 177–187 (1998).
- Badovinac, V. P., Porter, B. B. & Harty, J. T. Programmed contraction of CD8⁺ T cells after infection. *Nature Immunol.* **3**, 619–626 (2002).
- Jameson, S. C. Maintaining the norm: T-cell homeostasis. *Nature Rev. Immunol.* **2**, 547–556 (2002).
- Marrack, P. & Kappler, J. Control of T cell viability. *Annu. Rev. Immunol.* **22**, 765–787 (2004).
- Schluns, K. S. & Lefrancois, L. Cytokine control of memory T-cell development and survival. *Nature Rev. Immunol.* **3**, 269–279 (2003).
- Lefrancois, L. & Masopust, D. T cell immunity in lymphoid and non-lymphoid tissues. *Curr. Opin. Immunol.* **14**, 503–508 (2002).

- Masopust, D., Vezys, V., Marzo, A. L. & Lefrancois, L. Preferential localization of effector memory cells in nonlymphoid tissue. *Science* **291**, 2413–2417 (2001).
- Lanier, L. L. NK cell recognition. *Annu. Rev. Immunol.* **23**, 225–274 (2005).
- Lanier, L. L. Back to the future—defining NK cells and T cells. *Eur. J. Immunol.* **37**, 1424–1426 (2007).
- Glas, R. et al. Recruitment and activation of natural killer (NK) cells *in vivo* determined by the target cell phenotype. An adaptive component of NK cell-mediated responses. *J. Exp. Med.* **191**, 129–138 (2000).
- O'Leary, J. G., Goodarzi, M., Drayton, D. L. & von Andrian, U. H. T cell- and B cell-independent adaptive immunity mediated by natural killer cells. *Nature Immunol.* **7**, 507–516 (2006).
- Arase, H. et al. Direct recognition of cytomegalovirus by activating and inhibitory NK cell receptors. *Science* **296**, 1323–1326 (2002).
- Brown, M. G. et al. Vital involvement of a natural killer cell activation receptor in resistance to viral infection. *Science* **292**, 934–937 (2001).
- Daniels, K. A. et al. Murine cytomegalovirus is regulated by a discrete subset of natural killer cells reactive with monoclonal antibody to Ly49H. *J. Exp. Med.* **194**, 29–44 (2001).
- Smith, H. R. et al. Recognition of a virus-encoded ligand by a natural killer cell activation receptor. *Proc. Natl Acad. Sci. USA* **99**, 8826–8831 (2002).
- Vidal, S. M. & Lanier, L. L. NK cell recognition of mouse cytomegalovirus-infected cells. *Curr. Top. Microbiol. Immunol.* **298**, 183–206 (2006).
- Dokun, A. O. et al. Specific and nonspecific NK cell activation during virus infection. *Nature Immunol.* **2**, 951–956 (2001).
- Yokoyama, W. M., Kim, S. & French, A. R. The dynamic life of natural killer cells. *Annu. Rev. Immunol.* **22**, 405–429 (2004).
- Bakker, A. B. et al. DAP12-deficient mice fail to develop autoimmunity due to impaired antigen priming. *Immunity* **13**, 345–353 (2000).
- Homann, D., Teyton, L. & Oldstone, M. B. Differential regulation of antiviral T-cell immunity results in stable CD8⁺ but declining CD4⁺ T-cell memory. *Nature Med.* **7**, 913–919 (2001).
- Williams, M. A., Ravkov, E. V. & Bevan, M. J. Rapid culling of the CD4⁺ T cell repertoire in the transition from effector to memory. *Immunity* **28**, 533–545 (2008).
- Stetson, D. B. et al. Constitutive cytokine mRNAs mark natural killer (NK) and NK T cells poised for rapid effector function. *J. Exp. Med.* **198**, 1069–1076 (2003).
- Badovinac, V. P., Messingham, K. A., Hamilton, S. E. & Harty, J. T. Regulation of CD8⁺ T cells undergoing primary and secondary responses to infection in the same host. *J. Immunol.* **170**, 4933–4942 (2003).
- Belz, G. T. et al. Minimal activation of memory CD8⁺ T cell by tissue-derived dendritic cells favors the stimulation of naive CD8⁺ T cells. *Nature Immunol.* **8**, 1060–1066 (2007).
- Grayson, J. M. et al. Differential sensitivity of naive and memory CD8⁺ T cells to apoptosis *in vivo*. *J. Immunol.* **169**, 3760–3770 (2002).
- Jabbari, A. & Harty, J. T. Secondary memory CD8⁺ T cells are more protective but slower to acquire a central-memory phenotype. *J. Exp. Med.* **203**, 919–932 (2006).
- Zimmermann, C., Prevost-Blondel, A., Blaser, C. & Pircher, H. Kinetics of the response of naive and memory CD8 T cells to antigen: similarities and differences. *Eur. J. Immunol.* **29**, 284–290 (1999).
- Bukowski, J. F., Warner, J. F., Dennert, G. & Welsh, R. M. Adoptive transfer studies demonstrating the antiviral effect of natural killer cells *in vivo*. *J. Exp. Med.* **161**, 40–52 (1985).
- Sun, J. C. & Bevan, M. J. Cutting edge: long-lived CD8 memory and protective immunity in the absence of CD40 expression on CD8 T cells. *J. Immunol.* **172**, 3385–3389 (2004).
- Bubic, I. et al. Gain of virulence caused by loss of a gene in murine cytomegalovirus. *J. Virol.* **78**, 7536–7544 (2004).

Supplementary Information is linked to the online version of the paper at www.nature.com/nature.

Acknowledgements We thank the Lanier laboratory for comments and discussions, and R. Locksley and W. Seaman for critical reading of this manuscript. The work was supported by National Institutes of Health grant AI068129. J.C.S. is supported by the Irvington Institute for Immunological Research. J.N.B. is supported by the Juvenile Diabetes Research Foundation. L.L.L. is an American Cancer Society Research Professor.

Author Contributions J.C.S. and J.N.B. contributed to project planning, experimental work, data analysis and writing the manuscript. L.L.L. contributed to project planning, data analysis and writing the manuscript.

Author Information Reprints and permissions information is available at www.nature.com/reprints. Correspondence and requests for materials should be addressed to L.L.L. (lewis.lanier@ucsf.edu).

LETTERS

Rapid heating of the atmosphere of an extrasolar planet

Gregory Laughlin¹, Drake Deming², Jonathan Langton¹, Daniel Kasen¹, Steve Vogt¹, Paul Butler³, Eugenio Rivera¹ & Stefano Meschiari¹

Near-infrared observations of more than a dozen ‘hot-Jupiter’ extrasolar planets have now been reported^{1–5}. These planets display a wide diversity of properties, yet all are believed to have had their spin periods tidally spin-synchronized with their orbital periods, resulting in permanent star-facing hemispheres and surface flow patterns that are most likely in equilibrium. Planets in significantly eccentric orbits can enable direct measurements of global heating that are largely independent of the details of the hydrodynamic flow⁶. Here we report 8- μm photometric observations of the planet HD 80606b during a 30-hour interval bracketing the periastron passage of its extremely eccentric 111.4-day orbit. As the planet received its strongest irradiation (828 times larger than the flux received at apastron) its maximum 8- μm brightness temperature increased from $\sim 800\text{ K}$ to $\sim 1,500\text{ K}$ over a six-hour period. We also detected a secondary eclipse for the planet, which implies an orbital inclination of $i \approx 90^\circ$, fixes the planetary mass at four times the mass of Jupiter, and constrains the planet’s tidal luminosity. Our measurement of the global heating rate indicates that the radiative time constant at the planet’s 8- μm photosphere is $\sim 4.5\text{ h}$, in comparison with 3–5 days in Earth’s stratosphere⁷.

The giant planet orbiting the solar-type star HD 80606 is unique among the nearly 300 extrasolar planets that have been found so far⁸. On a three-month timescale, it shuttles between the inner edge of its parent star’s habitable zone and the highly irradiated close-in realm of the so-called hot Jupiters. Its extremely eccentric orbit provides compelling evidence of a peculiar dynamical history⁹, and the planet itself can be used as a laboratory to study the atmospheric dynamics of extrasolar planets. Clues to the planet’s interior structure can be gained by measuring the amount of tidal heating experienced by the planet. If its tidal quality factor, Q , is of order 3×10^5 (consistent with that observed for Jupiter)^{10,11} then tidal and stellar contributions to the planetary heating should be roughly equal, yielding an orbit-averaged effective temperature of $T_{\text{int}} \approx 700\text{ K}$ (ref. 9).

The solar-type parent star, HD 80606 (with $M_\star \approx M_\odot$, $R_\star \approx R_\odot$ and $T_{\text{eff}} = 5,800\text{ K}$, M_\odot and R_\odot respectively being the solar mass and radius)⁸, has a binary companion, HD 80607, lying 17 arcsec to the east. Given the 58-pc distance to the system, this implies a projected separation of $d \approx 1,000\text{ AU}$, and the two stars have nearly equal masses and luminosities. We monitored HD 80606 and HD 80607 continuously over a 29.75-h period using the 8- μm channel of the NASA Spitzer Space Telescope’s¹² Infrared Array Camera (IRAC)¹³. We observed in stellar mode with a cadence of $\sim 14\text{ s}$. Our observational campaign was timed to start $\sim 20\text{ h}$ before periastron. The geometry of the encounter is shown in Fig. 1. Before the observations, the planet’s orbital inclination was unknown, with the orbital geometry and stellar size indicating a $\sim 15\%$ chance of occurrence of a secondary

eclipse centred on the epoch of superior conjunction ($\sim 3\text{ h}$ before periastron). Spitzer collected $8,051\ 256 \times 256$ pixel images during the observational campaign.

At periastron, HD 80606b responds to the pronounced increase in insolation by absorbing a fraction of the incident stellar radiative flux. A portion of this absorbed radiation is then re-radiated at $8\text{ }\mu\text{m}$ in a time-varying manner. The rate of this emission depends on the detailed thermal, chemical and radiative properties of the atmosphere. At present, existing near-infrared observations of tidally circularized hot Jupiters present an incomplete and somewhat contradictory overall picture. It is not understood, for example, how the wind vectors and temperature distributions on the observed planets behave as a function of pressure depth, planetary longitude and planetary latitude. Most importantly, the effective radiative time constant in the atmospheres of short-period planets has not been directly measured, and as a result, dynamical calculations of the expected planet-wide flow patterns^{14–17} have not come to a full consensus regarding how the surface flow should appear. The lack of agreement between the models stems in part from the paucity of unambiguous measurements of the basic thermal structure of the atmospheres of short-period planets. Hence, photometric near-infrared time series of planets such as HD 80606b that are subject to strongly time-dependent heating can provide crucial input data for the next generation of extrasolar-planetary global circulation models.

As expected from earlier experience with IRAC^{1,3,4}, the data show the effect of a detector sensitivity that gradually increases with time. This rise (the ‘ramp’) amounts to several per cent over the course of our observations and is signal dependent, with strongly illuminated pixels showing a more rapid rise, followed by saturation. Removal of the ramp is complicated by image motion effects arising from tiny drift in the telescope pointing during the long-duration observation. The data contain a net ~ 0.5 -pixel image motion over 30 h, encompassing both a long-term trend and a short-term (1-h) oscillation. Image motion affects the shape of the ramp for each pixel because the illumination of each pixel has a different time dependence and because the ramp has a logarithmic, rather than linear, shape. We therefore correct for the first-order (linear) shifting-of-photons effect simultaneously with a ramp correction based on a linear-plus-logarithmic term, as described in detail in the Supplementary Information. The comparison star was analysed using an identical method. An advantage of the per-pixel ramp removal is that it eliminates need to divide the HD 80606 time series by that of HD 80607, or to normalize with respect to it in any way. Instead, with ramp removal applied to both stars, the HD 80607 time series can be used as an independent control.

The calibrated time series for both HD 80606 and HD 80607 are shown in Fig. 2. Whereas the HD 80607 time series shows no

¹UCO/Lick Observatory, University of California, Santa Cruz, California 95064, USA. ²NASA/Goddard Space Flight Center, Planetary Systems Branch, Code 693, Greenbelt, Maryland 20771, USA. ³Carnegie Institute of Washington, Department of Terrestrial Magnetism, 5241 Broad Branch Road, NW, Washington DC 20015, USA.

significant structure, there are several features of interest in the HD 80606 photometry. Most notably, there is an increase in flux of order $\Delta F/F = 0.001 \pm 0.0002$ during the second half of the time series, which we interpret as arising from an increase in the planet's 8- μ m emission during the course of the observations.

We model the planetary response during the periastron encounter with a global, two-dimensional hydrodynamical model that employs a one-layer, two-frequency radiative transfer scheme¹⁷. We assume a planetary radius, R_{pl} , of 1.1 times that of Jupiter¹⁸ and an $i = 90^\circ$ orbit with the parameters given by the best-fit radial velocity solution, with the time of periastron adjusted to HJD 2454424.86. Given the planet's small periastron distance, it is expected that the planetary spin angular frequency, Ω_{spin} , will have been pseudo-synchronized¹⁹ to a rate that is similar to the instantaneous orbital angular frequency at periastron. There are several competing theories of the pseudo-synchronous frequency²⁰. We adopt the following expression, where Ω_{orbit} is the orbital angular frequency¹⁹:

$$\frac{\Omega_{\text{spin}}}{\Omega_{\text{orbit}}} = \frac{1 + (15/2)e^2 + (45/8)e^4 + (5/16)e^6}{(1 + 3e^2 + (3/8)e^4)(1 - e^2)^{3/2}} \quad (1)$$

This yields a planetary spin period of 40.7 h.

Our hydrodynamical model contains three free parameters. The first, $p_{8\mu\text{m}}$, is the atmospheric pressure at the 8- μ m photosphere; the second, X , corresponds to the fraction of the incoming optical flux that is absorbed at or above the 8- μ m photosphere; and the third, p_b , corresponds to the pressure at the base of our modelled layer. We adopt parameter values that put our model's light curve in good agreement with the observed high-signal-to-noise 8- μ m time series for HD 189733 (refs 4, 17). Specifically, we use $p_{8\mu\text{m}} = 570$ mbar (adjusted for the surface gravity on HD 80606b, which is higher than that on HD 189733b), $p_b = 4$ bar and $X = 0.5$. Our model photometric light curve is then obtained by integrating at each time step over the planetary hemisphere visible from Earth, and assuming that each patch of the planet radiates a black-body spectrum corresponding to the local temperature.

The photometry shows a noticeable dip of duration ~ 0.07 d and amplitude $\Delta F/F = 0.001 \pm 0.0002$ centred near HJD 2454424.74. We identify this feature with a secondary eclipse, as a result of two lines of evidence. First, our fit to the radial velocity data predicts a mid-secondary transit epoch of HJD 2454424.72 \pm 0.02, which is consistent with the centre of the observed feature. Second, we evaluate the significance of the detection using a bootstrap technique. From the full 8,051-frame time series, a sequence of 50,000 bootstrap trials is created on the basis of random scramblings of the deviations from our hydrodynamical model with no transit assumed. For each trial, we adopt a reverse top-hat function (of fixed predicted central transit duration of 0.07 d) and fit it to the data by varying the depth and time of the centre. We record the best-fit depth at each choice of time. For the real unscrambled data, the top-hat fit finds a maximum eclipse amplitude of 0.0015 near HJD 2454424.73. With the planetary and stellar properties given above, and with an $i = 90^\circ$ orbit, the depth of the transit implies an 8- μ m brightness temperature for the planet of $T_{\text{pl}} \approx 800$ K. The bootstrap trials indicate that this secondary eclipse has been detected with 7σ confidence.

Having established the occurrence of the secondary eclipse, we can obtain a fit to the eclipse parameters. Using the flux baseline provided by the hydrodynamical model, we construct a grid of eclipse curves having different centre times, in-eclipse widths, and ingress/egress times. At each grid point, we fit the eclipse depth and the baseline with a scale factor using linear regression. The three-dimensional space of fitted parameters can be fully sampled, allowing for a direct determination of the minimum χ^2 value. Uncertainties are estimated using a standard bootstrap resampling procedure²¹. We find the following best-fit values: eclipse centre time, $T_c = \text{HJD } 2454424.736 \pm 0.003$; ingress/egress times, $T_{1,2} = T_{3,4} = 0.005 \pm 0.005$ d; in-eclipse time, $T_{2,3} = 0.070 \pm 0.009$ d; eclipse depth, $d = 0.00136 \pm 0.00018$.

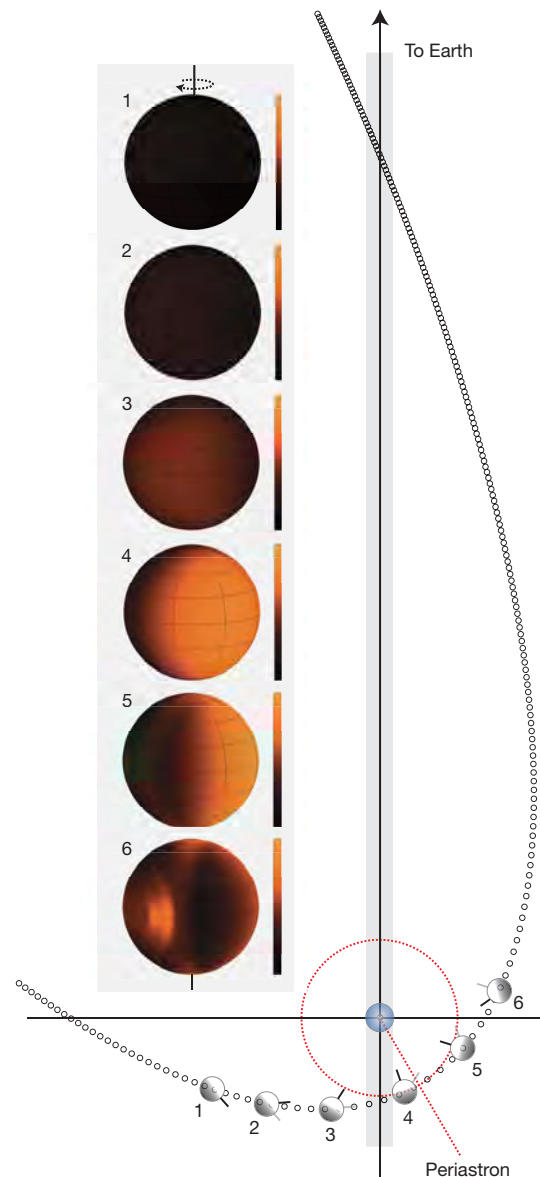


Figure 1 | Orbital geometry of the HD 80606b system. The small circles show the position of the planet in its orbit at 1-h intervals relative to the predicted periastron passage at HJD 2454424.84. The size of the parent star HD 80606 is drawn in correct relative scale to the orbit. The positions of the planet at times HJD (heliocentric Julian day) 2454424.2 (labelled 1), HJD 2454424.4 (2), HJD 2454424.6 (3), HJD 2454424.8 (4), HJD 2454425.0 (5) and HJD 2454425.2 (6) are shown, with the illuminated hemisphere indicated in each case. HD 80606b induces stellar reflex velocity variations of more than 900 m s^{-1} , and the stellar velocity can be measured to a precision of $1.5\text{--}2.5 \text{ m s}^{-1}$ (ref. 25). This high reflex velocity signal-to-noise allows the planet's orbital parameters to be accurately determined, despite the relatively long orbital period. Using the Keck I telescope (W. M. Keck Observatory, Hawaii), we have extended our data set for HD 80606b to 62 Doppler velocities (tabulated in the Supplementary Information), which, when combined with previously published data⁷, give an orbital period of $P = 111.4277 \pm 0.0032$ d, an eccentricity of $e = 0.9327 \pm 0.0023$, a longitude of periastron of $= 300.4977^\circ \pm 0.0045^\circ$, and a radial-velocity half-amplitude of $K = 471 \pm 5 \text{ m s}^{-1}$. The accuracy to which the orbital elements can be determined enabled the scheduling of the Spitzer telescope to observe the star–planet system in the infrared during the periastron passage of 20 November 2007. The pseudo-synchronous rotation rate of the planet is indicated by the successive positions of the small black bar (located at the longitude containing the substellar point at periastron). The temperature distribution on the planet (as predicted by our hydrodynamical model, and as seen by an observer looking down the vertical axis) at times 1–6 is shown in the inset diagram. The temperature scale runs from 750 K (dark) to 1,800 K (light).

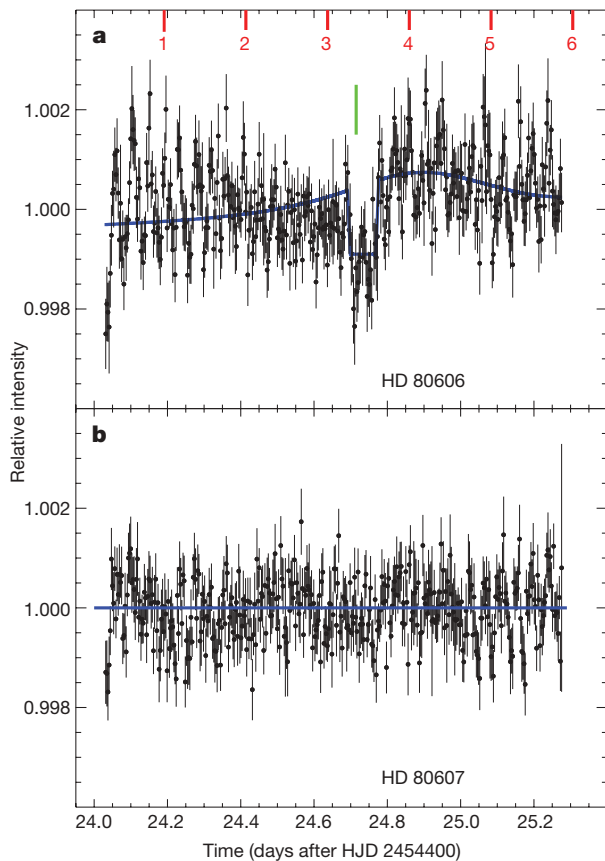


Figure 2 | The light curve of a planet undergoing a close approach to a star. Infrared photometric time series data for HD 80606 (a) and HD 80607 (b) for the Spitzer 8- μ m observations described in the text. The labels 1–6 correspond to the orbital positions indicated in Fig. 1. Our model light curve for HD 80606b is shown in blue, and the predicted midpoint for the secondary transit (from the fit to the radial velocities) is indicated in green. The model assumes an orbital inclination of $i = 90^\circ$. The depth and duration of the eclipse are determined by our estimates of the planetary and stellar sizes. The error bars on the photometric data indicate s.d., as described in detail in the Supplementary Information.

The secondary eclipse depth and our fit to the photometry indicate that HD 80606b had an effective temperature of $T = 725$ K at the beginning of the photometric observations, which is in accord with the energy output expected for tidal quality factors $Q \geq 3 \times 10^5$. Our model predicts that the planetary effective temperature on the Earth-facing hemisphere reaches $T_{\text{max}} \approx 1,250$ K before starting to decrease near the end of the observational window, and that the effective radiative time constant is $\tau_{\text{rad}} = 4.5 \pm 2$ h at the 8- μ m photosphere. The actual Spitzer 8- μ m photometry is broadly consistent with this model, although there is little indication of the predicted downturn at the end of the observations. If real, this apparent absence of a flux decrease could signal either rapid advection of heat onto the unilluminated hemisphere, or, alternatively, the failure of pseudo-synchronization theory to predict Ω_{spin} correctly. The heating rate is consistent with predictions of detailed multi-frequency model calculations of ‘pL’-type cloud-free atmospheres²², and suggests that the optical albedo of the planet should be low, in agreement with optical full-phase photometry by the Canadian Microvariability and Oscillations of Stars satellite for hot Jupiters on tidally circularized orbits²³.

The depth and duration of the secondary eclipse are consistent with an $i \approx 90^\circ$ orbital inclination for HD 80606b, implying a probability of $P \approx 15\%$ that the planet can also be observed in transit. Our radial velocity solution indicates that a central transit (were it to occur) would have a duration of 17 h, with a midpoint ~ 6 d after the secondary eclipse. Our predicted midpoint times are

$T_{\text{tr}} = \text{HJD } 2454653.68 + N \times 111.4277$, where N is any integer. The long duration of the transit would allow for precise determination of parameters such as R_{pl}/R_\star and i . As a consequence of the planetary deceleration with respect to the star during the transit epoch, the resulting photometric light curve would harbour a detectable asymmetry. Transits would also enable unprecedentedly accurate spectroscopic measurement of the Rossiter–McLaughlin effect^{24,25} giving the angle, λ , between the stellar rotational axis and the orbital angular momentum vector. If HD 80606b owes its current configuration to Kozai migration, then these two vectors would not be expected to be aligned.

Received 8 June; accepted 14 November 2008.

- Deming, D., Seager, S., Richardson, L. J. & Harrington, J. Infrared radiation from an extrasolar planet. *Nature* **434**, 740–743 (2005).
- Charbonneau, D. *et al.* Detection of thermal emission from an extrasolar planet. *Astrophys. J.* **626**, 523–529 (2005).
- Deming, D., Harrington, J., Seager, S. & Richardson, L. J. Strong infrared emission from the extrasolar planet HD 189733b. *Astrophys. J.* **644**, 560–564 (2006).
- Knutson, H. A. *et al.* A map of the day–night contrast of the extrasolar planet HD 189733b. *Nature* **447**, 183–186 (2007).
- Grillmair, C. J. *et al.* A Spitzer spectrum of the exoplanet HD 189733b. *Astrophys. J.* **658**, L115–L118 (2007).
- Langton, J. & Laughlin, G. Hydrodynamic simulations of unevenly irradiated Jovian planets. *Astrophys. J.* **674**, 1106–1116 (2007).
- Salby, M. L. *Fundamentals of Atmospheric Physics* 248 (Academic, 1996).
- Naef, D. *et al.* HD 80606b, a planet on an extremely elongated orbit. *Astron. Astrophys.* **375**, L27–L30 (2001).
- Wu, Y. & Murray, N. Planet migration and binary companions: The case of HD 80606b. *Astrophys. J.* **589**, 605–614 (2003).
- Goldreich, P. & Soter, S. Q in the solar system. *Icarus* **5**, 375–389 (1965).
- Peale, S. J. Origin and evolution of the natural satellites. *Annu. Rev. Astron. Astrophys.* **37**, 533–602 (1999).
- Werner, M. W. *et al.* The Spitzer Space Telescope mission. *Astrophys. J.* **154** (Suppl.), 1–9 (2004).
- Fazio, G. G. *et al.* The Infrared Array Camera (IRAC) for the Spitzer Space Telescope. *Astrophys. J.* **154** (Suppl.), 10–17 (2004).
- Cho, J. Y.-K., Menou, K., Hansen, B. M. S. & Seager, S. The changing face of the extrasolar giant planet HD 209458b. *Astrophys. J.* **587**, L117–L120 (2003).
- Burkert, A., Lin, D. N. C., Bodenheimer, P. H., Jones, C. A. & Yorke, H. W. On the surface heating of synchronously spinning short-period Jovian planets. *Astrophys. J.* **618**, 512–523 (2005).
- Showman, A. P., Cooper, C. S., Fortney, J. J. & Marley, M. S. Atmospheric circulation of hot Jupiters: Three-dimensional circulation models of HD 209458b and HD 189733b with simplified forcing. *Astrophys. J.* **618**, 559–576 (2008).
- Langton, J. & Laughlin, G. A new atmospheric model for HD 189733b. *Astrophys. J.* (submitted).
- Bodenheimer, P., Laughlin, G. & Lin, D. On the radii of extrasolar giant planets. *Astrophys. J.* **592**, 555–563 (2003).
- Hut, P. Tidal evolution in close binary systems. *Astron. Astrophys.* **99**, 126–140 (1981).
- Ivanov, P. B. & Papaloizou, J. C. B. Dynamic tides in rotating objects: orbital circularization of extrasolar planets for realistic planet models. *Mon. Not. R. Astron. Soc.* **376**, 682–704 (2007).
- Press, W. H., Teukolsky, S. A., Vetterling, W. T. & Flannery, B. P. *Numerical Recipes in FORTRAN. The Art of Scientific Computing* 2nd edn (Cambridge Univ. Press, 1992).
- Fortney, J. J., Lodders, K., Marley, M. S. & Freedman, R. S. A unified theory for the atmospheres of the hot and very hot Jupiters: Two classes of irradiated atmospheres. *Astrophys. J.* **678**, 1419–1435 (2008).
- Rowe, J. F. *et al.* The very low albedo of an extrasolar planet: MOST spacebased photometry of HD 209458. *Astrophys. J.* (submitted); preprint at (<http://arxiv.org/abs/0711.4111>) (2007).
- Queloz, D. *et al.* Detection of a spectroscopic transit by the planet orbiting the star HD 209458. *Astron. Astrophys.* **359**, L13–L17 (2000).
- Winn, J. *et al.* Measurement of spin–orbit alignment in an extrasolar planetary system. *Astrophys. J.* **631**, 1215–1226 (2000).

Supplementary Information is linked to the online version of the paper at www.nature.com/nature.

Acknowledgements We thank P. Bodenheimer, D. Charbonneau, J. Fortney, N. Iro and H. Knutson for discussions. This work is based on observations made with the Spitzer Space Telescope, which is operated by the Jet Propulsion Laboratory (JPL), California Institute of Technology (Caltech), under contract to NASA. Support for this work was provided by NASA through an award issued by JPL/Caltech.

Author Information Reprints and permissions information is available at www.nature.com/reprints. Correspondence and requests for materials should be addressed to G.L. (laughlin@ucoolick.org).

Nearly isotropic superconductivity in (Ba,K)Fe₂As₂

H. Q. Yuan^{1,2}, J. Singleton², F. F. Balakirev², S. A. Baily², G. F. Chen³, J. L. Luo³ & N. L. Wang³

Superconductivity was recently observed^{1–7} in iron-arsenic-based compounds with a superconducting transition temperature (T_c) as high as 56 K, naturally raising comparisons with the high- T_c copper oxides. The copper oxides have layered crystal structures with quasi-two-dimensional electronic properties, which led to speculation that reduced dimensionality (that is, extreme anisotropy) is a necessary prerequisite for superconductivity at temperatures above 40 K (refs 8, 9). Early work on the iron-arsenic compounds seemed to support this view^{7,10}. Here we report measurements of the electrical resistivity in single crystals of (Ba,K)Fe₂As₂ in a magnetic field up to 60 T. We find that the superconducting properties are in fact quite isotropic, being rather independent of the direction of the applied magnetic fields at low temperature. Such behaviour is strikingly different from all previously known layered superconductors^{9,11}, and indicates that reduced dimensionality in these compounds is not a prerequisite for ‘high-temperature’ superconductivity. We suggest that this situation arises because of the underlying electronic structure of the iron-arsenic compounds, which appears to be much more three dimensional than that of the copper oxides. Extrapolations of low-field single-crystal data incorrectly suggest a high anisotropy and a greatly exaggerated zero-temperature upper critical field.

(Ba,K)Fe₂As₂ was the first superconductor found in the (A,K)Fe₂As₂ (A = Ba, Sr) (or 122) series⁶; its superconducting T_c can be as high as 38 K. Its parent compound BaFe₂As₂ shows a first-order structural phase transition from tetragonal to orthorhombic with the simultaneous onset of long-range antiferromagnetic order around 140 K (refs 7, 12). Thermodynamic and transport measurements have been used to extract the $H_{c2}(T)$ dependences (where H_{c2} is the upper critical field and T is temperature) at low magnetic fields for fields applied both within the a - b planes and parallel to the c axis. The estimated $H_{c2}(0)$ based on these low-field $H_{c2}(T)$ experiments is anisotropic and exceeds 100 T at low temperatures⁷. However, experience with other quasi-two-dimensional superconductors such as organics and copper oxides shows that the low-field temperature dependence of $H_{c2}(T)$ is often a very poor guide to both its detailed behaviour at lower temperatures and its eventual $T = 0$ limit^{9,11}. Measurements in high magnetic fields are therefore very important, as they alone can give quantitative values of $H_{c2}(T \rightarrow 0)$, thereby probing the mechanisms that limit the robustness of the superconducting state.

Figure 1a shows the zero-field resistivity as a function of temperature for a single crystal of (Ba,K)Fe₂As₂. (This sample, denoted A, has the formula Ba_{1-x}K_xFe₂As₂, where $x \approx 0.4$ (nominal value, below same)) A very sharp superconducting transition can be clearly observed with a midpoint at $T_c \approx 28.2$ K, indicating good sample quality. Within the normal state (either temperature- or field-induced), the Hall resistance follows a linear field dependence up to 60 T; this is in contrast to the underdoped ReFeAs(O,F) (1111-type) compounds in which the Hall resistance deviates from linearity at high fields and low temperatures (H.Q.Y., unpublished results). The Hall coefficient R_H of

(Ba,K)Fe₂As₂ is plotted as a function of temperature in Fig. 1a inset. Note that R_H decreases monotonically with increasing temperature above T_c , consistent with an increase in the number of dominant hole carriers with increasing temperature.

The rather isotropic behaviour of $H_{c2}(T)$ at low temperatures that is the main focus of this Letter is already evident in Fig. 1b, c; at the same temperature, superconductivity is suppressed by similar values of the field applied parallel or perpendicular to the c axis (denoted respectively by $H//c$ and $H \perp c$). However, the normal state just above the critical field displays a distinct field-orientation dependence: as the temperature decreases, the high-field resistance exhibits a slight ‘hump’ for $H//c$, but decreases monotonically for in-plane magnetic fields. This is shown in greater detail in Fig. 2. Similar phenomena occur in the underdoped 1111-type polycrystalline samples¹³, high- T_c copper oxides⁹ and organic metals¹⁴; in the latter case the ‘hump’ is attributed to magnetoresistance caused by semiclassical electron trajectories across the Fermi surface¹⁵.

Figure 3 plots the resistive midpoint upper critical fields H_{c2} versus temperature for two different samples of (Ba,K)Fe₂As₂ (samples A and B, both cut from the same batch) which have almost exactly the same T_c (~ 28 K) and resistive upper critical field behaviour. The most remarkable aspect of Fig. 3 is the fact that the resistive upper critical field of (Ba,K)Fe₂As₂ extrapolates to a similar zero-temperature value (~ 70 T), irrespective of whether the field is applied parallel or perpendicular to the c axis. This is in great contrast to the behaviour of other quasi-two-dimensional superconductors, such as the crystalline organic metals^{11,14} or the copper oxides^{9,16,17}, where the in-plane critical fields are many times larger than those for fields applied perpendicular to the quasi-two-dimensional planes.

The magnetic-field-orientation dependence of the resistive upper critical field depends on two inter-related properties of the superconductor in question: (1) the underlying Fermi-surface topology and (2) the nature of the vortices that form in the mixed state^{9,14,16,17}. The Fermi-surface topology uniquely determines the velocities of the electrons involved in forming Cooper pairs and thus the ability of the material to support the circulatory currents involved in forming vortices^{9,14,16,17}. Topologically, circulatory currents are possible if the intersections of planes perpendicular to the applied field and the Fermi surface produce closed loops¹¹. If such currents occur, the additional ‘orbital energy’ accumulated by the vortex system eventually destroys the superconducting state as the applied field increases.

In the case of the layered copper oxides and organic superconductors, the Fermi surfaces are very two-dimensional, with a cross-sectional area that varies little in the interlayer direction^{9,14,18}. Hence, fields applied exactly within the conducting planes cannot induce significant circulating currents, as the Fermi-surface cross-sections perpendicular to this are almost all open¹⁵. This prevents orbital mechanisms from limiting the upper critical field^{14,16,17}. In such cases, the superconductivity is suppressed at the Clogston–Chandrasekhar limit (CCL), in which the magnetic energy associated with the spin susceptibility in the normal

¹Department of Physics, Zhejiang University, Hangzhou, Zhejiang 310027, China. ²NHML, Los Alamos National Laboratory, MS E536, Los Alamos, New Mexico 87545, USA. ³Beijing National Laboratory for Condensed Matter Physics, Institute of Physics, Chinese Academy of Science, Beijing 10080, China.

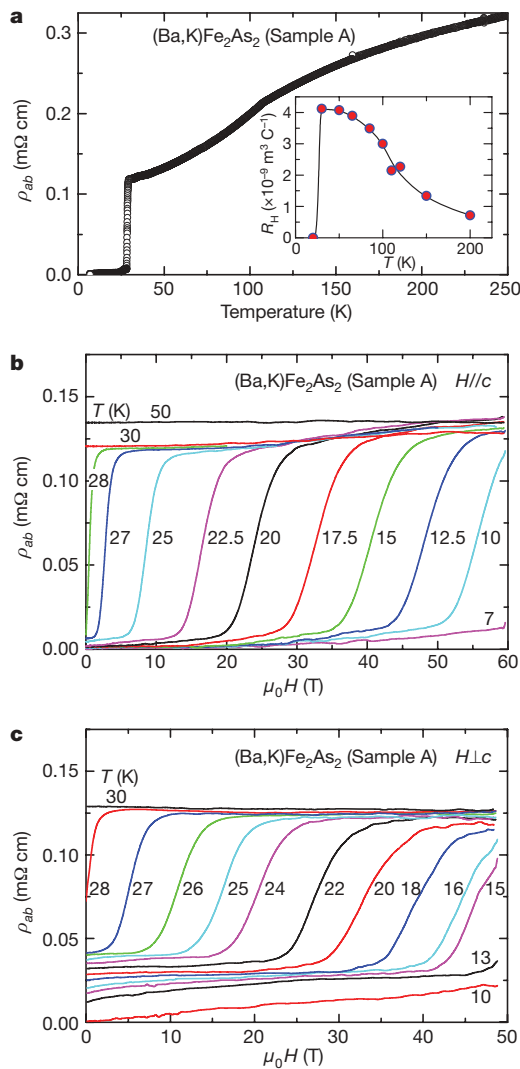


Figure 1 | In-plane electrical resistivity of single crystal $(\text{Ba,K})\text{Fe}_2\text{As}_2$ measured in pulsed high magnetic fields. **a**, The temperature dependence of the resistivity $\rho_{ab}(T)$ at zero magnetic field. Note that there is a weak kink around 108 K in $\rho_{ab}(T)$, which may correspond to a spin-density-wave or structural transition^{7,12}. This indicates that the sample is located on the underdoped side. Inset, temperature dependence of the Hall coefficient R_H obtained in pulsed magnetic fields of up to 60 T. **b**, **c**, The field dependence of the resistivity $\rho(B)$ at various temperatures for fields respectively parallel and perpendicular to the c axis. In contrast to the broad superconducting-to-normal transitions observed in the 1111-type polycrystals^{13,25} and some 'high- T_c ' copper oxides⁹, the single-crystal $\text{Ba}_{1-x}\text{K}_x\text{Fe}_2\text{As}_2$ grown from Sn flux with a nominal potassium content of $x \approx 0.4$ (ref. 26) shows sharp transitions even in high fields, permitting accurate evaluations of the resistive upper critical field H_{c2} . To minimize the self-heating effect in a pulsed magnetic field, samples with typical size of about $2 \text{ mm} \times 0.5 \text{ mm} \times 0.02 \text{ mm}$ were cleaved off from the large batch for resistivity measurement and no obvious heating effects were observed, judging from the almost identical resistance curves collected in the up-sweeping and down-sweeping of the magnet. Longitudinal resistivity and transverse Hall resistivity were simultaneously measured with a typical 5-probe method in pulsed fields of up to 60 T at Los Alamos National High Magnetic Field Laboratory. Forward- and reverse-field shots were made at the same temperatures for Hall resistance measurements to eliminate the effects of contact asymmetries. The data traces were recorded on a digitizer using a custom high-resolution, low-noise synchronous lock-in technique. The temperature dependence of the resistivity was measured with a Lakeshore resistance bridge.

state exceeds the condensation energy in the superconducting state^{19,20}. However, as the field is tilted away from the conducting planes, orbital mechanisms become feasible, producing an upper critical field that

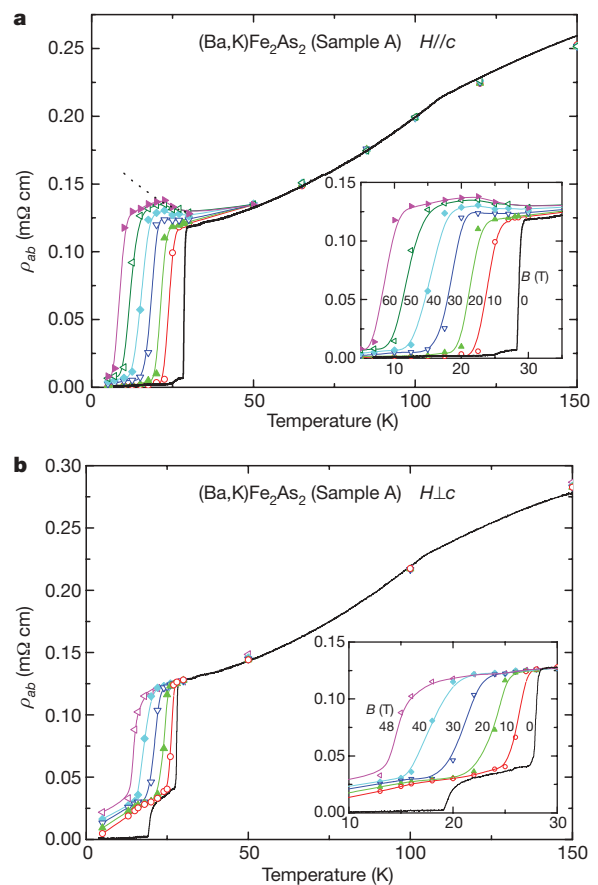


Figure 2 | Electrical resistivity versus temperature at selected magnetic fields. **a**, $H//c$; **b**, $H\perp c$. Different symbols represent the resistivity $\rho_{ab}(T)$ at different magnetic fields, as labelled in the insets. The solid lines are guides to the eye and the dashed line in **a** highlights the upturn in the resistivity at low temperatures for $H//c$. The insets are expansions of the superconducting regions. Note that apart from the main superconducting transition there is an additional lower temperature/lower field transition in **b** and Fig. 1c, suggesting the presence of a small amount of a second structural or chemical phase with a lower T_c . The amount (or visibility) of the second phase develops over time and with repeated thermal cycling of the samples; it is absent from 'virgin' crystals. Note that **b** and Fig. 1c were recorded several days after **a** and Fig. 1b, with a number of thermal cycles between room and cryogenic temperatures. The visibility of the lower temperature transition increased with each thermal cycling.

declines rapidly with increasing angle^{11,14,16,17}. The combination of the CCL and quasi-two-dimensional Fermi surface results in a very anisotropic critical field in the organics and copper oxides, strongly peaked for in-plane fields^{11,14,16,17}. Even a cursory inspection of the data in Fig. 3 shows that this is definitely not the case in $(\text{Ba,K})\text{Fe}_2\text{As}_2$.

The vortex structure is the second ingredient in the angle dependence of the resistive upper critical field in layered materials^{9,11,14}. For superconductors with weakly coupled layers, pancake vortices are observed for fields applied perpendicular to the quasi-two-dimensional planes, whereas Josephson vortices occur for in-plane fields. At intermediate orientations, the two types coexist, with their relative densities determined by the components of the field perpendicular and parallel to the layers. This results in a resistive transition with a shape that varies with field orientation, as seen in the organic superconductors and copper oxides^{14,16,17}. To show that such behaviour does not occur in $(\text{Ba,K})\text{Fe}_2\text{As}_2$, a single-crystal sample was rotated *in situ* using a cryogenic goniometer, and the resistance measured at a fixed temperature of about 20 K for several field orientations. Data for the onset, midpoint and upper limit of the resistive transition are shown as a function of orientation in Fig. 3 upper inset. (Shown here are data for sample C, $\text{Ba}_{1-x}\text{K}_x\text{Fe}_2\text{As}_2$ with $x \approx 0.4$.) It is

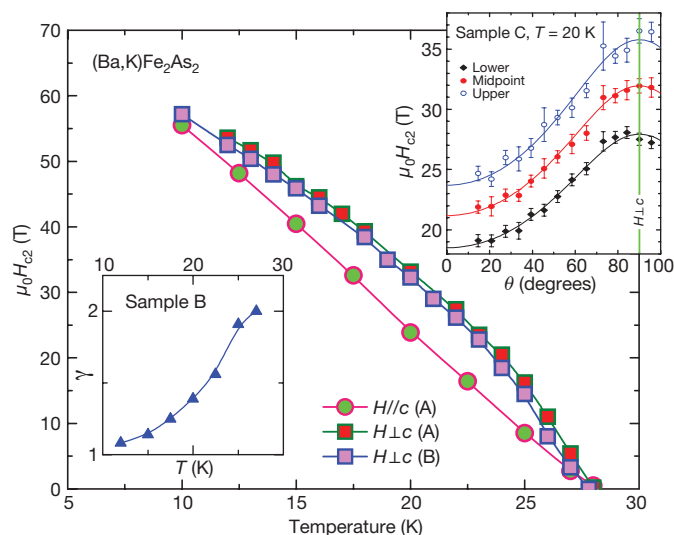


Figure 3 | The upper critical field $H_{c2}(T)$. The main figure shows H_{c2} versus temperature for magnetic fields parallel to the c axis (circles) and perpendicular to the c axis (squares), in which the critical fields $H_{c2}(T)$ are determined from the midpoint of the sharp resistive superconducting transitions. Remarkably, the two samples (A and B) behave nearly identically. Lower inset, the anisotropy parameter $\gamma = H_{c2}^{H_{\perp}c} / H_{c2}^{H//c}$ plotted as a function of temperature. The parameter γ is about 2 near T_c , a value close to that derived by other groups using low-field measurements⁷, but decreases with decreasing temperature and approaches 1 as $T \rightarrow 0$, indicating isotropic superconductivity. Upper inset, the upper critical field $\mu_0 H_{c2}$ (sample C, $T_c \approx 28$ K), derived at the upper, midpoint and lower limits of the main resistive transition, plotted as a function of the tilt angle θ at $T = 20$ K, where θ is the angle between the applied magnetic field (\mathbf{H}) and the crystallographic c axis. The error bars mark the maximum deviation of the rounded transitions from the sharp part of the superconducting transition to the monotonically increasing normal-state resistivity (upper limit), to zero resistance (lower limit) and the width of the sharp transition (midpoint), respectively. For the angle-dependence measurements, the electrical current is applied perpendicular to the direction of magnetic field. The angle dependence of $\mu_0 H_{c2}$ can be well scaled by $\varepsilon(\theta)H_{c2} = H_{c2}[\cos^2(\theta) + \gamma^{-2} \sin^2(\theta)]^{-0.5}$; the obtained effective mass anisotropy γ (1.5 ± 0.1) is very close to the value (1.4 ± 0.1) we derived from $\gamma = H_{c2}^{H_{\perp}c} / H_{c2}^{H//c}$ as shown in the lower inset.

clear that the resistive transition varies in width and position very smoothly with field orientation, strongly suggesting that $(\text{Ba,K})\text{Fe}_2\text{As}_2$ does not behave as a weakly coupled layered superconductor, but instead that the vortex arrangement is similar at all field orientations.

The nearly isotropic critical field of $(\text{Ba,K})\text{Fe}_2\text{As}_2$ might be linked to its distinctive Fermi surface. Published calculations²¹, supported by recent magnetic quantum-oscillation measurements on its sister compound SrFe_2As_2 (ref. 22), give a Fermi surface consisting of a number of strongly corrugated or flared tubes with relatively small (compared to the Brillouin zone) cross-sectional areas. Both calculated and measured effective masses are relatively light (a few times the free-electron mass), so that most probably orbital effects limit the upper critical field in $(\text{Ba,K})\text{Fe}_2\text{As}_2$ for $H//c$, as is seen in the copper oxides and organics. However, in contrast to the very weakly corrugated Fermi surfaces of the latter superconductors^{15,18}, that of $(\text{Ba,K})\text{Fe}_2\text{As}_2$ shows considerable dispersion along the c direction in momentum space (denoted k_c), manifested as a strong oscillation of the cross-sectional area of the various sections as k_c varies; the Fermi surface is much more three dimensional. The much larger corrugations in the Fermi surface of $(\text{Ba,K})\text{Fe}_2\text{As}_2$ are sufficient to permit circulating currents at all field orientations; hence, orbital limiting effects might persist at all field angles, leading to the observed rather isotropic upper critical field.

Although the low-temperature upper critical field is rather isotropic, the initial slope of $H_{c2}(T)$ near T_c does show some dependence

on the field orientation (Fig. 3), perhaps resulting from details of the vortex structure (which will affect the magnetoresistance close to the transition¹⁴) or the Fermi-surface topology. In our resistive critical field data, $dH_{c2}/dT(T = T_c)$ is determined to be about 2.9 T K^{-1} for $H//c$ and 5.4 T K^{-1} for $H \perp c$. These are close to the values found for $(\text{Ba,K})\text{Fe}_2\text{As}_2$ in d.c. field measurements⁷. In contrast to the high- T_c copper oxides and the dirty MgB_2 in which a strong upturn curvature was observed in $H_{c2}(T)$ at very low temperatures^{23,24}, $H_{c2}(T)$ in $(\text{Ba,K})\text{Fe}_2\text{As}_2$ shows a convex shape for $H \perp c$, but follows an almost linear temperature dependence down to 10 K for $H//c$. The strong, experimentally measured, curvature of $H_{c2}(T)$ for $H \perp c$ leads to a significantly lower zero-temperature upper critical field than do typical extrapolation methods; the latter yield values beyond 100 T, much higher than our experimentally inferred value of 70 T.

As far as we are aware, no other layered superconductors exhibit upper critical fields that behave in the same way as those of $(\text{Ba,K})\text{Fe}_2\text{As}_2$. The difference is, we believe, associated with this material's distinctive Fermi-surface topology, the strong corrugations of which—a manifestation of essentially three-dimensional band structure—permit orbital limiting of the upper critical field at all field orientations. Therefore the 122-type ternary iron arsenides are unique in possessing both a rather high T_c and essentially three-dimensional electronic properties. In contrast to common assumptions based on the properties of the copper oxides, it seems that reduced dimensionality is not necessarily a prerequisite for 'high-temperature' superconductivity.

Note added in proof: We have recently become aware that megahertz penetration depth measurements in fields up to 45 T (ref. 27) further support our conclusion.

Received 27 July; accepted 24 November 2008.

- Kamihara, Y., Watanabe, T., Hirano, M. & Hosono, H. Iron-based layered superconductor $\text{La}[\text{O}_{1-x}\text{F}_x]\text{FeAs}$ ($x = 0.05\text{--}0.12$) with $T_c = 26$ K. *J. Am. Chem. Soc.* **130**, 3296–3297 (2008).
- Chen, X. H. *et al.* Superconductivity at 43 K in $\text{SmFeAsO}_{1-x}\text{F}_x$. *Nature* **453**, 761–762 (2008).
- Chen, G. F. *et al.* Superconductivity at 41 K and its competition with spin-density-wave instability in layered $\text{CeO}_{1-x}\text{F}_x\text{FeAs}$. *Phys. Rev. Lett.* **100**, 247002 (2008).
- Ren, Z. A. *et al.* Superconductivity in the iron-based F-doped layered quaternary compound $\text{Nd}[\text{O}_{1-x}\text{F}_x]\text{FeAs}$. *Europhys. Lett.* **82**, 57002 (2008).
- Wang, C. *et al.* Thorium-doping induced superconductivity up to 56 K in $\text{Gd}_{1-x}\text{Th}_x\text{FeAsO}$. *Europhys. Lett.* **83**, 67006 (2008).
- Rotter, M., Tegel, M. & Johrendt, D. Superconductivity at 38 K in the iron arsenide $(\text{Ba}_{1-x}\text{K}_x)\text{Fe}_2\text{As}_2$. *Phys. Rev. Lett.* **101**, 107006 (2008).
- Ni, N. *et al.* Anisotropic thermodynamic and transport properties of single crystalline $(\text{Ba}_{1-x}\text{K}_x)\text{Fe}_2\text{As}_2$ ($x = 0$ and 0.45). *Phys. Rev. B* **78**, 014507 (2008).
- Anderson, P. W. *The Theory of Superconductivity in the High- T_c Cuprate Superconductors* (Princeton Univ. Press, 1997).
- Shrieffer, J. R. & Brooks, J. S. *Handbook of High-Temperature Superconductivity* (Springer, 2006).
- Ding, H. *et al.* Observation of Fermi-surface-dependent nodeless superconducting gaps in $\text{Ba}_{0.6}\text{K}_{0.4}\text{Fe}_2\text{As}_2$. *Europhys. Lett.* **83**, 47001 (2008).
- Singleton, J. & Mielke, C. Quasi-two-dimensional organic superconductors: A review. *Contemp. Phys.* **43**, 63–96 (2002).
- Huang, Q. *et al.* Magnetic order in BaFe_2As_2 , the parent compound of the FeAs based superconductors in a new structural family. Preprint at (<http://arxiv.org/abs/0806.2776>) (2008).
- Riggs, S. C. *et al.* Log-T divergence and insulator-to-metal crossover in the normal state resistivity of fluorine doped $\text{SmFeAsO}_{1-x}\text{F}_x$. Preprint at (<http://arxiv.org/abs/0806.4011>) (2008).
- Nam, M. S. *et al.* Angle dependence of the upper critical field in the layered organic superconductor $\kappa\text{-(BEDT-TTF)}_2\text{Cu}(\text{NCS})_2$ ($\text{BEDT-TTF} \equiv \text{bis(ethylene-dithio)tetrahydrofulvalene}$). *J. Phys. Condens. Matter* **11**, L477–L484 (1999).
- Singleton, J. *et al.* Persistence to high temperatures of interlayer coherence in an organic superconductor. *Phys. Rev. Lett.* **99**, 027004 (2007).
- Vedenev, S. I. *et al.* Reaching the Pauli limit in the cuprate $\text{Bi}_2\text{Sr}_2\text{CuO}_{6+\delta}$ in high parallel magnetic field. *Phys. Rev. B* **73**, 014528 (2006).
- Li, P. C., Balakirev, F. F. & Greene, R. L. Upper critical field of electron-doped $\text{Pr}_{2-x}\text{Ce}_x\text{CuO}_{4-\delta}$ in parallel magnetic fields. *Phys. Rev. B* **75**, 172508 (2007).
- Sebastian, S. E. *et al.* A multi-component Fermi surface in the vortex state of an underdoped high- T_c superconductor. *Nature* **454**, 200–203 (2008).
- Clogston, A. M. Upper limit for the critical field in hard superconductors. *Phys. Rev. Lett.* **9**, 266–267 (1962).
- Chandrasekhar, B. S. A note on the maximum critical field of high-field superconductors. *Appl. Phys. Lett.* **1**, 7–8 (1962).

21. Liu, C. *et al.* K-doping dependence of the Fermi surface of the iron-arsenic $\text{Ba}_{1-x}\text{K}_x\text{Fe}_2\text{As}_2$ superconductor using angle resolved photoemission spectroscopy. *Phys. Rev. Lett.* **101**, 177005 (2008).
22. Sebastian, S. E. *et al.* Quantum oscillations in the undoped parent magnetic phase of a high temperature superconductor. *J. Phys. Condens. Matter* **20**, 422203 (2008).
23. Gurevich, A. Limits of the upper critical field in dirty two-gap superconductors. *Physica C* **456**, 160–169 (2007).
24. Ando, Y. *et al.* Resistive upper critical fields and irreversibility lines of optimally doped high T_c cuprates. *Phys. Rev. B* **60**, 12475–12479 (1999).
25. Hunte, F. *et al.* Two-band superconductivity in $\text{LaFeAsO}_{0.89}\text{F}_{0.11}$ at very high magnetic fields. *Nature* **453**, 903–905 (2008).
26. Chen, G. F. *et al.* Transport and anisotropy in single-crystalline SrFe_2As_2 and $\text{A}_{0.6}\text{K}_{0.4}\text{Fe}_2\text{As}_2$ ($\text{A} = \text{Sr}, \text{Ba}$) superconductors. Preprint at (<http://arXiv.org/abs/0806.2648>) (2008).
27. Altarawneh, M. *et al.* Determination of anisotropic H_{c2} up to 45 T in $(\text{Ba}_{0.55}\text{K}_{0.45})\text{Fe}_2\text{As}_2$ single crystals. Preprint at (<http://arxiv.org/abs/0807.4488>) (2008).

Acknowledgements We acknowledge S. Riggs and J. Betts for experimental assistance and F. C. Zhang, P. Goddard and S. Blundell for discussions. Work at NHMFL-LANL is performed under the auspices of the National Science Foundation, Department of Energy and State of Florida. The experiments reported here are supported by the DOE BES program ‘Science in 100T’, the NHMFL-UCGP, the National Science Foundation of China, the National Basic Research Program of China (973 Program) and the Chinese Academy of Sciences. H.Q.Y. is also supported by PCSIRT of the Ministry of Education of China.

Author Contributions H.Q.Y. designed this study, did the main experiments and analysed the data. F.F.B. and J.S. provided experimental support. S.A.B. measured the angle dependence of H_{c2} . Samples were grown by G.F.C., J.L.L. and N.L.W. The paper was written by H.Q.Y. and J.S.

Author Information Reprints and permissions information is available at www.nature.com/reprints. Correspondence and requests for materials should be addressed to H.Q.Y. (hqyuan@zju.edu.cn).

(π, π) electronic order in iron arsenide superconductors

V. B. Zabolotnyy¹, D. S. Inosov^{1,2}, D. V. Evtushinsky¹, A. Koitzsch¹, A. A. Kordyuk^{1,3}, G. L. Sun², J. T. Park², D. Haug², V. Hinkov², A. V. Boris^{2,4}, C. T. Lin², M. Knupfer¹, A. N. Yaresko², B. Büchner¹, A. Varykhalov⁵, R. Follath⁵ & S. V. Borisenko¹

The distribution of valence electrons in metals usually follows the symmetry of the underlying ionic lattice. Modulations of this distribution often occur when those electrons are not stable with respect to a new electronic order, such as spin or charge density waves. Electron density waves have been observed in many families of superconductors^{1–3}, and are often considered to be essential for superconductivity to exist⁴. Recent measurements^{5–9} seem to show that the properties of the iron pnictides^{10,11} are in good agreement with band structure calculations that do not include additional ordering, implying no relation between density waves and superconductivity in these materials^{12–15}. Here we report that the electronic structure of $\text{Ba}_{1-x}\text{K}_x\text{Fe}_2\text{As}_2$ is in sharp disagreement with those band structure calculations^{12–15}, and instead reveals a reconstruction characterized by a (π, π) wavevector. This electronic order coexists with superconductivity and persists up to room temperature (300 K).

Calculations of the electronic structure of the new pnictide superconductors unanimously predict a Fermi surface consisting of a hole-like pocket at the centre (Γ point) of the Brillouin zone and electron-like ones at the corners (X points) of the Brillouin zone. A shift by a (π, π) vector would result in a significant overlap of these Fermi surfaces. Such an electronic structure is highly unstable because any interaction allowing an electron to gain a (π, π) momentum would favour a density-wave order, resulting in a shift of the aforementioned type and a concomitant opening of the gaps, thus strongly reducing the electronic kinetic energy. It is surprising that angle-resolved photoemission spectroscopy (ARPES) data are reported to be in general, and sometimes in very detailed⁹, agreement with calculations that give a potentially unstable solution^{5–7}. Even in the parent compound, where the spin-density-wave transition is clearly seen using other techniques^{16,17}, no evidence for the expected energy gap has been detected in photoemission experiments^{7,8}. In fact, no consensus exists regarding the overall Fermi surface topology. According to refs 5 and 6, there is a single electron-like Fermi surface pocket around X, whereas ref. 18 reported two intensity spots without any discernible signature for the electron pocket in the normal state. Intensity spots near X were also reported in refs. 6, 7 and 9, but those are interpreted as parts of electron-like pockets. Such substantial variations in the photoemission signal preclude unambiguous assignment of the observed features to the calculated Fermi surface, leaving the electronic structure of the arsenides unclear.

In Fig. 1, we show the experimental Fermi surface map of $\text{Ba}_{1-x}\text{K}_x\text{Fe}_2\text{As}_2$ (BKFA) measured in the superconducting state. To eliminate possible effects of photoemission matrix elements, as well as to cut the electronic structure at different values of momentum, k_z , we made measurements at several excitation energies (Fig. 1a, b) and polarizations (Fig. 1c, d). Although there are obvious changes in the intensities of the features, no signatures indicating k_z dispersion can be conclusively identified. With this in mind, the apparently different intensity distributions at neighbouring Γ points appear unusual. In

the first Brillouin zone, the two concentric contours are broadly consistent with band structure calculations, but the ‘design wheels’ centred at the Γ points (Fig. 1a, b) in the second Brillouin zone are at variance with predicted hole-like circles. The major discrepancy with theoretical calculations and ARPES data^{5–9,18} is observed near X, where, according to the calculations, a sizeable double-walled electron pocket is expected. Instead, we observe a propeller-shaped structure consisting of five small Fermi surface sheets: a pocket, situated directly at X, and four ‘blades’ surrounding it. Fig 1c, d shows that these Fermi surfaces are not only well separated but also have different symmetries.

To examine the topology of these five pockets, we look at the momentum distribution of intensity below and above the Fermi level. As can be seen in Fig. 2a–c, the size of the X-centred pocket

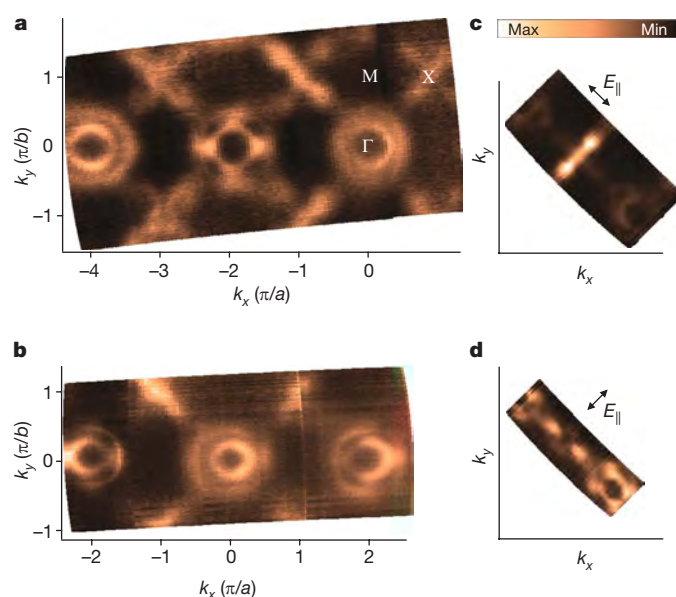


Figure 1 | Fermi surface topology of $\text{Ba}_{1-x}\text{K}_x\text{Fe}_2\text{As}_2$. The colour plots display the photoelectron intensity distribution as a function of quasi-momentum, k_{\parallel} , integrated over a small energy window of 15 meV around the Fermi level. **a, b**, Fermi surface maps of $\text{Ba}_{1-x}\text{K}_x\text{Fe}_2\text{As}_2$ measured using respective excitation energies of $h\nu = 80$ and 50 eV at $T = 14$ K (here ν denotes frequency and h denotes Planck's constant). **c, d**, These images, measured at $h\nu = 80$ eV, demonstrate the strong effect of light polarization on the photoemission from the four small Fermi surfaces surrounding X. The component of the electric field parallel to the sample surface, E_{\parallel} , is indicated by a double-headed arrow. Experimental details concerning the sample preparation can be found in Supplementary Information. **a, b**, lattice parameters.

¹Institute for Solid State Research, IFW-Dresden, PO Box 270116, 01171 Dresden, Germany. ²Max-Planck-Institute for Solid State Research, Heisenbergstrasse 1, 70569 Stuttgart, Germany. ³Institute of Metal Physics of National Academy of Sciences of Ukraine, 03142 Kyiv, Ukraine. ⁴Department of Physics, Loughborough University, Loughborough, LE11 3TU, UK. ⁵Elektronenspeicherring BESSY II, Helmholtz-Zentrum Berlin für Materialien und Energie, Albert-Einstein-Strasse 15, 12489 Berlin, Germany.

clearly increases when the electronic structure is cut above the Fermi level, and decreases when the cut is made below the Fermi level, which confirms its electron-like topology. On the other hand, the blades surrounding X have the opposite behaviour, which shows that they are hole-like. In Fig. 2e–i, we analyse the band dispersions along the cuts given in Fig. 2d, and again find support for these conclusions (see also Supplementary Information). Therefore, the observed topology of the Fermi surface is different from that predicted by band structure calculations. However, in the following we will argue that the results of the calculations can be reconciled with the experimental data, provided the system reacts to the predicted nesting instability and an ordered state develops.

In Fig. 3, we collate the ARPES data taken at low temperatures for the parent compound with the spectra of the doped superconductor, measured using the same light polarization as in Fig. 1d. The photoemission intensity distributions shown in Fig. 3a, b are comparable when the difference in the charge carrier concentrations is taken into account. Moreover, the momentum–energy cuts (Fig. 3c–h) show that there is a one-to-one correspondence between the underlying band dispersions in the parent and superconducting samples. Similar locations in the momentum–energy space, as well as the characteristic, polarization-induced intensity variations, clearly suggest that the blades are also present in BaFe_2As_2 (BFA). Notably, the distance between the centres of opposite blades tracks the size of the Γ -Fermi surface. Closer inspection of all existing ARPES data on arsenides confirms the universality of this observation^{6–9,18}.

The origin of the unexpected Fermi surface topology near X is clarified in Fig. 3i, j, where momentum–energy cuts separated by the (π, π) vector are shown: the blades in the parent compound are

created by the interaction of the (π, π) replica of the Γ -centred Fermi surface with the X-centred electron-like Fermi surface predicted in the calculations. Such a (π, π) folding implies the presence of additional ordering that sets in to relax the nesting instability. The formation of the blades, within this picture, is illustrated by simple sketch in Fig. 3k. The intensity of the Γ -derived band in Fig. 3j is lower than that shown in Fig. 3i owing to the weakness, relative to the original crystalline potential, of the scattering potential introduced by the new order^{19,20}. This is also the case for the Fermi surface map in Fig. 3a, where the ARPES intensities near Γ and X still differ. Similarly, in superconducting BKFA this effect prevents immediate detection of the ordered state suggested by the blades. By recovering the band dispersion in the vicinity of the Fermi level, as shown in Fig. 3l–m, we can identify new Brillouin zone boundaries (white lines).

An immediate interpretation of the observed similarity in the electronic structures of the $x = 0.0$ and $x = 0.3$ compounds shown in Fig. 3 would be the persistence of magnetic order in the superconducting case, which does not contradict the phase diagram suggested in ref. 21. However, the temperature evolution of the photoemission intensity of the blades presented in Fig. 4b rules out any direct connection between the observed Fermi surface topology and the static magnetic order. Despite the blades having a noticeably lower spectral weight in comparison with the Γ -Fermi surface sheets, these hole-like structures clearly persist to room temperature (Fig. 4a), which is above the structural, magnetic and superconducting transitions in arsenides. Such temperature behaviour also rules out the possibility that the observed Fermi surface topology near the X points is a consequence of a pronounced deformation of the calculated band structure, which would destroy the Fermi surface nesting. To account

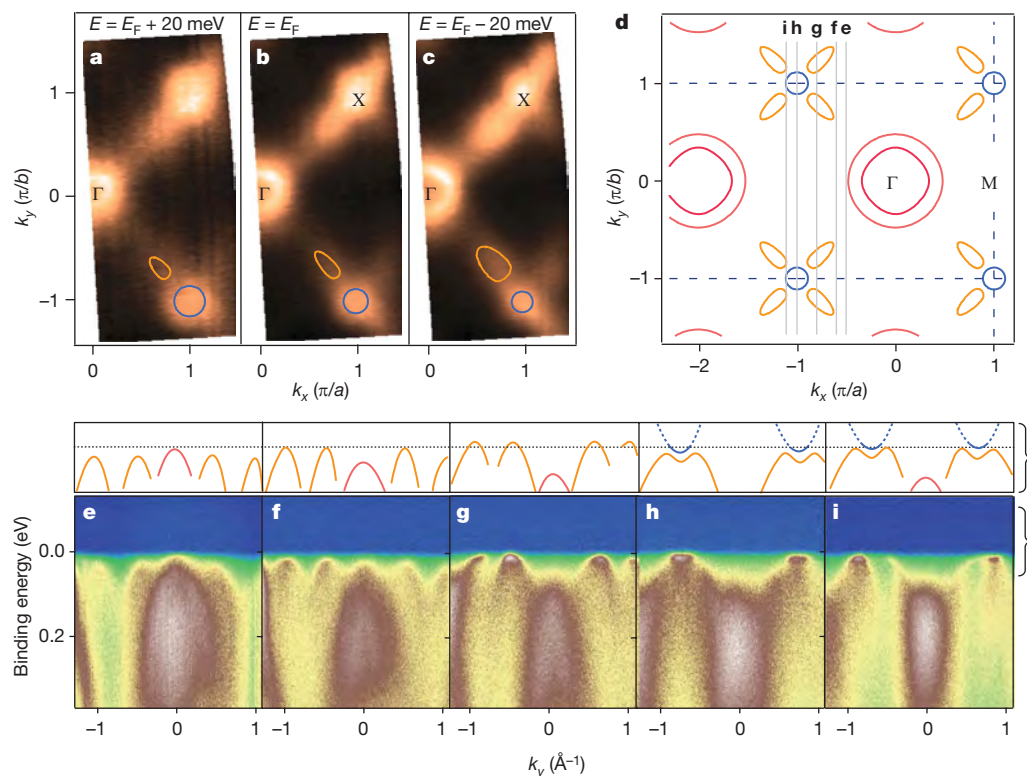


Figure 2 | Low-energy electronic structure of $\text{Ba}_{1-x}\text{K}_x\text{Fe}_2\text{As}_2$. **a–c**, Momentum dependence of the photoemission intensity at constant-energy cuts for $\text{Ba}_{1-x}\text{K}_x\text{Fe}_2\text{As}_2$ ($T = 150$ K, $h\nu = 70$ eV). The size of the blade pockets (outlined by the orange lines) increases with cut energy, E , and signals their hole-like topology. The opposite trend for the X-centred pocket (blue circles) implies the electron-like topology of that pocket. To avoid obscuring the experimental data, we display the guide lines only in the lower parts of the images. E_F , Fermi energy. **d**, Summary of the derived Fermi surface topology. **e–i**, Energy–momentum cuts showing low-energy band

dispersions ($T \leq 15$ K, $h\nu = 80$ eV). The cartoon above each image outlines the band dispersions and the formation of the hole and electron pockets at the Fermi level. In cut **e**, five parabolic bands with similar dispersions can be seen approaching, but not crossing, the Fermi level. With movement away from Γ (cuts **f–g**), the four bands on the sides finally cross the Fermi level, forming the blade structure near the X points. However, when the cut passes directly through the X points (cut **h**), these four hole-like bands again drop below the Fermi level, and instead two electron-like bands, of curvature opposite to that of the previous bands, appear from above the Fermi level.

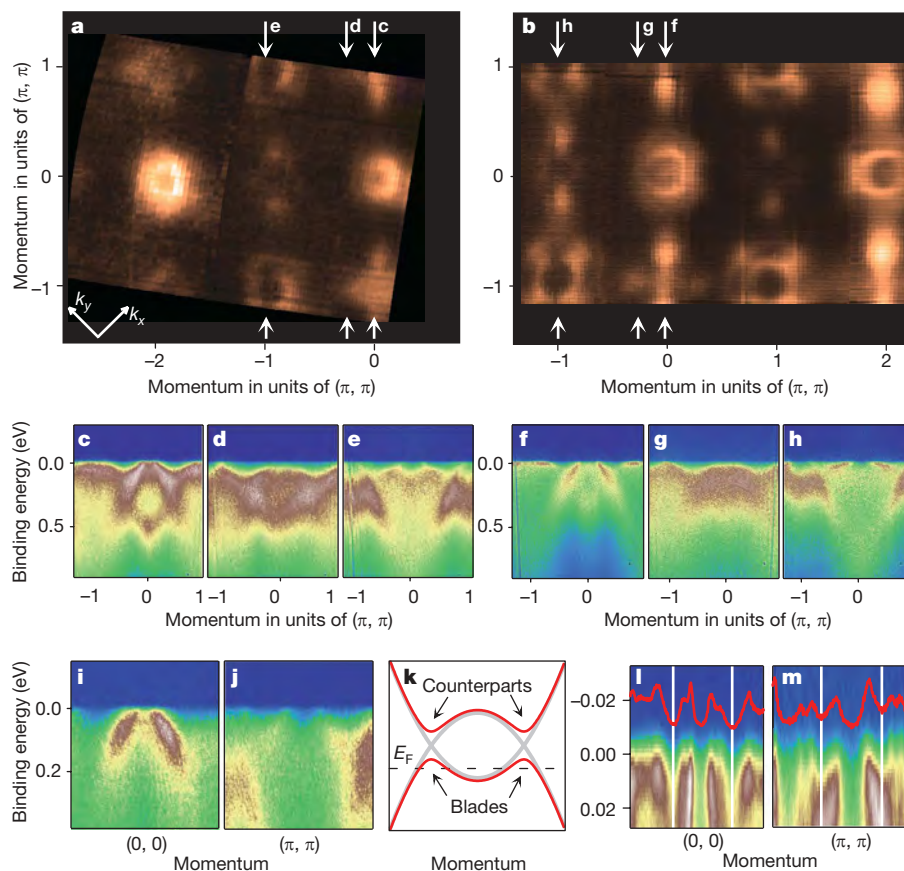


Figure 3 | (π, π) reconstruction of the electronic structure. **a, b**, Fermi surface maps for BFA and BKFA, respectively ($h\nu = 80$ eV). **c–h**, Several typical energy-momentum cuts, normalized to integrated intensity, showing similar band dispersions for BFA (**c, d, e**) and BKFA (**f, g, h**). The cut positions in momentum space are indicated by the arrows in **a** and **b**. **i, j**, Parallel cuts through the electronic structure of BFA, set apart by the

(π, π) vector. **k**, Simplest model showing the result of folding of single hole- and electron-like bands. **l, m**, Parallel cuts through Γ and X in the electronic structure of BKFA, set apart by the (π, π) vector. Red curves are the momentum distribution curves integrated within the 8-meV-wide energy window, showing the symmetric behaviour about the new Brillouin zone boundaries (white lines) due to (π, π) folding of the original structure.

for the observed hole-like structures, some of bands at X would have to be shifted by 250 meV (refs 5, 13–15), which is not likely to occur. In addition, the potential candidates to form the hole and electron pockets at X do not interact, for reasons of symmetry, and thus would not be able to account for the picture shown in Fig. 3k (Supplementary Information).

Our ARPES data manifest the presence of electronic order of a special kind. This order sets in at high temperatures and is dictated by the nesting instability predicted in the calculations. Most likely it is this electronic order that results in the structural transition at lower temperatures in the parent compound, as in the case of

$\text{La}[\text{O}_{1-x}\text{F}_x]\text{FeAs}$ the static magnetic order develops only after the structural transition and magnetic moments are much smaller than theoretically expected^{16,17}. On the other hand, presence of the (π, π) excitations (wavevector, $q = 1.15 \text{ \AA}^{-1}$) above the superconducting transition is implied by the inelastic neutron scattering data²², and their transformation into a resonance below the critical temperature (T_c) could indicate their crucial role in the mechanism of superconductivity. If these excitations correspond to a fluctuating stripe-like order, the propeller structure could result from a superposition of two pairs of blades originating from folding associated with (π, π) and $(\pi, -\pi)$ wavevectors.

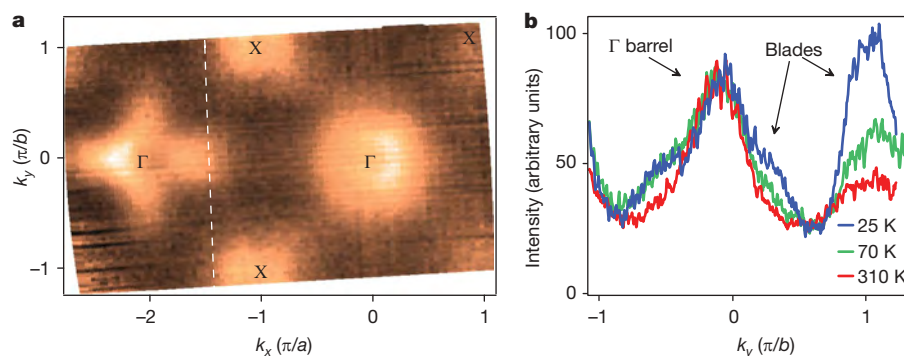


Figure 4 | Blade structure at X. **a**, Fermi surface map measured at $T = 300$ K ($h\nu = 50$ eV), demonstrating persistence of the blade-related intensity to high temperatures. **b**, Temperature dependence of the blade intensity

compared with that of the Γ barrel. The plot represents the intensity along the cut shown in **a** (dashed line) and was integrated in the 100-meV window centred on the Fermi level.

The observed order is not a conventional charge density wave, as the atoms respond only at considerably lower temperatures^{16,17}; but because the low-lying electronic structure is formed exclusively by the *d* electrons, it may be related to a more complex order parameter, as in the case of the hidden-order picture suggested for the cuprates⁴. Observation of the reconstruction below T_c implies the coexistence of the (π, π) order and the superconductivity, which is confirmed by opening of the superconducting gaps on the 'propeller' Fermi surface²³. The order weakens with doping, which may explain why it is no longer strong enough to cause the structural transition and/or static magnetism, but is sufficient to open smaller (π, π) gaps near *X*, thus providing a high density of states at the Fermi level that might be necessary for superconductivity²⁴.

Received 11 September; accepted 2 December 2008.

1. Wise, W. D. *et al.* Charge-density-wave origin of cuprate checkerboard visualized by scanning tunnelling microscopy. *Nature Phys.* **4**, 696–699 (2008).
2. Kawasaki, S. *et al.* Enhancing the superconducting transition temperature of $\text{CeRh}_{1-x}\text{Ir}_x\text{In}_5$ due to the strong-coupling effects of antiferromagnetic spin fluctuations: an ^{115}In nuclear quadrupole resonance study. *Phys. Rev. Lett.* **96**, 147001 (2006).
3. Morosan, E. *et al.* Superconductivity in Cu_xTiSe_2 . *Nature Phys.* **2**, 544–550 (2006).
4. Chakravarty, S. *et al.* Hidden order in the cuprates. *Phys. Rev. B* **63**, 094503 (2001).
5. Liu, C. *et al.* K-doping dependence of the Fermi surface of the iron-arsenic $\text{Ba}_{1-x}\text{K}_x\text{Fe}_2\text{As}_2$ superconductor using angle-resolved photoemission spectroscopy. *Phys. Rev. Lett.* **101**, 177005 (2008).
6. Ding, H. *et al.* Observation of Fermi-surface-dependent nodeless superconducting gaps in $\text{Ba}_{0.6}\text{K}_{0.4}\text{Fe}_2\text{As}_2$. *Europhys. Lett.* **83**, 47001 (2008).
7. Zhang, Y. *et al.* Correlation effects of exchange splitting and coexistence of spin-density-wave and superconductivity in single crystalline $\text{Sr}_{1-x}\text{K}_x\text{Fe}_2\text{As}_2$. Preprint at (<http://arxiv.org/abs/0808.2738v1>) (2008).
8. Yang, L. X. *et al.* Electronic structure and exotic exchange splitting in spin-density-wave states of BaFe_2As_2 . Preprint at (<http://arxiv.org/abs/0806.2627v2>) (2008).
9. Lu, D. H. *et al.* Electronic structure of the iron-based superconductor LaOFeP . *Nature* **455**, 81–84 (2008).
10. Chen, X. H., Wu, T., Wu, G., Liu, R. H. & Fang, D. F. Superconductivity at 43 K in $\text{SmFeAsO}_{1-x}\text{F}_x$. *Nature* **453**, 761–762 (2008).
11. Kamihara, Y., Watanabe, T., Hirano, M. & Hosono, H. Iron-based layered superconductor $\text{La}[\text{O}_{1-x}\text{F}_x]\text{FeAs}$ ($x = 0.05 - 0.12$) with $T_c = 26$ K. *J. Am. Chem. Soc.* **130**, 3296–3297 (2008).
12. Singh, D. J. Electronic structure and doping in BaFe_2As_2 and LiFeAs : density functional calculations. Preprint at (<http://arxiv.org/abs/0807.2643v1>) (2008).
13. Ma, F., Lu, Z.-Y. & Xiang, T. Electronic band structure of BaFe_2As_2 . Preprint at (<http://arxiv.org/abs/0806.3526v1>) (2008).
14. Nekrasov, I. A., Pchelkina, Z. V. & Sadovskii, M. V. Electronic structure of prototype AFe_2As_2 and ReOFeAs high-temperature superconductors: a comparison. *JETP Lett.* **88**, 155–160 (2008).
15. Mazin, I. I., Singh, D. J., Johannes, M. D. & Du, M. H. Unconventional sign-reversing superconductivity in $\text{LaFeAsO}_{1-x}\text{F}_x$. *Phys. Rev. Lett.* **101**, 057003 (2008).
16. de la Cruz, C. *et al.* Magnetic order close to superconductivity in the iron-based layered $\text{LaO}_{1-x}\text{F}_x\text{FeAs}$ systems. *Nature* **453**, 899–902 (2008).
17. Huang, Q. *et al.* Neutron-diffraction measurements of magnetic order and a structural transition in the parent BaFe_2As_2 compound of FeAs-based high-temperature superconductors. *Phys. Rev. Lett.* **101**, 257003 (2008).
18. Zhao, L. *et al.* Multiple nodeless superconducting gaps in $(\text{Ba}_{0.6}\text{K}_{0.4})\text{Fe}_2\text{As}_2$ superconductor from angle-resolved photoemission spectroscopy. *Chin. Phys. Lett.* **25**, 4402–4405 (2008).
19. Brouet, V. *et al.* Angle-resolved photoemission study of the evolution of band structure and charge density wave properties in RFe_3 ($\text{R} = \text{Y, La, Ce, Sm, Gd, Tb, and Dy}$). *Phys. Rev. B* **77**, 235104 (2008).
20. Borisenko, S. V. *et al.* Pseudogap and charge density waves in two dimensions. *Phys. Rev. Lett.* **100**, 196402 (2008).
21. Chen, H. *et al.* Coexistence of the spin-density-wave and superconductivity in the $\text{Ba}_{1-x}\text{K}_x\text{Fe}_2\text{As}_2$. *Europhys. Lett.* **85**, 17006 (2009).
22. Christianson, A. D. *et al.* Resonant spin excitation in the high temperature superconductor $\text{Ba}_{0.6}\text{K}_{0.4}\text{Fe}_2\text{As}_2$. Preprint at (<http://arxiv.org/abs/0807.3932v1>) (2008).
23. Evtushinsky, D. V. *et al.* Momentum dependence of the superconducting gap in $\text{Ba}_{1-x}\text{K}_x\text{Fe}_2\text{As}_2$. Preprint at (<http://arxiv.org/abs/0809.4455v1>) (2008).
24. Radtke, R. J. & Norman, M. R. Relation of extended Van Hove singularities to high temperature superconductivity within strong-coupling theory. *Phys. Rev. B* **50**, 9554–9560 (1994).

Supplementary Information is linked to the online version of the paper at www.nature.com/nature.

Acknowledgements The project was supported, in part, by the Deutsche Forschungsgemeinschaft under grant numbers KN393/4 and BO 1912/2-1. We are grateful to I. Eremin, O. K. Andersen, L. Boeri, I. Mazin and M. Rümeli for discussions. We thank R. Hübner for technical support.

Author Information Reprints and permissions information is available at www.nature.com/reprints. Correspondence and requests for materials should be addressed to S.V.B. (s.borisenko@ifw-dresden.de).

Total synthesis of a chlorosulpholipid cytotoxin associated with seafood poisoning

Christian Nilewski¹, Roger W. Geisser¹ & Erick M. Carreira¹

Each year, there are many cases of seafood poisoning in humans worldwide¹. Among the various toxins isolated that contribute to these poisonings^{2,3}, the chlorosulpholipids are particularly intriguing because of their structural and stereochemical complexity^{4–12}. The mechanism of biological activity remains unknown and, although chlorosulpholipids are associated with membranes in the organisms from which they are isolated, little is understood about their role within biological membranes. The lack of availability of the natural products has impaired more in-depth biochemical studies. So far, none of the chlorosulpholipids have been obtained from total synthesis, and efficient routes to their synthesis would be desirable for the preparation of material for pharmacological characterization and proper evaluation of the risk to human health. Despite the notable advances in the science of organic synthesis, reliable methods for stereoselective construction of polychlorinated acyclic substrates are lacking, although some preliminary investigations have appeared^{13–15}. Here we report the synthesis of a chlorosulpholipid cytotoxin, leading to confirmation of the proposed structure and the discovery of unanticipated reactivity of polychlorinated hydrocarbons. The concise synthetic approach should enable the preparation of material in sufficient quantities to facilitate biological studies.

Marine toxins have attracted the interest of investigators as a consequence of the associated health risk to human populations and the accompanying socioeconomic impact³. Seafood poisoning is partly associated with the consumption of shellfish contaminated with viral and bacterial microorganisms. Additionally, a significant percentage of cases is caused by toxins produced by microalgae, especially dinoflagellates, and transferred to humans by marine bivalve molluscs^{1,2}. The ensuing food poisoning can be severe and even life threatening¹. Marine toxins such as the tetrodotoxins, saxitoxins, ciguatera toxins and brevetoxins^{2,3} have been classified according to their chemical structures, and have been subjects of enormous interest to the chemical, biological and medical communities (see refs 16 and 17 and references within). A class of marine toxins that has received less attention is the chlorosulpholipids, which bear stereochemically complex, polychlorinated acyclic carbon chains and one or two *O*-sulphate esters. Chlorosulpholipids were first isolated in the late 1960s from the phytoflagellate *Ochromonas danica*⁴; the most abundant of these was later identified as compound **1** (Fig. 1)⁵.

Although a large number of algae have been examined^{7,8}, only a few chlorosulpholipids have been structurally characterized, such as malhamensilipin A (**2**) (Fig. 1)⁹. This compound is responsible for the major antimicrobial activity in the extract of the chrysophyte *Poteriochromonas malhamensis* and displays activity in kinase assays⁹. The first chlorosulpholipids (**3–5**) whose relative and absolute configuration have been assigned using *J*-based configuration analysis (see ref. 18 and references within) were isolated only a few years ago from organisms in the Adriatic Sea and probably originate from

harmful microalgae accumulated in mussels (Fig. 1)^{10–12}. They have also been screened for their antiproliferative activity and shown to inhibit cell growth^{10–12}.

Chlorosulpholipid **5** drew our attention as a target for synthetic studies because of its stereochemical complexity and, more significantly, the embedded issues of reactivity that these structures present. The result of initial synthetic efforts involving model systems led us to conclude that construction of such systems would have to take into account the unique behaviour and properties of a polychlorinated backbone with electron-withdrawing groups. As a relevant benchmark, sucralose, the key ingredient of Splenda, incorporates two 1° and one 2° chlorides on a disaccharide core and is sufficiently stable and safe to be widely used as an artificial sweetener. In a similar fashion, in preliminary investigations we observed that displacement reactions of activated alcohol derivatives to furnish the corresponding alkyl chlorides proved unworkable when the carbinol bears two methine substituents with electron-withdrawing groups, such as chlorides. Additionally, we noted that α - and β -chlorinated alde-

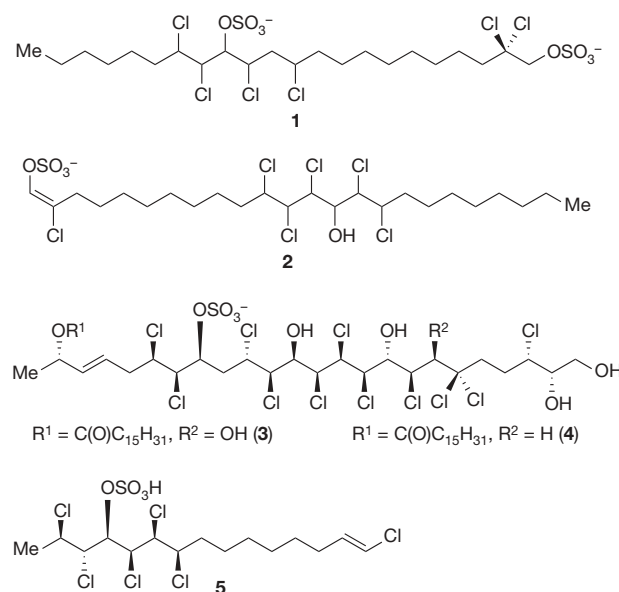


Figure 1 | Structurally characterized docosane, tetracosane and pentadecane chlorosulpholipids that originate from microalgae. Disulphate **1** and vinyl sulphate **2** have been isolated from *Ochromonas danica* and *Poteriochromonas malhamensis*, respectively, and their configurations have not been assigned. Lipids **3–5** have been extracted from digestive glands of contaminated shellfish *Mytilus galloprovincialis* along the Adriatic coast of Italy and are associated with seafood poisoning. They have been configurationally assigned by NMR spectroscopy using *J*-based configuration analysis. Me, H₃C.

¹Laboratorium für Organische Chemie, ETH Zürich, CH-8093 Zürich, Switzerland.

hydres are fleeting intermediates, which undergo enolization, hydration or elimination too rapidly. Thus, we sought to implement strategic approaches that would circumvent these limitations in crafting a synthesis route to chlorosulpholipid 5.

The synthesis began with stereospecific dichlorination of ethyl sorbate (6) using $(\text{H}_5\text{C}_2)_4\text{NCl}_3$ ¹⁹. This step was followed by reduction of the ester in 7 (diisobutylaluminium hydride (DIBAL), 72% yield) and protection of the hydroxyl function in the ensuing alcohol 8 to furnish 9. Dihydroxylation of 9 with *N*-methylmorpholine-*N*-oxide (NMO) and 5 mol% OsO_4 afforded a mixture of diastereomers in a selectivity of 5.6:1, with a 68% yield of the major diastereomer. At this point in the synthesis, we assumed that the configuration of the major diol corresponded to that expected from Kishi's empirical rule, which has proven to be highly reliable in predicting the relative configuration for the dihydroxylation reaction of allylic alcohols²⁰. Treatment of the major diol diastereomer with triflic anhydride and 1,4-diazabicyclo[2.2.2]octane (DABCO) and subsequent desilylation led to *cis*-epoxide 10 (74% yield over two steps). The structure of the epoxide was determined by careful analysis of the ^1H NMR spectrum of 10 and later by *J*-based configuration analysis of 15 and 16 (see Supplementary Information), which indicated an *anti*-relationship between C3 and C4.

Epoxide 10 was converted into 12 as a mixture of alkenes (*Z/E* isomeric ratio, 4.2:1) through the sequence of reactions including oxidation and Wittig olefination with phosphonium bromide 11. We were then able to examine a key transformation involving regioselective opening of the epoxide with chloride to furnish the targeted chlorohydrin. As discussed below, this had unexpected results.

After separation of *Z*-12 from the obtained *Z/E* mixture, we treated it with $(\text{H}_3\text{C})_3\text{SiCl}$, which led to a mixture of diastereomeric allylic chlorides *Z*-15 in 39% yield (56% based on recovered starting material),

minor amounts of *Z*-16 (4%) and a 10% yield of $\text{S}_{\text{N}}2'$ products. The major isolated chlorohydrin diastereomer (*Z*-15) was initially assumed to have the 4,5-*syn* relative configuration found in the natural product. Given the proximity to the end of the synthesis, we were confident that comparison to the natural product would prove decisive. Thus, allylic chloride 15 was transformed to chlorosulpholipid 17 in a few steps involving desilylation, oxidation, Takai–Utimoto olefination²¹ and a final *O*-sulphation (Fig. 2). Surprisingly, the spectral data for 17 did not match that reported for the natural product 5 in the characteristic region of 4–5 p.p.m. of the ^1H NMR spectrum.

This unexpected result compelled us to re-examine and re-evaluate the various steps in the sequence described above. Studies conducted in parallel involving the isolation and characterization of various diastereomers of crystalline polychlorinated diols with subsequent *J*-based configuration analysis (see ref. 18 and references within) enabled the spectroscopic determination of the relative configuration of polychlorinated structure 15. The key data were extracted using HETLOC (analysis of heteronuclear long-range couplings), HECAD (heteronuclear couplings from ASSCI-domain experiments with E.COSY-type cross peaks)²², refocused PS-HMBC (phase-sensitive heteronuclear multiple-bond correlation), as well as NOESY (nuclear Overhauser enhancement spectroscopy). The small $^3J(\text{H},\text{H})$ coupling constant of 2.3 Hz between H4 and H5, in combination with the corresponding pairwise large and small $^2J(\text{H},\text{C})$ and $^3J(\text{H},\text{C})$ coupling constants in allylic chloride *Z*-15, indicated that the stereogenic centres C4 and C5 possessed *anti*-configuration and not the anticipated *syn*-arrangement. Inevitably, this meant that opening of allylic epoxide *Z*-12 (*12* → *15*) had preferentially occurred with retention of configuration rather than the predicted inversion. Additional data (see Supplementary Information) allowed us to identify the minor diastereomeric product *Z*-16 as possessing the desired C4–C5

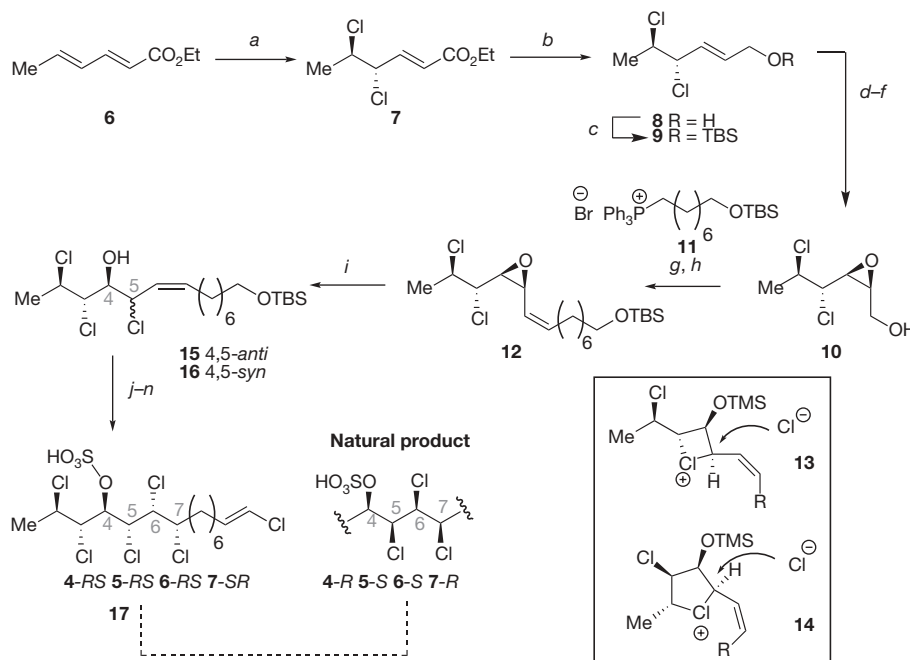


Figure 2 | Initial synthetic studies of chlorosulpholipid 5. Reagents and conditions: (a) $(\text{H}_5\text{C}_2)_4\text{NCl}_3$, CH_2Cl_2 , 0 °C, 45 min, 68%; (b) DIBAL (2.3 equiv.), $\text{H}_5\text{C}_2\text{H}_5\text{Cl}$, 0 °C, 10 min, 72%; (c) imidazole (1.5 equiv.), *t*-Bu $(\text{H}_3\text{C})_2\text{SiCl}$ (1.2 equiv.), CH_2Cl_2 , 0 °C to room temperature (RT, 20 °C), 30 min, 87%; (d) OsO_4 (5 mol%), NMO (1.1 equiv.), acetone/ H_2O , RT, 19 h, 68%; (e) DABCO (3.0 equiv.), $(\text{F}_3\text{CSO}_2)_2\text{O}$ (1.0 equiv.), –78 °C, 10 min, then diol, –78 °C to RT, 15 h, 75% (96% based on recovered starting material); (f) (+)-CSA (0.1 equiv.), $(\text{H}_3\text{C})\text{OH}$, RT, 3 h, 98%; (g) $(\text{COCl})_2$ (1.3 equiv.), $(\text{H}_3\text{C})_2\text{SO}$ (2.5 equiv.), CH_2Cl_2 , –78 °C, 10 min, then 10 (1.0 equiv.), –78 °C, 30 min, then $(\text{H}_5\text{C}_2)_3\text{N}$ (5.4 equiv.), –78 °C to RT, 1 h; (h) 11 (1.05 equiv.), *n*-BuLi (1.05 equiv.), THF, –78 °C, then RT, 10 min,

followed by aldehyde (1.0 equiv.) at –78 °C, 5 min, then RT, 30 min, 62% over two steps; (i) $(\text{H}_3\text{C})_3\text{SiCl}$ (2.0 equiv.), CH_2Cl_2 , $\text{H}_3\text{CCO}_2\text{C}_2\text{H}_5$, 11.5 h, 39% 15, 4% 16, 10% mixture of $\text{S}_{\text{N}}2'$ products (31% starting material recovered); (j) $(\text{H}_5\text{C}_2)_4\text{NCl}_3$ (3.0 equiv.), CH_2Cl_2 , 0 °C, 10 min, 51%; (k) (+)-CSA (10 mol%), H_3COH , 12 h, 80%; (l) DAIB (1.1 equiv.), TEMPO (0.1 equiv.), CH_2Cl_2 , RT, 16.5 h; (m) CrCl_2 (6.9 equiv.), CHCl_3 (2.6 equiv.), THF, 65 °C, 49% over two steps; (n) SO_3 -pyridine (6.0 equiv.), THF, 30 min, 27% (66% starting material recovered). Bu, H_2C_4 ; CSA, 10-camphorsulphonic acid; THF, tetrahydrofuran; DAIB, (diacetoxyiodo)benzene; TEMPO, 2,2,6,6-tetramethylpiperidine-1-oxyl; TBS, *t*- $\text{H}_2\text{C}_4(\text{H}_3\text{C})_2\text{Si}$; TMS, $(\text{H}_3\text{C})_3\text{Si}$.

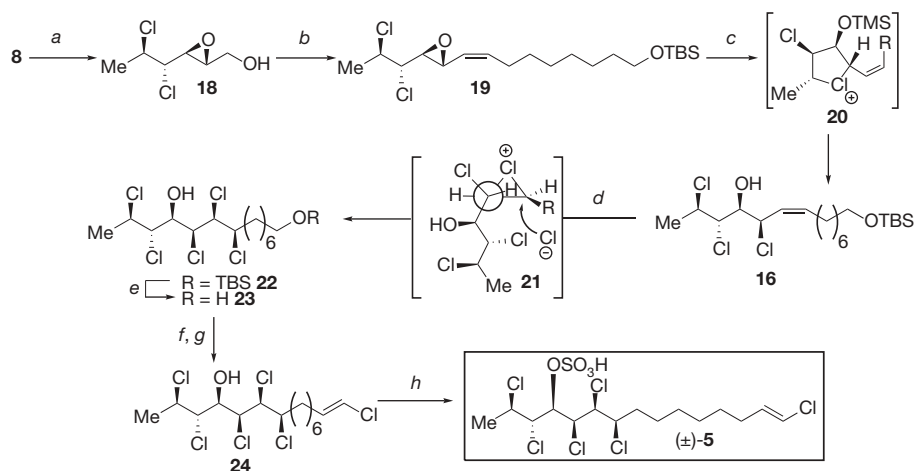


Figure 3 | Total synthesis of chlorosulpholipid cytotoxin 5. Reagents and conditions: (a) *m*-CPBA, CH₂Cl₂, 0 °C to RT, d.r. = 1:1, 95% overall; (b) 4 Å molecular sieves, NMO (1.1 equiv.), TPAP (5 mol%), CH₂Cl₂, 6 h; **11** (1.6 equiv.), *n*-BuLi (1.6 equiv.), THF, -78 °C, RT, 10 min; then addition of the aldehyde solution to the phosphonium ylide at -78 °C, 1 h, then RT, 1.5 h, 34% (56% based on recovered starting material); (c) (H₃C)₃SiCl (2.0 equiv.), CH₂Cl₂, H₃CCO₂C₂H₅, 9 h, 43% (73% based on recovered

starting material); (d) (H₅C₂)₄NCl₃ (3.0 equiv.), CH₂Cl₂, -78 °C, 2 h, d.r. = 10:1, 93% overall; (e) (+)-CSA (10 mol%), H₃COH, 12 h, 98%; (f) DAIB (1.3 equiv.), TEMPO (0.2 equiv.), CH₂Cl₂, RT, 16.5 h; (g) CrCl₂ (6.8 equiv.), CHCl₃ (2.5 equiv.), THF, 65 °C, 47% over two steps; (h) SO₃-pyridine (3.0 equiv.), THF, 20 min, 99%. TPAP, tetra-*n*-propylammonium perruthenate(VII).

syn-configuration. We hypothesize that anchimeric participation of one of the chlorides at C2 and C3 over the course of the ring-opening reaction is key to understanding the unexpected stereochemical outcome.

A small number of mechanistic studies from the 1960s and 1970s suggest the intervention of four- and five-membered ring chloronium ions as intermediates in solvolytic displacement reactions in F₃CCO₂H, H₃CCO₂H or HCO₂H (ref. 23; for anchimeric participation of chloride in epoxide opening processes, see ref. 24). It was shown that solvolysis of *erythro* and *threo* 5-chloro-2-hexyl tosylates occurs with up to 92% retention, depending on the solvent²³. This suggested anchimeric participation through formation of a chloronium intermediate in these simple systems and was supported by kinetic studies²³. On the basis of this data, it may seem that the five-membered chloronium ion **14** should be favoured over the four-membered chloronium ion **13**. However, in the absence of additional data for the more complicated systems discussed here, we are not able to distinguish unambiguously between the two alternatives (Fig. 2).

The finding that ring opening of the allylic epoxide can suffer interference from neighbouring chlorides necessitated alteration of the strategy. Because the problem is associated with one of the epoxide termini, the solution required investigating the ring-opening reaction of the corresponding *trans*-epoxide. However, it is important to note that for this solution to be workable, it is a necessary requirement that opening of the *trans*-epoxide diastereomer proceeds with retention of configuration, following the mechanistic pathway observed for the *cis*-stereoisomer.

The required allylic *trans*-epoxide **18** was prepared as shown in Fig. 3. Allylic alcohol **8** was treated with *m*-chloroperbenzoic acid (*m*-CPBA) to afford a diastereomeric mixture of epoxy alcohols (diastereomeric ratio (d.r.) = 1:1), which could be separated by chromatography on silica gel. The two regioisomeric diols obtained by treatment of **18** with TiCl(O*i*-C₃H₇)₃ were crystalline, and therefore allowed the epoxide configuration to be established unambiguously using X-ray structural analysis (Fig. 4). Ley oxidation of alcohol **18** and *in situ* Wittig olefination²⁵ gave alkene **19**. Notably, the selectivity (*Z/E*, 7:1) was considerably improved over that observed for **12**. Treatment of **19** with (H₃C)₃SiCl gave chlorohydrin **16** in 73% yield (based on recovered starting material). The opening was demonstrated to proceed exclusively with retention of configuration (judged using ¹H NMR), in analogy to that observed above for *cis*-epoxide **12**.

Dichlorination of alkene **16** with (H₅C₂)₄NCl₃ at -78 °C gave pentachloride **22** together with a minor diastereomer (d.r. = 10:1) in 93% yield. As investigated using *J*-based configuration analysis, the diastereoselectivity is in agreement with model **21** (ref. 26). Deprotection of the silyl ether with acid, selective oxidation of the primary alcohol with TEMPO and H₅C₆I(O₂CCH₃)₂ and subsequent Takai–Utimoto olefination²¹ produced alcohol **24**. Treatment of **24** with py-SO₃-pyridine afforded **5** in 99% yield. The spectroscopic data for **5** are in agreement with that reported for the natural product in both *d*₆-acetone as well as *d*₄-methanol (see Supplementary Information)¹⁰. To further confirm the identity of the synthetic and natural cytotoxin **5**, we independently analysed the homonuclear (H,H) and heteronuclear (H,C) coupling constants of **5**, which led to the assignment of the same relative configuration as that originally proposed in ref. 10.

In conclusion, we have presented the diastereoselective synthesis of a member of the chlorosulpholipid cytotoxin family. Our studies led to the confirmation of the proposed relative configuration and, more broadly, contribute to a database to facilitate *J*-based configuration analysis of polychlorinated structures, which may assist in the

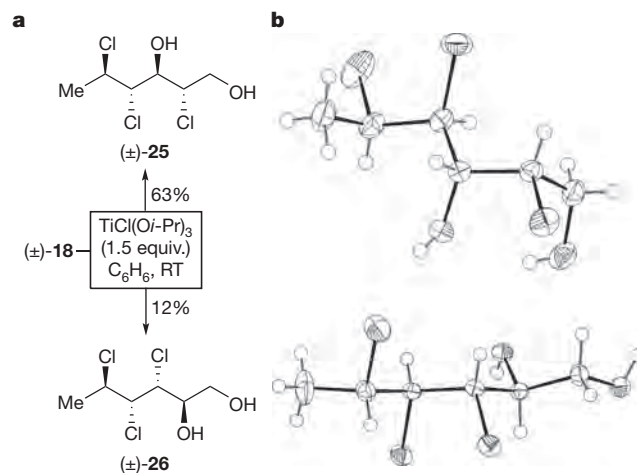


Figure 4 | Determination of the relative configuration of epoxyalcohol 18. a, Treatment of **18** with TiCl(O*i*-C₃H₇)₃ provided a mixture of crystalline diols **25** and **26**. b, The X-ray structures allowed the determination of the relative configuration of diols **25** and **26**, which in turn permitted the configurational assignment of epoxyalcohol **18**.

stereochemical assignment of numerous other chlorosulfolipids such as **1** and **2**. A key observation in the synthetic studies is the retentive epoxide-opening reaction that most likely involves an intermediate cyclic chloronium ion. In this respect, the proposed anchimeric participation of chlorides in these complex systems will need to be given careful consideration in any future efforts towards synthesizing the chlorosulfolipids. Additionally, the concise synthesis can provide enough material for biological and pharmacological studies and, thus, the evaluation of the role of chlorosulfolipid cytotoxins in marine ecosystems and their effects on human health.

METHODS SUMMARY

All reactions were carried out under argon under anhydrous conditions, unless otherwise stated. Commercially available reagents were purchased and used without further purification unless otherwise noted. Reactions were monitored by thin-layer chromatography and products identified by NMR and infrared spectroscopy as well as mass spectrometry. For experimental details and characterization of all new compounds (^1H NMR, ^{13}C NMR, infrared, mass spectrometry, melting points), the determination of the relative configuration of epoxyalcohol **18** including the crystallographic data of diols **25** and **26**, the data for *J*-based configuration analysis of compounds **15**, **16**, **22** and synthetic (\pm)-**5** and the ^1H NMR spectra of the key compounds **8**, **10–12**, **15–19**, **22**, **32** and synthetic (\pm)-**5**, see the Supplementary Information.

Full Methods and any associated references are available in the online version of the paper at www.nature.com/nature.

Received 7 October; accepted 18 December 2008.

1. Ahmed, F. E. Naturally occurring seafood toxins. *J. Toxicol. Toxin Rev.* **10**, 263–287 (1991).
2. Ciminiello, P. & Fattorusso, E. Shellfish toxins – Chemical studies on Northern Adriatic mussels. *Eur. J. Org. Chem.* **2004**, 2533–2551 (2004).
3. Yasumoto, T. & Murata, M. Marine toxins. *Chem. Rev.* **93**, 1897–1909 (1993).
4. Elovson, J. & Vagelos, P. R. A new class of lipids: Chlorosulfolipids. *Proc. Natl Acad. Sci. USA* **62**, 957–963 (1969).
5. Elovson, J. & Vagelos, P. R. Structure of the major species of chlorosulfolipid from *Ochromonas danica*. 2,2,11,13,15,16-hexachloro-N-docosane 1,14-disulfate. *Biochemistry* **9**, 3110–3126 (1970).
6. Haines, T. H. Halogen- and sulfur-containing lipids of *Ochromonas*. *Annu. Rev. Microbiol.* **27**, 403–411 (1973).
7. Mercer, E. I. & Davies, C. L. Chlorosulfolipids of *Tribonema aequale*. *Phytochemistry* **13**, 1607–1610 (1974).
8. Mercer, E. I. & Davies, C. L. Chlorosulfolipids in algae. *Phytochemistry* **14**, 1545–1548 (1975).
9. Chen, J. L., Proteau, P. J., Roberts, M. A. & Gerwick, W. H. Structure of malhamensilipin A, an inhibitor of protein tyrosine kinase, from the cultured chrysophyte *Poterioochromonas malhamensis*. *J. Nat. Prod.* **57**, 524–527 (1994).
10. Ciminiello, P. *et al.* Structural elucidation of a new cytotoxin isolated from mussels of the Adriatic Sea. *J. Org. Chem.* **66**, 578–582 (2001).
11. Ciminiello, P. *et al.* Structure and stereochemistry of a new cytotoxic polychlorinated sulfolipid from Adriatic shellfish. *J. Am. Chem. Soc.* **124**, 13114–13120 (2002).
12. Ciminiello, P. *et al.* A new cytotoxic polychlorinated sulfolipid from contaminated Adriatic mussels. *Tetrahedron* **60**, 7093–7098 (2004).
13. Shibuya, G. M., Kanady, J. S. & Vanderwal, C. D. Stereoselective dichlorination of allylic alcohol derivatives to access key stereochemical arrays of the chlorosulfolipids. *J. Am. Chem. Soc.* **130**, 12514–12518 (2008).
14. Yoshimitsu, T., Fukumoto, N. & Tanaka, T. Enantiocontrolled synthesis of polychlorinated hydrocarbon motifs: A nucleophilic multiple chlorination process revisited. *J. Org. Chem.* **74**, 696–702 (2009).
15. Hunter, L., O'Hagan, D. & Slawin, A. M. Z. Enantioselective synthesis of an all-syn four vicinal fluorine motif. *J. Am. Chem. Soc.* **128**, 16422–16423 (2006).
16. Nakata, T. Total synthesis of marine polycyclic ethers. *Chem. Rev.* **105**, 4314–4347 (2005).
17. Kang, S. H., Kang, S. Y., Lee, H.-S. & Buglass, A. J. Total synthesis of natural tert-alkylamino hydroxy carboxylic acids. *Chem. Rev.* **105**, 4537–4558 (2005).
18. Matsumori, N., Kaneno, D., Murata, M., Nakamura, H. & Tachibana, K. Stereochemical determination of acyclic structures based on carbon-proton spin-coupling constants. A method of configuration analysis for natural products. *J. Org. Chem.* **64**, 866–876 (1999).
19. Schlama, T., Gabriel, K., Gouverneur, V. & Mioskowski, C. Tetraethylammonium trichloride: A versatile reagent for chlorinations and oxidations. *Angew. Chem. Int. Edn Engl.* **36**, 2342–2344 (1997).
20. Cha, J. K., Christ, W. J. & Kishi, Y. On stereochemistry of osmium tetroxide oxidation of allylic alcohol systems – Empirical rule. *Tetrahedron* **40**, 2247–2255 (1984).
21. Takai, K., Nitta, K. & Utimoto, K. Simple and selective method for $\text{RCHO} \rightarrow (E)\text{-RCH=CHX}$ conversion by means of a $\text{CHX}_3\text{-CrCl}_2$ system. *J. Am. Chem. Soc.* **108**, 7408–7410 (1986).
22. Kozminski, W. & Nanz, D. HECAD: HMQC- and HSQC-based 2D NMR experiments for accurate and sensitive determination of heteronuclear coupling constants from E-COSY-type cross peaks. *J. Magn. Reson.* **124**, 383–392 (1997).
23. Petersen, P. E. *et al.* Solvents of low nucleophilicity. IX. Inductive and participation effects in carbonium ion reactions in acetic, formic, and trifluoroacetic acid. *J. Am. Chem. Soc.* **89**, 5902–5911 (1967).
24. Petersen, P. E., Indelicato, J. M. & Bonazza, B. R. Halogen participation in the protonation of 5-halo-epoxides with trifluoroacetic acid. *Tetrahedr. Lett.* **12**, 13–16 (1971).
25. MacCoss, R. N., Balskus, E. P. & Ley, S. V. A sequential tetra-*n*-propylammonium perruthenate (TPAP)-Wittig oxidation olefination protocol. *Tetrahedr. Lett.* **44**, 7779–7781 (2003).
26. Paddon-Row, M. N., Rondon, N. G. & Houk, K. N. Staggered models for asymmetric induction: Attack trajectories and conformations of allylic bonds from ab initio transition structures of addition reactions. *J. Am. Chem. Soc.* **104**, 7162–7166 (1982).

Supplementary Information is linked to the online version of the paper at www.nature.com/nature.

Acknowledgements We thank M.-O. Ebert for acquisition and discussion of the NMR data needed for *J*-based configuration analysis as well as W. B. Schweizer for the X-ray crystallographic analysis. C.N. thanks the Stiftung Stipendien-Fonds des Verbandes der Chemischen Industrie for a Kekulé-Fellowship. This research was supported by the Swiss National Science Foundation and ETH Zürich. We are grateful for support for our program from F. Hoffmann-La Roche, Eli Lilly and Boehringer Ingelheim.

Author Information Supplementary crystallographic data for this paper has been deposited at the Cambridge Crystallographic Data Centre under deposition numbers CCDC 711103 and CCDC 711104. These data can be obtained free of charge from www.ccdc.cam.ac.uk/data_request/cif. Reprints and permissions information is available at www.nature.com/reprints. Correspondence and requests for materials should be addressed to E.M.C. (carreira@org.chem.ethz.ch).

METHODS

General methods. All reactions were carried out under an argon atmosphere in flame-dried glassware, unless stated otherwise. THF, $(\text{H}_5\text{C}_2)_2\text{O}$, H_3CCN , toluene and CH_2Cl_2 were dried by passage over activated alumina under argon atmosphere (H_2O content <30 p.p.m., Karl Fischer titration)²⁷. $\text{N}(\text{C}_2\text{H}_5)_3$ was distilled under nitrogen from KOH. H_3COH was used from Fluka (*pro analysi* grade) without further purification. All other chemicals were purchased from Acros, Aldrich, Fluka, Merck or Lancaster and used as such unless noted otherwise. Reactions were monitored by thin-layer chromatography using Merck silica gel 60 F254 TLC glass plates and visualized with ceric ammonium molybdate or potassium permanganate staining solution. Chromatographic purification was performed as flash chromatography on Brunschwig silica 32-63, 60 Å, using a forced flow of eluant at 0.3 bar. Concentration under reduced pressure was performed by rotary evaporation at 40 °C at the appropriate pressure. Yields refer to chromatographically purified and spectroscopically pure compounds, unless noted otherwise.

Spectroscopic and spectrometric methods. NMR spectra were recorded on a Varian Mercury 300 spectrometer (operating at 300 MHz for ^1H and 75 MHz for ^{13}C acquisitions), Bruker DRX400 and AV400 spectrometers (operating at 400 MHz for ^1H , 101 MHz for ^{13}C and 162 MHz for ^{31}P acquisitions) and a Bruker Avance II 600 spectrometer (operating at 600 MHz for ^1H and 151 MHz for ^{13}C acquisitions).

Chemical shifts δ are reported in parts per million with tetramethylsilane (0.00 p.p.m. (^1H NMR), 0.00 p.p.m. (^{13}C NMR)) or the solvent resonance as the internal standard (*d*1-chloroform: 7.26 (^1H NMR), 77.2 (^{13}C NMR); *d*4-methanol: 3.34 (^1H NMR), 49.0 (^{13}C NMR); *d*8-THF: 1.73, 3.58 (^1H NMR), 25.5, 67.7 (^{13}C NMR); *d*6-acetone: 2.05 (^1H NMR), 29.8 and 206.3 (^{13}C NMR)). ^{31}P NMR shifts are reported in parts per million relative to 85% H_3PO_4 in water. IR spectra were obtained on a Perkin Elmer Spectrum RX-I FT-IR as thin film or on a Perkin Elmer Spectrum One FT IR Spectrometer (ATR). Mass spectra were obtained on a Waters/Micromass AutoSpec Ultima (EI), a Waters/Micromass Q-TOF Ultima (ESI), a Varian IonSpec FT-ICR (ESI) or a Bruker maXis (ESI) spectrometer.

Melting points. Melting points were measured on a Büchi B-540 melting point apparatus using open glass capillaries and are uncorrected.

27. Pangborn, A. B., Giardello, M. A., Grubbs, R. H., Rosen, R. K. & Timmers, F. J. Safe and convenient procedure for solvent purification. *Organometallics* **15**, 1518–1520 (1996).

Southern Ocean deep-water carbon export enhanced by natural iron fertilization

Raymond T. Pollard¹, Ian Salter^{1,2}, Richard J. Sanders¹, Mike I. Lucas³, C. Mark Moore¹, Rachel A. Mills¹, Peter J. Statham¹, John T. Allen¹, Alex R. Baker⁴, Dorothee C. E. Bakker⁴, Matthew A. Charette⁵, Sophie Fielding⁶, Gary R. Fones⁷, Megan French⁴, Anna E. Hickman⁸, Ross J. Holland¹, J. Alan Hughes¹, Timothy D. Jickells⁴, Richard S. Lampitt¹, Paul J. Morris¹, Florence H. Nédélec⁹, Maria Nielsdóttir¹, Hélène Planquette¹⁰, Ekaterina E. Popova¹, Alex J. Poulton¹, Jane F. Read¹, Sophie Seeyave¹, Tania Smith¹, Mark Stinchcombe¹, Sarah Taylor¹, Sandy Thomalla¹¹, Hugh J. Venables⁶, Robert Williamson¹¹ & Mike V. Zubkov¹

The addition of iron to high-nutrient, low-chlorophyll regions induces phytoplankton blooms that take up carbon^{1–3}. Carbon export from the surface layer and, in particular, the ability of the ocean and sediments to sequester carbon for many years remains, however, poorly quantified³. Here we report data from the CROZEX experiment⁴ in the Southern Ocean, which was conducted to test the hypothesis that the observed north–south gradient in phytoplankton concentrations in the vicinity of the Crozet Islands is induced by natural iron fertilization that results in enhanced organic carbon flux to the deep ocean. We report annual particulate carbon fluxes out of the surface layer, at three kilometres below the ocean surface and to the ocean floor. We find that carbon fluxes from a highly productive, naturally iron-fertilized region of the sub-Antarctic Southern Ocean are two to three times larger than the carbon fluxes from an adjacent high-nutrient, low-chlorophyll area not fertilized by iron. Our findings support the hypothesis that increased iron supply to the glacial sub-Antarctic may have directly enhanced carbon export to the deep ocean⁵. The CROZEX sequestration efficiency⁶ (the amount of carbon sequestered below the depth of winter mixing for a given iron supply) of 8,600 mol mol^{−1} was 18 times greater than that of a phytoplankton bloom induced artificially by adding iron⁷, but 77 times smaller than that of another bloom⁸ initiated, like CROZEX, by a natural supply of iron. Large losses of purposefully added iron can explain the lower efficiency of the induced bloom⁶. The discrepancy between the blooms naturally supplied with iron may result in part from an underestimate of horizontal iron supply.

In many open ocean regions there is low phytoplankton biomass despite there being a large macronutrient reservoir³. The Southern Ocean is the most biogeochemically significant of these high-nutrient, low-chlorophyll (HNLC) regions, owing to its large spatial extent and influence on global nutrient cycles⁹. Mesoscale iron enrichment experiments have demonstrated that iron addition modifies phytoplankton processes, enhancing diatom biomass^{10,11} and increasing atmospheric carbon dioxide drawdown¹. Observing bloom decline and quantifying the sequestration of photosynthetically fixed carbon resulting from iron addition has been achieved more rarely^{7,12}.

An alternative way to determine the role of iron in regulating the biological carbon pump in the Southern Ocean is to study regions of high phytoplankton biomass stimulated by natural iron inputs from shallow topography or islands. Recently KEOPS⁸ (the Kerguelen ocean and plateau compared study) demonstrated enhanced carbon export to below 200 m in the naturally iron-fertilized bloom over the Kerguelen plateau. The Crozet Islands and Plateau (hereafter Crozet), located in the Polar Frontal Zone at the northern boundary of the Southern Ocean, is another region characterized by a marked annual phytoplankton bloom (Fig. 1). The sub-Antarctic Front of the generally eastward-flowing Antarctic Circumpolar Current turns north past Crozet (Fig. 1) and then east again when it encounters the Agulhas Return Current¹³. Thus, south of Crozet HNLC conditions prevail⁴, whereas north of Crozet an annual bloom covering 120,000 km² (the size of Ireland and 50 times larger than the SOFeX (Southern Ocean iron experiment) bloom^{2,11}) results from iron supplied from Crozet¹⁴. Iron enrichment over the light-limited winter period leads in spring to a strong north–south gradient in phytoplankton biomass (Fig. 1), productivity, community structure¹⁵ and uptake of dissolved inorganic carbon¹⁶ and nitrate¹⁷, once stratification and increased solar irradiance reduce the mixed layer below the critical depth¹⁸. Weak circulation in the bloom region is such that water has a residence time there of ~60 days⁴.

During austral summer 2004–2005, we conducted an extensive oceanographic research programme (CROZEX) around Crozet⁴ to test the hypotheses that the north–south gradient in chlorophyll *a* is, first, induced by natural iron fertilization and, second, causes enhanced organic carbon flux into the deep ocean. To capture this flux, sediment traps were moored north (M10), east (M5) and south (M2, M6) of Crozet (Fig. 1). Short sediment cores were collected at M5, M6 and M10. Weak eastward flow past M2 and M6 and the absence of upstream blooms¹³ characterized these HNLC ‘control’ (−Fe) sites south of the bloom. M10 was under the bloom (+Fe) and M5 was under the eastward extension of the bloom. East–southeast flow along the sub-Antarctic Front towards M5, the large spatial extent of the bloom combined with weak circulation within it and the predominance of *Eucampia antarctica* (a diatom that responded strongly to iron enrichment¹⁹) in the 3,000-m M10 and M5 traps (but

¹National Oceanography Centre Southampton, Natural Environment Research Council and University of Southampton, European Way, Southampton SO14 3ZH, UK. ²Observatoire Océanologique, Avenue de Fontaulé, BP44, F-66651 Banyuls-sur-Mer, France. ³Department of Zoology, University of Cape Town, Rondebosch 7701, South Africa. ⁴School of Environmental Sciences, University of East Anglia, Norwich NR4 7TJ, UK. ⁵Department of Marine Chemistry and Geochemistry MS25, Woods Hole Oceanographic Institution, Woods Hole, Massachusetts 02543, USA. ⁶British Antarctic Survey, High Cross, Madingley Road, Cambridge CB3 0ET, UK. ⁷School of Earth and Environmental Sciences, University of Portsmouth, Burnaby Building, Burnaby Road, Portsmouth PO1 3QL, UK. ⁸Department of Earth and Ocean Sciences, University of Liverpool, L69 3GP, UK. ⁹Laboratoire Environnement et Ressources de Normandie, IFREMER, Avenue du Général de Gaulle - B.P.32, 14 520 Port-en-Bessin, France. ¹⁰Institute of Marine and Coastal Sciences, Rutgers University, New Brunswick, New Jersey 08901, USA. ¹¹Department of Oceanography, University of Cape Town, Rondebosch 7701, South Africa.

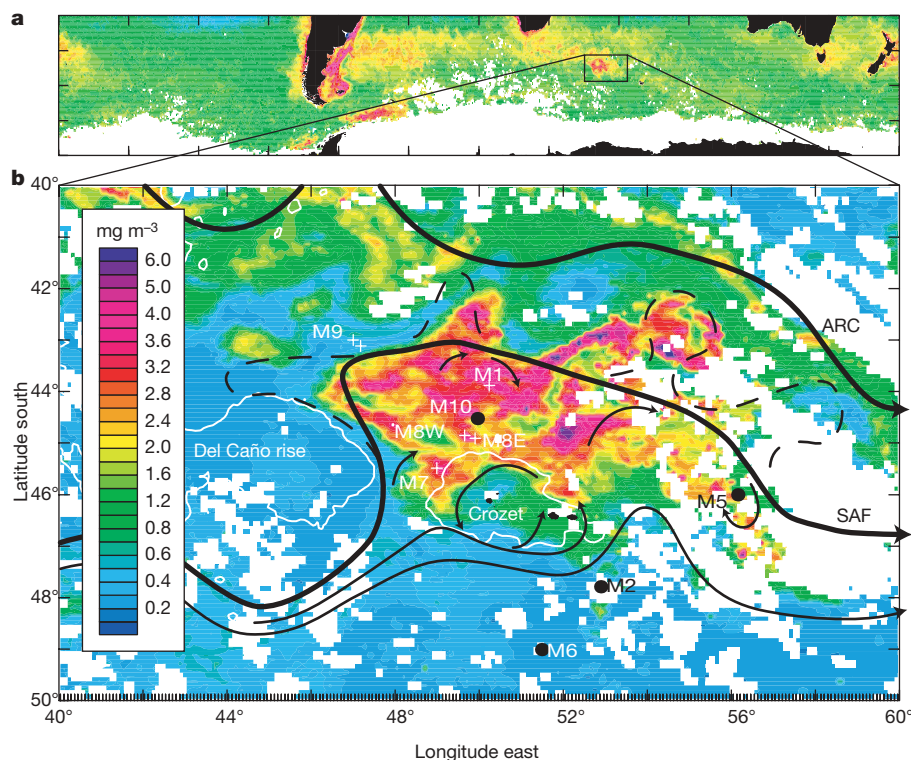


Figure 1 | Chlorophyll *a* images of Crozet region. **a**, Chlorophyll *a* in October for the whole of the Southern Ocean, showing location of Crozet. Colour indicates concentration as shown in **b**. **b**, Merged SeaWiFS/MODIS (sea-viewing, wide-field-of-view sensor/moderate-resolution imaging spectroradiometer) chlorophyll *a* image for the eight-day peak bloom period 23–30 October 2004. Solid and dashed lines show mean and eddy

circulations, respectively¹³, with the sub-Antarctic Front (SAF, the northern boundary of the Antarctic Circumpolar Current) and the Agulhas Return Current (ARC) shown bold. Main sampling (+) and coring (•) sites are labelled. Thin white lines are the 2,000-m depth contour, with the main Crozet Islands (Île de la Possession, Île de l'Est) seen at 46.5° S, 52° E.

its absence from the M2 and M6 traps) confirm that the M10 and M5 traps received export flux from the iron-enhanced bloom. KEOPS and CROZEX are compared in Supplementary Table 1.

It has been shown¹⁴ that the dissolved iron (DFe; <0.2- μ m fraction) originates from Crozet, with maximum estimated input to the bloom of 550 nmol m⁻² d⁻¹ comprising 390, 60 and 100 nmol m⁻² d⁻¹ for the horizontal, vertical and atmospheric fluxes, respectively. As the bloom occurs in deep (>2,000-m) water away from Crozet, horizontal flux dominates DFe supply, as expected. A range of 180–390 nmol m⁻² d⁻¹ (0.018–0.039 mmol m⁻² integrated over a winter period of 100 days) is estimated (Supplementary Information) for the enhancement in iron supply to the +Fe region relative to that to the -Fe region. These are probably underestimates, as additional sources of iron such as the dissolution of small lithogenic particles²⁰ will increase iron supply.

Significant differences were observed in the magnitude, timing, duration and community structure of plankton blooms between the +Fe and -Fe regions. In the -Fe region, chlorophyll *a* peaked at 0.6 mg m⁻³ in early December (Fig. 2a), when HNLC conditions (nitrate concentration, ~24 μ mol kg⁻¹; silicate concentration, ~16 μ mol kg⁻¹) prevailed⁴. In the +Fe region, chlorophyll *a* peaked at over 3 mg m⁻³ in October (locally >6 mg m⁻³; Fig. 1) and was elevated (>1 mg m⁻³) for 72 days¹⁸ (Supplementary Table 2). Although fertilized by macronutrients from the -Fe region and by winter upwelling in the Polar Frontal Zone, silicate was already becoming limited (<2 μ mol kg⁻¹; nitrate, 16 μ mol kg⁻¹) when first sampled in November⁴, indicating a ratio of silicate drawdown to nitrate drawdown of about 2:1, consistent with lower iron stress than in the -Fe region¹⁹. Low ambient silicate concentrations, common over much of the sub-Antarctic Southern Ocean¹¹, predisposed a shift in phytoplankton community structure from diatoms to *Phaeocystis*¹⁵. The bloom peaked <10 days after exceeding

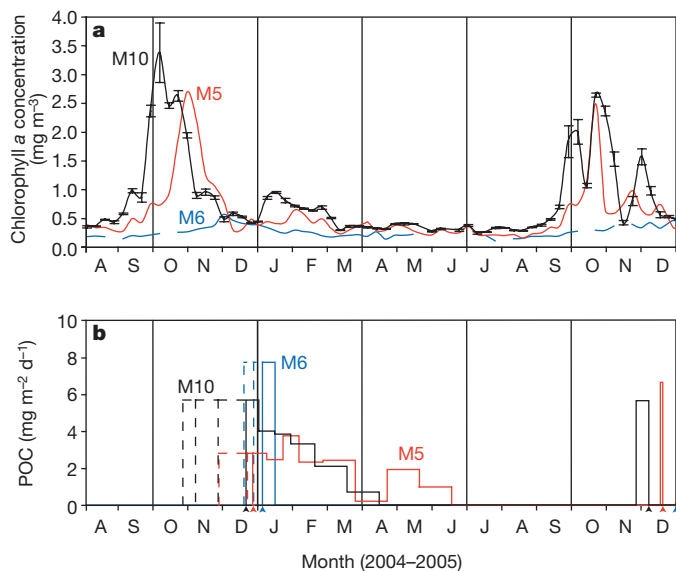


Figure 2 | Time series of chlorophyll *a* and particulate organic carbon (POC). **a**, Chlorophyll *a*, obtained for each eight-day merged SeaWiFS/MODIS image by averaging all non-cloud pixels in a circle of radius 45 km about each mooring site. Error bars (for M10 only) give the standard deviation of the mean of these pixels. **b**, POC (solid line) obtained from deep sediment traps at each site (Methods). Arrowheads mark mooring deployment and recovery events. The traps could not be deployed until after export from the 2004–2005 bloom had begun, so the export rate into the first cup has been extrapolated (Supplementary Information) using a range of sinking rates after the peak of chlorophyll *a* to give minimum, mean and maximum (dashed) seasonal integrals of total export.

1 mg m⁻³ but remained >1 mg m⁻³ for another month, potentially sustained by *Phaeocystis* using regenerated iron and nitrogen²¹, as +Fe nitrate values remained ~16 µmol kg⁻¹ throughout December and January.

An important difference from purposeful iron enrichment experiments is that iron concentrations accumulate in the +Fe region during winter. Removal of light limitation in spring¹⁸, not iron addition, determines bloom onset. Consequently, net growth rates in the bloom phase (0.05 d⁻¹; Fig. 2a) are probably light limited and 2–18 times lower than those for artificial experiments (0.10–0.90 d⁻¹)³. Weak circulation in the +Fe region ensures that neither macronutrients nor iron can be resupplied to the extensive bloom area during the bloom development period. A possible exception was close to the islands, where a small-area bloom in January¹⁸ may have been fuelled by resupply of iron and silicate.

The flux of organic carbon from the surface ocean to the ocean interior has been calculated using ²³⁴Th at 100 m (ref. 22; Table 1). Following the chlorophyll peak (Fig. 2a) in each region (+Fe, -Fe), mean daily rates of carbon export were similar (16 mmol m⁻² d⁻¹; Supplementary Table 2). Thus, any difference in seasonally integrated export between the two regions depends on the duration of the export events. We estimated export duration by closing the silicate budget, dividing the near-surface silicate drawdown (corrected for biogenic silica production) by the opal export rate estimated from ²³⁴Th deficits and ²³⁴Th/opal ratios. This approach yielded export durations (61 and 17 days in the +Fe and -Fe regions, respectively) consistent with the observed satellite-derived chlorophyll time series (Fig. 2, Supplementary Table 2). The resulting seasonally integrated carbon export in the +Fe region (960 mmol m⁻²) was three times greater (Table 1) than export in the -Fe region (290 mmol m⁻²), consistent with the independently diagnosed increase in new production¹⁷.

Fluxes of particulate organic carbon (POC) to 3,000 m differed remarkably in duration and composition. In the +Fe region (Fig. 2b), POC flux peaked at or before trap deployment in late December, decreasing to near zero over several months. In the -Fe region, POC export was confined to an unusually short but substantial event (Fig. 2b) observed at both M2 and M6 and at two depths (for sinking rates and export flux ranges, see Supplementary Information). Substantial silicate drawdown between November and January (Supplementary Table 2) reduced surface silicate to <2.0 µmol kg⁻¹ at M2 and M6, suggesting that iron limitation in the -Fe region resulted in heavily silicified diatoms²³ that sank rapidly in January. Despite this event, the longer duration of POC flux over the 2004–2005 summer season in the +Fe region resulted in three times greater seasonal export in the +Fe region than the -Fe region (Table 1). POC flux at 3,000 m was 3% of that at 100 m in the +Fe region and 4% of that at 100 m in the -Fe region (Table 1),

indicating that remineralization rates were marginally enhanced by iron availability.

The organic carbon content of the core-top (surface-mixed-layer) sediments sampled several times during separate corer deployments was significantly higher in the +Fe region than the -Fe region (Supplementary Table 3). Significant sediment focusing and winnowing occurs in this region and thus data are expressed as ²³⁰Th_{xs}-corrected, preserved fluxes (equivalent to the preserved vertical rain rate at the sea floor). A twofold increase in the ²³⁰Th_{xs}-corrected, preserved, core-top, organic carbon accumulation was observed in the +Fe region relative to the -Fe region (Table 1). This is consistent with published data from a suite of export production proxies that imply enhanced phytoplankton growth, export and burial throughout the Holocene epoch at this site²⁴.

Our analyses thus indicate that shallow, seasonally integrated export, annually integrated deep-water POC flux and core-top organic carbon accumulation were all enhanced two- to threefold as a result of the iron-fertilized bloom (Table 1). Our results support Martin's hypothesis⁵ that relief of iron deficiency enhances carbon sequestration into the deep ocean (here >3,000 m) and sediment. Results from CROZEX thus support increased atmospheric iron deposition¹ as a mechanism for the inferred increase in organic carbon flux in the sub-Antarctic during the Last Glacial Maximum^{24,25}.

The ratio of carbon exported below some depth to iron added at the surface, (C/Fe) is termed the export efficiency or (if below the depth of winter mixing) sequestration efficiency^{6,8}. Our ²³⁴Th-derived estimates of the seasonal enhanced (+Fe minus -Fe) POC flux at 100 m (670 mmol m⁻²) and additional iron supply (0.039 mmol m⁻²) lead to a C/Fe ratio (at 100 m) of 17,200 mol mol⁻¹ (range, 5,400–60,400; Table 1). This value for the shallow export efficiency from CROZEX was somewhat higher than comparable values from iron-addition experiments (6,600 for SOFeX¹², 1,200 for SERIES (the sub-Arctic ecosystem response to iron enrichment study)⁷). Interpolating with a Martin curve²⁶ to a winter mixed-layer depth of 150–200 m (ref. 18), we further calculated a seasonal C/Fe sequestration efficiency of 11,500–8,600 (Table 1), compared with previous estimates of 500–3,300 (refs 7, 12) and the KEOPS⁸ seasonal estimate of 668,000. Given the different methods used to estimate both additional iron supply and carbon export between studies^{3,7,8,12}, the reasons for the wide range of export efficiencies are unclear. However, we note that the KEOPS result depends on a combination of an eightfold-lower estimate for seasonal iron supply and a tenfold-higher estimate for carbon export (Supplementary Table 1). It is possible that iron supply was higher to the KEOPS bloom before the late-summer observation period on which the seasonal iron supply was based, owing either to enhanced vertical supply before surface-water stratification in spring, coupled with luxury iron uptake²⁷ (that is, more than is absolutely necessary), or to horizontal input of lithogenic material from nearby islands^{28,29}.

The results from CROZEX indicate that natural iron fertilization enhanced new production¹⁷ and near-surface export at 100 m two- to threefold (Table 1). Moreover, we present evidence that carbon fluxes at 3,000 m and the sediment were similarly two to three times higher beneath the natural fertilized region than for a nearby HNLC region with similar end-of-winter macronutrient concentrations. Carbon sequestered past 200 m was only 50% of that exported past 100 m. Although the CROZEX estimate of carbon sequestration for a given iron supply was 20 times that of SERIES⁷, it still falls 15–50 times short of some geo-engineering estimates⁶, with significant implications for proposals to mitigate the effects of climate change through purposeful addition of iron to the ocean.

METHODS SUMMARY

Chlorophyll was determined using remote-sensing techniques referenced to *in situ* data. Iron concentrations in the bloom were estimated using a simple model including horizontal and vertical advection and atmospheric deposition. Organic carbon and opal export rates were determined using ²³⁴Th deficits

Table 1 | Seasonally integrated carbon fluxes at naturally iron fertilized and HNLC sites and the sequestration efficiency, C/Fe

	Carbon (mmol m ⁻² y ⁻¹)		C/Fe (mol mol ⁻¹)
	+Fe (fertilized)	-Fe (HNLC)	
²³⁴ Th via Si* at 100 m	960	290	17,190
Range	626–1,252	166–415	5,420–60,360
Deep flux† at 3,000 m	25.0	7.1	—
Best estimate‡	28.9	11.6	440
Range‡	25.0–34.2	7.1–17.4	195–1,506
Core top§	9.3 ± 0.5	4.5 ± 0.4	123
Interpolated flux at 150 m¶	642	194	11,487
Interpolated flux at 200 m¶	483	146	8,641

* Summarized from Supplementary Table 2.

† From Fig. 2.

‡ Summarized from Supplementary Information.

§ Summarized from Supplementary Table 3.

|| Calculated from the differences between +Fe and -Fe carbon fluxes divided by winter-period iron supply (0.018–0.039 mmol m⁻²).

¶ Calculated from 100-m flux (F) values using a Martin curve $F(z) = F(100\text{ m}) \times (z/100)^b$, where $b = -0.99$ to fit the 3,000-m carbon flux values.

and ^{234}Th /opal and organic carbon ratios from large particles. Biogenic silica was determined by spectrophotometric analysis of silicate levels in digested filtered samples. Sediment traps were McClane traps. Core data were derived from analysis of multiple gravity and Megacorer-derived samples.

Full Methods and any associated references are available in the online version of the paper at www.nature.com/nature.

Received 23 October; accepted 8 December 2008.

- Watson, A. J., Bakker, D. C. E., Ridgwell, A. J., Boyd, P. W. & Law, C. S. Effect of iron supply on Southern Ocean CO_2 uptake and implications for glacial atmospheric CO_2 . *Nature* **407**, 730–733 (2000).
- De Baar, H. J. W. et al. Synthesis of iron fertilization experiments: From the iron age in the age of enlightenment. *J. Geophys. Res.* **110**, doi:10.1029/2004JC002601 (2005).
- Boyd, P. W. et al. Mesoscale iron enrichment experiments 1993–2005: Synthesis and future directions. *Science* **315**, 612–617 (2007).
- Pollard, R. T., Sanders, R., Lucas, M. I. & Statham, P. J. The Crozet Natural Iron Bloom and Export Experiment (CROZEX). *Deep-Sea Res.* **54**, 1905–1914 (2007).
- Martin, J. H. Glacial-interglacial CO_2 change: the iron hypothesis. *Paleoceanography* **5**, 1–13 (1990).
- Buesseler, K. O. & Boyd, P. W. Will ocean fertilization work? *Science* **300**, 67–68 (2003).
- Boyd, P. W. et al. The decline and fate of an iron-induced subarctic phytoplankton bloom. *Nature* **428**, 549–553 (2004).
- Blain, S. et al. Effect of natural iron fertilization on carbon sequestration in the Southern Ocean. *Nature* **446**, 1070–1074 (2007).
- Sarmiento, J. L., Gruber, N., Brzezinski, M. A. & Dunne, J. P. High-latitude controls of thermocline nutrients and low latitude biological productivity. *Nature* **427**, 56–60 (2004).
- Boyd, P. W. et al. A mesoscale phytoplankton bloom in the polar Southern Ocean stimulated by iron fertilization. *Nature* **407**, 695–702 (2000).
- Coale, K. et al. Southern Ocean iron enrichment experiment: Carbon cycling in high- and low-Si waters. *Science* **304**, 408–414 (2004).
- Buesseler, K. O., Andrews, J. E., Pike, S. M. & Charette, M. A. The effects of iron fertilization on carbon sequestration in the Southern Ocean. *Science* **304**, 414–417 (2004).
- Pollard, R. T., Venables, H. J., Read, J. F. & Allen, J. T. Large scale circulation around the Crozet Plateau controls an annual phytoplankton bloom in the Crozet Basin. *Deep-Sea Res.* **54**, 1915–1929 (2007).
- Planquette, H. F. et al. Dissolved iron in the vicinity of the Crozet Islands, Southern Ocean. *Deep-Sea Res.* **54**, 1999–2019 (2007).
- Poulton, A. J. et al. Phytoplankton community composition around the Crozet Plateau, with emphasis on diatoms and *Phaeocystis*. *Deep-Sea Res.* **54**, 2085–2105 (2007).
- Bakker, D. C. E., Nielsdóttir, M. C., Morris, P. J., Venables, H. J. & Watson, A. J. The island mass effect and biological carbon uptake for the subantarctic Crozet Archipelago. *Deep-Sea Res.* **54**, 2174–2190 (2007).
- Sanders, R. et al. New production and the f-ratio around the Crozet Plateau in austral summer 2004–2005 diagnosed from seasonal changes in inorganic nutrient levels. *Deep-Sea Res.* **54**, 2191–2207 (2007).
- Venables, H. J., Pollard, R. T. & Popova, E. K. Physical conditions controlling the development of a regular phytoplankton bloom north of the Crozet Plateau, Southern Ocean. *Deep-Sea Res.* **54**, 1949–1965 (2007).
- Moore, C. M., Hickman, A. E., Poulton, A. J., Seeyave, S. & Lucas, M. I. Iron-light interactions during the CROZEX natural iron bloom and EXport experiment (CROZEX) II: taxonomic responses and elemental stoichiometry. *Deep-Sea Res.* **54**, 2066–2084 (2007).
- Planquette, H. F. *Iron Biogeochemistry in the Waters Surrounding the Crozet Islands, Southern Ocean*. PhD thesis, Southampton Univ. (2008).
- Lucas, M. I., Seeyave, S., Sanders, R., Moore, C. M. & Williamson, R. Nitrogen uptake responses to a naturally Fe-fertilised phytoplankton bloom during the 2004/2005 CROZEX study. *Deep-Sea Res.* **54**, 2138–2173 (2007).
- Morris, P. J., Sanders, R., Turnewitsch, R. & Thomalla, S. ^{234}Th -derived particulate organic carbon export compared to new production from an island induced phytoplankton bloom in the Southern Ocean. *Deep-Sea Res.* **54**, 2208–2232 (2007).
- Franck, V. M., Brzezinski, M. A., Coale, K. H. & Nelson, D. M. Iron and silicic acid concentrations regulate Si uptake north and south of the Polar Frontal Zone in the Pacific Sector of the Southern Ocean. *Deep-Sea Res.* **47**, 3315–3338 (2000).
- Marsh, R., Mills, R. A., Green, D. R. H., Salter, I. & Taylor, S. Controls on sediment geochemistry in the Crozet region. *Deep-Sea Res.* **54**, 2260–2274 (2007).
- Kohfeld, K. E., Le Quéré, C., Harrison, S. P. & Anderson, R. F. Role of marine biology in glacial-interglacial CO_2 cycles. *Science* **308**, 74–78 (2005).
- Buesseler, K. O. et al. Revisiting carbon flux through the ocean's twilight zone. *Science* **316**, 567–570 (2007).
- Mongin, M., Molina, E. & Trull, T. W. Seasonality and scale of the Kerguelen plateau phytoplankton bloom: a remote sensing and modeling analysis of the influence of natural iron fertilization in the Southern Ocean. *Deep-Sea Res.* **55**, 880–892 (2008).
- Zhang, Y., Lacan, F. & Jeandel, C. Dissolved rare earth elements tracing lithogenic inputs over the Kerguelen Plateau (Southern Ocean). *Deep-Sea Res.* **55**, 638–652 (2008).
- van Beek, P. et al. Radium isotopes to investigate the water mass pathways on the Kerguelen Plateau (Southern Ocean). *Deep-Sea Res.* **55**, 622–637 (2008).

Supplementary Information is linked to the online version of the paper at www.nature.com/nature.

Acknowledgements We thank the operators, master and crew of RRS *Discovery* for their support. CROZEX was a component of Biophysical Interactions and Controls on Export Production, a five-year project at the National Oceanography Centre, Southampton, supported by the Natural Environment Research Council (NERC).

Author Contributions R.T.P. led the project, the first cruise and the physics analysis (J.T.A., J.F.R., H.J.V.). R.J.S. led the second cruise and the nutrient chemistry analysis (M.F., R.S.L., P.J.M., I.S., M.S., S.T.), P.J.S. the iron and radium chemistry analysis (A.R.B., M.A.C., G.R.F., T.D.J., F.H.N., H.P.), M.I.L. the biology analysis (C.M.M., S.F., A.E.H., R.J.H., A.J.P., S.S., R.W., M.V.Z.), D.C.E.B. the carbon dioxide chemistry analysis (M.N.), R.A.M. the sediment chemistry analysis (S.T.) and J.A.H. the benthic biology analysis (T.S.). R.T.P. wrote the paper, assisted by R.J.S., C.M.M., I.S. (sediment traps), H.F.P. (iron), P.J.M. (^{234}Th), R.A.M. (cores) and M.I.L. (biology), with all authors commenting.

Author Information Data are held at the British Oceanographic Data Centre (<http://www.bodc.ac.uk>). Reprints and permissions information is available at www.nature.com/reprints. Correspondence and requests for materials should be addressed to R.J.S. (rics@noc.soton.ac.uk).

METHODS

Chlorophyll *a*. Chlorophyll *a* (Figs 1 and 2) was determined from NASA's merged SeaWiFS/MODIS products, adjusted to match *in situ* data¹⁸.

Iron concentrations in the bloom region¹⁴. Iron concentrations were estimated by considering lateral advection of DFe from the islands into the surrounding water, vertical mixing of iron from beneath the seasonal thermocline and atmospheric deposition. Total dissolved iron concentrations (DFe <0.2- μ m fraction) were determined using flow-injection catalytic spectrophotometric detection. Horizontal iron flux was estimated from samples of DFe collected along a series of stations extending seawards from the northern coast of Île de la Possession and by using the terrestrially derived, short-lived radium isotopes ²²³Ra and ²²⁴Ra to estimate horizontal mixing coefficients at the same stations³⁰. Horizontal gradients in these species were combined with estimates of the plateau circumference to estimate total DFe release from the plateau over the 100-day winter period when the mixed-layer depth is such that the surface ocean is in contact with plateau sediments. Vertical iron flux was diagnosed from analysis of ²²⁸Ra and DFe profiles. Finally, the estimated atmospheric (wet and dry) iron flux was based on calcium and silicon concentrations in aerosols and DFe measurements in rain samples by ICP-OES (inductively coupled plasma-optical emission spectrometer). The flux of DFe to surface waters was extrapolated to, and integrated over, the winter period. Values are consistent with atmospheric dust transport models.

Organic carbon and opal export. Shallow rates were estimated by multiplying the observed 0–100-m deficit of the short-lived natural radioisotope ²³⁴Th by the ²³⁴Th/POC or ²³⁴Th/Opal ratio in large-volume samples of large particulate material (>53 μ m) collected using a Stand-Alone Pumping System deployed approximately 20 m below the mixed layer²².

Biogenic silica. Measurements of biogenic silica were made on 1-litre seawater samples filtered onto 0.4- μ m polycarbonate filters, stored at –20 °C, digested in 0.2 mol sodium hydroxide and neutralized with 0.1 mol hydrochloric acid^{31,32} and analysed using a Skalar Sanplus autoanalyser. Opal accumulation was estimated by integrating values in the upper 100 m.

Sediment traps. Traps were McLane 21-cup time-series arrays deployed on bottom-tethered moorings. Sampling bottles were filled with buffered preservative solution according to Joint Global Ocean Flux Study protocols. Upon recovery, samples were filtered through a 1-mm Nitex mesh. Swimmers were carefully removed from the <1-mm fraction. The >1-mm fraction was comprised exclusively of large swimmers. Some cups were contaminated by fish (*Notolepis coatsi*) feeding on the sinking material. All fish debris was picked out by hand. All chemical analysis was performed on the <1-mm fraction after it had been freeze-dried and homogenized. Following acidification with hydrochloric acid, particulate organic carbon and nitrogen were measured using a Carlo Erba NA 1500 elemental analyser following standardization with acetanilide.

Core-top accumulation rates. A Megacorer was used to obtain sediment cores with an undisturbed sediment–water interface and gravity core deployments were used to sample deeper sediments. Samples from the surface mixed layer (0–10 cm below the surface) were dried, ground and subjected to the same methodology as described for the sediment trap material for particulate organic carbon and nitrogen at the National Oceanography Centre, Southampton, and NERC Isotope Geosciences Laboratory. U-series isotopes were determined by isotope dilution multi-collector ICP-MS (inductively coupled plasma mass spectrometry) at the Department of Earth Sciences, University of Oxford. ²³⁰Th-normalized, preserved organic carbon fluxes were estimated from the sediment composition and the ²³⁰Th-normalized sediment accumulation rate (measured ²³⁸U/²³²Th activity ratio of detrital end-member is 0.9). These data supplement published data²⁴ also tabulated for comparison.

30. Charette, M. *et al.* Radium isotopes as tracers of iron sources fueling a Southern Ocean phytoplankton bloom. *Deep-Sea Res. II* **54**, 1989–1998 (2007).
31. Brown, L., Sanders, R., Savidge, G. & Lucas, C. H. The uptake of silica during the spring bloom in the Northeast Atlantic Ocean. *Limnol. Oceanogr.* **48**, 1831–1845 (2003).
32. Poulton, A. J. *et al.* Phytoplankton mineralisation in the tropical and subtropical Atlantic Ocean. *Glob. Biogeochem. Cycles* **20**, BG4002 (2006).

Detoxification of sulphidic African shelf waters by blooming chemolithotrophs

Gaute Lavik^{1*}, Torben Stührmann^{1*}, Volker Brüchert^{1†}, Anja Van der Plas², Volker Mohrholz³, Phyllis Lam¹, Marc Mußmann⁴, Bernhard M. Fuchs¹, Rudolf Amann¹, Ulrich Lass³ & Marcel M. M. Kuypers¹

Coastal waters support ~90 per cent of global fisheries and are therefore an important food reserve for our planet¹. Eutrophication of these waters, due to human activity, leads to severe oxygen depletion and the episodic occurrence of hydrogen sulphide—toxic to multi-cellular life—with disastrous consequences for coastal ecosystems^{2–5}. Here we show that an area of ~7,000 km² of African shelf, covered by sulphidic water, was detoxified by blooming bacteria that oxidized the biologically harmful sulphide to environmentally harmless colloidal sulphur and sulphate. Combined chemical analyses, stoichiometric modelling, isotopic incubations, comparative 16S ribosomal RNA, functional gene sequence analyses and fluorescence *in situ* hybridization indicate that the detoxification proceeded by chemolithotrophic oxidation of sulphide with nitrate and was mainly catalysed by two discrete populations of γ - and ϵ -proteobacteria. Chemolithotrophic bacteria, accounting for ~20 per cent of the bacterioplankton in sulphidic waters, created a buffer zone between the toxic sulphidic subsurface waters and the oxic surface waters, where fish and other nekton live. This is the first time that large-scale detoxification of sulphidic waters by chemolithotrophs has been observed in an open-ocean system. The data suggest that sulphide can be completely consumed by bacteria in the subsurface waters and, thus, can be overlooked by remote sensing or monitoring of shallow coastal waters. Consequently, sulphidic bottom waters on continental shelves may be more common than previously believed, and could therefore have an important but as yet neglected effect on benthic communities.

The subtropical eastern boundary current regions (for example Peru-Humboldt, California, Canary and Benguela) are naturally eutrophic, and although they comprise only 0.1% of the global ocean volume, 17% of the global fish catch occurs there⁶. In terms of primary productivity, the most productive of these systems is the Benguela system off Namibia⁶. However, the Benguela system is the least productive with respect to fish catch, yielding a catch of only 0.5×10^6 tons of fish per year (in comparison with $\sim 11 \times 10^6$ tons per year in the Peru-Humboldt system)⁶. This apparent anomaly has been attributed to the episodic occurrence of hydrogen sulphide gas, which is toxic to economically important fish in the southwest African shelf waters. In fact, scientific reports of massive fish mortality in the Namibian coastal waters associated with sulphidic shelf waters date back more than half a century^{7,8}. The regulation of these sulphidic events is poorly understood; however, their initiation has been attributed to either the eruptive release of methane and sulphide from gas-loaded shelf sediments^{9,10} or the diffusive flux of sulphide from the sulphidic sediments¹¹. Even less is known about

the termination of these events, and it is unclear by which route the detoxification of hydrogen sulphide proceeds.

During an RV *Alexander von Humboldt* cruise (AHAB1) in January 2004, we recorded the spatial extent and the temporal development of a sulphidic event in the southwest African shelf waters (Fig. 1; see also Supplementary Information). The shelf waters were generally depleted in oxygen below 60-m water depth north of 27° S, and towards the end of the cruise, on 24 January 2004, sulphide-containing waters were recorded to cover approximately 7,000 km² of the shelf (Fig. 1a). At the start of the cruise, on 8 January, the shelf waters off Walvis Bay (23° S) were sulphide free, but 120 km farther south (24° S) we found sulphidic bottom waters. A sampling site at 24° S (18 km off shore; Fig. 1), located at the centre of this sulphidic water mass, was visited three times during a period of nine days. At this site, sulphide concentrations 3 m above the sediment increased from 5 μ M on 10 January to 19 μ M on 15 January and to 25 μ M on 18 January (Supplementary Fig. 1). A similar increase in sulphide concentrations was observed in the originally sulphide-free bottom waters at 23° S from 17 to 23 January. Assuming that the concentration profile of sulphide at 24° S represents a steady state (Fig. 2b; see also Supplementary Discussion), we calculated a flux of ~ 8 mmol m⁻² d⁻¹ from the sediment for 24° S by using a reaction diffusion model¹², which is comparable to the range (12–22 mmol m⁻² d⁻¹) of sedimentary sulphide fluxes previously reported for this region¹¹. On the basis of the benthic sulphide flux, it would require 8 to 15 days to accumulate the observed sulphide concentration in the shelf waters observed on 15 January (Fig. 2b), without taking sulphide oxidation in the water column into account.

At all stations with sulphidic bottom waters, sulphide disappeared well below the oxic zone (Figs 1d–f, 2a, b), and at 24° S the sulphide front descended ~15 m in the suboxic water column between 15 and 18 January despite increasing sulphide concentration in the lower bottom waters (Supplementary Fig. 3). This apparent sulphide sink in the suboxic zone strongly suggests that sulphide was oxidized anaerobically in the water column. In the absence of oxygen, nitrate is the best electron acceptor for sulphide oxidation. Nitrate and sulphide profiles overlapped in the suboxic zone between depths of ~86 and 90 m at 24° S (Fig. 2b). The sulphide flux into the suboxic zone at 24° S was ~ 2.3 mmol m⁻² d⁻¹, whereas the nitrate flux was 3.3 mmol m⁻² d⁻¹.

In addition to dissolved sulphide, ammonium diffused from the sediments into the suboxic zone (Fig. 2a). Similar concentrations of ammonium and sulphide were detected in the bottom water, but ammonium disappeared just above dissolved sulphide at 80 m, indicating that ammonium was also oxidized anaerobically. Recently, it was shown that anaerobic ammonium oxidation with nitrate and/or

¹Max Planck Institute for Marine Microbiology, Celsiusstrasse 1, D-28359 Bremen, Germany. ²National Marine Information & Research Centre Ministry of Fisheries & Marine Resources, PO Box 912, Swakopmund, Namibia. ³Baltic Sea Research Institute Warnemünde, Seestrassse 15, D-18119 Rostock, Germany. ⁴Department of Microbial Ecology, Vienna Ecology Centre, University of Vienna, Althanstrasse 14, A-1090 Vienna, Austria. [†]Present address: Department of Geology and Geochemistry, Stockholm University, Svante Arrhenius väg 8C, 106 91 Stockholm, Sweden.

*These authors contributed equally to this work.

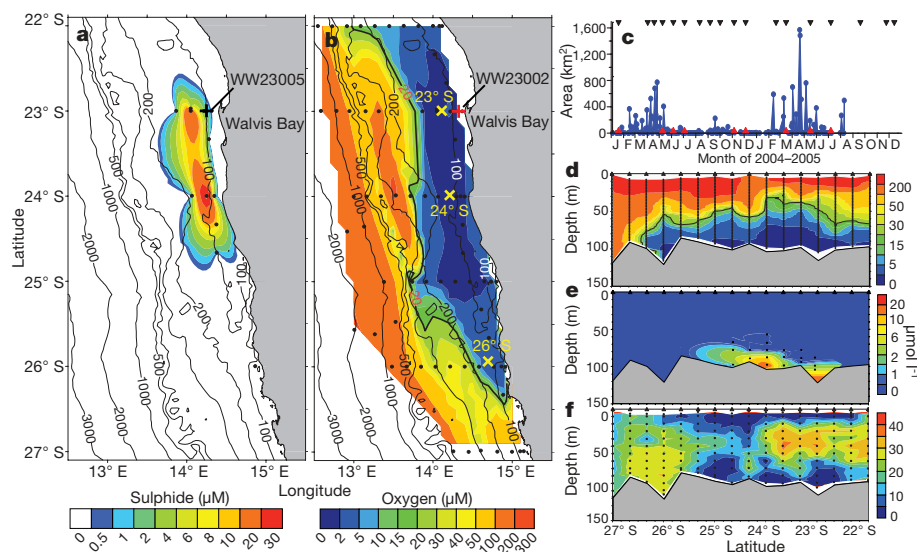


Figure 1 | Spatial and temporal distribution of sulphidic shelf waters off Namibia during 2004–2005. **a, b**, Bottom-water concentrations (~ 2 m above the sediment) of sulphide (**a**) and oxygen (**b**). **c**, Occurrence of, and surface water area with turquoise discolouration specific to the presence of, colloidal sulphur (S^0 ; blue trace)²⁸; black triangles indicate the monitoring (and major) cruises, red triangles indicate the detection of free sulphide in shelf waters at 23° S during these cruises. **d–f**, North–south transects (100–130-m water depth) parallel to the Namibian coast for the

concentrations of oxygen (**d**), sulphide (**e**) and nitrate (**f**). All data incorporated in the contour plots were retrieved from 124 CTD-rossette and pump-CTD casts between 4 and 20 January 2004, during the cruise AHAB1. The main sampling sites at 23° S, 24° S and 26° S are marked with crosses in **b**. Our monitoring stations at positions WW23005 and WW23002 are indicated with pluses in **a** and **b**, respectively. The black numbering on the thin contours indicates water depth in metres. The red numbering on the thick contour in **b** indicates oxygen concentration in μ M.

nitrite by anammox (anaerobic ammonium oxidation) bacteria is responsible for massive nitrogen loss in the suboxic waters of the Benguela upwelling zone¹³. The calculated ammonium flux into the suboxic zone was $\sim 2.3 \text{ mmol m}^{-2} \text{ d}^{-1}$. Ammonium diffused 5 m farther into the suboxic zone than dissolved sulphide, and would thus have been oxidized first by nitrate/nitrite. The stoichiometry of the anammox reaction (1 mol NO_3^- or NO_2^- per mole NH_4^+) leaves $1 \text{ mmol m}^{-2} \text{ d}^{-1}$ of the nitrate flux to oxidize sulphide. Hence, 1 mol nitrate was consumed per $\sim 2.3 \text{ mol}$ sulphide, which is very close to the 1:2.5 stoichiometry for chemolithotrophic oxidation of sulphide with nitrate according to the following equation:



The detection of elemental sulphur (S^0) at a concentration of $22 \mu\text{M}$ and a water depth of 87 m (Fig. 2b) in the centre of the nitrate and sulphide mixing zone is evidence for this reaction pathway. This incomplete oxidation of sulphide to colloidal sulphur with nitrate occurs under nitrate-limiting conditions¹⁴, which applies to the bottom waters at 24° S. Complete sulphide oxidation to sulphate may have occurred where the nitrate flux exceeded the sulphide flux, such as at 23° S on 18 January (Supplementary Fig. 2b). Additional evidence for the anaerobic oxidation of sulphide with nitrate was obtained from incubation experiments with $^{15}\text{NO}_3^-$, which indicated that denitrification was the main process of fixed inorganic nitrogen removal at 90 m at 24° S (Fig. 2c). The nitrate reduction rate of $\sim 0.6 \mu\text{M d}^{-1}$ determined from ^{15}N experiments was also in good agreement with the rate ($\sim 0.7 \mu\text{M d}^{-1}$) calculated for the zone of overlapping nitrate and sulphide profiles by fitting the profiles to a one-dimensional reaction-transport model¹².

Comparative 16S rRNA gene- and functional gene-sequence analyses and fluorescence *in situ* hybridization (FISH) revealed that two discrete populations of γ - and ϵ -proteobacteria were involved in the chemolithotrophic oxidation of sulphide with nitrate (Fig. 3; see also Supplementary Discussion). A 16S rRNA gene library retrieved from the sulphidic Namibian shelf waters was dominated by a tight cluster of γ -proteobacterial clones (121 of 271 clones, γ -proteobacterial sulphur oxidizer (GSO) cluster) displaying 95–96% sequence identity to

the 16S rRNA gene sequence of ‘*Candidatus Ruthia magnifica*’ (Fig. 3a), the sulphide-oxidizing gill endosymbiont of the mussel *Calypogena magnifica* inhabiting sulphide-rich vent and seep environments^{15,16}. 16S rRNA gene sequences of the GSO cluster were previously retrieved from sulphidic shelf waters off Namibia on 22 May 1998 (B.M.F., previously unpublished data; 80-m water depth, $24^\circ 45.0' \text{ S}$, $14^\circ 19.5' \text{ E}$, AMT6 cruise) and other sulphidic environments^{17,18}.

In accordance with the findings from 16S rRNA phylogeny, we also identified gene sequences encoding the alpha subunits of two enzymes in the sulphur oxidation pathway, the dissimilatory adenosine 5'-phosphosulphate reductase (AprBA) and the reverse dissimilatory sulphite reductase (rDsrAB) most closely related to ‘*Candidatus Ruthia magnifica*’ (Supplementary Fig. 4). These endosymbionts are known to oxidize sulphide to elemental sulphur^{17,19} and, subsequently, to sulphate using rDsrAB and AprBA (ref. 16). The amino-acid sequence identities were 81% (rDsrA clone Nam73_rDsr_23) and 92% (AprA clone Nam73_aprA_14), respectively (Supplementary Fig. 4). In summary, the congruent phylogenies of genes encoding 16S rRNA, rDsrA and AprA indicate the sulphur oxidation capability of the GSO bacteria (Supplementary Discussion). In the 16S rRNA gene library, we also detected a tight cluster of seven ϵ -proteobacterial sequences that had 94%, 92% and 83% sequence identities to *Arcobacter nitrofigilis*²⁰, ‘*Candidatus Arcobacter sulfidicus*’²¹ and *Sulfurimonas denitrificans*²², respectively (Fig. 3a). The capacity of this ϵ -proteobacterial group to oxidize sulphide to elemental sulphur has been demonstrated for pure cultures²³.

A sulphide oxidation rate of $\sim 7 \text{ fmol per cell per day}$ was determined for these pure cultures of ϵ -proteobacteria oxidizing sulphide with nitrate²³. Assuming a similar cell-specific activity for the Namibian shelf waters, $2.5 \times 10^5 \text{ cell ml}^{-1}$ would be required in order to account for the observed sulphide oxidation rates in the suboxic zone. Quantification of the ϵ -proteobacterial genus *Arcobacter* and members of the GSO cluster by FISH revealed a spike in cell densities of $2.3 \times 10^5 \pm 3,000 \text{ cell ml}^{-1}$ (8.7% of 4,6-diamidino-2-phenylindole (DAPI)) and $3.1 \times 10^5 \pm 2,000 \text{ cell ml}^{-1}$ (11.1% of DAPI), respectively, at the top of the sulphidic zone, where nitrate disappears

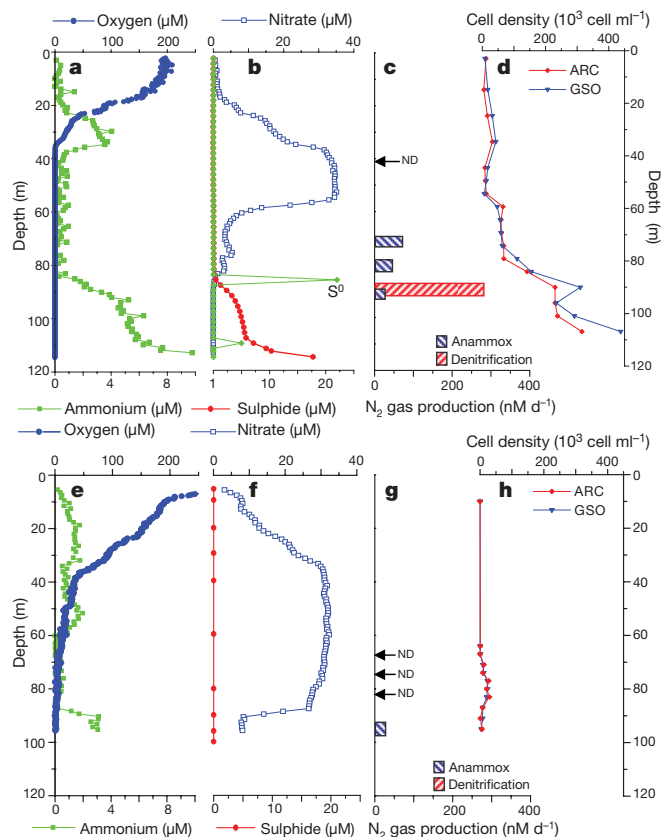


Figure 2 | Chemical zonation and distribution of indicators for bacterial sulphide oxidation. **a–d**, Data from 24° S, 15 January 2004; **e–h**, data from 23° S, 8 January 2004. **a, e**, Concentrations of oxygen and ammonium; **b, f**, concentrations of nitrate, sulphide (continuously measured, red line) and colloidal sulphur (S⁰, green diamonds, same scale as sulphide). Note that colloidal sulphur that forms upon incomplete anaerobic oxidation of sulphide maximizes exactly in the zone of overlapping nitrate and sulphide profiles at 24° S, and that there is a second colloidal sulphur peak at ~110 m, where there is a change in sulphide gradient, which may reflect an earlier oxidation front. **c, g**, Denitrification and anammox rates determined from *in situ* ¹⁵NO₃⁻ incubations. ND, not detected. **d, h**, Depth profile of ϵ -proteobacteria (*Arcobacter*) as determined by *in situ* hybridization with the specific ARC94 oligonucleotide probe and γ -proteobacteria hybridizing with the specific GSO477 oligonucleotide probe. The location of the sampling sites is shown in Fig. 1.

(~90 m; Figs 2b, d). Below this upper spike, cell abundances on 15 January increased with depth, indicating that their activity optimum (that is, the sulphide–nitrate transition) was previously located closer to the sediment. Substantial changes in the position of the sulphide–nitrate transition at 24° S were also observed during the second week of our cruise, with the sulphide front descending between 15 and 18 January as described above (Supplementary Fig. 3). The second colloidal sulphur peak at ~110 m at 24° S supports our hypothesis that the sulphide oxidation front was previously located closer to the sediment (Fig. 2b).

Although the cell abundance of the described γ - and ϵ -proteobacterial populations were sufficient to account for the observed sulphide oxidation rates, our rDsrAB functional gene library indicates that other microbes might also be involved in the detoxification of the sulphidic Namibian waters (Supplementary Discussion). Further north, at 23° S, γ - and ϵ -proteobacterial cells were present only in low abundance ($<0.2 \times 10^5$ cell ml⁻¹) on 8 January, when no sulphide was detected (Fig. 2e–h), but were three to four times more abundant (each $>0.6 \times 10^5$ cell ml⁻¹) in the sulphidic waters ten days later (Supplementary Fig. 2b, d). This increase in cell abundance was accompanied by an increase in abundance of the gene encoding

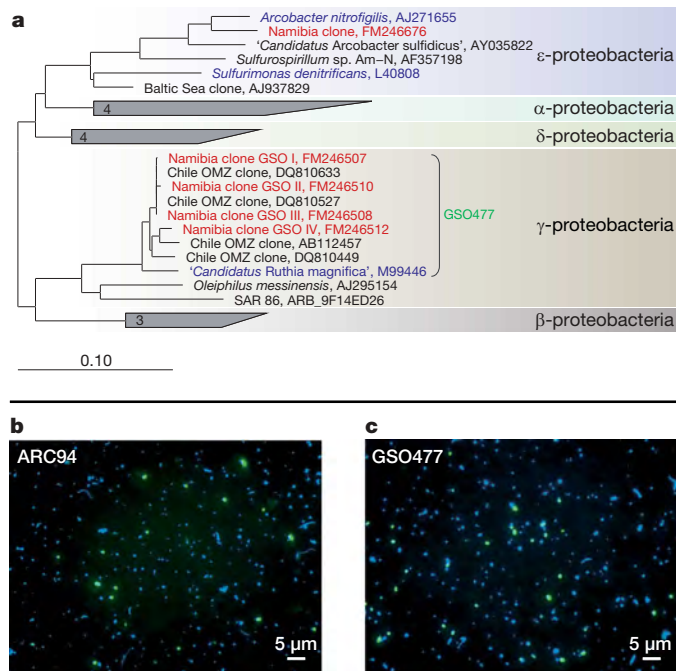


Figure 3 | Affiliation and morphology of sulphide-oxidizing bacteria from the Namibian shelf waters. **a**, Phylogenetic tree of the identified γ - and ϵ -proteobacterial phylotypes based on comparative 16S rRNA sequence analysis. Sequences written in red were obtained from the Namibian upwelling system and sequences written in blue are of special interest to this study. The phylogenetic tree was calculated by maximum-likelihood analysis using the ARB software package²⁹. Scale bar shown in units of sequence divergence. **b, c**, Micrographs of Namibian bacterioplankton from the sulphidic layer (24° S, 95 m) stained with DAPI (blue) and specific probes (green). Probe ARC94 (**b**) targets the 16S rRNA of the ϵ -proteobacterial genus *Arcobacter*. Probe GSO477 (**c**) targets the γ -proteobacterial GSO cluster and hybridized to a morphologically homogenous population of coccoidal cells.

the GSO-related enzyme rDsrA (Supplementary Discussion). Although there was no detectable denitrification at 23° S on 8 January, substantial denitrification occurred in the zone of overlapping nitrate and sulphide profiles on 18 January (Supplementary Fig. 2b, c). The cell-specific denitrification rates (~8 fmol N₂ per cell per day) at 23° S on 18 January were similar to those detected at 24° S on 15 January (~6 fmol N₂ per cell per day), providing additional evidence for the involvement of these organisms in the anaerobic sulphide oxidation. These chemolithotrophs were not detected at nearby stations before or after our cruise, or in the suboxic waters to the south of the sulphidic water mass (at 26° S; Supplementary Fig. 2e–h). In addition to the rapid increase in both cell numbers and the abundance of genes encoding rDsrA at 23° S, the regular size and shape of the cells supports a bloom-like growth of these chemolithotrophs (Fig. 3b, c). Pure cultures of nitrate-reducing, sulphide-oxidizing bacteria have doubling times as short as ~1.5 h (ref. 22), indicating that these chemolithotrophs are capable of creating blooms under the correct conditions. The combined results indicate that the observed bloom of chemolithotrophs was sufficient to create a buffer zone between the oxic environment—where fish and other nekton live—and the toxic sulphidic Namibian shelf waters, by oxidizing sulphide with nitrate.

The findings from a series of monitoring cruises to the same area during 2004–2005 revealed that the sulphidic event observed in January 2004 was not a singular event and that sulphidic bottom waters frequently occur at the Namibian shelf (Fig. 1c, Supplementary Table 1). During 18 one-day monitoring cruises to two sites off Walvis Bay (23° S; Fig. 1c), sulphide was detected three times at the inshore coastal station (3.5 km off shore) and nine times

at the more distant station (~8 km off shore). Owing to the limited spatial and temporal resolution of the monitoring cruises, several other sulphidic events may have remained undetected. Remote satellite sensing is generally used to monitor large ocean areas on a day-to-day basis and, for 2004–2005, 16 larger (>200-km² surface area) events of colloidal sulphur were recorded by satellite imaging (Fig. 1c). Owing to the superior temporal (day versus month) and spatial resolution (22° S–27° S versus 23° S) of the satellite observations, a nearly complete record of all events would be expected. However, five of the nine occasions on which sulphide was detected in the shelf waters could not be related to colloidal sulphur clouds in the surface waters (Fig. 1c). On the basis of these observations, sulphide must be consumed in the subsurface shelf waters; the temporal bloom of pelagic sulphur-oxidizing bacteria reported in this study could account for this.

Current estimates postulate that the occurrence of shelf hypoxia, due to both human-induced eutrophication^{3,24} and global warming^{25,26}, will strongly increase in the coming decades. In fact, hypoxic events, and the episodic occurrence of hydrogen sulphide, have been reported in other coastal waters, for example those of western India, Europe and California and the Gulf of Mexico^{2–5,24,27}. On the basis of our results from Namibia, we postulate that many sulphidic events in coastal waters may go unnoticed because bacteria consume sulphide before it reaches the surface.

METHODS SUMMARY

Water samples for biogeochemical and microbiological analyses were obtained using a pump conductivity–temperature–depth (pump-CTD) system and Niskin bottles. Nutrient and sulphide concentrations were determined on board with an autoanalyser immediately after sampling. Sulphide, ammonium and nitrate fluxes and rates of sulphide oxidation and nitrate reduction were calculated from the concentration profiles and a vertical diffusion coefficient (K_z) with the program Profile¹². To determine denitrification and anammox rates, Namibian shelf water collected from specific water depths with the pump-CTD system was incubated at *in situ* temperatures after the addition of ¹⁵N-labelled substrates. ³⁵S-sulphate-tracer experiments were performed to determine water-column sulphate-reduction rates.

Particulate organic matter for phylogenetic and catalysed-reporter-deposition FISH (CARD-FISH) analyses was collected from specific water depths by onboard filtration, and *in situ* filtration of large volumes of water through glass-fibre filters was used to obtain DNA for quantitative PCR. In the laboratory, 16S rRNA, *aprA* and *rdsrA* were amplified and cloned and the obtained sequences were subsequently used to reconstruct phylogenetic trees. The *rdsrA*-encoding gene was quantified using quantitative PCR with a specifically designed primer set. CARD-FISH with specific horseradish peroxidase-labelled oligonucleotide probes was used to determine the abundance of members of the GSO and *Arcobacter* clusters in the Namibian waters.

Full Methods and any associated references are available in the online version of the paper at www.nature.com/nature.

Received 22 May 2007; accepted 21 October 2008.

Published online 10 December 2008.

1. Pauly, D. *et al.* Towards sustainability in world fisheries. *Nature* **418**, 689–695 (2002).
2. Diaz, R. J. & Rosenberg, R. Marine benthic hypoxia: a review of its ecological effects and the behavioral responses of benthic macrofauna. *Oceanogr. Mar. Biol. Annu. Rev.* **33**, 245–303 (1995).
3. Naqvi, S. W. A. *et al.* Increased marine production of N₂O due to intensifying anoxia on the Indian continental shelf. *Nature* **408**, 346–349 (2000).
4. Rabalais, N. N., Turner, R. E. & Scavia, D. Beyond science into policy: Gulf of Mexico hypoxia and the Mississippi River. *Bioscience* **52**, 129–142 (2002).
5. Malakoff, D. Death by suffocation in the Gulf of Mexico. *Science* **281**, 190–192 (1998).
6. Carr, M.-E. Estimation of potential productivity in eastern boundary currents using remote sensing. *Deep-Sea Res. II* **49**, 58–80 (2002).

7. Copenhagen, W. J. The periodic mortality of fish in the Walvis Bay region. *Invest/Rep. Div. Sea Fish S. Afr.* **14**, 1–35 (1953).
8. Hart, T. J. & Currie, R. I. The Benguela current. *Discovery Rep.* **31**, 123–297 (1960).
9. Emeis, K. C. *et al.* Shallow gas in shelf sediments of the Namibian coastal upwelling ecosystem. *Contin. Shelf Res.* **24**, 627–642 (2004).
10. Weeks, S. J., Currie, B. & Bakun, A. Satellite imaging: Massive emissions of toxic gas in the Atlantic. *Nature* **415**, 493–494 (2002).
11. Bruchert, V. *et al.* in *Past and Present Water Column Anoxia* (ed. Neretin, L. N.) 161–193 (NATO Science Series 40, Springer, 2006).
12. Berg, P., Risgaard-Petersen, N. & Rysgaard, S. Interpretation of measured concentration profiles in sediment pore water. *Limnol. Oceanogr.* **43**, 1500–1510 (1998).
13. Kuypers, M. M. M. *et al.* Massive nitrogen loss from the Benguela upwelling system through anaerobic ammonium oxidation. *Proc. Natl Acad. Sci. USA* **102**, 6478–6483 (2005).
14. Cardoso, R. B. *et al.* Sulfide oxidation under chemolithoautotrophic denitrifying conditions. *Biotechnol. Bioeng.* **95**, 1148–1157 (2006).
15. Peek, A. S., Feldman, R. A., Lutz, R. A. & Vrijenhoek, R. C. Cospeciation of chemoautotrophic bacteria and deep sea clams. *Proc. Natl Acad. Sci. USA* **95**, 9962–9966 (1998).
16. Newton, I. L. G. *et al.* The Calyptogen magnifica chemoautotrophic symbiont genome. *Science* **315**, 998–1000 (2007).
17. Madrid, V. M., Taylor, G. T., Scranton, M. I. & Chistoserdov, A. Y. Phylogenetic diversity of bacterial and archaeal communities in the anoxic zone of the Cariaco basin. *Appl. Environ. Microbiol.* **67**, 1663–1674 (2001).
18. Sunamura, M., Higashi, Y., Miyako, C., Ishibashi, J. & Maruyama, A. Two bacteria phylotypes are predominant in the Suiko seamount hydrothermal plume. *Appl. Environ. Microbiol.* **70**, 1190–1198 (2004).
19. Vetter, R. D. Elemental sulfur in the gills of three species of clams containing chemoautotrophic symbiotic bacteria: a possible inorganic energy storage compound. *Mar. Biol.* **88**, 33–42 (1985).
20. Campbell, B. J. *et al.* The versatile epsilon-proteobacteria: key players in sulphidic habitats. *Nat. Rev. Microbiol.* **4**, 458–468 (2006).
21. Wirsén, C. O. *et al.* Characterization of an autotrophic sulfide-oxidizing marine *Arcobacter* sp that produces filamentous sulphur. *Appl. Environ. Microbiol.* **68**, 316–325 (2002).
22. Sievert, S. M. *et al.* Genome of the Epsilonproteobacterial chemolithoautotroph *Sulfurimonas denitrificans*. *Appl. Environ. Microbiol.* **74**, 1145–1156 (2008).
23. Gevertz, D. *et al.* Isolation and characterization of strains CVO and FWKO B, two novel nitrate-reducing, sulfide-oxidizing bacteria isolated from oil field brine. *Appl. Environ. Microbiol.* **66**, 2491–2501 (2000).
24. Beman, J. M., Arrigo, K. R. & Matson, P. A. Agricultural runoff fuels large phytoplankton blooms in vulnerable areas of the ocean. *Nature* **434**, 211–214 (2005).
25. Grantham, B. A. *et al.* Upwelling-driven nearshore hypoxia signals ecosystem and oceanographic changes in the northeast Pacific. *Nature* **429**, 749–754 (2004).
26. Sarmiento, J. L. *et al.* Simulated response of the ocean carbon cycle to anthropogenic climate warming. *Nature* **393**, 245–249 (1998).
27. Paerl, H. W. & Steppe, T. F. Scaling up: the next challenge in environmental microbiology. *Environ. Microbiol.* **5**, 1025–1038 (2003).
28. Ohde, T. *et al.* Identification and investigation of sulphur plumes along the Namibian coast using the MERIS sensor. *Contin. Shelf Res.* **27**, 744–756 (2007).
29. Ludwig, W. *et al.* ARB: a software environment for sequence data. *Nucleic Acids Res.* **32**, 1363–1371 (2004).

Supplementary Information is linked to the online version of the paper at www.nature.com/nature.

Acknowledgements We thank B. Barker Jørgensen, F. Inagaki, C. Hubert, T. Ferdman and G. Collins for discussions; the Namibian authorities for access to their national waters; the crew of RV *Alexander von Humboldt* for assistance onboard; S. Krüger for operating the pump-CTD and oceanographic equipment; T. Heene for assistance with the collection of oceanographic data and generating oceanographic plots; and G. Klockgether, J. Sawicka, J. Wulf, S. Lenk, D. Franzke and K. Nkandi for assistance with the analysis. The investigations were supported by the MPG, the BMBF programme Geotechnologien and the project NAMIBGAS, the DFG, BENEFIT and the Namibian Ministry of Fisheries and Natural Resources.

Author Information Sequences for the 16S rRNA, *aprA* and *rdsrA* genes obtained in this study have been submitted to GenBank under the accession numbers FM246507–FM246787, FM246819–FM246832 and FM246788–FM246818, respectively. Reprints and permissions information is available at www.nature.com/reprints. Correspondence and requests for materials should be addressed to M.M.M.K. (mkuypers@mpi-bremen.de).

METHODS

Chemical analysis. A pump-CTD system and Niskin bottles (Hydrobios) were used to obtain nutrient samples. Nitrate, nitrite and ammonium concentrations (respective detection limits, 0.1, 0.02 and 0.3 μM) were determined onboard with a TRAACS 800 autoanalyser. For online sulphide measurements, the water flow from the pump-CTD was directly connected to the autoanalyser. For discrete samples, sulphide concentrations (detection limit, 0.1 μM) were measured by spectrophotometry³⁰.

For elemental sulphur analysis (detection limit, $\sim 1 \mu\text{M}$), 1 ml seawater was added to 0.5 ml 1% zinc chloride solution and 9 ml 100% methanol. Samples were stored cold until analysis. Aliquots were filtered through 0.2- μm syringe tip filters (nylon Acrodisc filters) and analysed by reverse-phase high-performance liquid chromatography (Sykam UV-Vis detector S3200 at 265 nm; eluent, 100% methanol; pump rate, 1 ml min⁻¹) after separation on a Zorbax C18 reverse-phase column (Agilent) at room temperature.

¹⁵N incubations and analysis. ¹⁵N-labelling experiments were performed in gas- and light-tight bags³¹. 250-ml bags were filled directly with water from the pump-CTD system; care was taken to avoid contact with atmospheric oxygen and the bags were maintained at *in situ* temperatures. ¹⁵N-nitrate (final concentration, 20 μM) was injected through the rubber stoppers, which were used to close the glass outlets of the bags, and 15-ml aliquots of water were extracted from each bag with a gas-tight syringe at each time point (after 0, 6, 12, 24 and 48 h) and transferred to gas-tight exetainers containing 100 μl saturated mercuric chloride. The samples were stored upside down with a 2-ml helium headspace pending analyses. ¹⁴N¹⁵N, ¹⁴N¹⁴N and ¹⁵N¹⁵N:¹⁴N¹⁴N ratios were determined by GC-IRMS (VG Optima).

Production of N₂ through denitrification and anammox was calculated from the excess concentrations of ¹⁴N¹⁵N and ¹⁵N¹⁵N and the ¹⁵N-labelling of the NO₃⁻ pool (F), according to³²

$$D = {}^{15}\text{N}^{15}\text{N} \times F^{-2}$$

$$A = {}^{14}\text{N}^{15}\text{N} \times F^{-1} - [D \times 2 \times (1 - F)]$$

where *D* and *A* denote production of N₂ through denitrification and anammox, respectively.

Sulphate reduction rates. Water-column sulphate reduction rates were determined with duplicate 100-ml Winkler bottles at station MPI-3 (22° 38.3' S, 14° 18.27' E, 70-m water depth, occupied 5 March 2004), MPI-5 (23° 45.08' S, 14° 15.8' E, 112 m, occupied 6 March 2004), and MPI-9 (24° 55.115' S, 14° 25.248' E, 122 m, occupied 9 March 2004). To each bottle, 100 μl of carrier-free ³⁵S-sulphate (total activity, 10 MBq per bottle) were added. Bottles were incubated in the dark at 12 °C for 48 h. Subsequently, the contents were transferred to 40 ml 20% zinc acetate. At each station, zinc acetate was added to one Winkler bottle before the tracer addition to determine a procedural blank. The fixed samples were stored frozen until analysis. In the laboratory, the samples were acid-distilled with 6N HCl after the addition of 5 ml 1 mM ZnS to enhance recovery of the evolved ³⁵S-H₂S gas. The radioactivity of ³⁵S-H₂S and ³⁵S-sulphate was determined on a Packard TR100 scintillation counter. Sulphate reduction rates were calculated according to a previously described protocol³³ accounting for the blanks of ³⁵S-sulphate (15 cpm; *n* = 3) and ³⁵S-H₂S (35–65 cpm; *n* = 3).

Phylogenetic analysis. Amplification and cloning of 16S rRNA and *aprA* genes was performed as described previously^{34,35}. Partial *rdsrA* genes were amplified using primers 240F: GGNTAYTGGAARGGNGG and 403R: ARCCANCCY-TGNGTRTG. The following PCR conditions were applied: initial denaturation at 94 °C for 5 min, denaturation at 94 °C for 1 min, annealing at 55.5 °C for 1 min, elongation at 72 °C for 3 min, 35 cycles. The 16S rRNA clone library was generated from pooled DNA samples (83–103 m at 24 °S) whereas the *aprA* and *rdsrA* sequences were obtained from 95-m water depth at 24 °S. The recovered *rdsrA* fragments comprised $\sim 1,680$ bp, of which 984 bp were used for phylogenetic analysis using ARB²⁹. For the 16S rRNA phylogeny, only sequences longer than 1,200 bp were considered for tree reconstruction. Partial sequences (Chilean OMZ and Baltic Sea) were added with the Quick add function in ARB.

Quantitative polymerase chain reaction (qPCR). Water was filtered on to combusted glass-fibre filters (GF/F, 142- or 292-mm diameter; Whatman) with *in situ* pumps (McClane). DNA was extracted from a 2-cm-diameter subsample of the GF/F filters following the protocol of ref 36 and was further purified with the Wizard DNA Clean-up System (Promega). Total DNA concentrations were determined using a NanoDrop 1000 Spectrophotometer (Thermo Scientific). The *rdsrA*-encoding gene was quantified by qPCR with a specially designed primer set: *rdsr393f* (5'-ACAGGCGGCATTACGTACC-3') and *rdsr810r* (5'-AGTACGCTTCCACCCATG-3'). The thermal cycling conditions were as follows: initially 2 min at 50 °C, 10 min at 95 °C, followed by 50 cycles of 30 s at 95 °C, 1 min at 53 °C, 2 min at 72 °C and fluorescence detection at 76.9 °C. The correct sizes of qPCR products were verified by melting analysis and gel electrophoresis after amplification. For qPCR standards, partial sequences of *rdsrA* genes were amplified from sequenced plasmid DNA isolated from the corresponding clone library. The PCR products were then purified with QIAquick Spin Columns (Qiagen), and their sizes and corresponding concentrations were accurately determined with a DNA1000 chip on a Bioanalyser 2100 (Agilent). A dilution series with the DNA standard was analysed in parallel during each qPCR run. All qPCRs were performed using PowerSYBR Green Master Mixes (Applied Biosystems) and an iQ5 Real-Time PCR Detection System (Bio-Rad Laboratories).

CARD-FISH. Water samples (30 ml) were fixed with paraformaldehyde (final concentration, 2%) for CARD-FISH analyses and were filtered through 0.22- μm polycarbonate filters. Filter sections were hybridized with horseradish peroxidase-labelled oligonucleotide probes³⁷. Briefly, endogenous peroxidases were inactivated in a H₂O₂ solution (3%) for 7 min. The probe GSO477, designed specifically for detection of the entire GSO cluster (5'-CTAAAGTTAACGT-CAAGG-3') was hybridized at 35 °C with 35% formamide. The probe ARC94 (5'-TTAGCATCCCGCTTCGA-3') was hybridized at 46 °C with 20% formamide as described elsewhere³⁸. Washing, signal amplification and epifluorescence microscopy were conducted as described previously³⁹.

Flux modelling. Sulphide, ammonium and nitrate fluxes and rates of sulphide oxidation and nitrate reduction were calculated from the concentration profiles and a vertical diffusion coefficient (*K_z*) with the program Profile¹². A *K_z* value of 0.4 cm² s⁻¹ was reconstructed for the zone of overlapping nitrate and sulphide profiles from *in situ* density⁴⁰. The model predicted zones of net ammonium and sulphide consumption at 110–80 m and net nitrate consumption at 78–105 m.

30. Cline, J. D. Spectrophotometric determination of hydrogen sulfide in natural waters. *Limnol. Oceanogr.* **14**, 454–458 (1969).
31. Hansen, J. W., Thamdrup, B. & Jørgensen, B. B. Anoxic incubation of sediment in gas-tight plastic bags: a method for biogeochemical process studies. *Mar. Ecol. Prog. Ser.* **208**, 273–282 (2000).
32. Thamdrup, B. & Dalsgaard, T. Production of N₂ through anaerobic ammonium oxidation coupled to nitrate reduction in marine sediments. *Appl. Environ. Microbiol.* **68**, 1312–1318 (2002).
33. Kallmeyer, J., Ferdelman, T. G., Weber, A., Fossing, H. & Jørgensen, B. B. A cold chromium distillation procedure for radiolabeled sulfide applied to sulfate reduction measurements. *Limnol. Oceanogr. Methods* **2**, 171–180 (2004).
34. Blazejak, A. *et al.* Phylogeny of 16S rRNA, ribulose 1,5-bisphosphate carboxylase/oxygenase, and adenosine 5'-phosphosulfate reductase genes from gamma- and alphaproteobacterial symbionts in gutless marine worms (Oligochaeta) from Bermuda and the Bahamas. *Appl. Environ. Microbiol.* **72**, 5527–5536 (2006).
35. Kirchman, D. L. *et al.* Structure of bacterial communities in aquatic systems as revealed by filter PCR. *Aquat. Microb. Ecol.* **26**, 13–22 (2001).
36. Zhou, J., Bruns, M. A. & Tiedje, J. M. DNA recovery from soils of diverse composition. *Appl. Environ. Microbiol.* **62**, 316–322 (1996).
37. Pernthaler, A., Pernthaler, J. & Amann, R. Fluorescence in situ hybridization and catalyzed reporter deposition for the identification of marine bacteria. *Appl. Environ. Microbiol.* **68**, 3094–3101 (2002).
38. Snaird, J. *et al.* Phylogenetic analysis and in situ identification of bacteria in activated sludge. *Appl. Environ. Microbiol.* **63**, 2884–2896 (1997).
39. Gloeckner, F. O. *et al.* An in situ hybridization protocol for detection and identification of planktonic bacteria. *Syst. Appl. Microbiol.* **19**, 403–406 (1996).
40. Fennel, K. & Boss, E. Subsurface maxima of phytoplankton and chlorophyll: Steady-state solutions from a simple model. *Limnol. Oceanogr.* **48**, 1521–1534 (2003).

Allergenicity resulting from functional mimicry of a Toll-like receptor complex protein

Aurelien Trompette¹, Senad Divanovic¹, Alberto Visintin⁵, Carine Blanchard², Rashmi S. Hegde³, Rajat Madan¹, Peter S. Thorne⁶, Marsha Wills-Karp⁴, Theresa L. Gioannini^{7,8}, Jerry P. Weiss^{7,8} & Christopher L. Karp¹

Aeroallergy results from maladaptive immune responses to ubiquitous, otherwise innocuous environmental proteins¹. Although the proteins targeted by aeroallergic responses represent a tiny fraction of the airborne proteins humans are exposed to, allergenicity is a quite public phenomenon—the same proteins typically behave as aeroallergens across the human population. Why particular proteins tend to act as allergens in susceptible hosts is a fundamental mechanistic question that remains largely unanswered. The main house-dust-mite allergen, Der p 2, has structural homology with MD-2 (also known as LY96), the lipopolysaccharide (LPS)-binding component of the Toll-like receptor (TLR) 4 signalling complex^{2–4}. Here we show that Der p 2 also has functional homology, facilitating signalling through direct interactions with the TLR4 complex, and reconstituting LPS-driven TLR4 signalling in the absence of MD-2. Mirroring this, airway sensitization and challenge with Der p 2 led to experimental allergic asthma in wild type and MD-2-deficient, but not TLR4-deficient, mice. Our results indicate that Der p 2 tends to be targeted by adaptive immune responses because of its auto-adjuvant properties. The fact that other members of the MD-2-like lipid-binding family are allergens, and that most defined major allergens are thought to be lipid-binding proteins⁵, suggests that intrinsic adjuvant activity by such proteins and their accompanying lipid cargo may have some generality as a mechanism underlying the phenomenon of allergenicity.

Although the potential biological significance of several allergens having protease activity has received experimental attention^{5,6}, cogent mechanistic hypotheses for why most aeroallergens have a propensity to generate maladaptive effector T-cell responses are lacking. TLRs, receptors for conserved microbial structures, have a critical role in the controlling initiation and class specification of adaptive immune responses by antigen-presenting cells (APCs)⁷. Exogenous antigen presentation by APCs in the absence of direct TLR stimulation generally leads to tolerance⁸. Moreover, efficient generation of effector T-cell responses by APCs is dependent on the presence of TLR ligands in the phagosome containing the antigen being presented⁹.

House dust mites are a major source of aeroallergens for patients with allergic asthma¹⁰. Concentrated in mite faecal pellets¹¹, the major group 2 allergens, Der p 2 and Der f 2, are highly allergenic; among defined dust mite antigens, they have the highest rates of skin test positivity in atopic patients¹². Sequence homology places these allergens in the recently recognized MD-2-related lipid-recognition domain family of proteins¹³. Notably, the crystal structures of MD-2 and Der p 2 exhibit structural homology^{2–4}, as previously predicted¹⁴, with two anti-parallel β -pleated sheets stabilized by disulphide bonds and enclosing a hydrophobic cavity accessible from one end. Several

lines of evidence have linked exposure to LPS with regulation of the development of allergic asthma, as well as with exacerbation of existing asthma¹⁵.

These considerations suggested that there may also be functional homology between MD-2 and Der p 2. We examined the effect of Der p 2 on TLR4 signalling in HEK293 cells, which lack endogenous TLR4 and MD-2 but have fully functional TLR signalling machinery. Der p 2 reconstituted LPS-driven TLR4 signalling and interleukin (IL)-8 production in HEK293 cells in the absence of MD-2 (Fig. 1a). Furthermore, Der p 2 augmented LPS-driven IL-8 production in

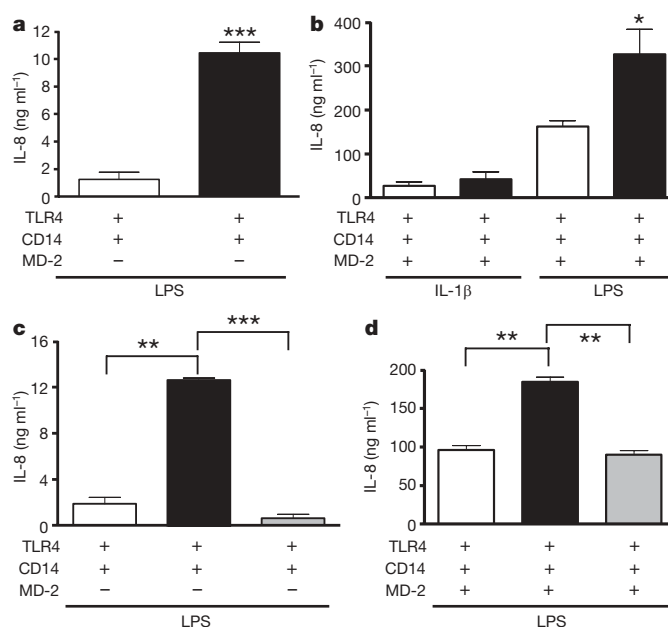


Figure 1 | Der p 2 reconstitutes and amplifies TLR4 signalling in the absence and presence of MD-2, respectively. **a**, HEK293 cells expressing CD14 and TLR4 (HEK293-CD14-TLR4) were transfected with Der p 2 (black bars) or empty vector (white bars), and stimulated (or mock-stimulated) with LPS (10 ng ml⁻¹). **b**, HEK293-CD14-TLR4 cells transfected with MD-2, plus Der p 2 (black bars) or empty vector (white bars), were stimulated (or mock-stimulated) with LPS (10 ng ml⁻¹) or IL-1 β (100 ng ml⁻¹). **c**, **d**, HEK293-CD14-TLR4 cells transfected with Der p 2 (black bars), Der p 2(Y91A) (grey bars) or empty vector (white bars), in the absence (**c**) or presence (**d**) of MD-2, were stimulated (or mock-stimulated) with LPS (10 ng ml⁻¹). Data represent mean and s.e.m. of cultures (stimulated and mock-stimulated) in a single experiment, representative of an experimental $n = 3-8$. * $P < 0.05$; ** $P < 0.005$; *** $P < 0.001$; unpaired t -test.

¹Division of Molecular Immunology, ²Division of Allergy and Immunology, ³Division of Developmental Biology, and ⁴Division of Immunobiology, Cincinnati Children's Hospital Medical Center and the University of Cincinnati College of Medicine, Cincinnati, Ohio 45229, USA. ⁵Division of Infectious Diseases & Immunology, Department of Medicine, University of Massachusetts Medical School, Worcester, Massachusetts 01606, USA. ⁶Department of Occupational and Environmental Health, and ⁷Inflammation Program, Department of Internal Medicine, University of Iowa, Iowa City, Iowa 52241, USA. ⁸Veteran's Affairs Medical Center, Iowa City, Iowa 52247, USA.

HEK293 cells co-expressing TLR4 and MD-2 (Fig. 1b). Notably, LPS-driven TLR4 signalling was more robust in the presence of MD-2 alone in comparison to Der p 2 alone. The effects of Der p 2 on HEK293 cell production of IL-8 were TLR4- and LPS-dependent (data not shown). In contrast, Der p 2 did not increase IL-1-driven IL-8 production (Fig. 1b), suggesting specific effects of Der p 2 on TLR4 activation and not on the signalling pathways shared with the IL-1 receptor. RP105–MD-1, a cell surface heterodimer structurally related to TLR4–MD-2, inhibits TLR4 signalling in myeloid and HEK293 cells; the interaction of RP105–MD-1 with TLR4–MD-2 reduces the ability of the latter complex to bind LPS¹⁶. Der p 2 blunted the decrease in LPS-driven IL-8 production observed in HEK293 cells expressing RP105–MD-1 as well as TLR4–MD-2 (Supplementary Fig. 1).

All sequenced MD-2 species contain a conserved tyrosine (Tyr 102) at a site functionally important for TLR4 signaling^{4,17} (Supplementary Fig. 2). This tyrosine, which resides in a loop formed between cysteines of a disulphide bridge (Cys 95–Cys 105 in MD-2; Cys 89–Cys 94 in Der p 2), is absent in MD-1 but conserved in Der p 2 (Tyr 91). Mutation of this tyrosine to alanine (Y91A) ablated the ability of Der p 2 to reconstitute LPS-driven IL-8 production in HEK293 cells expressing TLR4 without MD-2 (Fig. 1c), or to augment LPS-driven IL-8 production in HEK293 cells co-expressing TLR4 and MD-2 (Fig. 1d). Thus, in HEK293 cells, Der p 2 promotes LPS-induced TLR4 signalling in a manner that appears to depend on Der p 2 and TLR4 interactions.

The direct association of Der p 2 with TLR4 was demonstrated by co-immunoprecipitation in lysates of cells co-expressing epitope-tagged Der p 2–TLR4 (Fig. 2a). Interaction of Der p 2 with the ectodomain of TLR4 (TLR4_{ECD}) was shown by co-capture of Der p 2 by protein G beads after incubation of Der p 2 with a TLR4_{ECD}–Fc fusion protein (Supplementary Fig. 3). Like MD-2, recombinant Der p 2 (rDer p 2) forms disulphide-linked aggregates (Supplementary Fig. 4). In a further parallel with MD-2, it is the monomeric form of Der p 2 that co-immunoprecipitates with TLR4 and with MD-2 (data not shown). Direct association of Der p 2–HA and MD-2–Flag was shown by co-immunoprecipitation in cell lysates using antibodies to haemagglutinin (HA) and Flag (Fig. 2b). Like MD-2, Der p 2 also associated with CD14 (Fig. 2c). Of interest, whereas immunoprecipitation analysis of Der p 2(Y91A) suggested that this non-functional mutant interacts with TLR4 and MD-2 in a manner similar to that

of native Der p 2 (data not shown), Der p 2(Y91A) exhibited increased binding to CD14 in such assays (Supplementary Fig. 5). The ability of Der p 2(Y91A) to bind TLR4 is consistent with crystallographic data that does not show any direct involvement of MD-2 Tyr 102 in the TLR4 interaction⁴. The observed increased affinity of Der p 2(Y91A) for CD14 suggests that this mutation may interfere with TLR4 signalling by altering the dynamics of CD14 engagement and/or LPS transfer. Notably, the co-expression of Der p 2 with MD-2 and TLR4 increased the co-immunoprecipitation of TLR4 with MD-2 (Fig. 2d); this suggests that interactions between the heterodimers TLR4–MD-2 and TLR4–Der p 2 could contribute to the increased TLR4-dependent activation by LPS observed when cells co-expressing TLR4 and MD-2 also express Der p 2 (Fig. 1b, d). Similarly, Der p 2 reduced the co-immunoprecipitation of MD-2 with MD-1 (Supplementary Fig. 6), suggesting that the inhibition of interactions between RP105–MD-1 and MD-2–TLR4 by Der p 2 contributes to the increased activation by LPS of cells co-expressing TLR4–MD-2 and RP105–MD-1 when Der p 2 is present (Supplementary Fig. 1). Furthermore, like MD-2 (but not MD-1)¹⁶, Der p 2 binds LPS, as demonstrated by co-precipitation of Der p 2–HA with biotinylated LPS captured by streptavidin beads (Fig. 2e). Thus, Der p 2 can bind TLR4, MD-2, CD14 and LPS. Taken together, these data suggest that Der p 2 facilitates the aggregation of TLR4 needed for receptor activation by promoting interactions between TLR4–MD-2 and Der p 2–TLR4 in the presence of MD-2, and between TLR4–Der p 2 and Der p 2–TLR4 in the absence of MD-2.

To model the interactions of exogenously delivered Der p 2 with host cells important in inducing adaptive immune responses, we tested the effect of Der p 2 on primary APCs. Der p 2, immunoaffinity-purified from house dust mites, induced TNF- α secretion by mouse bone-marrow-derived dendritic cells (Supplementary Fig. 7). Like LPS-induced signalling in these cells, Der p 2-triggered activation was TLR4-dependent (Supplementary Fig. 7b) but not TLR2-dependent (Supplementary Fig. 7d). In contrast to LPS, Der p 2 could also activate dendritic cells from MD-2-null mice (Supplementary Fig. 7c), mimicking the TLR4-activating properties of LPS–MD-2 complexes^{18,19}. The immunoaffinity-purified Der p 2 was indeed contaminated with endotoxin-like activity (equivalent to 0.4 ng *Escherichia coli* LPS per μ g Der p 2), suggesting that the observed TLR4-dependent activation of dendritic cells by Der p 2 was mediated by endotoxin–Der p 2 complexes.

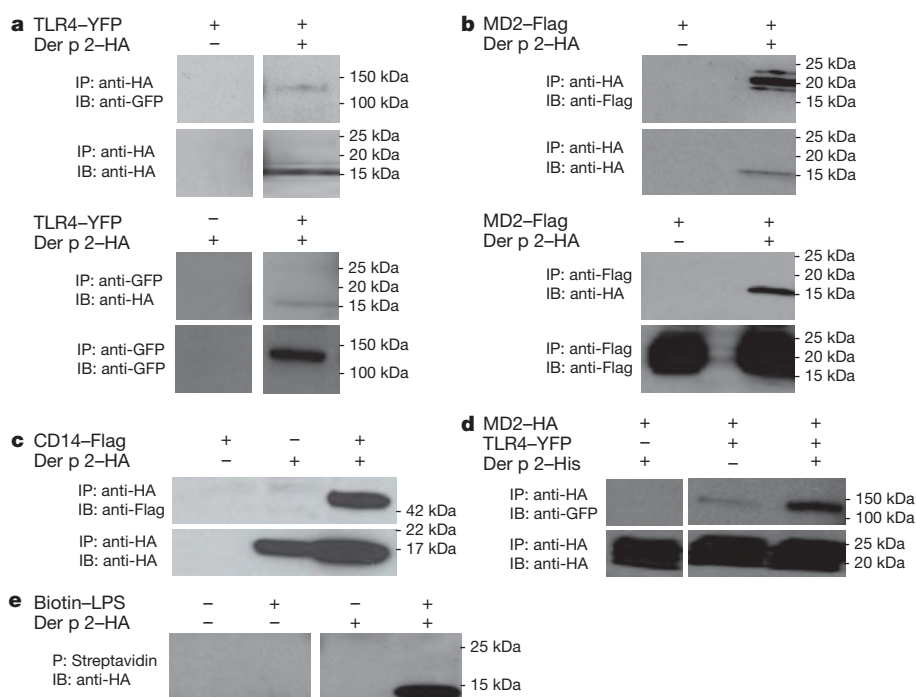


Figure 2 | Der p 2 interacts directly with the TLR4 complex and with LPS. **a**, Co-immunoprecipitation of Der p 2 with TLR4 in lysates of HEK293FT cells transfected with the indicated constructs or empty vector controls (–). GFP, green fluorescent protein; YFP, yellow fluorescent protein. **b**, Co-immunoprecipitation of Der p 2 with MD-2. **c**, Co-immunoprecipitation of Der p 2 with CD14. **d**, Effect of Der p 2 on co-immunoprecipitation of MD-2 with TLR4. **e**, Supernatants from HEK293FT cells transfected with HA-tagged Der p 2 (or empty vector) underwent incubation with biotinylated LPS, precipitation (P) with streptavidin beads, and immunoblotting (IB) with anti-HA antibody. Similar results were seen with immunoaffinity-purified Der p 2 and Der p 2 monoclonal antibody. Data are representative of an experimental $n = 2–8$.

To test this more directly, we generated recombinant Der p 2 in a baculovirus expression system. At physiological temperatures, MD-2 secreted into serum-free media rapidly loses biological activity in the absence of LPS¹⁸. Similarly, rDer p 2 secreted in the absence of LPS was inactive in functional assays (data not shown). Thus, we generated and purified rDer p 2 in the presence of defined amounts of *E. coli* LPS. rDer p 2 recovered under these conditions stimulated TLR4-dependent production of TNF- α , IL-12/23p40 and IL-6 by mouse peritoneal macrophages, in the presence and absence of MD-2 (Supplementary Fig. 8). The amount of LPS co-purified with Der p 2 (60 pg LPS per 100 μ g Der p 2) was sub-stoichiometric, and insufficient to activate the macrophages in the absence of Der p 2 (Supplementary Fig. 8a, c). Thus, exogenously delivered Der p 2 facilitates LPS signalling in primary APCs, with or without MD-2.

Taken together, these data suggest that the propensity of Der p 2 to be a target of adaptive immune responses is due to the fact that Der p 2 promotes TLR4 signalling and thus has auto-adjuvant activity. This also suggested a mechanism for allergenicity. High levels of exposure to bacterial products such as LPS in early life are inversely correlated with the development of atopy and allergic disease^{20–22}. Usually interpreted in the context of the hygiene hypothesis, it is thought that such exposures lead to the development of robust counter-regulatory responses²³. However, epidemiological and human challenge data indicate that LPS exposure can exacerbate established asthma, probably by stimulating pro-inflammatory responses in the airway^{20,24}.

In addition to confirming the ability of LPS to intensify established asthma²⁵, mouse models have provided mechanistic insight into the role of LPS in regulating the development of allergic asthma. Consonant with the hygiene hypothesis, an important variable appears to be the LPS dose. Whereas airway sensitization with a model antigen (ovalbumin; OVA) along with very low-dose (<1 ng) LPS induces tolerance, airway sensitization with OVA along with low-dose (100 ng) LPS drives T_H2 immune responses and allergic asthma in a TLR4-dependent fashion²⁶. Conversely, airway sensitization with OVA along with high-dose (100 μ g) LPS drives a T_H1 response, probably along with a robust regulatory response as well^{26,27}.

We tested the ability of Der p 2 to induce experimental allergic asthma. Sensitization and challenge with Der p 2, along with extremely

low-dose (low pg range) LPS, induced robust airway T_H2 inflammation—marked by airway eosinophilia and lymphocytosis, mucous metaplasia and increased plasma IgE concentrations—in wild type but not TLR4-deficient mice (Fig. 3). Notably, Der p 2 similarly induced T_H2 inflammation in the airways of MD-2-deficient mice (Fig. 4). On the other hand, mutant Der p 2(Y91A) failed to induce experimental allergic asthma (Supplementary Fig. 9). Thus, *in vivo* allergenic activity mirrors *in vitro* functional and biochemical activity: Der p 2 efficiently drives airway T_H2 inflammation *in vivo* in a TLR4-dependent manner, and retains the ability to drive such inflammation in the absence of MD-2.

Der p 2-mediated facilitation of TLR4 signalling under conditions of very low ambient LPS exposure, those associated with increasing rates of atopy and aeroallergy, may thus shift the LPS-response curve into the T_H2-inducing range. Similarly, Der p 2 probably promotes LPS-driven exacerbation of established asthma by facilitating TLR4 signalling by airway cells. Here, the ability of Der p 2 to reconstitute TLR4 signalling in the absence of MD-2 may well be of special importance as airway epithelial cells express TLR4, but little or no MD-2 (ref. 28).

Although the interaction of Der p 2 with vertebrate TLR4–MD-2 is unlikely to be of biological importance to the mite, it is tempting to speculate that Der p 2 has a physiological role in the innate immune system of the dust mite gut. The pathophysiological interactions of Der p 2 with the vertebrate immune system may be more than a unique oddity. Other MD-2-related lipid-recognition domain family members are aeroallergens¹³. More generally, more than 50% of defined major allergens are lipid-binding proteins⁵. Intrinsic adjuvant activity provided by associated lipids may well underlie the allergenicity of such proteins.

METHODS SUMMARY

Generation of recombinant Der p 2. Recombinant His-tagged Der p 2 (rDer p 2) was generated in baculovirus systems using the pAcGP67A transfer vector (BD Pharmingen) and Sf21 cells, and purification with Ni-NTA agarose beads (Qiagen). rDer p 2 was generated under FCS-free conditions (Baculogold Max-XP media, BD Pharmingen), in the presence of *E. coli* LPS (100 ng ml^{−1}) and LPS-free human serum albumin (HSA; 0.25%) as a carrier and for stability²⁹. ***In vitro* cell stimulation.** HEK293 cell stimulation and analysis was as described¹⁶. Bone-marrow-derived dendritic cells and thioglycollate-elicited

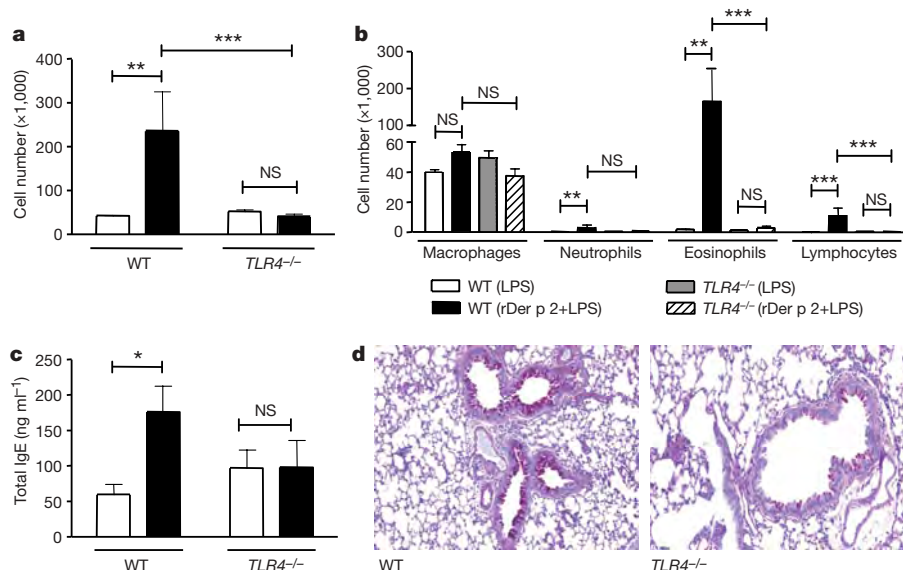


Figure 3 | TLR4-dependent induction of experimental allergic asthma by Der p 2. Wild type (WT) and TLR4-deficient mice were sensitized intranasally on days 0, 1 and 2 with rDer p 2 (0.1 μ g) plus LPS (0.026 pg) in PBS (black bars), or with PBS plus LPS (0.026 pg) (white bars), challenged intranasally with 1/4 of the sensitization dose on days 14, 15, 18 and 19, and analysed on day 21. **a**, Total cell numbers (white bars, PBS and LPS; black bars, Der p 2 and LPS).

b, Differential cell counts. **c**, Total serum IgE (bars as in **a**). **d**, Representative lung sections stained with periodic acid-Schiff. Data (**a–c**) represent mean and s.e.m. of 5–8 animals per group, and are representative of two independent experiments. Original magnification, $\times 100$. * P < 0.05, ** P < 0.01, *** P < 0.001; NS, not significant; two-way analysis of variance (ANOVA) on log-transformed data.

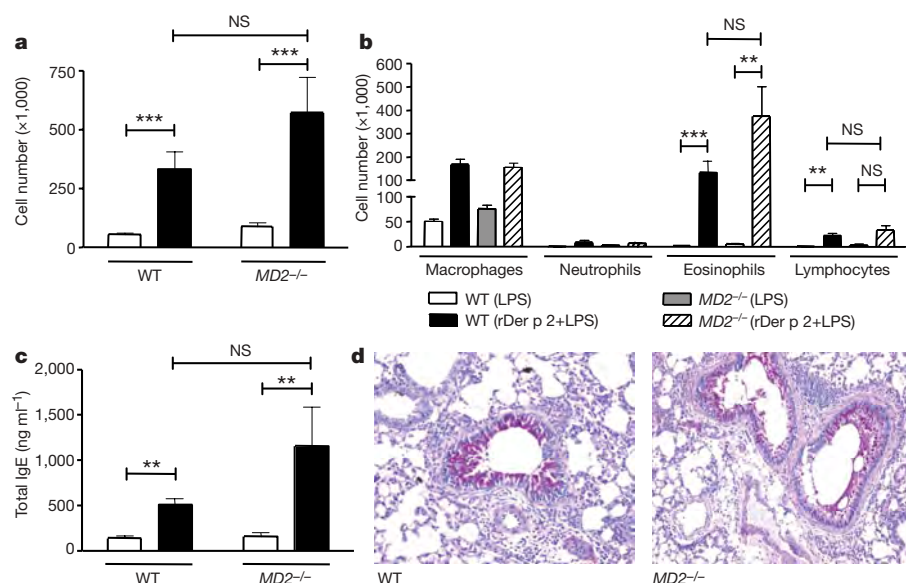


Figure 4 | Der p 2 induces experimental allergic asthma in the absence of MD-2. Wild-type (WT) and MD-2-deficient mice were sensitized, challenged and analysed as in Fig. 3, except for the use of 10-fold higher doses of Der p 2, given the less robust stimulation of TLR4 by Der p 2 observed in the absence of MD-2.

a, b, Inflammatory cells in bronchoalveolar lavage fluids. **a**, Total cell numbers (white bars, PBS and LPS; black bars, Der p 2 and LPS). **b**, Differential cell counts. **c**, Total serum IgE (bars as in **a**). **d**, Representative lung sections stained with periodic acid-Schiff. Data (**a–c**) represent mean and s.e.m. of 5–9 animals per group. Original magnification, $\times 100$. * $P < 0.05$, ** $P < 0.01$, *** $P < 0.001$; two-way ANOVA on log-transformed data.

peritoneal macrophages were generated as described¹⁶ from wild type, *MD-2*^{-/-} (K. Miyake), *Tlr2*^{-/-} and *Tlr4*^{-/-} mice (S. Akira)—all on a C57BL/6 background (>10 generations). Twenty-four hours after stimulation (or mock-stimulation), cell-free supernatants were collected and cytokine production was quantified by ELISA (BD Pharmingen).

Experimental allergic asthma model. Ten–twelve-week-old female wild type, *MD-2*^{-/-} and *Tlr4*^{-/-} mice were sensitized and challenged according to the protocol previously described²⁶, with minor modifications. In brief, mice anaesthetized with ketamine-xylazine were sensitized intranasally on days 0, 1 and 2 with either rDer p 2 (0.1 μ g) in PBS (co-purified with *E. coli* LPS (0.026 μ g) and HSA (0.3 ng)), or with PBS (with *E. coli* LPS (0.026 μ g) and HSA (0.3 ng)). Mice were subsequently challenged intranasally with 1/4 of the sensitization dose on days 14, 15, 18 and 19. For experiments with *MD-2*^{-/-} mice, sensitization and challenge doses of Der p 2–LPS were 10-fold higher. On day 21, mice were killed and airway inflammation, serum IgE concentrations and airway mucus metaplasia were assessed as previously described³⁰. Animal care was provided in accordance with National Institutes of Health guidelines in studies approved by the CCHMC IACUC.

Full Methods and any associated references are available in the online version of the paper at www.nature.com/nature.

Received 19 September; accepted 14 October 2008.

Published online 7 December 2008; corrected 29 January (details online).

- Wills-Karp, M. Immunologic basis of antigen-induced airway hyperresponsiveness. *Annu. Rev. Immunol.* **17**, 255–281 (1999).
- Ohto, U. et al. Crystal structures of human MD-2 and its complex with antiendotoxin lipid Iva. *Science* **316**, 1632–1634 (2007).
- Derewenda, U. et al. The crystal structure of a major dust mite allergen Der p 2, and its biological implications. *J. Mol. Biol.* **318**, 189–197 (2002).
- Kim, H. M. et al. Crystal structure of the TLR4-MD-2 complex with bound endotoxin antagonist eritoran. *Cell* **130**, 906–917 (2007).
- Thomas, W. R. et al. Structural biology of allergens. *Curr. Allergy Asthma Rep.* **5**, 388–393 (2005).
- Sokol, C. L. et al. A mechanism for the initiation of allergen-induced T helper type 2 responses. *Nature Immunol.* **9**, 310–318 (2008).
- Iwasaki, A. & Medzhitov, R. Toll-like receptor control of the adaptive immune responses. *Nature Immunol.* **5**, 987–995 (2004).
- Sporri, R. & Reis e Sousa, C. Inflammatory mediators are insufficient for full dendritic cell activation and promote expansion of CD4⁺ T cell populations lacking helper function. *Nature Immunol.* **6**, 163–170 (2005).
- Blander, J. M. & Medzhitov, R. Toll dependent selection of microbial antigens for presentation by dendritic cells. *Nature* **440**, 808–812 (2006).
- Maunsell, K. et al. Mites and house-dust allergy in bronchial asthma. *Lancet* **291**, 1270–1270 (1968).
- Park, G. M. et al. Localization of a major allergen, Der p 2, in the gut and faecal pellets of *Dermatophagoides pteronyssinus*. *Clin. Exp. Allergy* **30**, 1293–1297 (2000).
- Heymann, P. W. et al. Antigenic and structural analysis of group II allergens (Der p II and Der p II) from house dust mites (*Dermatophagoides* spp.). *J. Allergy Clin. Immunol.* **83**, 1055–1067 (1989).
- Inohara, N. & Nunez, G. ML—a conserved domain involved in innate immunity and lipid metabolism. *Trends Biochem. Sci.* **27**, 219–221 (2002).

- Gruber, A. et al. Structural model of MD-2 and functional role of its basic amino acid clusters involved in cellular lipopolysaccharide recognition. *J. Biol. Chem.* **279**, 28475–28482 (2004).
- Williams, L. K. et al. The role of endotoxin and its receptors in allergic disease. *Ann. Allergy Asthma Immunol.* **94**, 323–332 (2005).
- Divanovic, S. et al. Negative regulation of Toll-like receptor 4 signaling by the Toll-like receptor homolog RP105. *Nature Immunol.* **6**, 571–578 (2005).
- Kawasaki, K. et al. Identification of mouse MD-2 residues important for forming the cell surface TLR4-MD-2 complex recognized by anti-TLR4-MD-2 antibodies, and for conferring LPS and taxol responsiveness on mouse TLR4 by alanine-scanning mutagenesis. *J. Immunol.* **170**, 413–420 (2003).
- Kennedy, M. N. et al. A complex of soluble MD-2 and lipopolysaccharide serves as an activating ligand for Toll-like receptor 4. *J. Biol. Chem.* **279**, 34698–34704 (2004).
- Gioannini, T. L. et al. Isolation of an endotoxin-MD-2 complex that produces Toll-like receptor 4-dependent cell activation at picomolar concentrations. *Proc. Natl Acad. Sci. USA* **101**, 4186–4191 (2004).
- Braun-Fahrlander, C. et al. Environmental exposure to endotoxin and its relation to asthma in school-age children. *N. Engl. J. Med.* **347**, 869–877 (2002).
- Gehring, U. et al. House dust endotoxin and allergic sensitization in children. *Am. J. Respir. Crit. Care Med.* **166**, 939–944 (2002).
- Riedler, J. et al. Exposure to farming in early life and development of asthma and allergy: a cross-sectional survey. *Lancet* **358**, 1129–1133 (2001).
- Wills-Karp, M. et al. The germless theory of allergic disease: revisiting the hygiene hypothesis. *Nature Rev. Immunol.* **1**, 69–75 (2001).
- Michel, O. et al. Effect of inhaled endotoxin on bronchial reactivity in asthmatic and normal subjects. *J. Appl. Physiol.* **66**, 1059–1064 (1989).
- Tulic, M. K. et al. Modification of the inflammatory response to allergen challenge after exposure to bacterial lipopolysaccharide. *Am. J. Respir. Cell Mol. Biol.* **22**, 604–612 (2000).
- Eisenbarth, S. C. et al. Lipopolysaccharide-enhanced, toll-like receptor 4-dependent T helper cell type 2 responses to inhaled antigen. *J. Exp. Med.* **196**, 1645–1651 (2002).
- Herrick, C. A. & Bottomly, K. To respond or not to respond: T cells in allergic asthma. *Nature Rev. Immunol.* **3**, 405–412 (2003).
- Jia, H. P. et al. Endotoxin responsiveness of human airway epithelia is limited by low expression of MD-2. *Am. J. Physiol. Lung Cell. Mol. Physiol.* **287**, L428–L437 (2004).
- Teghanemt, A. et al. Transfer of monomeric endotoxin from MD-2 to CD14: characterization and functional consequences. *J. Biol. Chem.* **282**, 36250–36256 (2007).
- Wills-Karp, M. et al. Interleukin-13: central mediator of allergic asthma. *Science* **282**, 2258–2261 (1998).

Supplementary Information is linked to the online version of the paper at www.nature.com/nature.

Acknowledgements We thank S. Vogel for re-purified LPS; E. Kurt-Jones and R. Finberg for HEK293 cells expressing TLR4 complex proteins, N. J. Gay for discussions, and L. Flick and J. Bohnert for technical assistance. This work was funded by grants from the Sandler Foundation for Asthma Research (C.L.K.), the National Institute of Allergy and Infectious Diseases (C.L.K., J.P.W.), and the Veteran's Administration (T.L.G.).

Author Information Reprints and permissions information is available at www.nature.com/reprints. Correspondence and requests for materials should be addressed to C.L.K. (chris.karp@chmc.org).

METHODS

Reagents, expression constructs and cell lines. IL-1 β was from Peprotech. Repurified *E. coli* K235 LPS was from S. Vogel. Pam₃Cys was from EMC Microcollections. Complementary DNA encoding Der p 2 was from Heska Corp. Immunoaffinity-purified Der p 2 was from Indoor Biotechnologies. Recombinant His-tagged Der p 2 (rDer p 2) was generated in baculovirus systems using the pAcGP67A transfer vector (BD Pharmingen) and Sf21 cells, and purification was with Ni-NTA agarose beads (Qiagen). rDer p 2 was generated under FCS-free conditions (Baculogold Max-XP media, BD Pharmingen), in the presence of *E. coli* LPS (100 ng ml⁻¹) and LPS-free human serum albumin (HSA; 0.25%) as a carrier and for stability²⁹. Der p 2(Y91A) was generated by PCR-mediated mutagenesis. HEK293 cell lines stably expressing CD14–TLR4, and HEK293FT cells, have been described¹⁶. All cell lines were *Mycoplasma*-free. All reagents contacting cultured cells were LPS-free to the limits of detection of the *Limulus* amoebocyte lysate assay (Lonza) at the concentrations used, unless otherwise stated. Human RP105, MD-1, TLR4 and MD-2 expression constructs were as described¹⁶. Der p 2 was cloned into the pCEFL-HA mammalian expression vector (INSERM U482, France). Epitope-tagged constructs were generated by PCR. Transient transfections were performed using PolyFect (Qiagen).

Immunoprecipitation and western blotting. These were performed as described previously¹⁶.

In vitro cell stimulation. One day after transient transfection of HEK293 cells, media was replaced. Seventy-two hours later, cells were stimulated (or mock-stimulated) for a further 24 h. Cell-free supernatants were collected and IL-8 production was quantified by ELISA (BD Pharmingen). Bone marrow-derived dendritic cells and thioglycollate-elicited peritoneal macrophages were generated as described¹⁶ from wild type, *Md-2*^{-/-} (K. Miyake), *Tlr2*^{-/-} and *Tlr4*^{-/-} mice (S. Akira)—all on a C57BL/6 background (>10 generations). Twenty-four hours after stimulation (or mock-stimulation), cell-free supernatants were collected and TNF- α , IL-12/23p40 and IL-6 production were quantified by ELISA (BD Pharmingen).

Experimental allergic asthma model. Wild type, *Md-2*^{-/-} and *Tlr4*^{-/-} mice were sensitized and challenged according to the previously described protocol²⁶, with minor modifications. Ten–twelve-week-old female mice were used in all experiments. In brief, mice anaesthetized with ketamine-xylazine were sensitized intranasally on days 0, 1 and 2 with (a) rDer p 2 (0.1 μ g) in PBS (co-purified with *E. coli* LPS (0.026 μ g) and HSA (0.3 ng)) or (b) PBS (with *E. coli* LPS (0.026 μ g) and HSA (0.3 ng)). Mice were subsequently challenged intranasally with 1/4 of the sensitization dose on days 14, 15, 18 and 19. For experiments with *Md-2*^{-/-} mice, sensitization and challenge doses of Der p 2–LPS were 10-fold higher. On day 21, mice were killed, and airway inflammation, total serum IgE concentrations and airway mucus metaplasia were assessed as previously described³⁰. Animal care was provided in accordance with National Institutes of Health guidelines; studies were approved by the CCHMC IACUC.

WNT11 acts as a directional cue to organize the elongation of early muscle fibres

Jérôme Gros^{1,†}, Olivier Serralbo¹ & Christophe Marcelle¹

The early vertebrate skeletal muscle is a well-organized tissue in which the primitive muscle fibres, the myocytes, are all parallel and aligned along the antero-posterior axis of the embryo. How myofibres acquire their orientation during development is unknown. Here we show that during early chick myogenesis WNT11 has an essential role in the oriented elongation of the myocytes. We find that the neural tube, known to drive *WNT11* expression in the medial border of somites¹, is necessary and sufficient to orient myocyte elongation. We then show that the specific inhibition of *WNT11* function in somites leads to the disorganization of myocytes. We establish that WNT11 mediates this effect through the evolutionary conserved planar cell polarity (PCP) pathway, downstream of the WNT/ β -catenin-dependent pathway, required to initiate the myogenic program of myocytes and *WNT11* expression. Finally, we demonstrate that a localized ectopic source of WNT11 can markedly change the orientation of

myocytes, indicating that WNT11 acts as a directional cue in this process. All together, these data show that the sequential action of the WNT/PCP and the WNT/ β -catenin pathways is necessary for the formation of fully functional embryonic muscle fibres. This study also provides evidence that WNTs can act as instructive cues to regulate the PCP pathway in vertebrates.

In amniotes, the formation of the myotome is initiated at the medial border of the somite (the dorso-medial lip or DML²), directly opposite to the neural tube (Supplementary Fig. 1a, a'). Through a morphogenetic process that has yet to be characterized, cells from the DML enter the transition zone where they initiate the expression of muscle-specific markers (such as MYF5) and shut off the expression of dermomyotome-specific genes (such as PAX3 and PAX7; Supplementary Fig. 1b–d and Supplementary Movie 1). An analysis of a live chick embryo specimen using time-lapse video confocal microscopy showed that, within the transition zone, cells first lost

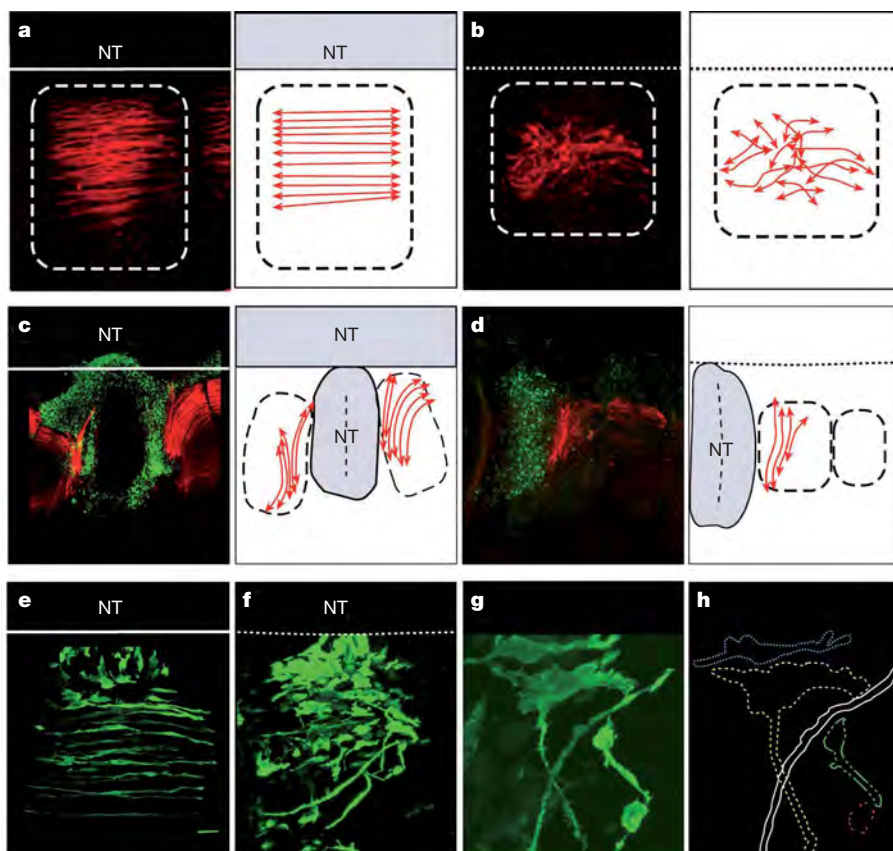
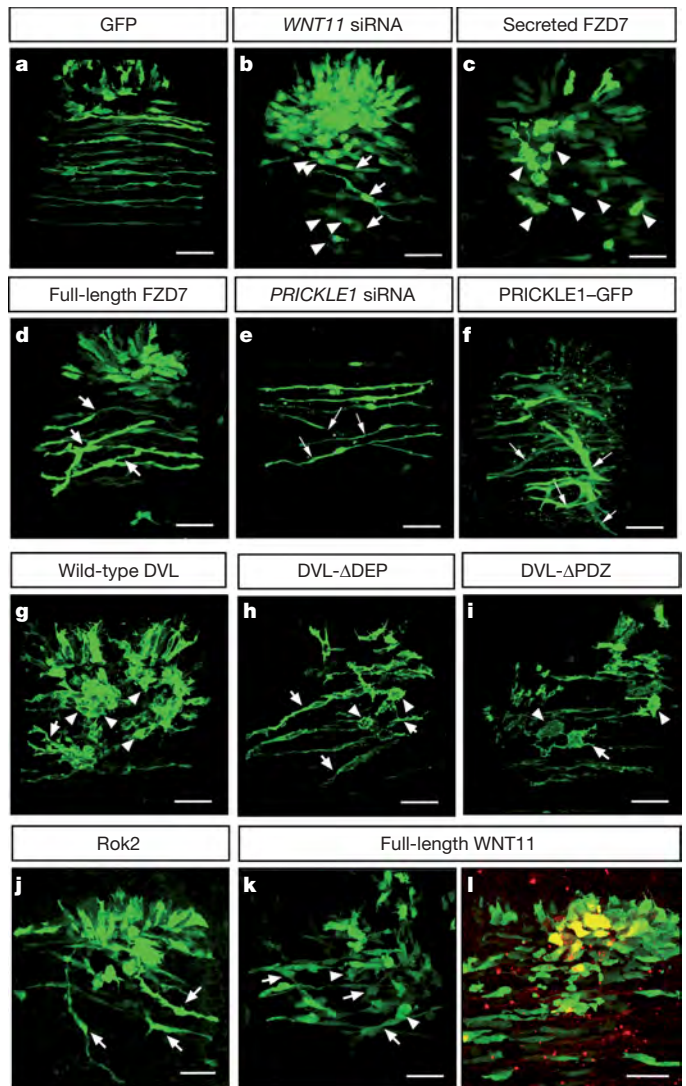


Figure 1 | The neural tube is necessary and sufficient for the oriented elongation of the myocytes. **a, b**, Myotome organization (revealed with a myosin heavy chain antibody) in the presence (**a**) or absence (**b**) of the neural tube (NT). **c, d**, Myotome organization after grafting an ectopic neural tube between two somites of a normal embryo (**c**) or of a neural-tube-ablated embryo (**d**). In **c** and **d**, red is myosin heavy chain staining, and green reveals the expression of *WNT11* messenger RNA by fluorescent *in situ* hybridization. **e–g**, Myocyte organization after electroporation of GFP in DML cells in control (**e**) or neural-tube-ablated (**f**) embryos. **g** is an enlargement of **f**. **h** summarizes the aberrant shapes and orientations of cells in **g**. Solid and dashed horizontal lines show the position of the neural tube in normal (solid) or neural tube-ablated (dashed) embryos. The dashed boxes outline the somites.

¹Developmental Biology Institute of Marseille Luminy (IBDML), Université de la Méditerranée, CNRS UMR 6216, Campus de Luminy, case 907, 13288 Marseille Cedex 09, France.
[†]Present address: Harvard Medical School Department of Genetics, 77 Avenue Louis Pasteur, NRB 360, Boston, Massachusetts 02115, USA.

We next determined whether WNT11 acts through the PCP pathway, as previously reported during convergence extension movements in vertebrates^{5,9–11}. Frizzled 7, 2 and 1 are expressed in the DML and in the transition zone¹². Because frizzled 7 (FZD7) has been shown to mediate WNT11 activity during convergence extension



movements in vertebrates^{13,14}, we electroporated a secreted form of FZD7, acting as a competitive inhibitor of FZD7 function¹⁵. Electroporated cells failed to elongate along the antero-posterior axis (Fig. 2c). Similarly, when a full-length FZD7 was overexpressed, myocytes elongated aberrantly (Fig. 2d). Prickle homologue 1 (PRICKLE1) is a core PCP molecule that does not have any known role in β -catenin-dependent WNT signalling and that is required for PCP in invertebrates and vertebrates¹⁶. PRICKLE1 is expressed by the elongating myocytes within the transition zone (ref. 17 and Supplementary Fig. 4e). The overexpression of a GFP-fusion chick PRICKLE construct and the specific knockdown of chick PRICKLE by siRNAs resulted in the disorganized elongation of myocytes (Fig. 2e, f and Supplementary Fig. 4c–d', f). The intracellular downstream effector of frizzled—dishevelled (DVL)—mediates the activity of both the β -catenin-dependent and the PCP pathways. Various *dvl* constructs have been shown to interfere with one or both pathways in *Drosophila* or *Xenopus*^{5,10,18,19}. The full-length *dvl*, and constructs that lack the PDZ domain (*dvl-APDZ*) or the DEP domain (*dvl-ADEP*), interfere with the WNT/PCP pathway during vertebrate gastrulation^{5,10,19}. The expression of all three constructs in the DML

resulted in failure of electroporated cells to elongate properly within the myotome (Fig. 2g–i). Downstream effectors of the WNT/PCP pathway comprise the small GTPases RHO and RAC and their associated kinases, ROCK and JNK, respectively. The overexpression of the RHO kinase *rok2* (also known as *rock2a*) (which acts downstream of WNT11 during fish gastrulation²⁰) in the DML resulted in the formation of mis-oriented or multipolar myocytes (Fig. 2j). Finally, *WNT11* overexpression in the DML led to myocyte elongation defects and resulted in a robust phosphorylation of JNK within the transition zone (Fig. 2k, l), indicating that WNT11 is able to activate this WNT/PCP target. All together, these data indicate that WNT11 regulates the polarized elongation of myocytes through the PCP pathway.

WNT11 can activate, in addition to the PCP pathway, the canonical, β -catenin-dependent pathway, for example, during axis formation in *Xenopus*²¹. We determined whether the regulation of the polarized elongation of myocytes by WNT11 and its downstream effectors is the result of activation of the PCP pathway only or of the canonical pathway as well. The initiation of MYF5 expression in the DML was shown to depend on WNT/ β -catenin-dependent signalling in mice²². Consistent with this, the electroporation of an activated form of β -catenin or of the full-length form of DVL, which both activate the WNT/ β -catenin-dependent pathway, resulted in the overexpression of MYF5 (Fig. 3d, e, i, j) in comparison with controls (Fig. 3a, f). In contrast, the electroporation of dominant-negative forms of β -catenin or lymphoid enhancer-binding factor 1 (LEF1), which repress the WNT/ β -catenin-dependent pathway, resulted in the inhibition of its expression (Fig. 3b, c, g, h). These results confirm that the WNT/ β -catenin-dependent pathway is necessary for muscle fate acquisition; they show that the expression of MYF5 can serve as a read-out of the activity of this pathway in the DML. When chick *WNT11*,

secreted *FZD7*, siRNAs directed against chick *WNT11*, *dvl-APDZ* or *dvl- Δ DEP* (the latter being a specific inhibitor of the WNT/PCP pathway^{23,24}) were electroporated in the DML, *MYF5* expression was neither upregulated nor downregulated, indicating that these constructs do not modulate the WNT/ β -catenin-dependent pathway within the transition zone (Fig. 3k–t). This indicates that the elongation defects provoked by these constructs are due to a modulation of the PCP pathway only. The inhibition of WNT/ β -catenin-dependent signalling also resulted in elongation defects of the electroporated cells. However, those cells did not activate *MYF5* expression (Fig. 3g, h), although they retained the expression of the dermomyotome marker PAX7 (not shown). It is likely that the blockage of the β -catenin-dependent pathway maintains the cells in an early, undifferentiated ($PAX7^+MYF5^-$) state that prevents their maturation into polarized and elongating myocytes. Together with the observation that canonical WNT signalling regulates *WNT11* expression (Supplementary Fig. 3), this indicates that β -catenin-dependent WNT signalling is a necessary step upstream of muscle fibre polarized elongation, itself regulated by the WNT11/PCP pathway.

In *Drosophila*, the establishment of planar cell polarity through the PCP pathway is thought to be WNT-ligand-independent. In vertebrates, although WNTs are required for the PCP pathway, experimental evidence indicates that these molecules act as permissive, rather than instructive, cues⁹. We tested whether *WNT11* expressed by the cells of the DML provides an instructive or a permissive signal to the elongating myocytes in the transition zone. We exposed differentiating myocytes to localized exogenous sources of WNT11. Cells expressing WNT11 were placed between two adjacent, newly formed somites. Myocytes that formed in these conditions elongated parallel to the grafted cells (Fig. 4b, e) whereas myocytes elongated normally in embryos grafted with control cells (Fig. 4a, d). Second,

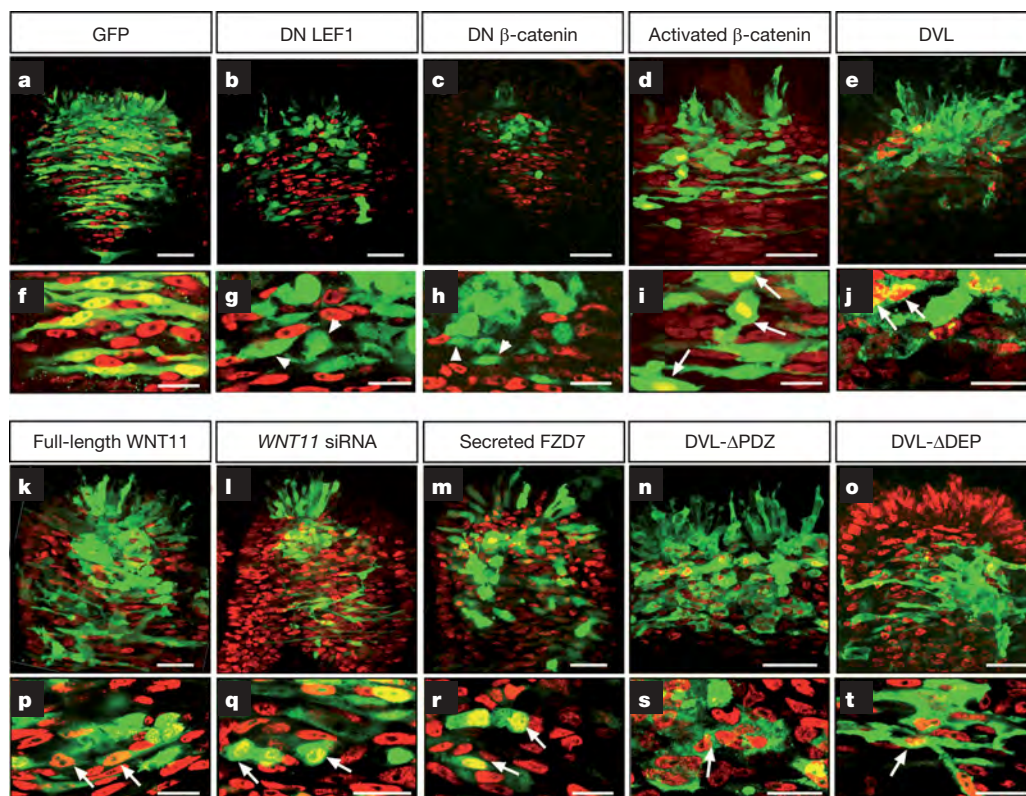


Figure 3 | The WNT/ β -catenin-dependent pathway, and not the PCP pathway, is required for muscle identity acquisition. a–t, Dorsal views of somites electroporated in the DML, immunostained for MYF5. All myocytes electroporated with GFP (a) within the myotome express the early muscle marker MYF5 (in red, f). Cells expressing dominant-negative (DN) LEF1 (b, g) or DN β -catenin (c, h) do not express MYF5; cells expressing an

activated form of β -catenin (d, i) or wild-type *dvl* (e, j) upregulate MYF5 expression (arrows). Cells expressing full-length *WNT11* (k, p), siRNA against *WNT11* (l, q), the secreted form of *FZD7* (l, r), *dvl- Δ PDZ* (n, s) or *dvl- Δ DEP* (o, t) do not display any change in MYF5 expression pattern. Scale bars, 50 μ m.

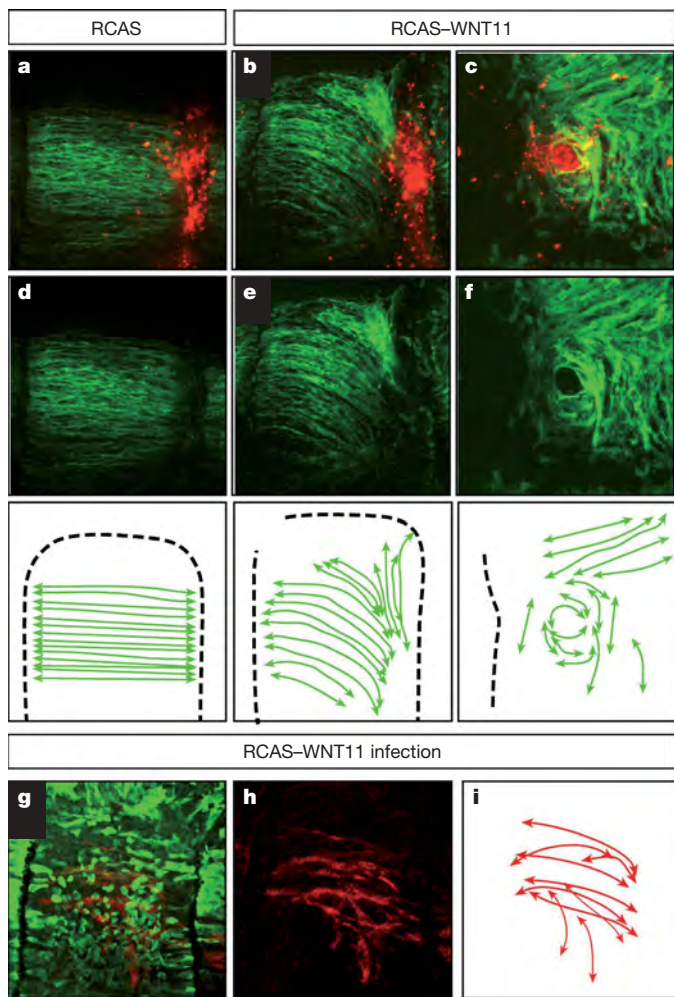


Figure 4 | WNT11 acts as an instructive cue during myocyte elongation. Dorsal views of somites where control cells (a, d) or WNT11-expressing cells (b, c, e, f) were placed between two somites (a, b, d, e) or within the myotome (c, f). The injected cells were labelled with the lipophilic dye Dil and are coloured red, whereas an antibody staining for myosin heavy chain (green) reveals the organization of the myotome. The bottom panels of d–f are schematics summarizing the results obtained in a–f, showing that control cells do not affect myocyte orientation whereas cells expressing WNT11 reorient myocytes according to the new source of WNT11. g–i, Dorsal view of an embryo homogeneously infected with RCAS-WNT11 retroviruses (in green) showing disorganized myocytes (in red).

when small aggregates of WNT11-expressing cells were placed within the somite, myocytes were found to swirl around the injected cells (Fig. 4c, f). These experiments demonstrate that myocytes elongate parallel to a localized source of WNT11. In a reverse experiment, myocytes elongating in a somite uniformly expressing WNT11 elongated in a disorganized manner (Fig. 4g–i). These results show the crucial importance of a local source of WNT11 for the oriented elongation of myocytes and they demonstrate that WNT11 acts as an instructive cue interpreted by myocytes to determine the orientation of their elongation.

The mechanism by which the WNT11 signal is translated intracellularly is unclear. We observed that electroporated DVL–GFP and PRICKLE1–GFP were recruited to the plasma membrane in normally elongating myocytes (Supplementary Fig. 5a, b'), probably reflecting the subcellular localization of their endogenous counterparts. The recruitment of the cytoplasmic proteins PRICKLE and DVL at the membrane by strabismus (STBM, also known as van gogh like 1, VANGL1) and frizzled is known to be associated with the activation of the PCP pathway^{19,25,26}. By contrast with the situation described in *Drosophila*, in which core PCP molecules are asymmetrically

distributed within the epithelial cells of the wing¹⁶, we did not observe an asymmetric localization of the GFP-tagged PRICKLE1 and DVL in elongating myocytes. Symmetric distribution of PCP core proteins has been reported in other PCP-driven processes, for example VANGL2 during mouse neural tube closure²⁷, PRICKLE and DVL during ascidian notochord convergence extension movements²⁸, or DVL2 during mouse neural tube closure²⁹. These are all examples of intercalating, rearranging cells within a tissue (as is myocyte elongation), and the symmetric localization of core PCP molecules might thus characterize such processes. Further analysis of myotome formation will help in elucidating how the positional information conveyed by the WNT11 signal is translated into polarized growth by elongating muscle fibres.

METHODS SUMMARY

Electroporation, confocal analysis and cell injection. Electroporation was performed as described previously^{2,30}. Antibodies used were mouse anti-myosin heavy chain (MF20), anti-PAX3 and anti-PAX7 (Hybridoma Bank); rabbit anti-GFP (Abcam); rabbit anti-RFP (MBL); rabbit anti-phosphorylated JNK (Santa Cruz); and rabbit anti-chick MYF5 (gift from B. Paterson).

The *Xenopus* complementary DNAs of *dvl*, *dvl-ADIX*, *dvl-ADEP* and *dvl-APDZ*, fused to GFP, were cloned into the pCAGG vector. A dominant-negative form of *Xenopus* β -catenin (provided by P. McCrea), a dominant-negative form of chick *LEF1* (provided by J. C. Izpisua-Belmonte), a dominant-negative form and the full-length cDNA of quail *WNT11* (ref. 1), full-length *Danio rerio rok2* cDNA (provided by L. Solnica-Kretzel), and full-length and secreted cDNA of chick *FZD7* were cloned into the pCLGFP electroporation vector. The RCAS–WNT11 construct was a gift from P. Francis-West.

siRNAs targeting *WNT11*, *PRICKLE1* and luciferase were designed and produced as described previously⁸. The target sequences for chick *WNT11* siRNA are AUCAGGAUCACAAGCCAAUAAA and GUGCUGCUAUGUCACCUGUAAA. Those for chick *PRICKLE1* are GUGAGAUACUGCCAGUCUUUAA and UCUUCUGAAGUUUGGUGAUAAA. *In situ* hybridizations were performed as described previously¹².

WNT11-producing chicken fibroblast cells (DF1), transfected with the RCAS–WNT11 construct, were pressure-injected into somites of E2.5 developing chick embryos as described previously¹².

Time-lapse experiments and confocal analysis. Embryos were electroporated with a floxed GFP vector ($1 \mu\text{g} \mu\text{l}^{-1}$) together with a Cre expression vector ($10 \text{ ng} \mu\text{l}^{-1}$; gifts from X. Morin) to generate isolated GFP-expressing cells within the transition zone. After 12–17 h of re-incubation, thick slices of embryos containing the electroporated somites were isolated. Embryo slices were filmed as described previously³⁰ with a confocal two-photon inverted Zeiss LSM510 NLO microscope and a Mai-Tai Laser (SpectraPhysics) at a wavelength of 870 nm. Image stacks (Supplementary Movie 1) were three-dimensionally rendered with Volocity software.

Full Methods and any associated references are available in the online version of the paper at www.nature.com/nature.

Received 7 August; accepted 15 October 2008.

Published online 5 November 2008.

- Marcelle, C., Stark, M. R. & Bronner-Fraser, M. Coordinate actions of BMPs, Wnts, Shh and noggin mediate patterning of the dorsal somite. *Development* **124**, 3955–3963 (1997).
- Gros, J., Scaal, M. & Marcelle, C. A two-step mechanism for myotome formation in chick. *Dev. Cell* **6**, 875–882 (2004).
- Kahane, N., Ben-Yair, R. & Kalcheim, C. Medial pioneer fibers pattern the morphogenesis of early myoblasts derived from the lateral somite. *Dev. Biol.* **305**, 439–450 (2007).
- Ikeya, M. & Takada, S. Wnt signaling from the dorsal neural tube is required for the formation of the medial dermomyotome. *Development* **125**, 4969–4976 (1998).
- Heisenberg, C. P. et al. Silberblick/Wnt11 mediates convergent extension movements during zebrafish gastrulation. *Nature* **405**, 76–81 (2000).
- Tada, M. & Smith, J. C. Xwnt11 is a target of *Xenopus* Brachyury: regulation of gastrulation movements via Dishevelled, but not through the canonical Wnt pathway. *Development* **127**, 2227–2238 (2000).
- Voiculescu, O., Bertocchi, F., Wolpert, L., Keller, R. E. & Stern, C. D. The amniote primitive streak is defined by epithelial cell intercalation before gastrulation. *Nature* **449**, 1049–1052 (2007).
- Das, R. M. et al. A robust system for RNA interference in the chicken using a modified microRNA operon. *Dev. Biol.* **294**, 554–563 (2006).
- Klein, T. J. & Mlodzik, M. Planar cell polarization: an emerging model points in the right direction. *Annu. Rev. Cell Dev. Biol.* **21**, 155–176 (2005).

10. Wallingford, J. B. *et al.* Dishevelled controls cell polarity during *Xenopus* gastrulation. *Nature* **405**, 81–85 (2000).
11. Wang, Y. & Nathans, J. Tissue/planar cell polarity in vertebrates: new insights and new questions. *Development* **134**, 647–658 (2007).
12. Linker, C., Lesbros, C., Stark, M. R. & Marcelle, C. Intrinsic signals regulate the initial steps of myogenesis in vertebrates. *Development* **130**, 4797–4807 (2003).
13. Djiane, A., Riou, J., Umbhauer, M., Boucaut, J. & Shi, D. Role of frizzled 7 in the regulation of convergent extension movements during gastrulation in *Xenopus laevis*. *Development* **127**, 3091–3100 (2000).
14. Witzel, S., Zimyanin, V., Carreira-Barbosa, F., Tada, M. & Heisenberg, C. P. Wnt11 controls cell contact persistence by local accumulation of Frizzled 7 at the plasma membrane. *J. Cell Biol.* **175**, 791–802 (2006).
15. Bhanot, P. *et al.* A new member of the frizzled family from *Drosophila* functions as a Wingless receptor. *Nature* **382**, 225–230 (1996).
16. Seifert, J. R. & Mlodzik, M. Frizzled/PCP signalling: a conserved mechanism regulating cell polarity and directed motility. *Nature Rev. Genet.* **8**, 126–138 (2007).
17. Cooper, O., Sweetman, D., Wagstaff, L. & Munsterberg, A. Expression of avian prickle genes during early development and organogenesis. *Dev. Dyn.* **237**, 1442–1448 (2008).
18. Axelrod, J. D., Miller, J. R., Shulman, J. M., Moon, R. T. & Perrimon, N. Differential recruitment of Dishevelled provides signaling specificity in the planar cell polarity and Wingless signaling pathways. *Genes Dev.* **12**, 2610–2622 (1998).
19. Rothbacher, U. *et al.* Dishevelled phosphorylation, subcellular localization and multimerization regulate its role in early embryogenesis. *EMBO J.* **19**, 1010–1022 (2000).
20. Marlow, F., Topczewski, J., Sepich, D. & Solnica-Krezel, L. Zebrafish Rho kinase 2 acts downstream of Wnt11 to mediate cell polarity and effective convergence and extension movements. *Curr. Biol.* **12**, 876–884 (2002).
21. Tao, Q. *et al.* Maternal wnt11 activates the canonical wnt signaling pathway required for axis formation in *Xenopus* embryos. *Cell* **120**, 857–871 (2005).
22. Borello, U. *et al.* The Wnt/beta-catenin pathway regulates Gli-mediated Myf5 expression during somitogenesis. *Development* **133**, 3723–3732 (2006).
23. Boutros, M., Paricio, N., Strutt, D. I. & Mlodzik, M. Dishevelled activates JNK and discriminates between JNK pathways in planar polarity and wingless signaling. *Cell* **94**, 109–118 (1998).
24. Li, L. *et al.* Dishevelled proteins lead to two signaling pathways. Regulation of LEF-1 and c-Jun N-terminal kinase in mammalian cells. *J. Biol. Chem.* **274**, 129–134 (1999).
25. Bastock, R., Strutt, H. & Strutt, D. Strabismus is asymmetrically localised and binds to Prickle and Dishevelled during *Drosophila* planar polarity patterning. *Development* **130**, 3007–3014 (2003).
26. Park, T. J., Gray, R. S., Sato, A., Habas, R. & Wallingford, J. B. Subcellular localization and signaling properties of dishevelled in developing vertebrate embryos. *Curr. Biol.* **15**, 1039–1044 (2005).
27. Torban, E. *et al.* Genetic interaction between members of the Vangl family causes neural tube defects in mice. *Proc. Natl Acad. Sci. USA* **105**, 3449–3454 (2008).
28. Jiang, D., Munro, E. M. & Smith, W. C. Ascidian prickle regulates both mediolateral and anterior-posterior cell polarity of notochord cells. *Curr. Biol.* **15**, 79–85 (2005).
29. Wang, J. *et al.* Dishevelled genes mediate a conserved mammalian PCP pathway to regulate convergent extension during neurulation. *Development* **133**, 1767–1778 (2006).
30. Gros, J., Manceau, M., Thome, V. & Marcelle, C. A common somitic origin for embryonic muscle progenitors and satellite cells. *Nature* **435**, 954–958 (2005).

Supplementary Information is linked to the online version of the paper at www.nature.com/nature.

Acknowledgements We thank C. Tabin for critical reading of the manuscript. The help of P. Weber for the two-photon imaging, and of the Zeiss team, are acknowledged. We are grateful to M. Manceau for Supplementary Fig. 1d, and to R. Kanadia for his help. This study was funded by grants from the Actions Concertées Incitatives (ACI), the Agence Nationale de la Recherche (ANR), the Association Française contre les Myopathies (AFM) and by the EU 6th Framework Programme Network of Excellence MYORES. J.G. was a Fellow of the AFM.

Author Information Reprints and permissions information is available at www.nature.com/reprints. Correspondence and requests for materials should be addressed to C.M. (marcelle@ibdm.univ-mrs.fr).

METHODS

Electroporation, confocal analysis and cell injection. The *Xenopus* cDNAs of *dvl*, *dvl-ΔDIX*, *dvl-ΔDEP* and *dvl-ΔPDZ*, fused to GFP¹⁹, were cloned into the pCAGG vector. The full-length and secreted cDNA of chick FZD7 (ref. 31), a dominant-negative form of *Xenopus* β-catenin (provided by P. McCrea)³², a dominant-negative form of chick LEF1 (provided by J. C. Ispizua-Belmonte)³³, a dominant-negative form and the full-length cDNA of quail *WNT11* (ref. 1), and the full-length *Danio rerio rok2* cDNA (provided by L. Solnica-Kretzel²⁰) were cloned into the pCLGFP electroporation vector³⁰. The *RCAS-WNT11* construct was a gift from P. Francis-West³⁴.

WNT11-producing cells were produced by transfecting DF1 chick fibroblast cells with an *RCAS-WNT11* construct. Cells were split in half every day for 6–7 days, when the culture was analysed for infection (using a p27 viral core protein rabbit antibody, SPAFAS). Infected cells were pressure-injected into somites of E2.5 developing chick embryos as described previously¹².

Time-lapse experiments and confocal analysis. Embryos were electroporated with a floxed GFP vector ($1\ \mu\text{g}\ \mu\text{l}^{-1}$) together with a Cre expression vector ($10\ \text{ng}\ \mu\text{l}^{-1}$; gifts from X. Morin³⁵) to generate isolated GFP-expressing cells within the transition zone. After 12–17 h of re-incubation, thick slices of embryos containing the electroporated somites were isolated. Embryos slices were filmed as described previously³⁰ with a confocal two-photon inverted Zeiss LSM510 NLO microscope and a Mai-Tai Laser (SpectraPhysics) at a wavelength of 870 nm.

Embryo slices preparation for time lapse. For the solution, 10 ml of 2% agarose low melting was prepared (0.2 g in 10 ml H₂O) in a tube and 12 ml H₂O was added to another tube. Agarose was cooled down to 42 °C and then the following was added to each tube: 6.7 ml of F12 3X medium (Gibco); 5 mM glutamine (200 mM stock, Gibco), 500 μl for a 20 ml gel; 1 mM sodium pyruvate (100 mM stock, Gibco), 200 μl for 20 ml gel; penicillin streptomycin (5,000 units ml⁻¹, Gibco), 200 μl for a 20 ml gel.

Embryo and slice preparation. Embryos were dissected in PBS at room temperature, removing all extra-embryonic membranes. The embryo was transferred in F12 without agarose (for equilibration) and cut into 100–250-μm-thick slices with tissue chopper (for example Mcllwain V800) or with sharp mini-scissors (for example Moria).

Mounting of slices. Sections were transferred in a glass-bottomed Petri dish (MatTek 35 mm or 50 mm dish, uncoated) with only a small amount of F12 medium. A few millilitres of F12 agarose medium was added to the dish. The section was oriented using Dumont number 5 forceps, and gently placed in contact with the glass coverslip. The agarose was left to set for 10–15 min, and some liquid medium added on top of agarose containing sections. Sections were then observed on an inverted confocal two-photon microscope.

31. Linker, C. *et al.* β-catenin-dependent Wnt signalling controls the epithelial organisation of somites through the activation of paraxis. *Development* **132**, 3895–3905 (2005).
32. Montross, W. T., Ji, H. & McCrea, P. D. A β-catenin/engrailed chimera selectively suppresses Wnt signaling. *J. Cell Sci.* **113**, 1759–1770 (2000).
33. Kengaku, M. *et al.* Distinct WNT pathways regulating AER formation and dorsoventral polarity in the chick limb bud. *Science* **280**, 1274–1277 (1998).
34. Anakwe, K. *et al.* 16 Wnt regulation of limb muscle differentiation. *J. Anat.* **201**, 421 (2002).
35. Morin, X., Jaouen, F. & Durbec, P. Control of planar divisions by the G-protein regulator LGN maintains progenitors in the chick neuroepithelium. *Nature Neurosci.* **10**, 1440–1448 (2007).

LETTERS

Enterotoxigenic *Escherichia coli* EtpA mediates adhesion between flagella and host cells

Koushik Roy¹, George M. Hilliard², David J. Hamilton³, Jiwen Luo¹, Marguerite M. Ostmann⁴ & James M. Fleckenstein^{1,2,5}

Adhesion to epithelial cells¹ and flagella-mediated motility are critical virulence traits for many Gram-negative pathogens, including enterotoxigenic *Escherichia coli* (ETEC)², a major cause of diarrhoea in travellers and children in developing countries^{3,4}. Many flagellated pathogens export putative adhesins belonging to the two-partner secretion (TPS) family⁵. However, the actual function of these adhesins remains largely undefined. Here we demonstrate that EtpA, a TPS exoprotein adhesin of enterotoxigenic *E. coli*⁶, mimics and interacts with highly conserved regions of flagellin, the major subunit of flagella, and that these interactions are critical for adherence and intestinal colonization. Although conserved regions of flagellin are mostly buried in the flagellar shaft⁷, our results suggest that they are at least transiently exposed at the tips of flagella where they capture EtpA adhesin molecules for presentation to eukaryotic receptors. Similarity of EtpA to molecules encoded by other motile pathogens suggests a potential common pattern for bacterial adhesion, whereas participation of conserved regions of flagellin in adherence has implications for development of vaccines for Gram-negative pathogens.

ETEC cause diarrhoea by delivery of heat-labile and/or heat-stable enterotoxins to the small intestine, a process that requires critical fimbrial bacterial adhesins known as colonization factors^{8,9}. These essential proteinaceous finger-like projections are central to ETEC vaccines currently in development¹⁰. Generally, adhesion to intestinal epithelium by diarrhoeagenic *E. coli* is a very complex process that may involve several structures including flagella¹¹. The role of flagella in ETEC pathogenesis has not been sufficiently explored¹². Flagella are complex cylindrical structures assembled from approximately 20,000 flagellin (FliC) molecules that travel down the nascent flagellar cylinder to the distal tip where they are directed by cap proteins (FliD)¹³ into the growing flagellum. Flagellin has several major domains: the central domain projects on the surface of the flagellar shaft, accounting for antigenic variation used in *E. coli* 'H' serotyping; conserved amino- and carboxy-regions interact with adjacent subunits, facing the inaccessible shaft core⁷.

Efficient adherence of ETEC to intestinal cells required both intact flagella and *etpA*; however, flagella-dependent adherence was independent of serotype, as complementation of a *fliC* (H11[−]) mutant with *fliC* (H48) restored both motility and adherence (Fig. 1a). Likewise, antibody generated against (H48) full-length flagellin inhibited adherence of ETEC (H11) (Supplementary Fig. 1a) in contrast to antibody against serotype-dependent regions of flagellin (Supplementary Fig. 1b). Similarly, anti-EtpA antibodies inhibited adherence by EtpA-producing ETEC of multiple (H11, H12 and H16) serotypes whereas amounts of endogenous (Supplementary Fig. 1c) or exogenously added EtpA (Supplementary Fig. 1d) paralleled the adherence phenotype.

Recombinant EtpA labelled (Supplementary Fig. 2a) and bound specifically to the surface of intestinal cells, whereas antibodies against EtpA prevented this interaction (Fig. 1b). Interestingly, labelled EtpA localized to mucin-producing regions of the small intestine (Supplementary Fig. 2b), suggesting that EtpA could promote ETEC interaction with intestinal mucosal surfaces.

Theoretically, EtpA must maintain contact with ETEC to promote adherence. Attempts to purify recombinant EtpA from *E. coli*⁶ were confounded by co-isolation of another protein (≈ 50 kilodaltons) despite attempted separation by column chromatography (Supplementary Fig. 3a), suggesting a potential protein–protein interaction¹⁴. Matrix-assisted laser desorption/ionization–time of flight (MALDI–TOF) definitively identified the co-purified protein as *E. coli* K-12 flagellin (H48, the same serotype as the recombinant used in the expression) (Supplementary Fig. 3b). Application of this purification strategy to ETEC strain H10407 (serotype H11) supernatants

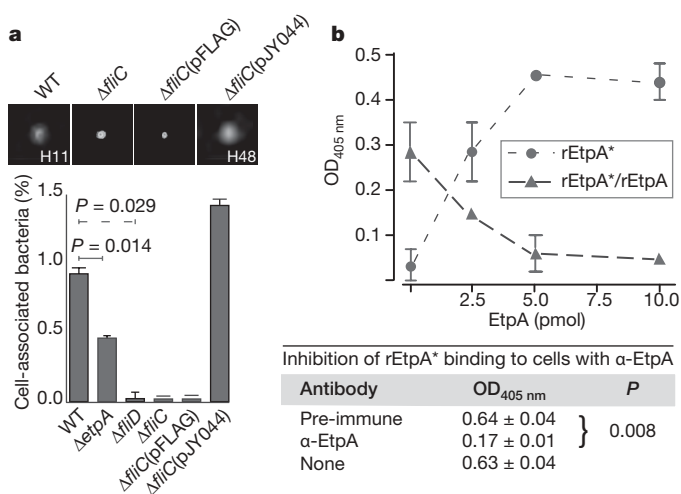


Figure 1 | EtpA and flagella contribute to ETEC adhesion. **a**, Efficient ETEC adherence requires production of EtpA and intact flagella, and is not dependent on flagellar serotype. WT, wild-type ETEC strain H10407. Complementation of the *fliC* (H11[−]) isogenic deletion strain with pJY044 expressing *fliC* gene from MG1655 (*E. coli* K-12, flagellar serotype H48) restored motility and adherence phenotypes. *P* values (Mann–Whitney) generated by a one-tailed test (*etpA* mutant and wild type); others were two-tailed tests (mean \pm s.d. for $n = 4$ replicates). **b**, EtpA binds specifically to target cells. Binding of purified biotinylated rEtpA (rEtpA*) to target Caco-2 epithelial cells was inhibited by unlabelled protein (mean values ($n = 3$) \pm s.e.m.). Table below the graph demonstrates inhibition of EtpA* binding with EtpA antisera (mean values ($n = 3$) \pm s.e.m.; $P = 0.0076$; unpaired *t*-test with Welch's correction).

¹Department of Medicine, ²Department of Molecular Sciences, ³Department of Comparative Medicine, University of Tennessee Health Science Center, 956 Court Avenue, Memphis, Tennessee 38163, Tennessee, USA. ⁴Research Service, ⁵Medicine Service, Veterans Affairs Medical Center, 1030 Jefferson Avenue, Memphis, Tennessee 38104, USA.

demonstrated that all EtpA-containing fractions also contained flagellin (Supplementary Fig. 3c), suggesting that EtpA interacts with multiple H serotypes of flagellin, and serendipitously alluding to a mechanism of action for EtpA. Co-immunoprecipitation of H10407 culture supernatants with anti-EtpA antibody⁶ confirmed that FliC (H11) and EtpA interact (Fig. 2a). FliC secreted by the *fliD* mutant, which cannot assemble monomers into intact flagella², still interacted with EtpA, implying that EtpA can bind monomeric flagellin. Glycosylation of EtpA, a process dependent on the *etpC* gene⁶, also did not appear to be required. In co-immunoprecipitation experiments using additional motile ETEC strains, we could immunoprecipitate flagellin from EtpA-producing strains E24377A (H28) and TX-1 (H12), but not the *etpA* mutant control. Similarly, immobilized flagellins from different serotypes (FliC_{H11}, and FliC_{H48}) captured biotin-labelled EtpA (Fig. 2b), further demonstrating that these interactions are not dependent on flagellar serotype.

These interactions of EtpA with FliC monomers of multiple serotypes suggest that EtpA engages highly conserved regions of these molecules. Interestingly, position-specific-iterative-BLAST (PSI-BLAST)¹⁵ searches identified not only putative bacterial adhesins, but subtle homology with amino- and carboxy-terminal regions of flagellins, raising the possibility that EtpA interacts with multiple serotypes by mimicking these conserved domains. We next constructed recombinant (H48) flagellin proteins representing the full-length molecule including the unique serotype-determining region, as well as a truncated version consisting of amino acids 1–173 (the conserved N-terminal domain), and a third peptide containing amino acids 174–498. The conserved N-terminal domain was both necessary and sufficient to pull down EtpA (Fig. 2c). In addition, antibodies against either the full-length H48 flagellin or the conserved N-terminal (1–173) region significantly inhibited adherence of

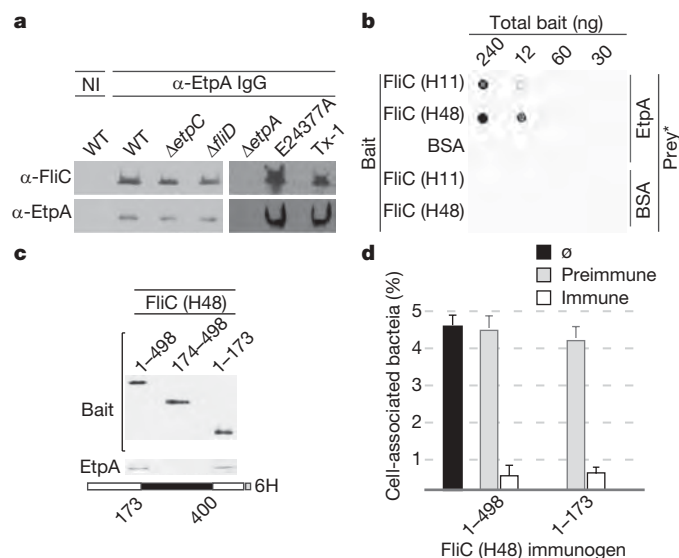


Figure 2 | EtpA interacts with conserved regions of flagellins. **a**, Co-immunoprecipitation of EtpA and flagellin from ETEC culture supernatants using anti-EtpA antibody. α-EtpA IgG, immune antibody; NI, purified non-immune IgG (same rabbit). From left to right: wild type, *etpC* mutant, *fliD* mutant; control isogenic *etpA* mutant (jfl668); other motile ETEC strains, E24377A (H28), TX-1 (H12). **b**, EtpA interacts with multiple flagellin serotypes. Membrane-immobilized FliC_{H11} and FliC_{H48} ('Bait') capture biotinylated rEtpA ('Prey*'). **c**, EtpA interacts with a conserved region of flagellin. Immunoblots (anti-flagella, top; anti-EtpA, bottom) represent molecular pull-down experiments using recombinant polyhistidine-tagged FliC H48-based molecules as bait. Schematic at bottom of figure depicts full-length recombinant flagellin serotype H48. Conserved (white), serotype-dependent (black) regions are shown. **d**, Antibodies against conserved regions of flagellin (H48) block adherence of ETEC strain H10407 (H11) to Caco-2 epithelial cells ($n = 3$, error bars = s.e.m.). ∅, No antibody.

ETEC H10407 (H11) to Caco-2 cells (Fig. 2d). Together, these data implicate highly conserved regions of flagellin molecules in both EtpA binding and adherence.

Intriguingly, after infection of host cells, ETEC were rapidly tethered to the surface by flagella (Fig. 3a–b). Although conserved regions of flagellin are largely buried within the flagellar shaft⁷, we reasoned that EtpA might interact with conserved regions of monomers available at the ends of flagella, particularly if the rotating FliD pentameric cap became dislodged from the tip. Accordingly, *in situ* immunogold labelling studies indicated that conserved FliC regions are available

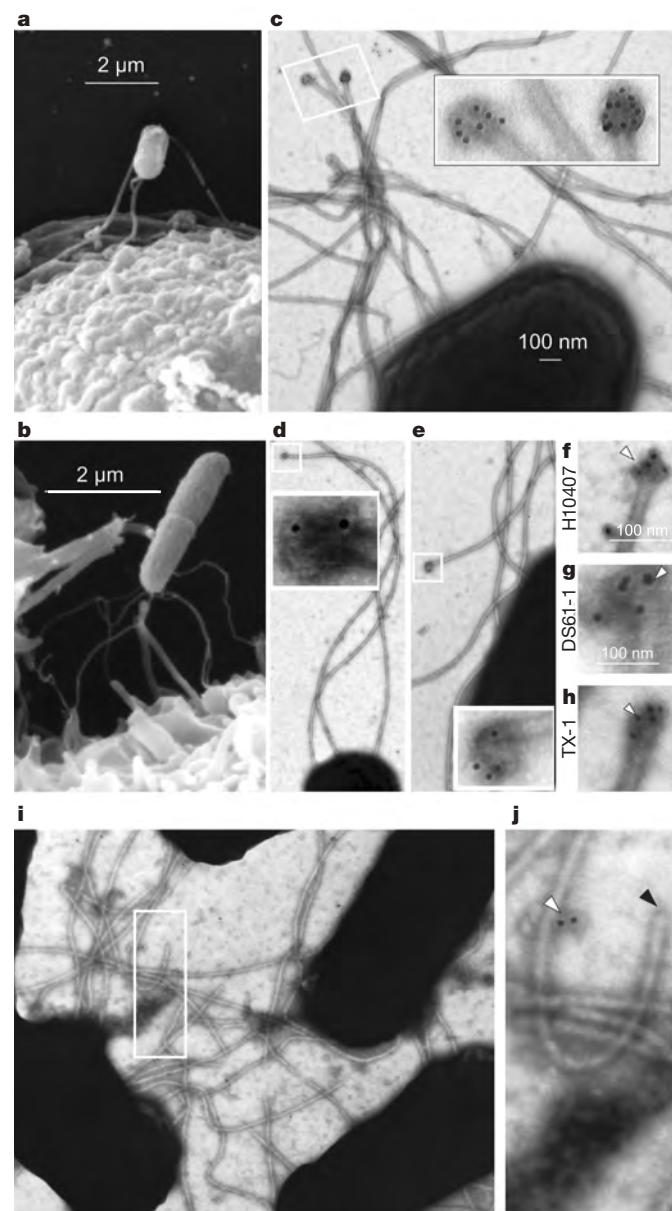


Figure 3 | ETEC engage host cells through tips of flagella where EtpA interacts with highly conserved regions of flagellin. **a**, **b**, ETEC initially engage cells through the ends of their flagella. **c–e**, Conserved regions of flagellin are exposed at the tips of H10407 (O78:H11) flagella shown by *in situ* immunolocalization using: **c**, anti-(H48) flagellar antibody affinity purified versus full-length (amino acids 1–498) rFliC_{H48}; **d**, **e**, affinity-purified antisera against highly conserved N-terminal 173 amino acids of H48 flagellin. **f–h**, EtpA concentrates at flagellar tips (white arrowhead) of motile EtpA-producing ETEC strains: **f**, H10407 (O78:H11); **g**, DS61-1 (O6:H16); **h**, TX-1 (O78:H12). **i–j**, Control labelling experiment with anti-EtpA antibody and secondary gold conjugate using an EtpA-negative strain (DS220-4) demonstrates minimal background (white arrowhead) with no labelling of flagellar tips (black arrowhead).

exclusively at the tips of flagella (Fig. 3c–e). Likewise, EtpA bound largely at tips of intact flagella from ETEC strains belonging to different serotypes (Fig. 3f–h). Conversely, fragmentation of flagella exposed additional EtpA binding sites, supporting the concept that EtpA interacts with regions of flagellin typically buried within the flagellar shaft.

Because EtpA appeared to be concentrated at the tips of flagella, we investigated whether rEtpA might also interact with the flagellar cap protein, FliD. However, we found no evidence for this in molecular pull-down experiments (Supplementary Fig. 4a). Additionally, we found that *in vitro* FliD inhibited interaction of EtpA with FliC (Supplementary Fig. 4b), suggesting that the FliD cap might inhibit binding of EtpA to (conserved regions) of flagellin. Similarly, we could not demonstrate co-localization of either the conserved regions or EtpA with the FliD protein (Supplementary Fig. 4c–i), arguing that when FliD is firmly attached, the conserved regions are inaccessible to EtpA. Exogenously added rEtpA localized to the flagellar tips of the *etpA* mutant (Supplementary Fig. 4j–k) without compromising length, and deletion of *etpA* had no effect on flagellar length (Supplementary Fig. 5). Collectively, these data suggest that EtpA binds opportunistically to conserved residues of flagellin at the tips of mature flagella when these domains are exposed by loss of the FliD cap protein complex⁷, or as these molecules leak¹⁶ from ends of flagella in the absence of an intact cap structure. We believe that our data, generated by *in situ* immunogold labelling¹⁷ of whole bacteria, are consistent with the highly dynamic rotating pentameric cap structure proposed previously based on electron cryomicroscopic techniques^{13,18}.

To investigate whether the EtpA–flagellin interaction was required for the adherence phenotype, we performed linker scanning mutagenesis¹⁹ of *etpA* (Fig. 4a). In general, mutations within the repeat

region of *etpA* did not interfere with secretion of EtpA or with binding to flagellin (Fig. 4b), suggesting that the 5' end of *etpA* encodes domains essential for secretion (similar to other TPS molecules) and for flagellin binding. Further analysis of in-frame mutations mapping to this region led to the identification of a secreted EtpA mutant molecule with an insertion beginning at residue Q₄₁₄ of EtpA, which retained its ability to bind to host cells (Fig. 4c, d) but which had lost the capacity to bind flagellin (Fig. 4e). Recombinant myc-tagged wild-type EtpA expressed in the *etpA* mutant localized to the tips of flagella (Fig. 4f), unlike the Q₄₁₄ molecule. Compared with the wild-type *etpA* gene, the mutant allele failed to complement the *in vitro* adherence defect in an isogenic *etpA* deletion strain (Fig. 4g), or when the mutated protein (EtpA_{Q414}) was added exogenously to this mutant (Fig. 4h). EtpA is required for optimal colonization of the intestine by ETEC²⁰. Likewise, bacteria expressing EtpA_{Q414} were not able to compete efficiently in intestinal colonization with those expressing the wild-type *etpA* gene (Fig. 4i), suggesting that the association of EtpA and flagellin is critical for efficient interaction of ETEC with target host cells, and for colonization of mucosal surfaces.

Similar to other enteric pathogens²¹, we found that production of intact flagella was also required for efficient intestinal colonization by ETEC (Fig. 5a). Because EtpA interactions with conserved regions of flagellin are critical to promoting colonization, and EtpA is a protective antigen in mice²⁰, we examined whether immunization of mice with a single H serotype of flagellin could target shared regions of flagellins, thereby affording heterologous protection against intestinal colonization. Immunization with full-length flagellin (H48) stimulated production of serum (Fig. 5b) and faecal²² (Fig. 5c) antibodies

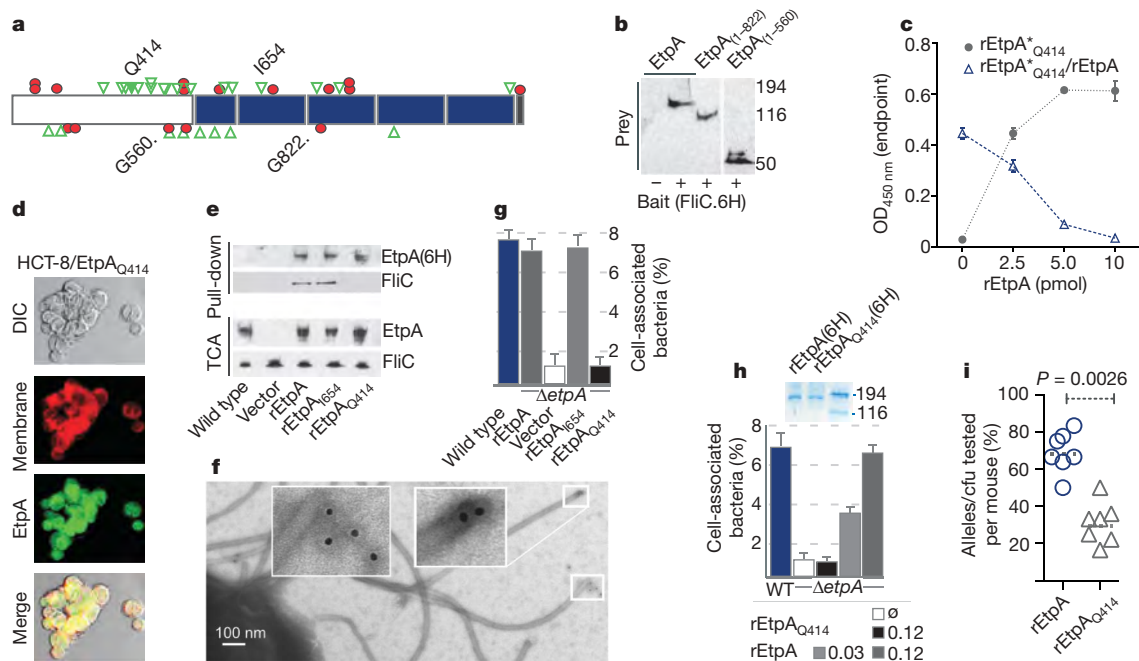


Figure 4 | ETEC adherence to epithelial cells *in vitro* and small intestinal colonization require the interaction of EtpA and flagellin. **a**, Linker scanning mutation map of EtpA (blue, repeats; red circles, stop codons; green triangles, in-frame insertions). **b**, Truncated N-terminal region of EtpA (M₁–G₅₆₀) is sufficient to interact with flagellin (H48) polyhistidine-tagged (FliC.6H) bait in molecular pull-downs. **c**, EtpA_{Q414} retains specific binding to Caco-2 cells. Circles, biotinylated (rEtpA^{*}_{Q414}); triangles, competition with unlabelled rEtpA (mean (*n* = 3) values \pm s.e.m.). **d**, EtpA_{Q414} retains binding to HCT-8 epithelial cells surfaces (confocal microscopy). **e**, EtpA_{Q414} does not interact with flagellin. *etpA* mutant (jfl1668) was complemented with myc-polyhistidine-tagged EtpA variants as indicated before pull-down studies of supernatants with metal affinity resin. TCA, trichloroacetic acid precipitation. **f**, rEtpA-myc-6H identified with anti-myc 1° monoclonal

antibody at flagellar tips of *etpA* mutant (jfl1668) expressing pJY017. **g**, EtpA_{Q414} expression in isogenic *etpA* mutant (jfl1668) fails to complement adherence (Caco-2) defect. Error bars, s.e.m. **h**, Exogenous rEtpA, but not rEtpA_{Q414}, complements the adherence defect in the *etpA* mutant. Error bars, s.e.m. SDS–polyacrylamide gel electrophoresis (SDS–PAGE) above the graph shows rEtpA(6H) and rEtpA_{Q414}(6H) used in assays. (Key, final (nanomolar) concentrations.) \emptyset , Nothing added. **i**, EtpA_{Q414} fails to complement colonization defect when expressed in isogenic *etpA* mutant. Graph shows the proportion of colony-forming units (c.f.u.) bearing either the wild-type allele (carried on pJL017) or mutant allele (carried on pJMF1087) recovered from each mouse (*n* = 7) after simultaneous challenge with 1×10^4 c.f.u. of both strains (*P* = 0.0026 (two-tailed Mann–Whitney *U*-test)). An average of 15 colonies per mouse were analysed by PCR and *PmeI* digestion.

recognizing conserved regions of flagellin, accessible at the tips of H11 flagella (Fig. 5d–g) and dramatically impaired colonization by ETEC (Fig. 5h). These antibodies also inhibited adherence of ETEC expressing the heterologous flagellin H11 serotype (Fig. 5i). Collectively,

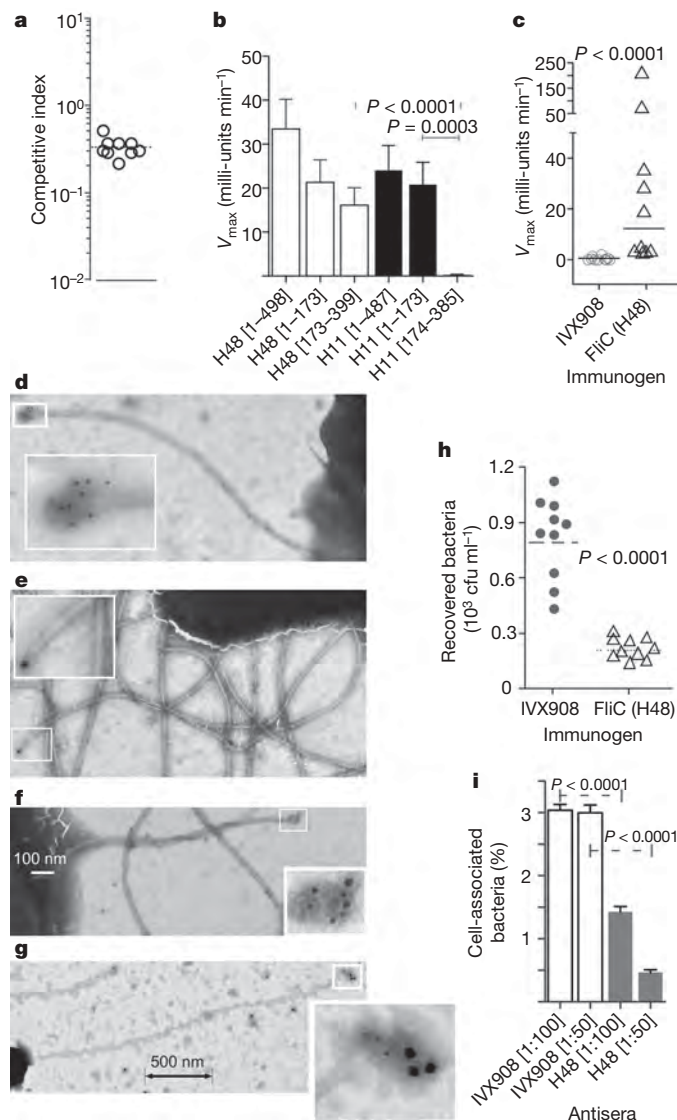


Figure 5 | Vaccination with flagellin inhibits ETEC infection in mice.

a, Motile ETEC bacteria out-compete *fliC*⁻ mutants (geometric mean index ≈ 0.33). **b**, Kinetic enzyme-linked immunosorbent assay (ELISA) demonstrating that sera (1:128 dilution) from mice ($n = 10$) immunized with H48 flagellin recognize full-length and N-terminal conserved regions of H48, and H11 molecules, serotype-specific region of H48 (H48(173–399)), not serotype-specific region of H11 (H11(174–385)). Values obtained with pooled sera from IVX908 control mice have been subtracted (error bars, s.e.m.). **c**, Mice vaccinated with full-length H48 recombinant flagellin produce faecal antibodies against conserved regions of H11 flagellin. Shown are kinetic ELISA data from mice vaccinated intranasally with FliC(H48)/IVX908 (triangles) versus IVX908 controls (circles). Horizontal bars, geometric mean values ($P < 0.0001$, two-tailed Mann–Whitney *U*-test). **d**, EtpA localized at tip of H10407 flagellum. **e**, Antisera from mice immunized with H48 recognize the tips of ETEC H10407 (H11) flagella. **f–g**, EtpA and conserved regions of flagellin co-localize at tips of H10407 flagella. Primary antisera: (1) pooled from H48-immunized mice with (2) rabbit anti-EtpA; secondary anti-mouse/anti-rabbit (IgG) gold conjugates: 10 nm/5 nm in **f**, 20 nm/10 nm in **g**. **h**, Vaccination with FliC(H48) flagellin protects against colonization with ETEC H10407 (H11). **i**, Polyclonal antisera from mice immunized with recombinant H48 flagellin inhibits adherence of H10407 (H11) to Caco-2 cells *in vitro*. Bars, mean \pm s.e.m. of ($n = 8$) wells (all *P* values calculated using two-tailed Mann–Whitney *U*-test, except in **i** (one-tailed test)).

these studies suggest that conserved residues of flagellin, implicated here in bacterial adherence and colonization, could also serve as viable vaccine targets.

These studies offer a novel model for bacterial adhesion as they demonstrate for the first time that a secreted virulence protein interacts with highly conserved regions of flagellin exposed at the tips of flagella, exploiting these long (≈ 10 – $15 \mu\text{m}$) appendages to tether EtpA adhesins that anchor bacteria on initial engagement of host cells. The precise contributions of EtpA and flagella relative to the established critical role of colonization factors in ETEC adherence remain undefined. However, preliminary data suggest that these are early transient interactions acting in concert to facilitate resilient pathogen–host interactions mediated by shorter (0.5 – $1 \mu\text{m}$) spring-like²³ colonization factors.

EtpA or EtpA-like molecules are present in many ETEC strains from multiple flagellar serotypes⁶, suggesting that interactions between EtpA and flagellin are not limited to a small subset of ETEC strains. Likewise, homology searches of EtpA revealed the presence of many potential EtpA-like molecules in other motile Gram-negative pathogens (Supplementary Fig. 6), raising the possibility that these could function in a similar fashion. Interestingly, another TPS exoprotein, HMW1 (*Haemophilus influenzae*), uses disulphide bonds between C-terminal cysteine residues to link fibrillar adhesin structures to the bacterial surface²⁴. Absence of similar residues in EtpA and EtpA-like TPS proteins identified in genomes of other flagellated pathogens⁵ may allow free secretion of these molecules for interactions with flagella.

Flagellar organelles have previously been dismissed in development of ETEC vaccines owing to substantial variation in H serotypes and the assumption that only variant FliC regions were exposed¹². The highly conserved flagellin domains implicated in the present studies, potent stimuli of innate immunity²⁵, might also be exposed on commensal organisms. However, dependence of ETEC flagella-mediated adhesion on TPS, a unique adaptation of pathogenic bacteria, is likely one critical step in a process involving several adhesins including well-defined ETEC fimbrial colonization factors⁸. Although the precise mechanism linking EtpA and flagella is not entirely clear, our data do suggest that EtpA and similar molecules, as well as highly conserved flagellin ligands, could serve as viable antigenic targets in design of novel vaccines to prevent infections caused by ETEC and other important motile pathogens.

METHODS SUMMARY

Detailed methods are contained within the Supplementary Information. A description of bacterial strains and plasmids used is given in Supplementary Table 1. Primers used are detailed in Supplementary Table 2. Adherence⁶ and motility assays² were done as previously described. Mouse intestinal colonization studies followed established protocols^{20,26}. Antisera against recombinant EtpA, FliC and FliD were generated in rabbits⁶, and mouse polyclonal antibodies were recovered as previously outlined²⁰. For *in situ* gold labelling¹⁷, bacteria were fixed on carbon-coated nickel grids and probed with anti-EtpA, -FliC or -FliD antibodies followed by immunodetection using secondary antibodies coupled to gold particles of various diameters.

Cloning, protein expression and purification techniques are described in detail in the Methods section of the Supplementary Information. Beads pre-charged with Co^{2+} (Talon, Clontech) were used to pull down polyhistidine-tagged proteins in protein interaction studies. Co-immunoprecipitation was performed using EtpA antibody bound to solid support gel matrix (Pierce).

Comparisons of data were performed using the non-parametric Mann–Whitney (two-tailed) test unless otherwise specified. Statistical calculations were performed using Prism version 4.0c and InStat version 3.0 (GraphPad Software).

Full Methods and any associated references are available in the online version of the paper at www.nature.com/nature.

Received 15 October 2007; accepted 14 October 2008.

Published online 7 December 2008.

- Torres, A. G., Zhou, X. & Kaper, J. B. Adherence of diarrheagenic *Escherichia coli* strains to epithelial cells. *Infect. Immun.* **73**, 18–29 (2005).
- Dorsey, F. C., Fischer, J. F. & Fleckenstein, J. M. Directed delivery of heat-labile enterotoxin by enterotoxigenic *Escherichia coli*. *Cell. Microbiol.* **8**, 1516–1527 (2006).

3. World Health Organization. Future directions for research on enterotoxigenic *Escherichia coli* vaccines for developing countries. *Wkly Epidemiol. Rec.* **81**, 97–104 (2006).
4. Qadri, F. *et al.* Enterotoxigenic *Escherichia coli* in developing countries: epidemiology, microbiology, clinical features, treatment, and prevention. *Clin. Microbiol. Rev.* **18**, 465–483 (2005).
5. Jacob-Dubuisson, F., Locht, C. & Antoine, R. Two-partner secretion in Gram-negative bacteria: a thrifty, specific pathway for large virulence proteins. *Mol. Microbiol.* **40**, 306–313 (2001).
6. Fleckenstein, J. M. *et al.* Identification of a two-partner secretion locus of enterotoxigenic *Escherichia coli*. *Infect. Immun.* **74**, 2245–2258 (2006).
7. Yonekura, K., Maki-Yonekura, S. & Namba, K. Complete atomic model of the bacterial flagellar filament by electron cryomicroscopy. *Nature* **424**, 643–650 (2003).
8. Evans, D. G. *et al.* Plasmid-controlled colonization factor associated with virulence in *Escherichia coli* enterotoxigenic for humans. *Infect. Immun.* **12**, 656–667 (1975).
9. Gastra, W. & Svennerholm, A. M. Colonization factors of human enterotoxigenic *Escherichia coli* (ETEC). *Trends Microbiol.* **4**, 444–452 (1996).
10. Svennerholm, A. M. & Tobias, J. Vaccines against enterotoxigenic *Escherichia coli*. *Expert Rev. Vaccines* **7**, 795–804 (2008).
11. Giron, J. A. *et al.* The flagella of enteropathogenic *Escherichia coli* mediate adherence to epithelial cells. *Mol. Microbiol.* **44**, 361–379 (2002).
12. Wolf, M. K. Occurrence, distribution, and associations of O and H serogroups, colonization factor antigens, and toxins of enterotoxigenic *Escherichia coli*. *Clin. Microbiol. Rev.* **10**, 569–584 (1997).
13. Yonekura, K. *et al.* The bacterial flagellar cap as the rotary promoter of flagellin self-assembly. *Science* **290**, 2148–2152 (2000).
14. Sudakin, V. in *Protein-Protein Interactions: A Molecular Cloning Manual* 2nd edn, Vol. 1 (eds Golemis, E. & Adams, P. D.) Ch. 3 37–54 (Cold Spring Harbor Laboratory Press, 2005).
15. Altschul, S. F. *et al.* Gapped BLAST and PSI-BLAST: a new generation of protein database search programs. *Nucleic Acids Res.* **25**, 3389–3402 (1997).
16. Komoriya, K. *et al.* Flagellar proteins and type III-exported virulence factors are the predominant proteins secreted into the culture media of *Salmonella typhimurium*. *Mol. Microbiol.* **34**, 767–779 (1999).
17. Jin, Q. & He, S. Y. Role of the Hrp pilus in type III protein secretion in *Pseudomonas syringae*. *Science* **294**, 2556–2558 (2001).
18. Maki-Yonekura, S., Yonekura, K. & Namba, K. Domain movements of HAP2 in the cap-filament complex formation and growth process of the bacterial flagellum. *Proc. Natl Acad. Sci. USA* **100**, 15528–15533 (2003).
19. Goff, S. P. & Prasad, V. R. Linker insertion mutagenesis as probe of structure–function relationships. *Methods Enzymol.* **208**, 586–603 (1991).
20. Roy, K. *et al.* The EtpA exoprotein of enterotoxigenic *Escherichia coli* promotes intestinal colonization and is a protective antigen in an experimental model of murine infection. *Infect. Immun.* **76**, 2106–2112 (2008).
21. Ottemann, K. M. & Miller, J. F. Roles for motility in bacterial–host interactions. *Mol. Microbiol.* **24**, 1109–1117 (1997).
22. Plotkin, S. A. Vaccines: correlates of vaccine-induced immunity. *Clin. Infect. Dis.* **47**, 401–409 (2008).
23. Mu, X. Q., Savarino, S. J. & Bullitt, E. The three-dimensional structure of CFA/I adhesion pili: traveler's diarrhea bacteria hang on by a spring. *J. Mol. Biol.* **376**, 614–620 (2008).
24. Buscher, A. Z. *et al.* Surface anchoring of a bacterial adhesin secreted by the two-partner secretion pathway. *Mol. Microbiol.* **61**, 470–483 (2006).
25. Smith, K. D. *et al.* Toll-like receptor 5 recognizes a conserved site on flagellin required for protofilament formation and bacterial motility. *Nature Immunol.* **4**, 1247–1253 (2003).
26. Allen, K. P., Randolph, M. M. & Fleckenstein, J. M. Importance of heat-labile enterotoxin in colonization of the adult mouse small intestine by human enterotoxigenic *Escherichia coli* strains. *Infect. Immun.* **74**, 869–875 (2006).

Supplementary Information is linked to the online version of the paper at www.nature.com/nature.

Acknowledgements We thank B. Westerlund-Wikström for supplying anti-flagellar antisera, K. Troughton of the Department of Anatomy and Neurobiology, University of Tennessee Health Science Center, for her assistance with transmission electron microscopy, and L. Boykins of the Integrated Microscopy Center at the University of Memphis for her assistance with scanning electron microscopy. We thank G. Byrne, H. Courtney, J. Dale, S. Dagogo-Jack and T. Strom for reading the manuscript. This research was supported by grants from the National Institutes of Health (National Center for Research Resources) RR16190-05, the Department of Veterans Affairs and funds from the University of Tennessee Microbial Pathogenesis Research Center.

Author Contributions K.R. performed adherence assays, transmission electron and confocal microscopy, mouse colonization studies, antibody purification and protein interaction studies. G.M.H. performed MALDI–TOF studies and D.J.H. assisted with mouse studies. J.L. performed cloning, sequencing and mutagenesis of the *etpA* locus. M.M.O. assisted with cloning, protein purification and protein interaction studies. J.M.F. assisted with study design, protein purification, linker mutagenesis, sample preparation, scanning electron microscopy, measurement of flagella and manuscript preparation.

Author Information Reprints and permissions information is available at www.nature.com/reprints. The authors declare competing financial interests: details accompany the full-text HTML version of the paper at www.nature.com/nature. Correspondence and requests for materials should be addressed to J.M.F. (jfleck1@tennessee.edu).

METHODS

Binding of EtpA to the surface of intestinal epithelial cells. Concentrated recombinant EtpA (rEtpA) was added to live HCT-8 or Caco-2 cells at a final concentration of $12.5 \mu\text{g ml}^{-1}$ in PBS. After incubation with the cells at 4°C for 1 h, cells were washed, and fixed with methanol. Bound EtpA was detected by immunofluorescence using anti-EtpA primary antibodies⁶, and secondary anti-rabbit Alexa Fluor 488-conjugated IgG. During subsequent washes 4',6-diamidino-2-phenylindole, dihydrochloride (DAPI) was added to stain nuclei. Plasma membranes were stained with CellMask (Deep Red, Molecular Probes) at a final concentration of $5 \mu\text{g ml}^{-1}$. Confocal immunofluorescence images acquired on a BioRad MRC 1024 imaging system equipped with a krypton/argon laser were coloured in ImageJ (<http://rsb.info.nih.gov/ij/>).

rEtpA, biotinylated with biotin LC hydrazide, and dialysed against PBS to remove excess biotin, was first added to target monolayers (paraformaldehyde-fixed, 1% BSA blocked) at final concentrations of 0.05, 0.1 and $0.2 \mu\text{M}$, and incubated at 37°C for 1 h. After washing with PBS, bound label was detected by using streptavidin-HRP (1:10,000) and tetramethylbenzidine/ H_2O_2 (TMB) peroxidase substrate. Reactions were stopped by addition of $1 \text{ M H}_2\text{SO}_4$, and the optical density ($\text{OD}_{405 \text{ nm}}$) determined. Experiments were then conducted using biotinylated rEtpA at a final concentration of $0.05 \mu\text{M}$ combined with increasing amounts of unlabelled EtpA.

To visualize EtpA binding to intestine, frozen sections of mouse ileum were blocked, incubated with biotinylated rEtpA, washed, and bound rEtpA was detected with streptavidin-coated quantum dots (Qdot525 ITK SA). Both CellMask membrane stain and DAPI were incorporated into final washes.

Expression and purification of recombinant EtpA. After induction of LMG194(pJY019)⁶ with arabinose, supernatant was sterile-filtered ($0.22 \mu\text{m}$), and concentrated (approximately $\times 150$) by 30,000 molecular weight cut-off (MWCO) filtration (YM30, Millipore). Retentate was desalted with 50 mM sodium phosphate, 150 mM NaCl, pH 7.2, concentrated by 100,000 MWCO filtration, and loaded onto a Sephacryl S-300 column. Elution of protein (flow rate of $0.5\text{--}1.0 \text{ ml min}^{-1}$) was monitored by absorbance at 280 nm. Fractions (1 ml) were then collected and stored at 4°C .

Identification by mass spectrometry. Bands of interest excised from Coomassie-stained polyacrylamide were prepared²⁷ and the mass spectra of the resulting peptides were recorded on a Bruker Ultraflex MALDI-TOF/TOF reflecting time-of-flight mass spectrometer (Bruker Daltonics). A non-redundant protein sequence collection (National Center for Biotechnology Information) was then searched with peptide mass data using ProFound²⁸ software at an error tolerance of 100 p.p.m. within the *E. coli* taxonomy.

Cloning, expression and purification of recombinant flagellin molecules. To clone the full-length *fljC* (H48) gene, primers jf030106.1 and jf030106.2 were used to amplify *fljC* from MG1655. The product was ligated into pTrcHisB in-frame with the polyhistidine-encoding region to produce pKR001b. Primers jf050206.1 and jf030106.2 were used to amplify and clone the region encoding amino acids 174–498 (*FliC*_{174–498}) to produce pKR005b. Finally, the region encoding residues 1–173 of *FliC* was amplified using primers jf030106.1 and jf050206.2 and cloned into pTrcHisB to produce pKR007b. These plasmids were introduced into Top10, which does not produce native flagellin²⁹. Recombinant flagellins with polyhistidine tags at their N termini were purified by nickel-affinity chromatography.

Membrane-based protein interaction studies. Varying amounts of target (bait) proteins were absorbed onto nitrocellulose, followed by addition of biotinylated prey proteins ($10 \mu\text{g ml}^{-1}$) and incubation (1 h) at room temperature. Strips

were washed to remove unbound prey protein. Bound biotinylated prey proteins were detected with streptavidin–horseradish peroxidase and chemiluminescent substrate.

Co-immunoprecipitation. Anti-EtpA IgG polyclonal antibodies were first purified from highly cross-absorbed anti-EtpA antisera⁶ by protein G affinity column chromatography (HiTrap ProteinG, Amersham Biosciences). Pre-immune sera from the same rabbit were treated in an identical fashion. The resulting antibodies ($200 \mu\text{g}$) were coupled to solid support gel matrix. Concentrated supernatants from ETEC were incubated overnight at 4°C with matrix containing either pre-immune IgG or anti-EtpA (IgG) antibodies. After washing, the matrix proteins were eluted (ImmunoPure, IgG Elution Buffer, pH 2.8, Pierce), separated by SDS–PAGE (10%) and transferred to nitrocellulose for subsequent immunoblotting.

Molecular pull-down assays. Polyhistidine-tagged flagellin molecules and rEtpA were added together in solution in a molar ratio of 1:1 (approximately 150 pmol each). After incubation for 1 h at 4°C , polyhistidine-tagged flagellins and interacting EtpA were pulled down by the addition of $100 \mu\text{l}$ of Co^{2+} metal affinity bead suspension in PBS. Bound proteins were released by incubation in SDS–PAGE sample buffer and used for immunoblotting.

Transmission and scanning electron microscopy. Immunogold labelling of EtpA and conserved regions of flagellin *in situ*¹⁷ used suspensions of live bacteria grown on the surface of ultraviolet-sterilized grids and fixed with formaldehyde and glutaraldehyde. Immunogold detection was then performed using highly cross-absorbed anti-EtpA polyclonal rabbit antisera or affinity-purified anti-flagellin antibodies followed by anti-rabbit IgG gold (10 nm) conjugate. Negative staining was then performed in 1% phosphotungstic acid, pH 6.5. Scanning images were acquired on a Philips XL30 ESEM instrument.

Linker scanning mutagenesis of *etpA*. pJL017 was the target for *in vitro* Tn7-based mutagenesis¹⁹. Plasmids with *etpA*-mapped, non-redundant insertions were digested with *PmeI*, and re-ligated to remove most of the transprimers. This yielded *etpA* mutants with 15-base-pair scar sequences that (along with pJL030) were used in transformation of Top10 to Amp^R/Cm^R . Plasmids encoding effectively secreted EtpA mutants in Top10 were introduced into isogenic *etpA* mutant jf1668 for subsequent adherence assays.

Intestinal competition. The previously described model of murine intestinal colonization²⁶ was used in competition between *etpA* mutant jf1668 complemented with EtpA expression plasmid pJL017, or the same mutant complemented with pJMF1087, which expresses EtpA that has lost the ability to bind to *FliC* after introduction of a linker mutation. Each mouse received 1×10^4 c.f.u. of jf1668(pJL017) and 1×10^4 c.f.u. of jf1668(pJMF1087) (together by gavage). After challenge, water supply for the mice included ampicillin ($50 \mu\text{g ml}^{-1}$) and arabinose (0.0002%), respectively. Twenty-four hours later, intestinal lysates²⁶ were plated onto Luria agar plates containing chloramphenicol and ampicillin. Amp^R/Cm^R colonies were subjected to PCR with primers jf122205.1 and jf092605.3 to generate an approximate 1,690-base-pair amplicon that was digested with *PmeI* to distinguish the wild-type allele from pJL017 from the mutant containing a *PmeI* site (pJMF1087).

27. Cummings, E. D. et al. High-throughput proteomics processing of proteins in polyacrylamide in a multiwell format. *J. Proteome Res.* **6**, 1603–1608 (2007).

28. Zhang, W. & Chait, B. T. ProFound: an expert system for protein identification using mass spectrometric peptide mapping information. *Anal. Chem.* **72**, 2482–2489 (2000).

29. Hayashi, F. et al. The innate immune response to bacterial flagellin is mediated by Toll-like receptor 5. *Nature* **410**, 1099–1103 (2001).

Frequent somatic mutations of *GNAQ* in uveal melanoma and blue naevi

Catherine D. Van Raamsdonk¹, Vladimir Bezrookove², Gary Green², Jürgen Bauer^{2,4}, Lona Gaugler², Joan M. O'Brien³, Elizabeth M. Simpson⁵, Gregory S. Barsh⁶ & Boris C. Bastian²

BRAF and *NRAS* are common targets for somatic mutations in benign and malignant neoplasms that arise from melanocytes situated in epithelial structures, and lead to constitutive activation of the mitogen-activated protein (MAP) kinase pathway^{1,2}. However, *BRAF* and *NRAS* mutations are absent in a number of other melanocytic neoplasms in which the equivalent oncogenic events are currently unknown³. Here we report frequent somatic mutations in the heterotrimeric G protein α -subunit, *GNAQ*, in blue naevi (83%) and ocular melanoma of the uvea (46%). The mutations occur exclusively in codon 209 in the Ras-like domain and result in constitutive activation, turning *GNAQ* into a dominant acting oncogene. Our results demonstrate an alternative route to MAP kinase activation in melanocytic neoplasia, providing new opportunities for therapeutic intervention.

Most melanocytic neoplasms—benign melanocytic naevi as well as melanomas—originate from melanocytes situated within epithelial structures throughout the body, mostly the sun-exposed skin of individuals with light complexion. Most naevi and melanomas show oncogenic mutations in signalling components of the MAP kinase pathway, in particular *BRAF* and *NRAS* (refs 1, 2). However, a subset of melanocytic neoplasms does not show mutations in *BRAF* and *NRAS* (ref. 3). One category, uveal melanoma, arises from melanocytes within the choroidal plexus of the eye and is biologically distinct from cutaneous melanoma by characteristic cytogenetic alterations⁴ and a very strong propensity to metastasize to the liver⁵. The other category comprises intradermal melanocytic proliferations, which can be congenital or acquired, and present in diverse ways ranging from discrete bluish moles (blue naevi) to large blue-grey patches affecting the conjunctiva and periorbital skin (naevus of Ota), shoulders (naevus of Ito) and the lower back (Mongolian spot)⁶. A potential connection between intradermal melanocytic neoplasms and uveal melanoma is suggested by the fact that naevus of Ota is a risk factor for uveal melanoma and by an overlap in some of the histomorphological features of the two conditions⁷.

Using a forward genetic screen in mice we previously identified hypermorphic mutations in *Gnaq* or *Gna11* as a cause of diffuse skin hyperpigmentation that was due to an increase of intradermal, but not epidermal, melanocytes⁸. *GNAQ* and *GNA11* encode members of the q class of G-protein α -subunits involved in mediating signals between G-protein-coupled receptors (GPCRs) and downstream effectors. To investigate whether similar pathways were involved in humans, we sequenced the entire coding regions of *GNAQ* and *GNA11* in a broad spectrum of benign and malignant melanocytic neoplasms. We found mutations in *GNAQ* in 83% of blue naevi ($n = 29$), 50% of 'malignant blue naevi' ($n = 2$) and 46% of uveal melanomas ($n = 48$) (Table 1 and Supplementary Fig. 1a). Naevus of

Ota is a condition in which a subtle proliferation of intradermal melanocytes results in hyperpigmentation of the conjunctiva and periorbital skin. To increase the detection limit for mutations in a background of normal cells, we used a mutation-specific assay and found a mutation in one of 14 cases (6%; Supplementary Fig. 1b). No somatic point mutations were found in *GNA11*.

All mutations in *GNAQ* were somatically acquired as assessed by sequencing DNA from adjacent tissue, and occurred exclusively at codon 209 (Supplementary Table 1). The glutamine at codon 209 lies within the Ras-like domain of *GNAQ* (corresponding to residue 61 of Ras) and is essential for GTP hydrolysis⁹. In Ras family members, mutations at this site, and at codon 12, cause loss of GTPase activity with constitutive activation^{9–11}. There is no equivalent of codon 12 in *GNAQ*. In contrast to the findings in humans, the mutations found in the dark-skinned mice occurred at I63, V179 and F335 in the mouse proteins and do not cause constitutive activation⁸.

So far, no mutations of *GNAQ* have been described in human neoplasia, but *GNAQ*^{Q209L} has been demonstrated to transform 3T3 cells¹¹. In addition, mutations of the corresponding codon in *G α _s* (*GNAS*) are found in human pituitary and thyroid tumours^{10,12}. To assess the effect of *GNAQ*^{Q209L} on human melanocytes, we established epitope-tagged lentiviral expression constructs to transfect normal and genetically

Table 1 | Frequency of *GNAQ* mutations in melanocytic neoplasms

Neoplasm type and diagnosis	Mutant (%)	<i>n</i>
Cutaneous and mucosal melanomas		
Melanoma on skin without chronic sun-induced damage ²²	0	15
Melanoma on skin with chronic sun-induced damage ²²	4	27
Acral melanoma	0	15
Mucosal melanoma	0	14
'Malignant blue naevus'	50	2
Melanoma arising in congenital naevus	0	3
Spitzoid melanoma	0	2
Total	-	78
Naevi		
Blue naevus	83	29
Naevus of Ota	6	17
Congenital naevus	0	7
Deep penetrating naevus	0	16
Proliferating nodule in giant congenital naevus	0	7
Spitz naevus	0	8
Total	-	84
Ocular melanomas		
Uveal melanoma	46	48
Uveal melanoma cell line	27	15
Conjunctival melanoma	0	11
Total	-	74
Grand total	-	236

The number and type of samples analysed is shown.

¹Department of Medical Genetics, University of British Columbia, Vancouver, British Columbia V6T1Z3, Canada. ²Department of Dermatology and Comprehensive Cancer Center, ³Department of Ophthalmology and Comprehensive Cancer Center, University of California, San Francisco, California 94143, USA. ⁴Department of Dermatology, University of Tübingen, Tübingen D-72076, Germany. ⁵Centre for Molecular Medicine and Therapeutics and Department of Medical Genetics, University of British Columbia, Vancouver, British Columbia V6T1Z3, Canada. ⁶Department of Genetics, Stanford University, Stanford, California 94305, USA.

modified human melanocytes. The latter have an extended lifespan through transduction with telomerase (*hTERT*) and inactivation of their p53 and p16/CDK4/RB pathways, but still require additional factors (cyclic AMP, 12-*O*-tetradecanoylphorbol-13-acetate (TPA)) for growth (hereafter called *hTERT*/CDK4^{R24C}/p53^{DD} melanocytes¹³). Stable transfection of *GNAQ*^{Q209L} into primary human melanocytes was insufficient to induce anchorage-independent growth (data not shown). In contrast, transfection of *GNAQ*^{Q209L} into *hTERT*/CDK4^{R24C}/p53^{DD} melanocytes resulted in anchorage-independent growth with efficiencies comparable or slightly greater than transfection with *NRAS*^{Q61R} (Fig. 1a and Supplementary Table 2). Furthermore, *GNAQ*^{Q209L} but not wild-type *GNAQ* induced abnormally enlarged nuclei with markedly irregular contours (Fig. 1b and

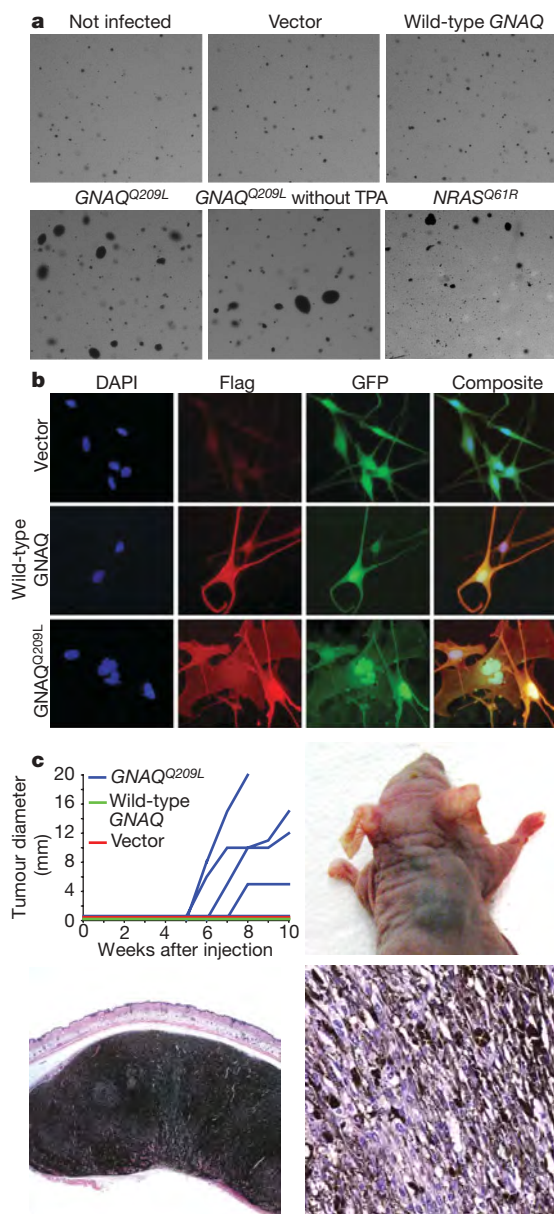


Figure 1 | *GNAQ*^{Q209L} transforms melanocytes. **a**, *GNAQ*^{Q209L} induces anchorage-independent growth in soft agar of *hTERT*/CDK4^{R24C}/p53^{DD} melanocytes in a TPA-independent manner with comparable efficiency as *NRAS*^{Q61R}. **b**, Cells expressing Flag-tagged *GNAQ*^{Q209L} showed enlarged nuclei with irregular contours after 5 days. **c**, Melan-a cells²³ stably transduced with *GNAQ*^{Q209L}, but not with wild-type *GNAQ* ($n = 3$) or vector control ($n = 4$), induce highly pigmented tumours of spindle and epithelioid melanocytes after 10 weeks in four out of five animals. The original magnifications for bottom-left and bottom-right panels of **c** are $\times 20$ and $\times 200$, respectively.

Supplementary Table 3). To validate *GNAQ*^{Q209L} as an oncogene *in vivo*, we performed tumorigenicity studies in nude mice (Fig. 1c). *GNAQ*^{Q209L}, but not wild-type *GNAQ* or vector-control-transfected melanocytes, gave rise to heavily pigmented tumours at the injection site. The tumour morphology resembled closely the spectrum of atypical blue naevus that in humans has been termed animal type melanoma or pigmented epithelioid melanocytoma⁶.

Signalling pathways downstream of *GNAQ* include activation of protein kinase C family members via the release of diacylglycerol (DAG) by phospholipase C β . Consistently, *GNAQ*^{Q209L}-transformed melanocytes grew in soft agar in the absence of TPA, a synthetic DAG analogue (Fig. 1a and Supplementary Table 2). Protein kinase C activation by way of *GNAQ* activation can activate the MAP kinase pathway in other cell types¹⁴. Uveal melanomas show MAP kinase activation¹⁵, but none of the uveal melanomas we examined in our study showed mutations in *BRAF* or *NRAS* (Supplementary Table 4), consistent with other studies³. We therefore tested whether *GNAQ*^{Q209L} would contribute to MAP kinase pathway activation in human melanocytes and uveal melanoma cells. As shown in Fig. 2, *GNAQ*^{Q209L} transfection into *hTERT*/CDK4^{R24C}/p53^{DD} melanocytes caused increased levels of phosphorylated ERK compared with control cells transfected with wild-type *GNAQ* or an empty vector. Similar results were obtained with *GNAQ*^{Q209L} transfection into primary human melanocytes and 293T cells (Supplementary Fig. 2). Conversely, short interfering RNA (siRNA)-mediated knockdown of *GNAQ* in the uveal melanoma cell line OMM1.3, which harbours the *GNAQ*^{Q209L} mutation, resulted in a decrease of phosphorylated ERK levels (Fig. 3a). In addition, *GNAQ* knockdown in OMM1.3 cells causes a substantial decrease in cell number (Fig. 3b), loss of anchorage-independent growth (Fig. 3c) and a marked increase in sub-G0/G1 population (Fig. 3d) as compared with control cells. Similar results were obtained when another uveal melanoma cell line, Mel202, was

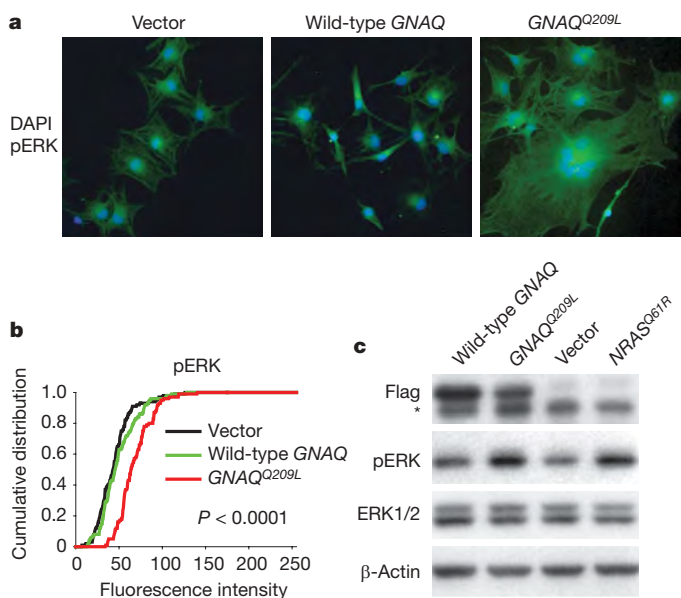


Figure 2 | *GNAQ*^{Q209L} induces MAP kinase activation. **a**, Increased expression of phosphorylated ERK in *hTERT*/CDK4^{R24C}/p53^{DD} melanocytes transfected with *GNAQ*^{Q209L} compared to similar melanocytes transfected with wild-type *GNAQ* or empty vector. DAPI, 4,6-diamidino-2-phenylindole. **b**, Cumulative distribution of mean pixel fluorescence intensity per cell obtained from immunofluorescent detection of phosphorylated ERK (P -value is for *GNAQ*^{Q209L} versus vector). **c**, Western blot showing increased phosphorylated ERK levels in *hTERT*/CDK4^{R24C}/p53^{DD} melanocytes expressing Flag-tagged *GNAQ*^{Q209L} compared to cells transfected with Flag-tagged wild-type *GNAQ* or vector control. *NRAS*^{Q61R} transduced melanocytes are shown as a positive control. The asterisk (labelling a band migrating just below the Flag band) indicates a nonspecific reactive band in the lysate.

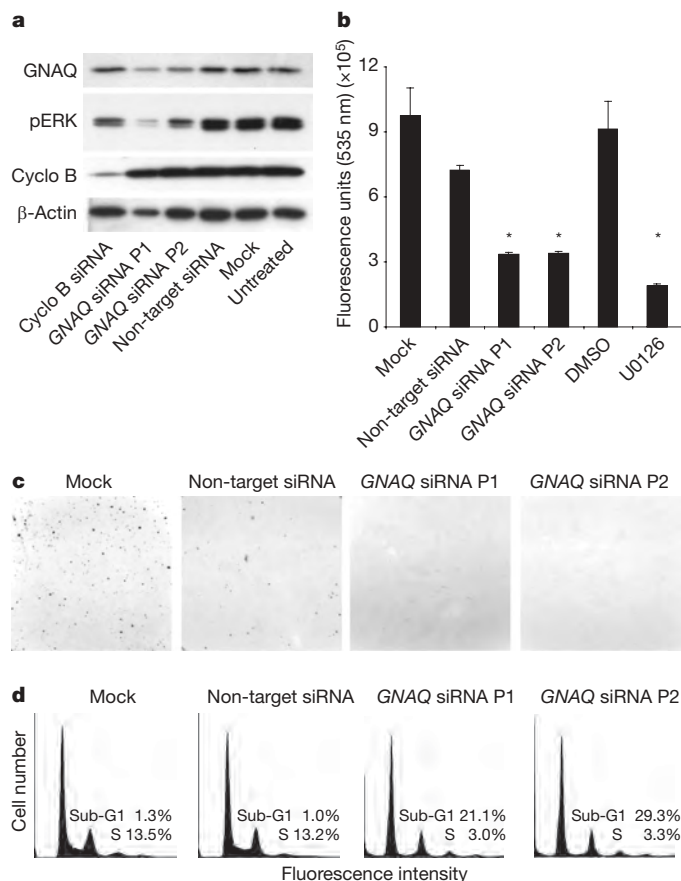


Figure 3 | Knockdown of *GNAQ* in OMM1.3 cells results in MAP kinase inhibition, reduced growth and apoptosis. **a**, Western blot after treatment with two pools of siRNAs against *GNAQ* shows decreased phosphorylated ERK levels compared with control treated cells: cyclophilin B and non-target siRNA. **b**, After 72 h, *GNAQ* knockdown results in marked reduction of cell numbers, similar to the effect of MAP-kinase kinase inhibitor U0126. Bars show means and standard error of five replicate assays. Asterisk, $P < 0.05$, t -test compared to mock or vehicle control, respectively. **c**, *GNAQ* knockdown reduces the number of colonies (upper-left corner) formed in soft agar. **d**, Cell cycle profiles showing an increase of the sub-G0/G1 population after *GNAQ* knockdown.

treated with siRNA against *GNAQ*^{Q209L} (Supplementary Fig. 3). Mel202 and OMM1.3 stem from different patients, as confirmed by DNA fingerprinting (data not shown).

Our data identify *GNAQ* as a novel oncogene in human neoplasia. *GNAQ* operates downstream of several GPCRs that are important in melanocyte homeostasis and neoplasia. *GNAQ* is involved in endothelin signalling, which is essential for melanocyte survival early during development¹⁶. G_q signalling may also contribute to the association observed for melanoma invasion and metastasis with Wnt family members¹⁷, as frizzled receptors can couple to G_q ¹⁸. Furthermore, G_q signalling probably underlies the ability of the metabotropic glutamate receptor gene, *Grm1*, to cause dermal melanocytic neoplasia and ocular melanoma in transgenic mice¹⁹.

The location of neoplastic melanocytes induced by somatic *GNAQ* mutation in humans is very similar to the location of melanocytes affected by germline *Gnaq* (and *Gna11*) mutations in mice⁸. In both cases, the melanocytic proliferations spare epithelial structures. However, our previous work in mice suggests that these mutations do not interfere with homing of melanocytes to epithelial structures, but instead lead to an increase of the total melanoblast pool⁸. In humans, it is not known whether the adult dermis contains any residual sparse populations of melanocytes in which *GNAQ* mutations could occur and induce intradermal melanocytic tumours^{6,20}.

Acquired blue naevi are typically small and well circumscribed, raising the possibility that they arise from an intradermal population of melanocytes that remains to be characterized. By contrast, naevus of Ota involves different structures such as periorbital skin, conjunctiva, neurovascular bundles, ganglia and uvea, suggesting that these *GNAQ* mutations may arise early in a migrating melanoblast. This later neoplasm shows strong similarities to the murine studies and indicates a specific window for G_q signalling in terms of cell type and developmental time that is conserved across species.

Our findings identify *GNAQ* as a genetic link between naevus of Ota and uveal melanoma and help to explain why naevi of Ota are a risk factor for uveal melanoma⁷. The risk is small, as only about 1 in 400 naevi of Ota progress to uveal melanoma, and future studies will have to elucidate the role of *GNAQ* mutations in this risk. In our experiments, *GNAQ* behaves similarly to the oncogenes *BRAF* and *NRAS* in that its mutation is insufficient for full progression to melanoma. This is illustrated best by blue naevi, which are generally stable lesions that rarely become malignant ('malignant blue naevus')⁶. Thus, MAP kinase activation seems to be an early event in neoplasms with *GNAQ* mutations, as it is in neoplasms with *BRAF* and *NRAS* mutations². Further studies are necessary to determine whether the difference in tissue involvement between melanocytic neoplasms with *BRAF* mutations and those with *GNAQ* mutations is a functional consequence of the mutations themselves, or indicates differences in the target cell populations in which these mutations occur.

Uveal melanoma is a highly aggressive cancer without any effective treatment options once it metastasizes. Although it only accounts for approximately 5% of all melanomas, it represents the most common intraocular malignancy in the United States and has a 5-year disease-specific survival rate of approximately 70%²¹. Our study identifies signalling components downstream of *GNAQ* as potential targets in this disease.

METHODS SUMMARY

GNAQ and *GNA11* were sequenced in DNA extracted from archival, paraffin-embedded biopsies under the approval of the institutional review boards at UCSF, Stanford and University of British Columbia (UBC). Primary, hTERT/CDK4^{R24C}/p53^{DD} and melan-a melanocytes were stably infected with FG12 lentiviral expression vectors expressing Flag-tagged wild-type *GNAQ* or *GNAQ*^{Q209L}, empty vector or *NRAS*^{Q61R}. Infection efficiencies were estimated by the proportion of cells expressing GFP. To assess anchorage-independent growth, melanocytes were plated on soft agar, cultured for 28 days and stained with 0.005% crystal violet. For tumorigenicity experiments, one million lentiviral transfected melan-a cells were injected into each nude mouse, housed at UBC according to CCAC guidelines. For immunofluorescence, lentiviral transfected cells were cultured on coverslips for 5 days and incubated with antibodies against pERK (E-4, Santa Cruz Biotechnology), cyclin D1 (M-20, Santa Cruz Biotechnology) and *GNAQ* (C-19, Santa Cruz Biotechnology). OMM1.3 and Mel202 cells were transfected with two different pools of siRNA against *GNAQ*: pool 1, 5'-CAAUAAGGCUCUAUGCACAUAU-3', 5'-CGACGAGAAUAUCAUAUAUUU-3', 5'-GCAAGAGUACGUUAUCAUAU-3', 5'-UAGUAGCGCUUAGUGAAUAUU-3'; pool 2, 5'-AUGCACAAUAGUUCGAGAAU-3', 5'-UAUGAUAGACGACGAGAAUUU-3', 5'-CAGACAAUGAGAACCGAAU-3', 5'-CGCCACAGACACGAGAAUUU-3'. For western blot analysis, 5–20 µg of protein was extracted from lentiviral or siRNA transfected cells. Primary antibodies were: pERK, cyclin D1, *GNAQ*, cyclophilin B (Abcam), anti-Flag M2 (Sigma), anti-ERK1/2 pAb (Promega), and β-actin (Sigma). Secondary antibodies were labelled with horseradish peroxidase. Relative cell numbers were quantified by the CyQUANT cell proliferation assay kit (Invitrogen). Cell cycle measurements were performed on a FACSCalibur after staining with propidium iodide. Student's t -test and Fisher's exact test were used for statistical comparison.

Full Methods and any associated references are available in the online version of the paper at www.nature.com/nature.

Received 25 January; accepted 17 October 2008.

Published online 10 December 2008.

1. Davies, H. *et al.* Mutations of the *BRAF* gene in human cancer. *Nature* 417, 949–954 (2002).

2. Pollock, P. M. *et al.* High frequency of BRAF mutations in nevi. *Nature Genet.* **25**, 25 (2002).
3. Saldanha, G. *et al.* High BRAF mutation frequency does not characterize all melanocytic tumor types. *Int. J. Cancer* **111**, 705–710 (2004).
4. Horsman, D. E. & White, V. A. Cytogenetic analysis of uveal melanoma. Consistent occurrence of monosomy 3 and trisomy 8q. *Cancer* **71**, 811–819 (1993).
5. Singh, A. D., Bergman, L. & Seregard, S. Uveal melanoma: epidemiologic aspects. *Ophthalmol. Clin. North Am.* **18**, 75–84 (2005).
6. Zembowicz, A. & Mihm, M. C. Dermal dendritic melanocytic proliferations: an update. *Histopathology* **45**, 433–451 (2004).
7. Singh, A. D. *et al.* Lifetime prevalence of uveal melanoma in white patients with ocular (dermal) melanocytosis. *Ophthalmology* **105**, 195–198 (1998).
8. Van Raamsdonk, C. D., Fitch, K. R., Fuchs, H., de Angelis, M. H. & Barsh, G. S. Effects of G-protein mutations on skin color. *Nature Genet.* **36**, 961–968 (2004).
9. Markby, D. W., Onrust, R. & Bourne, H. R. Separate GTP binding and GTPase activating domains of a G alpha subunit. *Science* **262**, 1895–1901 (1993).
10. Landis, C. A. *et al.* GTPase inhibiting mutations activate the α chain of G_s and stimulate adenylyl cyclase in human pituitary tumours. *Nature* **340**, 692–696 (1989).
11. Kalinec, G., Nazarali, A. J., Hermouet, S., Xu, N. & Gutkind, J. S. Mutated alpha subunit of the Gq protein induces malignant transformation in NIH 3T3 cells. *Mol. Cell. Biol.* **12**, 4687–4693 (1992).
12. Lyons, J. *et al.* Two G protein oncogenes in human endocrine tumors. *Science* **249**, 655–659 (1990).
13. Garraway, L. A. *et al.* Integrative genomic analyses identify MITF as a lineage survival oncogene amplified in malignant melanoma. *Nature* **436**, 117–122 (2005).
14. Hubbard, K. B. & Hepler, J. R. Cell signalling diversity of the Gq α family of heterotrimeric G proteins. *Cell. Signal.* **18**, 135–150 (2006).
15. Zuidervaart, W. *et al.* Activation of the MAPK pathway is a common event in uveal melanomas although it rarely occurs through mutation of BRAF or RAS. *Br. J. Cancer* **92**, 2032–2038 (2005).
16. Shin, M. K., Levorse, J. M., Ingram, R. S. & Tilghman, S. M. The temporal requirement for endothelin receptor-B signalling during neural crest development. *Nature* **402**, 496–501 (1999).
17. Dissanayake, S. K. *et al.* The Wnt5A/protein kinase C pathway mediates motility in melanoma cells via the inhibition of metastasis suppressors and initiation of an epithelial to mesenchymal transition. *J. Biol. Chem.* **282**, 17259–17271 (2007).
18. Sheldahl, L. C., Park, M., Malbon, C. C. & Moon, R. T. Protein kinase C is differentially stimulated by Wnt and Frizzled homologs in a G-protein-dependent manner. *Curr. Biol.* **9**, 695–698 (1999).
19. Marin, Y. E. *et al.* Stimulation of oncogenic metabotropic glutamate receptor 1 in melanoma cells activates ERK1/2 via PKC ϵ . *Cell. Signal.* **18**, 1279–1286 (2006).
20. Mizushima, J., Nogita, T., Higaki, Y., Horikoshi, T. & Kawashima, M. Dormant melanocytes in the dermis: do dermal melanocytes of acquired dermal melanocytosis exist from birth? *Br. J. Dermatol.* **139**, 349–350 (1998).
21. Chang, A. E., Karnell, L. H. & Menck, H. R. The National Cancer Data Base report on cutaneous and noncutaneous melanoma: a summary of 84,836 cases from the past decade. The American College of Surgeons Commission on Cancer and the American Cancer Society. *Cancer* **83**, 1664–1678 (1998).
22. Curtin, J. A. *et al.* Distinct sets of genetic alterations in melanoma. *N. Engl. J. Med.* **353**, 2135–2147 (2005).
23. Bennett, D. C., Cooper, P. J. & Hart, I. R. A line of non-tumorigenic mouse melanocytes, syngeneic with the B16 melanoma and requiring a tumour promoter for growth. *Int. J. Cancer* **39**, 414–418 (1987).

Supplementary Information is linked to the online version of the paper at www.nature.com/nature.

Acknowledgements We thank W. Harbour for providing additional DNA samples from uveal melanomas and P. Viciara-Rodriguez and A. Balmain for providing advice. hTERT/CDK4^{R24C}/p53^{DD} melanocytes were a gift from D. Fisher, Dana Farber Cancer Institute¹³, normal human melanocytes from foreskin were a gift from M. Herlyn, and OMM1.3 and Mel202 cells were originally from B. Ksander. The melan-a cells were a gift from D. Bennett, St George's University, London²³. This work was supported by grants from the National Cancer Institute (P01 CA025874 Project 2 to B.C.B.) the Melanoma Research Alliance, the Canadian Institutes of Health Research (MOP-79511 to C.D.V.R.), and the National Institutes of Health (G.S.B.).

Author Information Reprints and permissions information is available at www.nature.com/reprints. Correspondence and requests for materials should be addressed to B.C.B. (bastian@cc.ucsf.edu).

METHODS

DNA. DNA was obtained from archival paraffin-embedded biopsies under the approval of the institutional review boards at UCSF, Stanford and the University of British Columbia. For each sample, 20 µm sections were microdissected, washed in xylene and ethanol and digested with proteinase K. DNA was then extracted with phenol-chloroform-isoamyl-alcohol.

Sequencing. Biopsy DNA was amplified using polymerase chain reaction (PCR). For GNAQ exon 5, the primers used were 5'-CCCACACCTACTTTCTATCATTTAC-3' and 5'-TTTCCCTAAGTTTGTAAAGTAGTGC-3'. PCR products were used as templates for sequencing reactions using Big Dye (ABI). Samples identified with mutations in both sequencing directions were replicated at least twice. Mutations 1–3 were verified with restriction-fragment length polymorphism. Mutations 1 and 2 create an Eco0109I restriction site, whereas mutation 3 produces an AflIII restriction site.

Sensitive assay for Q209 mutations in mixed cell populations. The peptide nucleic acid, Ac-TCTCTGACCTTTGGC-CONH₂, was resuspended in 50% DMF and used at a final concentration of 4 µM against 2 ng template DNA in a 25 µl reaction. The reaction conditions were 0.25 mM dNTPs, 6× BSA, 2 U Hotstar Taq, 1× Hotstar Taq buffer, and 0.5 µM each primer, 5'-TTTCCCTAAGTTTGTAAAGTAGTGC-3' and 5'-ATCCATTTCTTCTCTCTGACC-3'. PCR consisted of 40 cycles of 95 °C (1 min), 73 °C (1 min), 57 °C (45 s) and 72 °C (1 min).

Plasmids. A GNAQ^{Q209L} cDNA plasmid was obtained from UMR cDNA Resource Center. The wild-type counterpart was generated by site-specific mutagenesis. The coding regions of both constructs were epitope-tagged with an N-terminal Flag tag and cloned into the lentiviral expression vector FG12. All constructs were sequenced for confirmation.

Cell culture. hTERT/CDK4^{R24C}/p53^{DD} melanocytes were cultured in glutamine containing Ham's F12 media supplemented with 7% FBS, 50 ng ml⁻¹ TPA, 0.1 mM IBMX, 10 µM Na₃VO₄ and 1 mM dbcAMP. Primary normal melanocytes were cultured in MCDB153 supplemented 20% FBS, 2% chelated FBS, 5 µg ml⁻¹ L-glutamin, 15 µg ml⁻¹ cholera toxin, 0.5 ng ml⁻¹ bFGF, 100 nM ET3 and 1.68 mM SCF. Cell lines OMM1.3, Mel202 and 293T were cultured in RPMI supplemented with 10% fetal bovine serum. Melan-a cells were cultured in glutamine-containing RPMI media supplemented with 10% FCS and 200 nM TPA.

Lentiviral infection. Viral supernatants were generated using 293T cells transfected with 10 µg plasmid and appropriate lentiviral packaging plasmids. Media was changed 16 h after transfection and the virus was collected 40 to 56 h later. hTERT/CDK4^{R24C}/p53^{DD}, melan-a and normal melanocytes were infected and infection efficiencies were estimated by the presence of GFP-expressing cells.

Transient transfection. 293T cells were seeded in 6-well plates at 1 × 10⁶ cells per well with RPMI/10% FCS. Transfections were carried out using Lipofectamine 2000 (Invitrogen) and 2 µg plasmid pcDNA6.2/V5-DEST Gateway vector (Invitrogen) alone or containing the complete coding region for either GNAQ^{Q209L} or wild-type GNAQ, respectively. Cells were lysed 48 h after transfection and assayed for protein content.

Tumorigenicity study. Melan-a cells were lentiviral transfected with wild-type GNAQ, GNAQ^{Q209L} and empty vector control. Seven days after infection, cells were resuspended in DMEM at five million cells per millilitre. Four-month-old, albino female nude mice (NU/J) were injected with 0.2 ml subcutaneously. Mice were palpated weekly.

Cell proliferation assay. Relative cell numbers were quantified by the CyQUANT Cell (Invitrogen) proliferation assay kit according to the manufacturer's protocol

using 96-well plates. 7.5 × 10³ cells were transfected and the fluorescent intensity was read after 72 h.

Immunofluorescence. Human primary and hTERT/CDK4^{R24C}/p53^{DD} melanocytes were cultured on coverslips in 6-well plates and infected with lentiviral vectors containing either GNAQ^{Q209L}, wild-type GNAQ, or an empty vector as control. Five days after infection, cells were fixed with 4% formaldehyde in PBS, permeabilized with 0.2% Triton X-100 and incubated with 3% BSA. Antibodies against pERK (E-4, Santa Cruz Biotechnology), cyclin D1 (M-20, Santa Cruz Biotechnology) and GNAQ (C-19, Santa Cruz Biotechnology) were detected using secondary antibodies labelled with Alexa Fluor 594 and 532 (Molecular Probes). Images were taken at fixed exposures with an Axio Image M1 microscope (Zeiss). The fluorescence intensities were quantified using ImageJ software and the mean pixel intensities were used for statistical analysis using Microsoft Excel and Data Desk (Data Description, Inc.).

Soft agar assay. 10 × 10³ human primary melanocytes, hTERT/CDK4^{R24C}/p53^{DD} melanocytes stably expressing GNAQ^{Q209L}, wild-type GNAQ, NRAS^{Q61R} or vector control and siRNA-treated OMM1.3 and Mel202 cells were suspended in full media containing 0.35% agar and plated on a lower layer of 0.5% agar in 6-well plates. After 28 days, cells were stained with 0.005% crystal violet. Colony number and size were quantified using ImageJ software.

Cell cycle analysis. Seventy-two hours after transfection with siRNA against GNAQ, OMM1.3 and Mel202 cells were trypsinized, washed with cold PBS and fixed with 70% ethanol. Fixed cells were stained with propidium iodide. Cell cycle measurements were performed on a FACSCalibur (BD Biosciences), with a minimum of 20,000 events, and profiles were analysed using FlowJo and ModFit.

siRNA transfection. OMM1.3 and Mel202 cells were plated in RPMI/10% FCS in 6-well or 96-well plates at 1.5 × 10⁵ or 5 × 10³ cells per well, respectively. Two different pools, each comprised of four siRNA duplexes (pool 1, 5'-CAAUAAGGCUCAUGCACAAUU-3', 5'-CGACGAGAAUAUCAUUAUUU-3', 5'-GCAAGAGUACGUUUUAUCAAUU-3', 5'-UAGUAGCGCUUAGUGAAU-3'; pool 2, 5'-AUGCACAUAUAGUUCGAGAUU-3', 5'-UAUGAUAGACGACGAGAAUUU-3', 5'-CAGACAAUGAGAACCGAAUUU-3', 5'-CGC-CACAGACACCGAGAAUUU-3') against GNAQ and ON-TARGETplus controls (all Dharmacon), were transfected in lipofectamine RNAiMax (1 µl pmol⁻¹ siRNA) at 100 nM. siRNA complexes were formed in OptiMEM. Cells were lysed for analysis 72–96 h after transfection. For soft agar assay, 48 post-transfection cells were used.

Western blot analysis. Cells were washed twice with ice-cold PBS and lysed in 50 mM Tris-HCl pH 7.8, 1% NP-40, 10% glycerol, 150 mM NaCl, 1% sodium deoxycholate, 1% sodium dodecyl sulphate, supplemented with protease inhibitor, phosphatase inhibitor and EDTA (Pierce Biotechnologies). The protein content of the lysates was determined by the BCA Protein Assay Reagent (Pierce Biotechnologies). 5–20 µg of protein were separated by SDS-PAGE and transferred to Immobilon-P membrane (Millipore). Primary antibodies were pERK (E-4, Santa Cruz Biotechnology), cyclin D1 (M-20, Santa Cruz Biotechnology), GNAQ (C-19, Santa Cruz Biotechnology), cyclophilin B (Abcam), anti-Flag M2 (Sigma), anti-ERK1/2 pAb (Promega) and β-actin (Sigma). Secondary antibodies were labelled with horseradish peroxidase.

Statistical analysis. Immunofluorescence data and CyQUANT measurements were analysed using Student's *t*-test. Fisher's exact test was used to compare the proportion of atypical cells.

Prominin 1 marks intestinal stem cells that are susceptible to neoplastic transformation

Liqin Zhu¹, Paul Gibson¹, D. Spencer Currel¹, Yiai Tong¹, Robert J. Richardson¹, Ildar T. Bayazitov¹, Helen Poppleton¹, Stanislav Zakharenko¹, David W. Ellison² & Richard J. Gilbertson^{1,3}

Cancer stem cells are remarkably similar to normal stem cells: both self-renew, are multipotent and express common surface markers, for example, prominin 1 (PROM1, also called CD133)¹. What remains unclear is whether cancer stem cells are the direct progeny of mutated stem cells or more mature cells that reacquire stem cell properties during tumour formation. Answering this question will require knowledge of whether normal stem cells are susceptible to cancer-causing mutations; however, this has proved difficult to test because the identity of most adult tissue stem cells is not known. Here, using an inducible Cre, nuclear LacZ reporter allele knocked into the *Prom1* locus (*Prom1*^{C-L}), we show that Prom1 is expressed in a variety of developing and adult tissues. Lineage-tracing studies of adult *Prom1*^{+/C-L} mice containing the *Rosa26-YFP* reporter allele showed that Prom1⁺ cells are located at the base of crypts in the small intestine, co-express *Lgr5* (ref. 2), generate the entire intestinal epithelium, and are therefore the small intestinal stem cell. Prom1 was reported recently to mark cancer stem cells of human intestinal tumours that arise frequently as a consequence of aberrant wingless (Wnt) signalling^{3–5}. Activation of endogenous Wnt signalling in *Prom1*^{+/C-L} mice containing a Cre-dependent mutant allele of β -catenin (*Ctnnb1*^{lox(ex3)}) resulted in a gross disruption of crypt architecture and a disproportionate expansion of Prom1⁺ cells at the crypt base. Lineage tracing demonstrated that the progeny of these cells replaced the mucosa of the entire small intestine with neoplastic tissue that was characterized by focal high-grade intraepithelial neoplasia and crypt adenoma formation. Although all neoplastic cells arose from Prom1⁺ cells in these mice, only 7% of tumour cells retained Prom1 expression. Our data indicate that Prom1 marks stem cells in the adult small intestine that are susceptible to transformation into tumours retaining a fraction of mutant Prom1⁺ tumour cells.

The hypothesis that cancers are generated by rare populations of cancer stem cells that are more tumorigenic than other cancer cells has gained increasing credence¹. This has followed consistent observations that some solid tumours and leukaemias contain small numbers of self-renewing cells that propagate the disease when transplanted in mice^{3,4,6–8}. Cancer stem cells also express markers of normal stem cells, and in the brain, exist in microenvironments that mimic normal stem cell niches^{9,10}.

Although there is an expanding literature to support the existence of cancer stem cells, important caveats of these studies continue to provoke debate. The current definitive test of a cancer stem cell is the capacity to propagate tumours as xenografts in immunocompromized mice¹¹; however, it has been argued that species differences alone might account for the selective growth of subpopulations of cells in these assays. Indeed, most cells in a mouse lymphoma were shown recently to possess tumour-initiating capacity when allografted

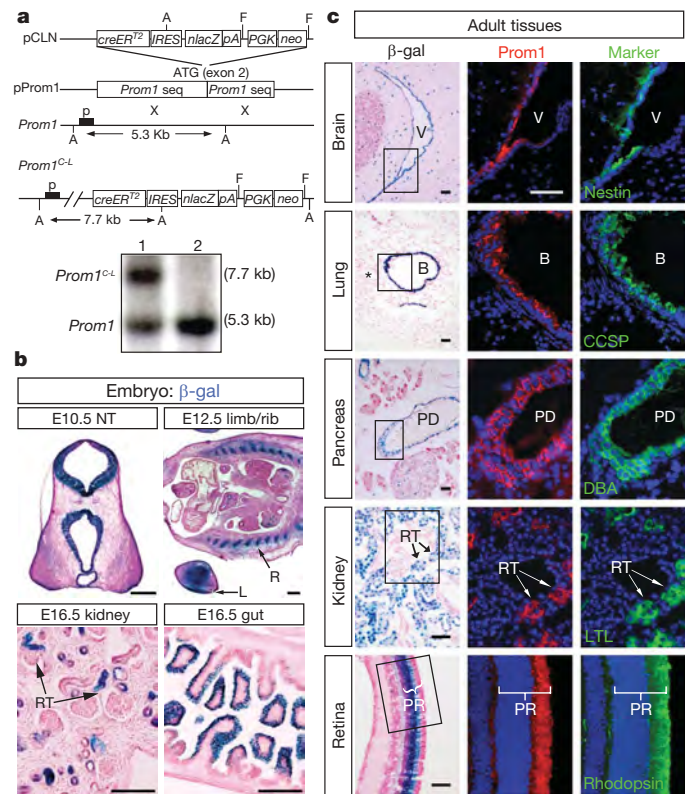


Figure 1 | Generation of *Prom1*^{C-L} mice and reporter analysis. **a**, Top to bottom: *creER*^{T2}-IRES-nLacZ-PGK-neo was cloned into the ATG site of *Prom1*. p*Prom1* was subject to homologous recombination with wild-type *Prom1* to generate the *Prom1*^{C-L} targeted allele. PGK-neo was excised by flip-recombination. A, ApaI sites; FRT, flip recombinase targets; p, Southern blot probe. The bottom panel shows Southern blot of mouse tissues heterozygous for the targeted allele (lane 1) and homozygous for the wild-type allele (lane 2). **b**, Expression of nLacZ from the *Prom1*^{C-L} allele in embryonic tissues. L, limb; NT, neural tube; R, rib; RT, renal tubule. Scale bars: 200 μ m. **c**, Prom1 and nLacZ expression in adult mouse (3 month) tissues. β -galactosidase staining (left column), Prom1 protein (middle column, immunofluorescence) and markers (right column) of neural stem and progenitor cells (nestin), Clara cells (Clara cell specific protein (CCSP)), pancreatic ductal cells (*Dolichos biflorus* agglutinin (DBA)-fluorescein), proximal renal tubular endothelial cells (*Lotus tetragonolobus* lectin (LTL)-fluorescein) and photoreceptors (rhodopsin) are shown. The middle and right columns are adjacent sections of the boxed areas in the left column. B, bronchiole; PD, pancreatic duct; PR, photoreceptor; RT, renal tubule; V, ventricle. The asterisk indicates a vessel at bronchioalveolar junction. Scale bars: 50 μ m.

¹Department of Developmental Neurobiology, ²Pathology and ³Oncology, St Jude Children's Research Hospital, 262 Danny Thomas Place, Memphis, Tennessee 38105, USA.

into syngenic mice¹². Further controversy has surrounded the use of stem cell surface markers to isolate cancer stem cells. Notable among these is PROM1, a five-transmembrane-domain-containing glycoprotein that is expressed on the surface of a variety of normal stem cells^{13–15}. Cancer stem cells of brain^{7,16}, gut^{3,4} and pancreatic¹⁷ tumours have been isolated using PROM1 antibodies; however, most PROM1 antibodies recognize glycosylation-dependent epitopes that vary with the differentiation and transformation status of the cell¹⁸, complicating the use of these reagents to fractionate stem cells. Without better understanding of normal tissue stem cells and their susceptibility to neoplastic transformation, it will be difficult to conduct definitive studies of the existence and origins of cancer stem cells.

To understand better the identity of normal tissue stem cells and their role in the cancer process, we generated a knockin allele in which we integrated a *creER*^{T2}-IRES-*nLacZ* cassette (where *nLacZ* indicates nuclear *lacZ*) at the first ATG codon of *Prom1* (*Prom1*^{C-L}), thereby creating a null allele (Fig. 1a and Supplementary Fig. 1). *Prom1*^{C-L/C-L} mice were born and aged normally, indicating that *Prom1* is dispensable for gross embryonic and postnatal development. *nLacZ* expression in *Prom1*^{C-L} embryos that retained one copy of the wild-type allele was restricted to the central nervous system, kidney, intestine and developing skeletal system (Fig. 1b). The tissue distribution of *Prom1* expression increased with subsequent development and was detected ultimately in several organs of adult *Prom1*^{C-L} mice (Fig. 1c,

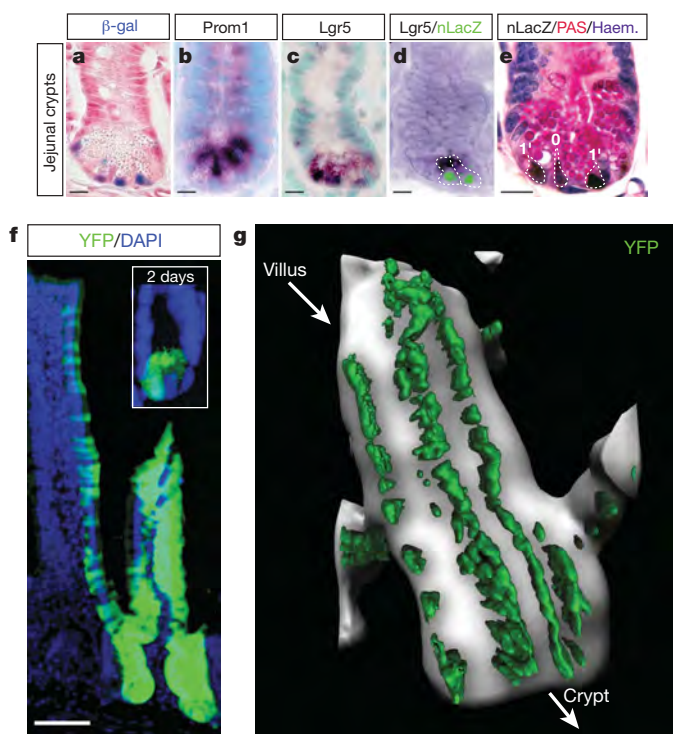


Figure 2 | *Prom1* marks small intestinal crypt stem cells. **a–c**, Expression of *Prom1*^{C-L} (β-galactosidase; **a**) and *Prom1* wild-type (*Prom1* in situ hybridization; **b**) alleles is confined to the small intestinal crypt base in *Prom1*^{C-L} mice and overlaps with *Lgr5* expression (in situ hybridization; **c**). **d**, *Lgr5* (in situ hybridization, cytoplasmic dark stain) and *Prom1* (green, *nLacZ* immunofluorescence) are co-expressed in the same cells (broken lines indicate cell boundaries). **e**, *nLacZ* immunohistochemistry (brown nuclear immunostain) counterstained with periodic acidic Schiff (PAS) (pink), to detect Paneth cells and haematoxylin (blue) reveals the position of *Prom1*^{C-L} cells (numbers denote crypt cell positions) in *Prom1*^{C-L} mice. Scale bars: 10 μm. **f**, The inset shows YFP⁺ cells in the crypt base of *Prom1*^{C-L}; *Rosa26-YFP* mice 2 days after tamoxifen induction. The main panel shows YFP labelling of the crypts and epithelial surface of the villi, 60 days after tamoxifen induction. Scale bar: 50 μm. **g**, Two-photon laser-scanning microscopy (YFP, green) through 464 μm of adult *Prom1*^{C-L} mouse small intestinal villus 10 days after tamoxifen induction.

Supplementary Fig. 2 and Supplementary Table 1). Analysis of *nLacZ* and *Prom1* protein expression from the modified and wild-type alleles, respectively, as well as tissue-specific markers, detected *Prom1* in Nestin⁺ cells of the ependymal layer and subventricular zone of the adult brain; Clara cell specific protein (CCSP)⁺ cells at the bronchoalveolar junction in the lung; and cells lining the pancreatic ducts (Fig. 1c). Each of these cell populations has been reported to include adult stem cells^{19–22}. *nLacZ* and *Prom1* expression was also observed in numerous differentiated cells in *Prom1*^{C-L} mice, including proximal renal tubule cells, photoreceptors in the retina (both Fig. 1c), neurons in the adult brain, acinar and islet cells in the pancreas, and goblet and columnar epithelial cells lining the colon (Supplementary Fig. 2). This pattern of *Prom1* expression is in agreement with recent studies of the *Prom1* locus in mouse tissues²³, and indicates that *Prom1* expression is not confined to stem cells, but is expressed also in multiple types of differentiated cells.

In contrast to most tissues, *Prom1* expression was relatively restricted in the small intestine of *Prom1*^{C-L} adult mice. Less than 3% of cells covering the villi expressed *nLacZ* ($n = 82$ out of 3,305), versus 26% ($n = 106$ out of 402) of cells at the crypt base (β-galactosidase staining, $P < 0.0001$, chi-squared test, Fig. 2a and Supplementary Fig. 3). *Prom1* messenger RNA expression was similarly distributed in

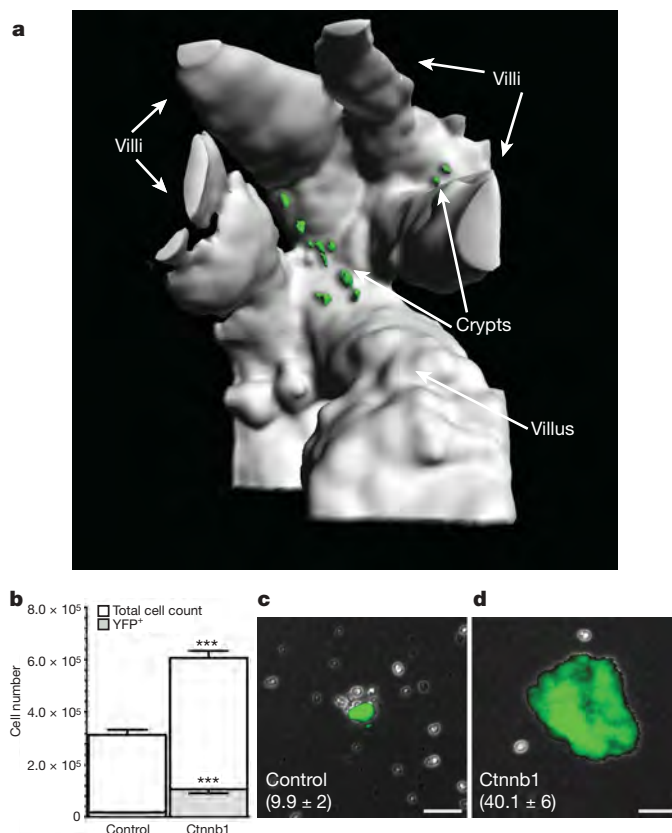


Figure 3 | Tumorigenesis in the mouse small intestine is initiated in *Prom1*⁺ crypt stem cells. **a**, View (394 μm depth) into the base of a small intestinal crypt in a *Prom1*^{C-L}; *Rosa26-YFP*; *Ctnnb1*^{+/lox(ex3)} mouse, 2 days after tamoxifen induction. Mice had 8.4 YFP⁺ cells per crypt (range 2–16; >210 crypts counted). **b**, Graph reporting the mean (±s.e.m., $n = 3$) number of total and YFP⁺ cells isolated 2 days after tamoxifen induction from *Prom1*^{C-L}; *Rosa26-YFP*; *Ctnnb1*^{+/+} (control) and *Prom1*^{C-L}; *Rosa26-YFP*; *Ctnnb1*^{+/lox(ex3)} (*Ctnnb1*) small intestinal mucosae (triple asterisk indicates $P < 0.0001$, Wilcoxon test). **c**, **d**, Colonies formed after 4 weeks in stem cell culture medium by single cells isolated 2 days after tamoxifen induction from *Prom1*^{C-L}; *Rosa26-YFP*; *Ctnnb1*^{+/+} (**c**) and *Prom1*^{C-L}; *Rosa26-YFP*; *Ctnnb1*^{+/lox(ex3)} (**d**) small intestinal mucosae. Numbers indicate total colonies per small intestinal culture (±s.e.m., $n = 10$, $P < 0.0001$, Wilcoxon test). Scale bars: 50 μm.

the small intestine and overlapped closely with that of *Lgr5*, which was reported recently to mark intestinal stem cells² (Fig. 2b, c and Supplementary Fig. 3). Therefore, as a first step to test if *Prom1* might be expressed by *Lgr5*⁺ crypt stem cells, we performed concurrent *Lgr5* *in situ* hybridization and nLacZ immunofluorescence analyses of adult *Prom1*^{+/C-L} mouse small intestine. Over 75% of *Lgr5*⁺ crypt cells contained nLacZ⁺ nuclei ($n = 390$ out of 500 cells counted), suggesting that *Prom1*⁺ crypt cells are predominantly stem cells (Fig. 2d). Furthermore, out of the 4.1 LacZ-positive nuclei (average, range 0–8 cells in 210 crypts counted) observed in each *Prom1*^{+/C-L} crypt, 23%, 30% and 17% were located at the 0, 1' and 2' cell positions, respectively, that are the sites most frequently occupied by *Lgr5*⁺ cells² (Fig. 2e). Together, these data indicate that *Lgr5*⁺ small intestinal stem cells express *Prom1*.

To test more directly whether *Prom1* marks stem cells in the small intestine, we used the Cre-dependent *Rosa26*-yellow fluorescence protein (*Rosa26*-YFP) reporter allele to trace the lineage of *Prom1*⁺ crypt cells. Two-month-old *Prom1*^{+/C-L}; *Rosa26*-YFP mice were treated with tamoxifen to activate CreER^{T2} expressed from the *Prom1*^{C-L} locus; thereby irreversibly activating YFP expression in *Prom1*⁺ cells and their progeny. Mice were killed 2, 10 and 60 days after induction. Two days after induction, an average of 2.5 YFP-labelled cells was seen in 25% of small intestinal crypts (>50 labelled crypts counted; Fig. 2f, inset). By 10 days, trains of contiguous YFP⁺ cells were observed emanating in single file from the base of crypts in a manner identical to that reported for the progeny of *Lgr5*⁺ stem

cells² (Fig. 2g). YFP cells remained present at 60 days, extended to the tip of the villi, and included the four differentiated cell types of the intestinal lining: enterocytes, Paneth cells, goblet cells and entero-endocrine cells (Fig. 2f and Supplementary Fig. 4). Thus, we conclude that the stem cells of the mouse small intestine are *Prom1*⁺. In contrast, immediately after induction, YFP labelling in the colon of these mice displayed the same broad distribution as *Prom1* expression, and gradually disappeared within 60 days. Therefore, *Lgr5*⁺/*Prom1*⁺ stem cells of the small intestine are distinct from *Lgr5*⁺/*Prom1*⁻ stem cells of the large intestine^{2,23}. YFP labelling of the brain, kidney, lung and pancreas remained relatively static between 2 and 60 days after tamoxifen induction (Supplementary Fig. 5 and data not shown). Because these organs have low rates of cell turnover, it remains possible that some *Prom1*⁺ cells in these tissues are quiescent adult stem cells.

Mutations that activate aberrant Wnt signalling, including mutations in β -catenin (*CTNNB1*), have been identified in over 80% of human colonic cancers^{5,24} and this tumour type was reported recently to contain *Prom1*⁺ cancer stem cells^{3,4}. Intestinal tumorigenesis caused by aberrant Wnt signalling has been modelled successfully in genetically engineered mice²⁵. Although tumours in these animals develop predominantly in the small intestine, the disease process mimics much of the cellular and molecular characteristics of human colonic polyposis^{25–29}. Therefore, to determine if intestinal tumours might arise directly from *Prom1*⁺ stem cells, we activated endogenous Wnt signalling in 2-month-old *Prom1*^{+/C-L} mice using a Cre-dependent

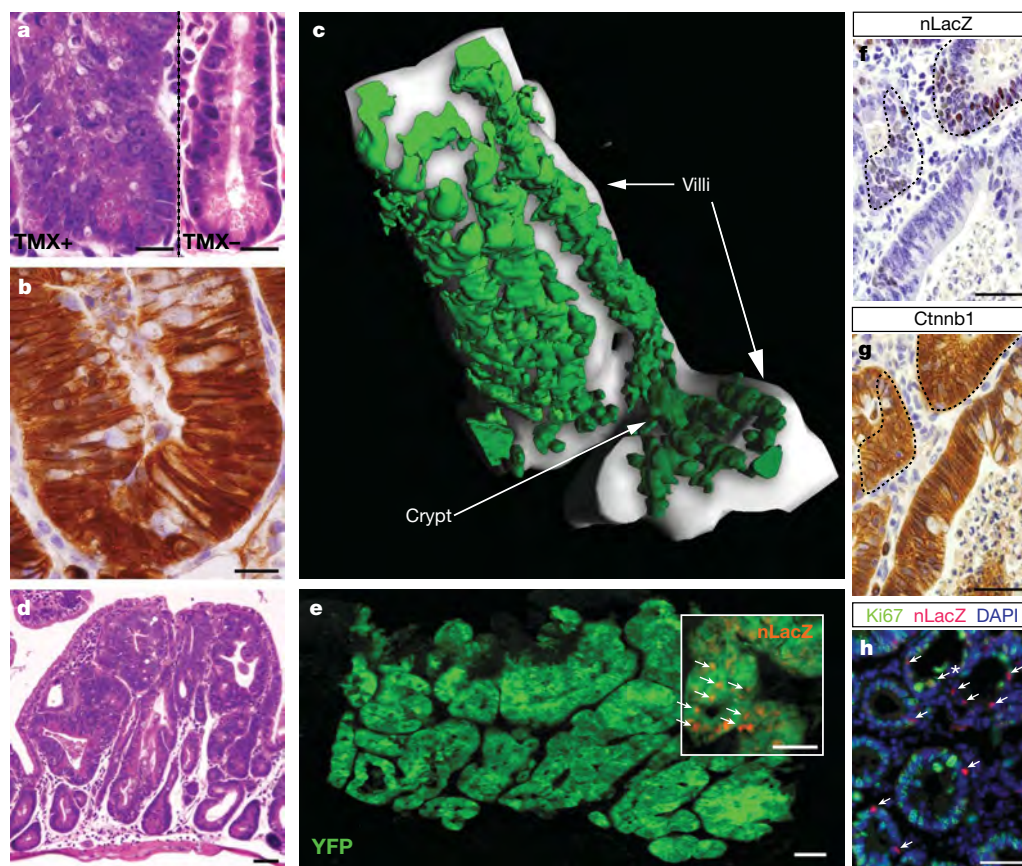


Figure 4 | *Ctnnb1*-mutant *Prom1*⁺ crypt stem cells produce diffuse small intestinal tumours in adult *Prom1*^{+/C-L}; *Rosa26*-YFP; *Ctnnb1*^{+/lox(ex3)} mice. **a**, Haematoxylin and eosin staining of a dysplastic small intestinal crypt 10 days after tamoxifen induction is shown (left). A normal crypt in a control mouse (no tamoxifen) is shown on the right. **b**, *Ctnnb1* immunostaining of crypt cells 10 days after tamoxifen induction. Scale bars: 10 μ m. **c**, Two-photon laser-scanning microscopy (578 μ m depth; YFP, green) of cells emerging from a small intestinal crypt, 10 days after tamoxifen induction. **d**, Haematoxylin and eosin stained section of a tumorous small intestine

60 days after tamoxifen induction. **e**, YFP (green), nLacZ (red) co-immunofluorescence of neoplastic small intestine. In the inset, arrows indicate nLacZ⁺ nuclei. **f**, **g**, nLacZ (**f**) and *Ctnnb1* (**g**) immunostaining of adjacent sections of tumour. *Prom1*⁺ (nLacZ⁺) cells enclosed by dashed lines express nuclear *Ctnnb1*. **h**, Ki67 (green) and nLacZ (red) co-immunofluorescence of tumour. Note the small fraction of proliferating (co-expression of Ki67⁺ is indicated by an arrow and associated asterisk) *Prom1*⁺ tumour cells (arrows). Scale bars in **d–h** indicate 50 μ m.

mutant allele of *Ctnnb1* (*Ctnnb1*^{lox(ex3)})²⁹ and traced the lineage of these cells using the *Rosa26-YFP* allele. Two days after tamoxifen induction, we observed a marked increase in the number of YFP⁺ cells at the base of small intestinal crypts, but at no other site above crypt cell position 4, in *Prom1*^{+/C-L}; *Rosa26-YFP*; *Ctnnb1*^{+/lox(ex3)} mice relative to *Prom1*^{+/C-L}; *Rosa26-YFP*; *Ctnnb1*^{+/+} control mice (Fig. 3a). Two-photon laser-scanning microscopy demonstrated that these cells had a slim and elongated morphology compatible with them being crypt stem cells² (Supplementary Movie 1). Counting of cells isolated from the entire small intestinal mucosae of mice 2 days after tamoxifen induction confirmed the marked expansion in YFP⁺ cells in mice containing the *Ctnnb1*^{lox(ex3)} allele ($P < 0.0001$, Wilcoxon test, Fig. 3b). Cultures of these cells yielded four times as many, and much larger, YFP⁺ clonogenic colonies when isolated from *Prom1*^{+/C-L}; *Rosa26-YFP*; *Ctnnb1*^{+/lox(ex3)} mice compared with those from control animals ($P < 0.0001$, Wilcoxon test, Fig. 3c, d). Thus, activation of Wnt signalling in small intestinal *Prom1*⁺ stem cells induces first a marked expansion of these cells in the crypt base.

Ten days after tamoxifen induction, *Prom1*^{+/C-L}; *Rosa26-YFP*; *Ctnnb1*^{+/lox(ex3)} crypts were markedly disorganized and contained cells that were uniformly nuclear *Ctnnb1* immunoreactive, highly proliferative and disproportionately *Prom1*⁺ (nLacZ immunopositive) relative to controls (Fig. 4a, b and Supplementary Fig. 6a–c). Contiguous streams of YFP⁺ cells were now seen emanating from the crypt and migrating up the surface of the villi (Fig. 4c). In contrast to *Prom1*^{+/C-L}; *Rosa26-YFP*; *Ctnnb1*^{+/+} control mice, cells emanating from the crypts of *Prom1*^{+/C-L}; *Rosa26-YFP*; *Ctnnb1*^{+/lox(ex3)} mice were both hyperplastic and grossly dysplastic, forming a carpet of contiguous YFP⁺ cells from the base of the crypt to the tip of the villus (compare Figs 2g and 4c). All *Prom1*^{+/C-L}; *Rosa26-YFP*; *Ctnnb1*^{+/lox(ex3)} mice allowed to age after tamoxifen induction succumbed to their disease within 90 days ($n = 15$ out of 15). Sixty days after tamoxifen induction, the small intestine of *Prom1*^{+/C-L}; *Rosa26-YFP*; *Ctnnb1*^{+/lox(ex3)} mice was twice the width of that of control animals (Supplementary Fig. 6d). Gross inspection of the duodenal, jejunal and ileal lining revealed a thickened, rugous and YFP-fluorescent mucosa; no regions of normal tissue were identified (Supplementary Fig. 6e, f). Microscopic analysis revealed loss of the normal villus architecture across the entire small intestine that was replaced by dysplastic tissue, characterized by focal high-grade intraepithelial neoplasia and crypt adenoma formation (Fig. 4d and Supplementary Fig. 6f). In contrast, no gross or microscopic abnormalities were seen in the colon which lacks *Prom1*⁺ stem cells (Supplementary Fig. 6g). The absence of tumours in the colon in which *Ctnnb1* was activated in *Prom1*⁺ differentiated cells points to progenitor cells as the source of tumours in this tissue. All cells in the neoplastic small intestine of *Prom1*^{+/C-L}; *Rosa26-YFP*; *Ctnnb1*^{+/lox(ex3)} mice expressed YFP and nuclear *Ctnnb1* and therefore arose from within the *Prom1* lineage; however, only $7 \pm 15.5\%$ ($n = 36$ out of 502 YFP⁺ cells counted from five separate regions) of tumour cells retained expression of *Prom1* (Fig. 4 e–g). Dual Ki67 and nLacZ co-immunofluorescence analysis of tumours demonstrated that approximately 10% of *Prom1*⁺ tumour cells were proliferating (Fig. 4h). These data are compatible with the hypothesis that tumours in these animals contain a fraction of transformed stem cells.

Our data demonstrate that *Prom1* marks stem cells in the small intestine and that activation of endogenous Wnt signalling in these cells disrupts normal tissue maintenance that begins first in the crypt, expanding aberrantly the *Prom1*⁺ stem cell population, resulting ultimately in neoplastic transformation of the small intestinal mucosa. Therefore, we show that *Prom1* marks an adult solid tissue stem cell that is susceptible to neoplastic transformation, forming a model of a human tumour that contains *Prom1*⁺ cancer stem cells. Further analysis will determine whether the fraction of *Prom1*⁺ cells observed in the neoplastic small intestine of *Prom1*^{+/C-L}; *Rosa26-YFP*; *Ctnnb1*^{+/lox(ex3)} mice represents a remnant of mutated stem cells that may function as cancer stem cells. Our *Prom1*^{C-L} knockin mouse provides the research community with an extremely useful

tool to explore further the relationship between normal and malignant stem cells in the lung, kidney, brain, pancreas and other tissues.

METHODS SUMMARY

Mice. *Prom1*^{C-L} mice were generated by homologous recombination in 129SvEv mouse embryonic stem cells targeting a *creER*^{T2}-*ires-nlacZ-PGK-neo* cassette to the ATG of *Prom1*. *PGK-neo* flanked by flip-recombinase target (FRT) sites was subsequently excised by flip recombination by breeding with *Rosa26-FLPe* mice. *Rosa26-YFP* reporter and *Rosa26-FLPe* mice were obtained from the Jackson Laboratory. *Ctnnb1*^{lox(ex3)/lox(ex3)} mice were provided by M. Taketo²⁹. Mice aged 2 months were treated by oral gavage with 250 μ l tamoxifen in corn oil at 40 mg ml⁻¹ for two consecutive days.

Histology and microscopy. For nLacZ analysis, YFP microscopy and immunofluorescence, tissues were perfused and fixed in 2% paraformaldehyde (PFA) overnight, cryo-protected and frozen in OCT. For immunohistochemistry, tissues were fixed in 4% PFA and paraffin embedded. *In situ* probes for *Lgr5* and *Prom1* were generated from complementary DNA clones and BC156649 and BC028286, respectively. Alcian blue and PAS staining was performed on frozen sections following standard protocols. See Methods for details.

Explants and two-photon microscopy. Intestine from tamoxifen-treated mice was removed surgically and immediately submerged in Krebs' solution and superfused with a gas mixture of 95% O₂/CO₂. One-millimetre slices were placed on glass coverslips and stabilized with overlying mechanical support and maintained at 37 °C within the microscope chamber. Two-photon laser-scanning microscopy was performed using an Ultima imaging system (Prairie Technologies) and a Ti:sapphire Chameleon Ultra femtosecond-pulsed laser (910 nm) (Coherent). Images were analysed using Imaris software (Bitplane). Three-dimensional images were constructed from Z-series stacks taken in 1 μ m steps.

Culture of intestinal crypt stem cells. Intestinal epithelial cells were grown in RPMI supplemented with 2 mM L-glutamine, 100 units ml⁻¹ penicillin, 100 μ g ml⁻¹ streptomycin and 2.5% FBS. YFP⁺ cells and colonies (formed after 4 weeks in culture) were visualized and counted using fluorescence microscopy. See Methods for details.

Full Methods and any associated references are available in the online version of the paper at www.nature.com/nature.

Received 26 May; accepted 20 October 2008.

Published online 17 December 2008.

- Clarke, M. F. & Fuller, M. Stem cells and cancer: two faces of eve. *Cell* **124**, 1111–1115 (2006).
- Barker, N. *et al.* Identification of stem cells in small intestine and colon by marker gene *Lgr5*. *Nature* **449**, 1003–1007 (2007).
- Ricci-Vitiani, L. *et al.* Identification and expansion of human colon-cancer-initiating cells. *Nature* **445**, 111–115 (2007).
- O'Brien, C. A. *et al.* A human colon cancer cell capable of initiating tumour growth in immunodeficient mice. *Nature* **445**, 106–110 (2007).
- Sparks, A. B. *et al.* Mutational analysis of the APC/ β -catenin/Tcf pathway in colorectal cancer. *Cancer Res.* **58**, 1130–1134 (1998).
- Lapidot, T. *et al.* A cell initiating human acute myeloid leukaemia after transplantation into SCID mice. *Nature* **367**, 645–648 (1994).
- Singh, S. K. *et al.* Identification of human brain tumour initiating cells. *Nature* **432**, 396–401 (2004).
- Al-Hajj, M. *et al.* From the cover: Prospective identification of tumorigenic breast cancer cells. *Proc. Natl Acad. Sci. USA* **100**, 3983–3988 (2003).
- Calabrese, C. *et al.* A perivascular niche for brain tumor stem cells. *Cancer Cell* **11**, 69–82 (2007).
- Hambardzumyan, D. *et al.* PI3K pathway regulates survival of cancer stem cells residing in the perivascular niche following radiation in medulloblastoma *in vivo*. *Genes Dev.* **22**, 436–448 (2008).
- Clarke, M. F. *et al.* Cancer stem cells—Perspectives on current status and future directions: AACR Workshop on Cancer Stem Cells. *Cancer Res.* **66**, 9339–9344 (2006).
- Kelly, P. N. *et al.* Tumor growth need not be driven by rare cancer stem cells. *Science* **317**, 337 (2007).
- Yin, A. H. *et al.* AC133, a novel marker for human hematopoietic stem and progenitor cells. *Blood* **90**, 5002–5012 (1997).
- Miraglia, S. *et al.* A novel five-transmembrane hematopoietic stem cell antigen: isolation, characterization, and molecular cloning. *Blood* **90**, 5013–5021 (1997).
- Mizrak, D., Brittan, M. & Alison, M. R. CD133: molecule of the moment. *J. Pathol.* **214**, 3–9 (2008).
- Taylor, M. D. *et al.* Radial glia cells are candidate stem cells of ependymoma. *Cancer Cell* **8**, 323–335 (2005).
- Hermann, P. C. *et al.* Distinct populations of cancer stem cells determine tumor growth and metastatic activity in human pancreatic cancer. *Cell Stem Cell* **1**, 313–323 (2007).

18. Corbeil, D. *et al.* The human AC133 hematopoietic stem cell antigen is also expressed in epithelial cells and targeted to plasma membrane protrusions. *J. Biol. Chem.* **275**, 5512–5520 (2000).
19. Kim, C. F. *et al.* Identification of bronchioalveolar stem cells in normal lung and lung cancer. *Cell* **121**, 823–835 (2005).
20. Xu, X. *et al.* Beta cells can be generated from endogenous progenitors in injured adult mouse pancreas. *Cell* **132**, 197–207 (2008).
21. Lois, C. & Alvarez-Buylla, A. Proliferating subventricular zone cells in the adult mammalian forebrain can differentiate into neurons and glia. *Proc. Natl Acad. Sci. USA* **90**, 2074–2077 (1993).
22. Uchida, N. *et al.* Direct isolation of human central nervous system stem cells. *Proc. Natl Acad. Sci. USA* **97**, 14720–14725 (2000).
23. Shmelkov, S. V. *et al.* CD133 expression is not restricted to stem cells, and both CD133 and CD133 metastatic colon cancer cells initiate tumors. *J. Clin. Invest.* **22**, 22–30 (2008).
24. Bienz, M. & Clevers, H. Linking colorectal cancer to Wnt signaling. *Cell* **103**, 311–320 (2000).
25. Taketo, M. M. Wnt signaling and gastrointestinal tumorigenesis in mouse models. *Oncogene* **25**, 7522–7530 (2006).
26. Gaspar, C. *et al.* Cross-species comparison of human and mouse intestinal polyps reveals conserved mechanisms in adenomatous polyposis coli (APC)-driven tumorigenesis. *Am. J. Pathol.* **172**, 1363–1368 (2008).
27. Moser, A. R., Pitot, H. C. & Dove, W. F. A dominant mutation that predisposes to multiple intestinal neoplasia in the mouse. *Science* **247**, 322–324 (1990).
28. Su, L. K. *et al.* Multiple intestinal neoplasia caused by a mutation in the murine homolog of the APC gene. *Science* **256**, 668–670 (1992).
29. Harada, N. *et al.* Intestinal polyposis in mice with a dominant stable mutation of the β -catenin gene. *EMBO J.* **18**, 5931–5942 (1999).

Supplementary Information is linked to the online version of the paper at www.nature.com/nature.

Acknowledgements R.J.G. holds the Sydney Schlobohm Leadership Chair of Research from the Brain Tumor Society and the Howard C. Schott Research Chair from the Malia's Cord Foundation, and is supported by grants from the National Institutes of Health (R01CA129541, P01CA96832 and P30CA021765), the Collaborative Ependymoma Research Network (CERN) and by the American Lebanese Syrian Associated Charities (ALSAC). We are grateful to the staff of the ARC for technical assistance.

Author Contributions R.J.G. conceived the research, and with L.Z., planned experiments and analyses and wrote the paper; L.Z. also conducted the great majority of experiments. P.G., D.S.C., Y.T., R.J.R., I.T.B., H.P. and S.Z. conducted experiments and provided technical assistance. D.W.E. provided pathology review.

Author Information Reprints and permissions information is available at www.nature.com/reprints. Correspondence and requests for materials should be addressed to R.J.G. (Richard.Gilbertson@stjude.org).

METHODS

Generation of *Prom1*^{+/-C-L} mice. The 8.0-kilobase (kb) 5' end of the mouse *Prom1* gene (4.8 kb upstream of the ATG start codon and 3.2 kb downstream of ATG) was cloned into pBluescript KS+ plasmid by recombineering from the Ensembl 129S7-derived genomic BAC clone bMQ446F18. The ATG start codon was then replaced by the *creER*^{T2}-*IRES-lacZ-PGK-neo* cassette using the same recombineering-base cloning strategy. The *Prom1-creER*^{T2}-*IRES-lacZ* expression construct (25 µg) was linearized and transfected into 129SvEv mouse embryonic stem cells (Millipore, CMTI-1). Neomycin-resistant recombinant ES clones were selected in medium containing 350 µg ml⁻¹ G418 for days 2–3 and 150 µg ml⁻¹ for days 4–7. A total of 192 recombinant ES clones were picked into two 96-well plates and cultured to 70% confluence. Plates were then duplicated, one cryo-preserved and one that continued culture to 100% confluence for DNA isolation. DNA from all clones was screened for the correct targeting by long PCR (Platinum *Taq* polymerase high fidelity, Invitrogen, 11304-011) with primers flanking the 5' and 3' homology arms. All positive clones and randomly selected negative clones were then confirmed by Southern blotting using the 5' probe indicated in Fig. 1a. Positive clones were thawed, expanded and injected into C57BL/6 blastocysts following the standard protocol. Chimaeras were mated with C57BL/6 mice and the germline transmission in agouti offspring were confirmed by genotyping PCR. The neomycin selection cassette was later excised *in vivo* by crossing with Rosa26-FLPe mice (The Jackson Laboratory).

β-galactosidase staining. To prepare sections of all organs except the retina, mice were perfused and fixed with 2% paraformaldehyde (PFA) overnight at 4 °C, cryo-protected in 20% sucrose overnight at 4 °C and frozen in OCT. Frozen sections were washed in PBS for 5 min and incubated in the dark in standard β-gal substrate (5 mM potassium ferricyanide, 5 mM potassium ferrocyanide, 1 mg ml⁻¹ X-gal, 2 mM MgCl₂, 0.01% sodium deoxycholate, 0.02% NP-40 in PBS) overnight at 37 °C. To stain the retina, mouse eyes were removed and immersed immediately in cold PBS. The retina was isolated from the eyes and fixed at room temperature in 0.5% glutaraldehyde/PBS for 10 min, washed briefly and incubated in the rinse buffer (2 mM MgCl₂, 0.01% sodium deoxycholate, 0.02% NP-40 in PBS) for 30 min. The retina was subsequently stained in the same β-gal substrate for 30 min at 37 °C, rinsed in PBS and post-fixed in 4% PFA overnight. The retina was cryo-protected in 20% sucrose for 2 h before being frozen in OCT.

Microscopy. Standard immunofluorescence staining was performed on 16-µm frozen sections and immunohistochemistry on 5-µm paraffin sections. Antibodies included rat anti-Prom1 (eBioscience, 14-1331, 1:100), mouse anti-nerfin (Millipore, MAB353, 1:50), rabbit anti-uteroglobin (or CCSP; Abcam, ab40873, 1:1,000), mouse anti-rhodopsin (gift from M. Dyer, ref. 30, 1:500), rabbit anti-Ki67 (Vector, VP-RM04, 1:2,000), mouse anti-β-catenin (Becton Dickinson, 610154, 1:200), chicken anti-β-gal (Abcam, ab9361, 1:1,000), rabbit anti-β-gal (MP Biomedicals, 55976, 1:1,000), rabbit anti-synaptophysin (Dako, A 0010, 1:150), rabbit anti-amylase (Sigma, A8273, 1:1,000) and guinea-pig anti-insulin (Dako, A 0564, 1:250). Two lectins used were fluorescein-labelled DBA (Vector, FL-1031, 1:200) and fluorescein-labelled LTL (Vector, FL-1321, 1:200). To obtain the kidney images in Fig. 1c, the same section was sequentially stained with X-gal followed by

Prom1/LTL co-immunofluorescence. The same sequential X-gal/immunofluorescence staining was performed for Supplementary Fig. 2b. All cell counts in tissue sections were performed blind to genotype and tamoxifen treatment.

In situ hybridization. To obtain *Lgr5* probe, T3 promoter sequence (CATCTACTTTTGGCCGTTT) was added to *Lgr5* sense oligonucleotide and T7 promoter sequence (AAGTCATGGGGTAAGCTGGTG) to the antisense oligonucleotide. *Lgr5* template was amplified from its cDNA clone (BC156649) and the 828-bp PCR product was used as the template to generate Dig-cRNA probe (Roche). Probes to the mouse *Prom1* mRNA were similarly generated from its cDNA clone (BC028286). Frozen sections fixed in 4% PFA were pre-treated in graded alcohols from 70% to 100% to facilitate penetration of Dig-labelled cRNA probes. Sections were then incubated in the hybridization buffer (500 ng ml⁻¹ Dig-labelled cRNA probe, 50% formaldehyde, 4× SSC, 250 µg ml⁻¹ tRNA, 200 µg ml⁻¹ ssDNA and 10% dextran sulphate) at 55 °C overnight. After incubation sections were washed in degraded SSC buffers and incubated with anti-Dig antibody (Roche, 1:600) for 1.5 h at room temperature. Sections were subsequently washed and coloured with NCBI/NBT (Roche) for 3–16 h, counterstained with methyl green and mounted with 2% gelatin.

Culture of intestinal crypt stem cells. Small intestines were excised from each of two *Prom1*^{+/-C-L}; *Rosa26-YFP* and two *Prom1*^{+/-C-L}; *Rosa26-YFP*; *Ctnnb1*^{+/-lox(ex3)} mice induced with tamoxifen 2 days before they were killed, and rinsed repeatedly with sterile PBS. Crypts were isolated by incubating minced intestines with 3 mM EDTA and 0.5 mM dithiothreitol in PBS without Ca²⁺ and Mg²⁺ for 90 min at room temperature followed by vigorous shaking for 30 s to release large sheets of cells from their calcium- and magnesium-dependent interactions with the basement membrane and stromal cells. These were collected by centrifugation at 500 r.p.m. for 5 min at room temperature. To obtain a single-cell suspension, pelleted cells were incubated in 0.3% pancreatin (Sigma) in PBS for 90 min at room temperature. Cells were collected by centrifugation at 1,000 r.p.m. for 5 min at room temperature, washed with 3 mM EDTA and 0.5 mM dithiothreitol in PBS without Ca²⁺ and Mg²⁺ and grown in RPMI supplemented with 2 mM L-glutamine, 100 units ml⁻¹ penicillin, 100 µg ml⁻¹ streptomycin and 2.5% FBS. Colonies formed after approximately 4 weeks in culture.

RT-PCR. Total RNA was isolated from the kidney of adult *Prom1*^{+/-C-L} and *Prom1*^{C-L/C-L} mice following standard trizol/chloroform/isopropanol protocol. 1 µg RNA was reverse transcribed using the iScript reverse transcription kit (Bio-Rad, 170-8890). cDNA was then amplified using *Taq* polymerase and gene-specific primers for the 5' end of the *Prom1* transcript (5'-GAGTCCTTA-TCTGCGCCATC-3', 5'-CTGCTCCCCAGACTGCTTAG-3'), 3' end of the *Prom1* transcript (5'-GGATTGCAAAAGAGGTCGAG-3', 5'-AATTCAGAG-GGTCCGCAAC-3'), and *GAPDH* (5'-TGTTCCAGTATGACTCCACTCACG-3', 5'-GCCCTTCCACAATGCCAAAG-3'). Target sequences were amplified within linear ranges using 95 °C/30 s, 60 °C/30 s and 72 °C/50 s conditions. All primer pairs amplified regions crossing intron borders.

30. Zhang, J. *et al.* Rb regulates proliferation and rod photoreceptor development in the mouse retina. *Nature Genet.* **36**, 351–360 (2004).

LETTERS

Crypt stem cells as the cells-of-origin of intestinal cancer

Nick Barker^{1*}, Rachel A. Ridgway^{2*}, Johan H. van Es¹, Marc van de Wetering¹, Harry Begthel¹, Maaïke van den Born¹, Esther Danenberg¹, Alan R. Clarke³, Owen J. Sansom² & Hans Clevers¹

Intestinal cancer is initiated by Wnt-pathway-activating mutations in genes such as adenomatous polyposis coli (*APC*). As in most cancers, the cell of origin has remained elusive. In a previously established *Lgr5* (leucine-rich-repeat containing G-protein-coupled receptor 5) knockin mouse model, a tamoxifen-inducible Cre recombinase is expressed in long-lived intestinal stem cells¹. Here we show that deletion of *Apc* in these stem cells leads to their transformation within days. Transformed stem cells remain located at crypt bottoms, while fuelling a growing microadenoma. These microadenomas show unimpeded growth and develop into macroscopic adenomas within 3–5 weeks. The distribution of *Lgr5*⁺ cells within stem-cell-derived adenomas indicates that a stem cell/progenitor cell hierarchy is maintained in early neoplastic lesions. When *Apc* is deleted in short-lived transit-amplifying cells using a different *cre* mouse, the growth of the induced microadenomas rapidly stalls. Even after 30 weeks, large adenomas are very rare in these mice. We conclude that stem-cell-specific loss of *Apc* results in progressively growing neoplasia.

The anatomy of the intestinal crypt is uniquely suited to study adult stem cells in their niche. The epithelium of the murine small intestine renews every 5 days^{2,3}. We have recently identified slender *Lgr5*⁺ cells located at crypt bottoms as the stem cells of the small intestine and colon¹. Each crypt contains approximately six long-lived stem cells intermingled with Paneth cells in the small intestine and with goblet cells in colon (Fig. 1a). Counter-intuitively, these cells are not quiescent, but divide every day¹. These cells have been called crypt base columnar cells^{4,5}. Their daughter cells constitute the transit-amplifying crypt compartment. Transit-amplifying cells divide every 12–16 h, generating some 300 cells per crypt every day⁶; they reside within crypts for approximately 48 h, undergoing up to five rounds of cell division while migrating upwards⁶. When the committed transit-amplifying cells reach the crypt–villus junction, they rapidly differentiate while continuing their upward migration. Paneth cells escape this flow and reside for 3–6 weeks at the crypt base^{7–9}. Initiating mutations in intestinal malignancies target Wnt pathway components, most frequently the negative regulator *Apc*^{10,11}. This results in the constitutive activation of a Wnt target gene program that drives the formation of benign adenomas^{12–15}. However, it remains unclear which cell type sustains the cancer-initiating mutation.

The cytochrome P450-promoter-driven *Ah-cre* mouse allows conditional deletion of floxed alleles in the intestinal epithelium by induction with β -naphthoflavone (β -NF). The *Ah-cre* allele is highly active throughout the epithelium, including the stem cells¹⁶. We have previously used a floxed allele of *Apc* (ref. 17) with the *Ah-cre* mouse line to demonstrate that acute loss of *Apc* throughout the adult intestinal epithelium after intraperitoneal injection of β -NF instantly

transforms the epithelium¹⁶. This process depends on the Wnt target gene *c-myc*¹⁸. High-dose oral β -NF induces a more stochastic deletion of *Apc* (Supplementary Fig. 1), resulting in rapid adenoma formation throughout the intestine within 3 weeks¹⁹. Both of these high-dose induction protocols effect deletion in all compartments of the epithelium, including the stem cells at the crypt base.

We next sought the cell of origin of the adenomas. Careful titration revealed that after oral administration of 1 mg kg⁻¹ β -NF, the efficiency of Cre activation in the stem cells at the crypt base was extremely low. In a group of 15 mice, only 5.0 ± 3.0 lineage tracing events (that is, stem cell hits) were seen in the entire small intestine at 100 days after induction. This dose still very efficiently induced Cre activity in the transit amplifying and villus compartments, as visualized 1 day after oral induction using the *Rosa26R* mouse as Cre reporter (Fig. 1b, c). Of note, most 5-bromodeoxyuridine (BrdU)-pulsed transit-amplifying cells migrate onto villi within 24 h and are lost into the gut lumen at 48 h (ref. 20). This indicated that blue-stained cells on the bottom half of the villi (Fig. 1b, c) resided in crypts as transit-amplifying cells at the time of deletion. At day 7, blue staining could no longer be detected (not shown).

Using this regimen on *Ah-cre/Apc*^{fllox/fllox}/*Rosa26R* mice, multiple β -catenin^{high} foci became visible throughout upper crypt and villus at day 3 after induction (Fig. 1d–g). The foci were invariably LacZ⁺, confirming that Cre-mediated deletion had occurred (Fig. 1f and Supplementary Fig. 2). These β -catenin^{high} foci expressed the Wnt target gene *c-myc* and were actively proliferating (Supplementary Fig. 1). Of note, loss of *Apc* in a crypt cell induces maintenance of EphB expression in the resulting transformed clone^{21,22}. As a consequence, the clone fails to migrate out of its crypt and eventually invades the subepithelium²². Figure 1h quantifies focus induction in the different compartments at day 3 after induction.

Most of the *Apc*-deficient villus cells were lost after 4–5 days. The remaining foci within the crypts demonstrated very limited expansion over a 24-day period (Supplementary Fig. 3) and no macroscopic adenomas occurred. Notably, the foci persisted over at least a 284-day period (Fig. 1i), and only very rarely progressed to adenomas (Fig. 1j, quantification in Fig. 1k; for histological definition see Supplementary Fig. 4). In 5 mice at >100 days after induction, we observed 3 ± 2.3 macroscopic adenomas, correlating with the inordinately low frequency of Cre activation in stem cells (see above). Thus, the long-term persistence of microadenomas derived from transformed transit-amplifying cells might, in very rare cases, result in a progressively growing neoplasia, possibly when additional hits are sustained.

We then crossed the stem-cell-specific *Lgr5-EGFP-IRES-creER*^{T2} knockin mice to *Apc*^{fllox/fllox} mice. In the resulting mice, Cre was

¹Hubrecht Institute for Developmental Biology and Stem Cell Research, Uppsalalaan 8, 3584CT Utrecht & University Medical Centre Utrecht, Netherlands. ²Beatson Institute for Cancer Research, Glasgow G61 1BD, UK. ³Cardiff School of Biosciences, Cardiff CF10 3US, UK.

*These authors contributed equally to this work.

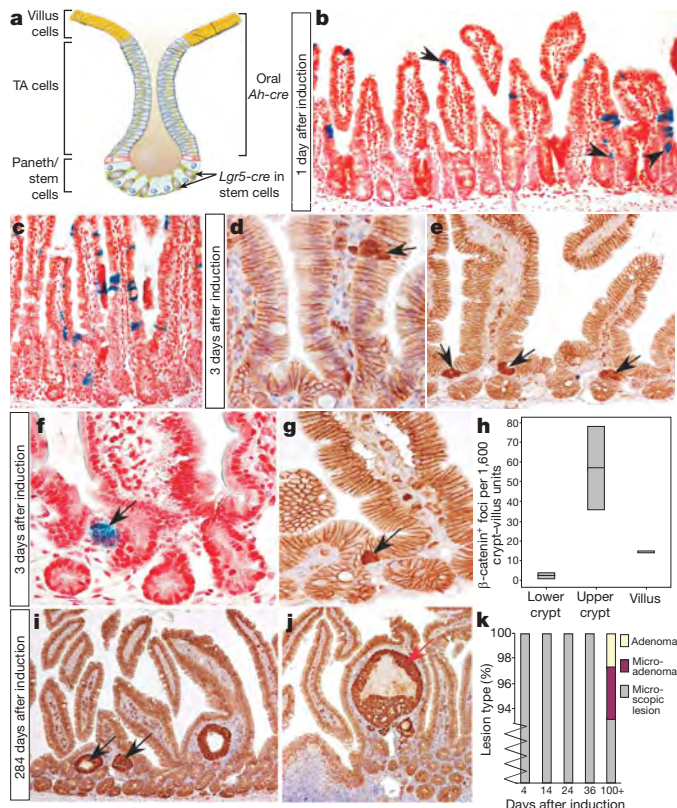


Figure 1 | Transformation of non-stem cell populations in *Ah-cre/Apc^{flox/flox}* intestines through low-dose oral β -NF-induced *Apc* deletion fails to drive intestinal neoplasia. **a**, Cartoon depicting the general organization of intestinal crypts. *Lgr5-EGFP-IRES-creER^{T2}* (*Lgr5-cre* for brevity) is activated by intraperitoneal administration of tamoxifen only in the stem cells located at the crypt base. Low-dose oral administration of β -NF activates *Ah-cre* in the upper transit-amplifying (TA) compartment and villus. **b, c**, LacZ-stained sections of intestine from an *Ah-cre/Rosa26R* mouse treated with a single low-dose oral gavage of 1 mg kg⁻¹ β -NF for 1 day. LacZ-positive cells were readily visible on the villi and upper crypts (black arrows) throughout the intestine, but were only very rarely observed at the crypt base. **d, e, g**, β -catenin immunohistochemistry performed on intestinal sections from *Ah-cre/Rosa26R/Apc^{flox/flox}* mice 3 days after a single gavage of 1.0 mg kg⁻¹ β -NF. Clusters of transformed cells with elevated levels of β -catenin (β -catenin^{high}) were frequently observed on the villus (**d**) and upper regions of the crypt (**e, g**). These clusters are highlighted with black arrows. **f**, The β -catenin^{high} clusters were invariably positive for LacZ (black arrow). **h**, Quantification of the location of the β -catenin^{high} cell clusters on intestinal sections from *Ah-cre/Rosa26R/Apc^{flox/flox}* mice 3 days after a single gavage of 1.0 mg kg⁻¹ β -NF. Box-plots show numbers of foci observed at the crypt base, the upper crypt and the villus in 1,600 crypt-villus units. Significantly more clusters/foci were seen in the upper regions of the crypt than any other region ($P = 0.04$, Mann-Whitney U -test, $n = 3$). **i, j**, β -catenin immunohistochemistry performed on intestinal sections from an *Ah-cre/Rosa26R/Apc^{flox/flox}* mouse 284 days after induction. Note single adenomatous crypts (black arrows) with nuclear β -catenin in every cell which have not progressed and are histologically identical to single adenomatous crypts seen 14, 24 and 36 days after *cre* activation (see Supplementary Fig. 3). **k**, Classification of LacZ⁺ intestinal lesions in *Ah-cre/Rosa26R/Apc^{flox/flox}* intestinal whole mounts (see Supplementary Fig. 4 and Methods for details). No adenomas and only one microadenoma were seen in mice at early time points (up to 36 days) after 1 mg kg⁻¹ β -NF (at least four mice at each time point), whereas in older mice rare adenomas were observed (3 ± 2.3 for 5 mice counted). 'Microscopic lesions' were histologically equivalent to single adenomatous crypts. Original magnifications: **b, c, i, l**, 10 \times ; **d, f, g**, 40 \times ; **e, 20 \times .**

activated with a single intraperitoneal injection of tamoxifen. Accumulation of β -catenin first occurred in isolated EGFP⁺ stem cells after 3 days (Fig. 2a–c) and was not seen in control mice (Supplementary Fig. 5). Thirty-one transformed cells were counted in a total

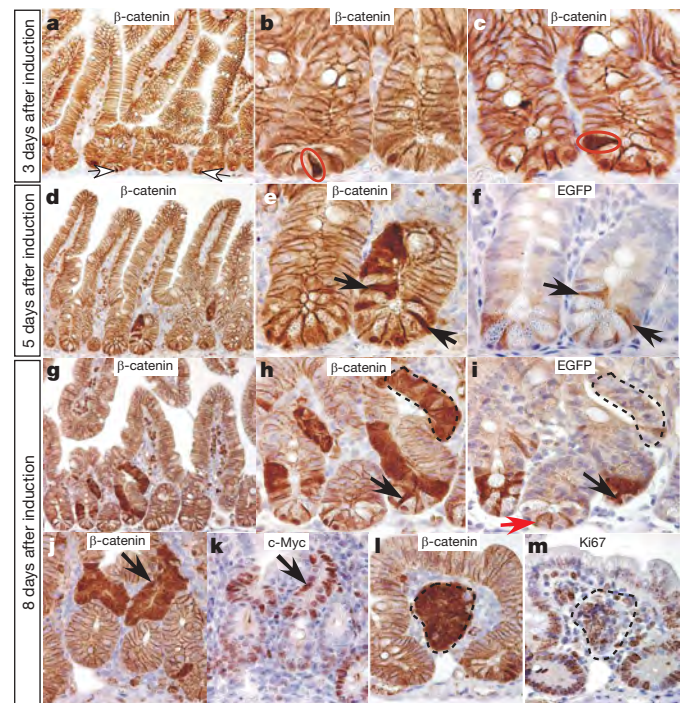


Figure 2 | *Lgr5-EGFP⁺* intestinal stem cells transformed after loss of *Apc* persist and fuel the rapid formation of β -catenin^{high} microadenomas. *Lgr5-EGFP-creER^{T2}/Apc^{flox/flox}* mice were treated with a single intraperitoneal injection of tamoxifen to activate the stem-cell-specific Cre and facilitate loss of *Apc*. **a–i**, The consequences of the resulting *Lgr5-EGFP⁺* intestinal stem cell transformation and their subsequent fate was tracked over an 8-day period using β -catenin and EGFP as markers of transformed cells and *Lgr5⁺* stem cells, respectively. **a–c**, Accumulation of the Wnt effector protein, β -catenin, was first observed in scattered *Lgr5⁺* stem cells at the crypt base 3 days after Cre induction (**a**; white arrows). **b, c**, Representative examples of β -catenin^{high}*Lgr5⁺* stem cells are circled in red. **d–f**, Five days after induction the transformed *Lgr5-EGFP⁺* stem cells remained (compare black arrows in **e** and **f**) and were associated with clusters of transformed (β -catenin^{high}) cells within the transit-amplifying compartment. **g, h**, Eight days after induction the clusters of transformed cells had expanded to fill the entire transit-amplifying compartment (**h**). The transformed β -catenin^{high}/EGFP⁺ stem cells at the crypt base persisted (compare black arrow in **h** with **i**), but expression of the stem cell marker *Lgr5-EGFP* was lost in most of the transformed cells higher up the crypt (compare outlined regions in **h** and **i**). *Lgr5-EGFP* expression in transformed stem cells was significantly higher than in non-transformed stem cells (**i**; red arrow), reflecting elevated expression of the Wnt target gene *Lgr5* after loss of *Apc*. **j, k**, β -catenin^{high} lesions (**j**; black arrow) generated after transformation of the stem cells expressed high levels of the Wnt target gene *c-myc* (**k**; black arrow), reflecting aberrant activation of the Wnt pathway. **l, m**, The early β -catenin^{high} lesions expressed the Ki67 marker (compare outlined regions in **l** and **m**), confirming their highly proliferative status. Original magnifications: **a, d, g**, 10 \times ; **b, c, e, f**, 60 \times ; **h–m**, 40 \times .

of 500 crypts in a representative mouse (~6%), a frequency which remained constant over the next 8 days and was comparable to the deletion rate observed for the oral β -NF protocol (~5%, see Fig. 1h). After 5 days, multiple crypts harboured transformed (that is, β -catenin^{high} EGFP⁺ stem cells associated with proliferative clusters of β -catenin^{high} cells within the transit-amplifying compartment (Fig. 2d–f). Thus, Wnt-transformed stem cells persisted at crypt bottoms, yet rapidly generated transformed progeny higher up in the crypts. Eight days after induction, the transformed cells had continued to expand (Fig. 2g–i). Microadenomas within the associated villus stroma became evident (Fig. 2j, l), expressing *c-Myc* and Ki67 (Fig. 2k, m). The lesions continued their aggressive expansion (Fig. 3). At day 14, a similar number (42 per 500 crypts, ~8%) of large, multi-villus adenomas was observed (Fig. 3a, b). At day 36, the mice had to be killed (Fig. 3g, h). Figure 4a gives a global view of the lesions.

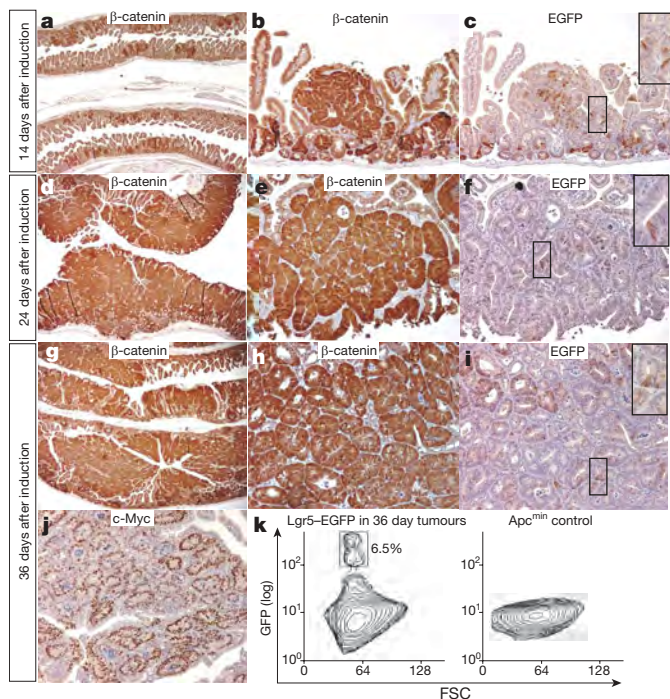


Figure 3 | Selective transformation of $Lgr5$ -EGFP⁺ stem cells after loss of *Apc* efficiently drives adenoma formation throughout the small intestine. **a–i**, The appearance and development of intestinal adenomas and expression of the $Lgr5$ -EGFP stem cell marker within these adenomas was tracked over a 36-day period using β -catenin (adenoma marker) and EGFP (stem cell marker) immunohistochemistry respectively. **a, b**, Multiple small, β -catenin^{high} adenomas were readily visible throughout the intestine 14 days after $Lgr5$ ⁺ stem cell transformation. **c**, $Lgr5$ -EGFP expression was restricted to scattered cells in these small adenomas (inset box shows magnified examples). **d, e**, Multiple macroscopic adenomas (>100) were present after 24 days. **g, h**, After 36 days a lethal adenoma burden was reached, with massive neoplasia evident along the entire length of the intestine. **f, i**, $Lgr5$ -EGFP expression in these macroscopic adenomas remained restricted to small populations of cells with characteristic crypt base columnar stem cell morphology (inset boxes show magnified examples). **j**, These adenomas expressed high levels of c-Myc, confirming aberrant activation of the Wnt pathway. **k**, Quantification of $Lgr5$ -EGFP expression in 36-day post-induction adenomas and control *Apc*^{min} mouse adenomas by FACS analysis. Left panel: adenomas from 36-day post-induction mice contained, on average, 6.5% $Lgr5$ -EGFP⁺ cells. Right panel: no EGFP expression was detected in adenomas from *Apc*^{min/WT} mice, confirming the specificity of the EGFP signal in the 36-day adenomas. Original magnifications: **a, d, g**, 2 \times ; **b, c, e, f, h, i**, 10 \times ; **j**, 4 \times ; all insets, 40 \times .

The *Lgr5* gene also marks stem cells in colon¹. Indeed, transformed β -catenin^{high} $Lgr5$ ⁺ stem cell populations at the base of colonic crypts became visible at day 8 after induction (Fig. 4b, c). The transformed crypts continued this steady expansion (Fig. 4e, f), forming microadenomas 3 weeks after induction (not shown). β -catenin^{high} colon adenomas of a considerable size were commonly observed at day 36 (Fig. 4h, i).

To investigate the hierarchy between the *Apc*-deficient stem cells and their transformed progeny, we studied $Lgr5$ -EGFP during adenoma formation in our model. Non-transformed stem cells express $Lgr5$ -EGFP¹. Expression was maintained in the transformed stem cells at day 5 (Fig. 2f) and day 8 (Fig. 2i). Notably, the marker was absent in most transit-amplifying cells of the β -catenin^{high} clones (outlined regions in Fig. 2h and i). The marker was expressed in scattered cells within adenomas at later time points (Fig. 3c, f, i and Supplementary Fig. 6). In contrast, another Wnt target gene, *c-myc*, was uniformly expressed throughout the adenomas (Fig. 3j). Quantification by fluorescence-activated cell sorting (FACS) at 36 days after induction revealed that $Lgr5$ ⁺ cells comprise 6.5% of the

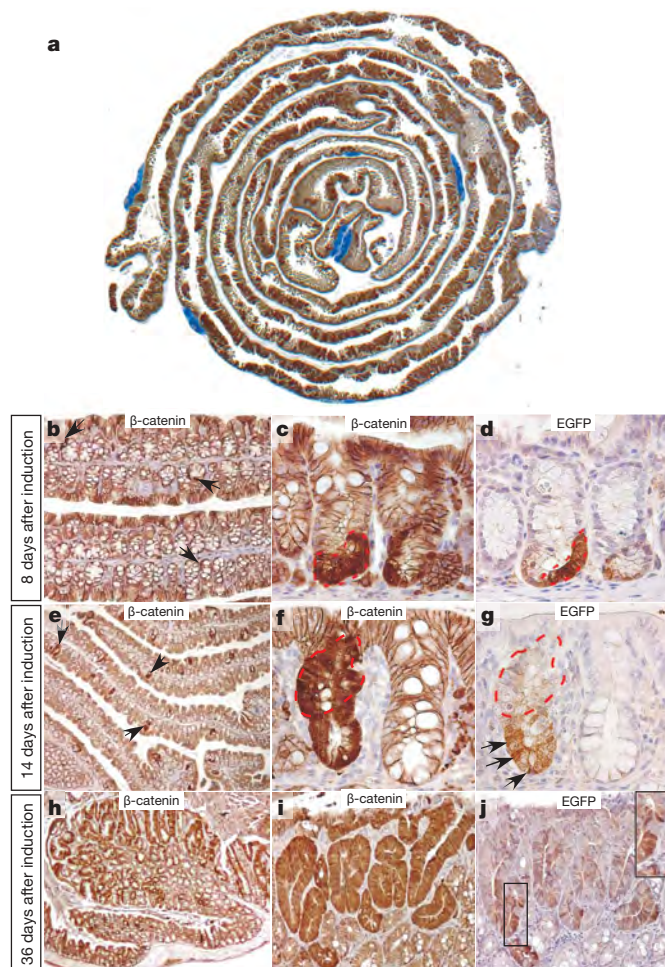


Figure 4 | Transformation of $Lgr5$ -EGFP⁺ stem cells drives intestinal neoplasia in both the small intestine and colon. **a**, A massive tumour burden is reached 36 days after transformation of the stem cells, with β -catenin^{high} macroscopic adenomas visible throughout the entire small intestine (Peyers patches are stained blue). **b–j**, The appearance and development of colonic adenomas and expression of the $Lgr5$ -EGFP stem cell marker within these adenomas was tracked over a 36-day period using β -catenin (adenoma marker) and EGFP (stem cell marker) immunohistochemistry, respectively. **b, c**, Small clusters of β -catenin^{high} cells were first observed in the $Lgr5$ ⁺ stem cell zone at the crypt base after 8 days (**b**, black arrows and **c**, outlined in red). **d**, High level expression of $Lgr5$ -EGFP was apparent in the transformed stem cell compartment (**d**, outlined in red), confirming aberrant activation of the Wnt pathway after loss of *Apc*. **e, f**, Fourteen days after induction the clusters of transformed cells had expanded to fill the entire colonic crypt. The transformed, β -catenin^{high}/ $Lgr5$ -EGFP⁺ stem cells persisted (black arrows), but expression of the stem cell marker $Lgr5$ -EGFP was lost in most of the transformed cells higher up the crypt (compare outlined regions in **f** and **g**). **h, i**, Multiple β -catenin^{high} adenomas were observed throughout the colon 36 days after induction. **j**, $Lgr5$ -EGFP expression in these colonic adenomas was restricted to small populations of cells with characteristic stem cell morphology (inset box shows magnified examples). Original magnifications: **b**, 4 \times ; **c, d, f, g**, 40 \times ; **h, i**, 2 \times ; **j**, 10 \times ; inset in **j**, 40 \times .

tumour population (Fig. 3k). A similar phenomenon was observed for the colonic adenomas (Fig. 4d, g, j).

Taken together, these data demonstrate that transformation of stem cells through loss of *Apc* is an extremely efficient route towards initiating intestinal adenomas. In a recent study, a *BmicreER* knockin allele visualized a potentially novel pool of intestinal stem cells by lineage tracing²³. *Lgr5* cells and *Bmi-1* cells both produce offspring within days, yet persist for at least a year and are multipotent. At first glance, there are also some significant differences, particularly in the relative location of the two stem cell types. *Bmi-1* cells are predominantly located at

position +4 directly above the Paneth cells and are restricted to the proximal small intestine. Thus, *Lgr5* and *Bmi-1* cells reportedly represent different pools of stem cells²³. *BmicreER* mice were crossed with a conditionally activatable β -catenin allele (*loxP(ex3)*)²⁴. Adenoma formation became visible 3–4 weeks after Cre induction. Although no comparison was made to *loxP(ex3)* activation in non-stem cells, these observations support the hypothesis that transformation of stem cells constitutes the principal route towards intestinal cancer.

Early studies on acute myelogenous leukaemia support the existence of tumour cells with stem-cell-like properties in this disease²⁵. On the basis of many subsequent studies, the cancer stem cell concept²⁶ postulates that a small reservoir of self-sustaining cells is exclusively able to self-renew and maintain a tumour. These cancer stem cells may be refractory to current therapies and may also be the most likely cells to metastasize. Recently, cancer stem cells have been identified in solid tumours²⁷. With the use of CD133 (refs 28, 29), a marker associated with stem and progenitor populations, or CD44 and EpCAM³⁰, human colon cancers have been demonstrated to contain cancer stem cells. Our observations on *Lgr5* expression suggest that a stem cell/progenitor cell hierarchy is maintained in early stem-cell-derived adenomas, which would lend support to the cancer stem cell concept. Testing of the tumorigenic potential of these *Lgr5*⁺ cells awaits the development of a transplantation assay for intestinal adenomas.

METHODS SUMMARY

Mice. *Ah-cre/Apc^{fllox/fllox}* mice were generated by interbreeding mice carrying a floxed *Apc* allele (*Apc^{580S/fllox}*)¹⁷ and the *Ah-cre* allele⁹. *Lgr5-EGFP-IRES-creER^{T2}/Apc^{fllox/fllox}* mice were generated by interbreeding mice carrying a floxed *Apc* allele, (*Apc^{580S/fllox}*)¹⁷ and the *Lgr5-EGFP-IRES-creER^{T2}* allele¹.

Oral β -NF induction. Mice aged 6–8 weeks were treated with a single oral gavage of 1 mg kg⁻¹ β -naphthoflavone (β -NF) in corn oil. All experiments were performed according to UK Home Office guidelines.

Tamoxifen induction. Mice aged 6–8 weeks were injected intraperitoneally with a single 200 μ l dose of tamoxifen in sunflower oil at 10 mg ml⁻¹.

LacZ analysis. To determine the pattern of recombination at the *Rosa26R lacZ* reporter locus, intestinal whole-mounts were prepared, fixed and exposed to X-gal substrate using a method previously reported (see Methods).

Tissue fixation and immunohistochemistry. Intestinal tissue was fixed and processed into paraffin blocks according to standard procedures. β -catenin, EGFP, c-Myc, CD44 and Ki67 immunohistochemistry was performed as previously described¹⁴ (see Methods).

Full Methods and any associated references are available in the online version of the paper at www.nature.com/nature.

Received 4 July; accepted 31 October 2008.

Published online 17 December 2008.

1. Barker, N. *et al.* Identification of stem cells in small intestine and colon by marker gene *Lgr5*. *Nature* **449**, 1003–1007 (2007).
2. Barker, N., van de Wetering, M. & Clevers, H. The intestinal stem cell. *Genes Dev.* **22**, 1856–1864 (2008).
3. Potten, C. S. Kinetics and possible regulation of crypt cell populations under normal and stress conditions. *Bull. Cancer* **62**, 419–430 (1975).
4. Cheng, H. & Leblond, C. P. Origin, differentiation and renewal of the four main epithelial cell types in the mouse small intestine. V. Unitarian Theory of the origin of the four epithelial cell types. *Am. J. Anat.* **141**, 537–561 (1974).
5. Cheng, H. & Leblond, C. P. Origin, differentiation and renewal of the four main epithelial cell types in the mouse small intestine. I. Columnar cell. *Am. J. Anat.* **141**, 461–479 (1974).

6. Marshman, E., Booth, C. & Potten, C. S. The intestinal epithelial stem cell. *Bioessays* **24**, 91–98 (2002).
7. Bjerknes, M. & Cheng, H. The stem-cell zone of the small intestinal epithelium. II. Evidence from paneth cells in the newborn mouse. *Am. J. Anat.* **160**, 65–75 (1981).
8. Bjerknes, M. & Cheng, H. The stem-cell zone of the small intestinal epithelium. I. Evidence from Paneth cells in the adult mouse. *Am. J. Anat.* **160**, 51–63 (1981).
9. Ireland, H., Houghton, C., Howard, L. & Winton, D. J. Cellular inheritance of a Cre-activated reporter gene to determine Paneth cell longevity in the murine small intestine. *Dev. Dyn.* **233**, 1332–1336 (2005).
10. Jones, S. *et al.* Comparative lesion sequencing provides insights into tumor evolution. *Proc. Natl Acad. Sci. USA* **105**, 4283–4288 (2008).
11. Kinzler, K. W. & Vogelstein, B. Lessons from hereditary colorectal cancer. *Cell* **87**, 159–170 (1996).
12. Korinek, V. *et al.* Constitutive transcriptional activation by a β -catenin-Tcf complex in APC^{-/-} colon carcinoma. *Science* **275**, 1784–1787 (1997).
13. Morin, P. J. *et al.* Activation of β -catenin-Tcf signaling in colon cancer by mutations in β -catenin or APC. *Science* **275**, 1787–1790 (1997).
14. van de Wetering, M. *et al.* The β -catenin/TCF-4 complex imposes a crypt progenitor phenotype on colorectal cancer cells. *Cell* **111**, 241–250 (2002).
15. Van der Flier, L. G. *et al.* The intestinal Wnt/TCF signature. *Gastroenterology* **132**, 628–632 (2007).
16. Sansom, O. J. *et al.* Loss of *Apc* *in vivo* immediately perturbs Wnt signaling, differentiation, and migration. *Genes Dev.* **18**, 1385–1390 (2004).
17. Shibata, H. *et al.* Rapid colorectal adenoma formation initiated by conditional targeting of the *Apc* gene. *Science* **278**, 120–123 (1997).
18. Sansom, O. J. *et al.* Myc deletion rescues *Apc* deficiency in the small intestine. *Nature* **446**, 676–679 (2007).
19. Sansom, O. J. *et al.* Cyclin D1 is not an immediate target of β -catenin following *Apc* loss in the intestine. *J. Biol. Chem.* **280**, 28463–28467 (2005).
20. Muncan, V. *et al.* Rapid loss of intestinal crypts upon conditional deletion of the Wnt/Tcf-4 target gene c-Myc. *Mol. Cell. Biol.* **26**, 8418–8426 (2006).
21. Batlle, E. *et al.* β -catenin and TCF mediate cell positioning in the intestinal epithelium by controlling the expression of EphB/ephrinB. *Cell* **111**, 251–263 (2002).
22. Cortina, C. *et al.* EphB-ephrin-B interactions suppress colorectal cancer progression by compartmentalizing tumor cells. *Nature Genet.* **39**, 1376–1383 (2007).
23. Sangiorgi, E. & Capecchi, M. R. *Bmi1* is expressed *in vivo* in intestinal stem cells. *Nature Genet.* **40**, 915–920 (2008).
24. Harada, N. *et al.* Intestinal polyposis in mice with a dominant stable mutation of the β -catenin gene. *EMBO J.* **18**, 5931–5942 (1999).
25. Bonnet, D. & Dick, J. E. Human acute myeloid leukemia is organized as a hierarchy that originates from a primitive hematopoietic cell. *Nature Med.* **3**, 730–737 (1997).
26. Clarke, M. F. *et al.* Cancer stem cells—perspectives on current status and future directions: AACR Workshop on cancer stem cells. *Cancer Res.* **66**, 9339–9344 (2006).
27. Al-Hajj, M., Wicha, M. S., Benito-Hernandez, A., Morrison, S. J. & Clarke, M. F. Prospective identification of tumorigenic breast cancer cells. *Proc. Natl Acad. Sci. USA* **100**, 3983–3988 (2003).
28. O'Brien, C. A., Pollett, A., Gallinger, S. & Dick, J. E. A human colon cancer cell capable of initiating tumour growth in immunodeficient mice. *Nature* **445**, 106–110 (2007).
29. Ricci-Vitiani, L. *et al.* Identification and expansion of human colon-cancer-initiating cells. *Nature* **445**, 111–115 (2007).
30. Dalerba, P. *et al.* Phenotypic characterization of human colorectal cancer stem cells. *Proc. Natl Acad. Sci. USA* **104**, 10158–10163 (2007).

Supplementary Information is linked to the online version of the paper at www.nature.com/nature.

Acknowledgements We thank M. Cozijnsen, J. Korving, C. Nixon, M. Macdonald and B. Doyle for technical help. O.J.S. is funded by Cancer Research UK. N.B. and H.C. are supported by KWF program grant PF-HUBR-2007-3956.

Author Information Reprints and permissions information is available at www.nature.com/reprints. Correspondence and requests for materials should be addressed to H.C. (h.clevers@niob.knaw.nl).

METHODS

Scoring of β -catenin⁺ foci. This was performed on sections stained with anti- β -catenin (BD Transduction labs). A crypt-villus unit was defined on histological cross-section when the crypt exits on both sides into a villus. β -catenin^{high} foci were scored as clusters of cells that showed both increased nuclear and cytoplasmic β -catenin when compared to surrounding cells. The following categories were recognized: base of crypts (β -catenin-positive cells were below position 10 of the crypt), upper crypt (β -catenin-positive cells were between position 10 and the top of the crypt), and villus (β -catenin-positive cells were clearly located within the villus). **Scoring of LacZ⁺ lesions on intestinal whole mounts.** Mice were culled, their intestines removed, opened up and pinned out as intestinal whole mounts. They were then stained for LacZ. Using a dissecting microscope, microscopic lesions, microadenomas and adenomas were counted for the entire intestine and converted to a percentage. For all the intestines scored for this analysis, there were at least 100 microscopic lesions per animal on whole-mount analysis. Lesions occurring after Apc loss were divided into three categories: microscopic lesions, microadenomas and adenomas. Microscopic lesions were those that could only be seen using the dissecting microscope and were less than 0.5 mm \times 0.5 mm. Microadenomas were judged as being visible without the dissecting microscope and ranged from 0.5 mm \times 0.5 mm to 2 mm \times 2 mm. Adenomas were greater than 2 mm \times 2 mm. This categorization fitted with our previous histological criteria, where lesions were subdivided into single crypt lesions (equivalent to the microscopic lesion), complex lesions were greater than one crypt (2–3) and situated near the surface, and adenomas comprised numerous crypt-like structures and had reached the surface of the epithelium.

β -galactosidase (LacZ) staining protocol. Intestines were isolated, immediately flushed with ice-cold fixative (1% formaldehyde, 0.2% glutaraldehyde, 0.02% NP40 in PBS0 (phosphate-buffered saline deficient in Mg²⁺ and Ca²⁺)) and incubated for 2 h in a 20-fold volume of the same ice-cold fixative at 4 °C on a rolling platform. The fixative was removed and the intestines washed twice in PBS0 for 20 min at room temperature on a rolling platform. The β -galactosidase substrate (5 mM K₃Fe(CN)₆, 5 mM K₄Fe(CN)₆·3H₂O, 2 mM MgCl₂, 0.02% NP40, 0.1% Nadeoxycholate, 1 mg ml⁻¹ X-gal in PBS0) was then added and the tissues incubated in the dark overnight at room temperature. The substrate was removed and the tissues washed twice in PBS0 for 20 min at room temperature on a rolling platform. The tissues were then fixed overnight in a 20-fold volume of 4% paraformaldehyde (PFA) in PBS0 at 4 °C in the dark on a rolling platform. The PFA was removed and the tissues washed twice in PBS0 for 20 min at room temperature on a rolling platform.

The stained tissues were transferred to tissue cassettes and paraffin blocks prepared using standard methods. Tissue sections (4 μ M) were prepared and counterstained with neutral red.

Immunohistochemistry protocol. Freshly isolated intestines were flushed with formalin (4% formaldehyde in PBS) and fixed by incubation in a tenfold excess of formalin overnight at room temperature. The formalin was removed and the

intestines washed twice in PBS at room temperature. The intestines were then transferred to a tissue cassette and dehydrated by serial immersion in 20-fold volumes of 70%, 96% and 100% EtOH for 2 h each at 4 °C. Excess ethanol was removed by incubation in xylene for 1.5 h at room temperature and the cassettes then immersed in liquid paraffin (56 °C) overnight. Paraffin blocks were prepared using standard methods and 4 μ M tissue sections generated. These sections were de-waxed by immersion in xylene (2 \times 5 min) and hydrated by serial immersion in 100% EtOH (2 \times 1 min), 96% EtOH (2 \times 1 min), 70% EtOH (2 \times 1 min) and distilled water (2 \times 1 min). Endogenous peroxidase activity was blocked by immersing the slides in peroxidase blocking buffer (0.040 M citric acid, 0.121 M disodium hydrogen phosphate, 0.030 M sodium azide, 1.5% hydrogen peroxide) for 15 min at room temperature. Antigen retrieval was performed (see details below for each antibody), and blocking buffer (1% BSA in PBS) added to the slides for 30 min at room temperature. Primary antibodies were then added and incubated as detailed below. The slides were then rinsed in PBS and secondary antibody added (polymer HRP-labelled anti-mouse/rabbit, Envision) for 30 min at room temperature. Slides were again washed in PBS and bound peroxidase detected by adding DAB substrate for 10 min at room temperature. Slides were then washed 2 \times in PBS and nuclei counterstained with Mayer's haematoxylin for 2 min, followed by two rinses in distilled water. Sections were dehydrated by serial immersion for 1 min each in 50% EtOH and 60% EtOH, followed by 2 min each in 70% EtOH, 96% EtOH, 100% EtOH and xylene. Slides were mounted in Pertex mounting medium and a coverslip placed over the tissue section.

For c-Myc (Santa Cruz, SC-764), antigen retrieval involved 20 min boiling in Tris-EDTA pH 9.0; staining involved 1/500 dilution in blocking buffer (0.05% BSA in PBS) or 4 days at 4 °C. For β -catenin (BD Transduction Labs, 610154), antigen retrieval involved 20 min boiling in Tris-EDTA pH 9.0; staining involved 1/100 dilution in blocking buffer (0.05% BSA in PBS) for 2 h at room temperature. For Ki67 (Monosan, MONX 10283 clone mm1), antigen retrieval involved 20 min boiling in 0.01 M citrate buffer pH 6.0; staining involved 1/250 dilution in blocking buffer (0.05% BSA in PBS) for 1 h at room temperature. For EGFP (In-House), antigen retrieval involved 20 min boiling in 0.01 M citrate buffer pH 6.0; staining involved 1/8,000 dilution in blocking buffer (0.05% BSA in PBS) for 4 days at 4 °C. For CD44 (In-House), antigen retrieval involved 20 min boiling in 0.01 M citrate buffer pH 6.0; staining involved 1/200 dilution in blocking buffer (0.05% BSA in PBS) for 1 day at 4 °C.

Isolation of adenoma cells. Freshly isolated small intestines were incised along their length and adenomas were removed using forceps. The adenoma tissue was then incubated in PBS plus 5 mM EDTA for 10 min. Vigorous shaking removed remaining villi and the adenomas were subsequently incubated in PBS supplemented with trypsin (10 mg ml⁻¹) and DNase (0.8 units per μ l) for 30 min at 37 °C. After incubation, cells were spun down, re-suspended in SMEM (Invitrogen) and filtered through a 40 μ M mesh. The cells were analysed using a MoFlo cell sorter (DAKO).

LETTERS

RAD6–RAD18–RAD5-pathway-dependent tolerance to chronic low-dose ultraviolet light

Takashi Hishida¹, Yoshino Kubota¹, Antony M. Carr² & Hiroshi Iwasaki³

In nature, organisms are exposed to chronic low-dose ultraviolet light (CLUV) as opposed to the acute high doses common to laboratory experiments. Analysis of the cellular response to acute high-dose exposure has delineated the importance of direct DNA repair by the nucleotide excision repair pathway¹ and for checkpoint-induced cell cycle arrest in promoting cell survival². Here we examine the response of yeast cells to CLUV and identify a key role for the RAD6–RAD18–RAD5 error-free postreplication repair (RAD6 error-free PRR) pathway^{3,4} in promoting cell growth and survival. We show that loss of the RAD6 error-free PRR pathway results in DNA-damage-checkpoint-induced G2 arrest in CLUV-exposed cells, whereas wild-type and nucleotide-excision-repair-deficient cells are largely unaffected. Cell cycle arrest in the absence of the RAD6 error-free PRR pathway was not caused by a repair defect or by the accumulation of ultraviolet-induced photoproducts. Notably, we observed increased replication protein A (RPA)– and Rad52–yellow fluorescent protein foci⁵ in the CLUV-exposed *rad18Δ* cells and demonstrated that Rad52-mediated homologous recombination is required for the viability of the *rad18Δ* cells after release from CLUV-induced G2 arrest. These and other data presented suggest that, in response to environmental levels of ultraviolet exposure, the RAD6 error-free PRR pathway promotes replication of damaged templates without the generation of extensive single-stranded DNA regions. Thus, the error-free PRR pathway is specifically important during chronic low-dose ultraviolet exposure to prevent counter-productive DNA checkpoint activation and allow cells to proliferate normally.

The importance of DNA repair and damage tolerance for sunlight-induced DNA damage is evident from the highly increased skin cancer incidence in patients with the genetic disease xeroderma pigmentosum⁶, which is caused by mutation of genes responsible for nucleotide excision repair (NER) or damage bypass by error-prone DNA polymerases. Four highly conserved DNA damage response mechanisms make large contributions to the ultraviolet response: NER, RAD6 damage tolerance, homologous recombination and the DNA damage checkpoint⁷.

In previous studies of the cellular ultraviolet response, high-dose ultraviolet light (that is, 1 to 500 J m⁻²) was delivered within a relatively short time. However, such acute conditions are rare in environmental situations; organisms are typically exposed continuously or intermittently to very-low-dose ultraviolet light for extended periods. We explore the biological effects of continuous irradiation by low-dose ultraviolet light, using budding yeast as a model. On a sunny day, sunlight at the earth's surface equates to a dose rate of ~0.1 J m⁻² min⁻¹ from a 254 nm ultraviolet light^{8,9}. Therefore, we established CLUV irradiation conditions by exposing cells to 0.18 J m⁻² min⁻¹ ultraviolet light using 254-nm germicidal lamps.

To examine cell growth, early logarithmic cells (liquid culture; 30 °C) were exposed to CLUV and samples were taken every 3 h to

determine plating efficiency (Fig. 1a). CLUV had no significant effect on growth of wild-type, homologous-recombination-deficient (*rad52Δ*), checkpoint-deficient (*mec1Δ*) or, surprisingly, NER-deficient (*rad14Δ*) cultures. In addition, base-excision-repair-deficient mutants (*apn1Δ*, *apn2Δ*, *ntg1Δ* and *ntg2Δ*) showed wild-type levels of CLUV sensitivity (Supplementary Fig. 1). In contrast, a RAD6 damage-tolerance-pathway-deficient strain (*rad18Δ*) did not increase in cell number and gradually lost viability. Similar results were observed in spot assays that examined effects of longer periods of CLUV exposure (Fig. 1b), whereas *rad14Δ* cells were hypersensitive

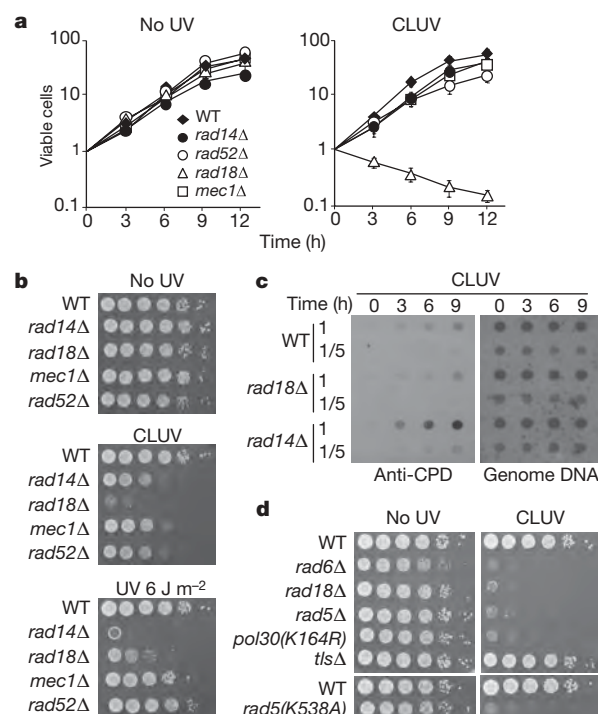


Figure 1 | Role of the RAD6 pathway in tolerance to CLUV exposure.

a, Asynchronous yeast cells were grown under CLUV irradiation and samples were taken every 3 h to determine plating efficiency. Viable cells are represented as relative colony-forming units (time 0 = 1 colony-forming unit). Error bars indicate s.d. ($n \geq 3$). The *mec1Δ* strain contains *smi1Δ*. The *smi1Δ* single mutation did not affect the growth under CLUV irradiation (data not shown). UV, ultraviolet irradiation. **b**, Tenfold serial dilutions of stationary-phase cells were spotted onto plates. Top, no ultraviolet; middle, CLUV (2 days); bottom, acute ultraviolet irradiation (6 J m⁻²). **c**, Dot blot analysis of DNA extracted from **a** using anti-CPD antibody (TDM2). WT, wild type. **d**, CLUV sensitivity of RAD6 pathway mutants. Cells were exposed to CLUV as in **b**.

¹Research Institute for Microbial Diseases, Osaka University, 3-1 Yamadaoka, Suita, Osaka 565-0871, Japan. ²MRC Genome Damage and Stability Centre, University of Sussex, Brighton BN1 9RQ, UK. ³International Graduate School of Arts and Sciences, Yokohama City University, 1-7-29, Suehiro, Tsurumi, Yokohama, Kanagawa 230-0045, Japan.

to acute ultraviolet light (6 J m^{-2}) and *rad18Δ* cells were only moderately sensitive (Fig. 1b).

Ultraviolet light generates multiple DNA lesions, including cyclobutane pyrimidine dimers (CPDs) and 6–4 photoproducts^{10,11}. To establish whether *rad18Δ* CLUV hypersensitivity results from a higher load of DNA lesions, we used an immunoblot assay¹² to quantify CPDs in CLUV-exposed cells. In wild-type and *rad18Δ* cells, CPDs accumulated to relatively low levels during 9 h of CLUV exposure (Fig. 1c). In NER-deficient (*rad14Δ*) cells, CPD concentrations increased to high levels. The dose delivered by CLUV during 9 h is $\sim 97 \text{ J m}^{-2}$. Wild-type and *rad18Δ* cells accumulated damage equivalent to 2.3 J m^{-2} (delivered in 5 s, see Supplementary Fig. 2), confirming that they are NER-proficient. Thus, the *RAD6–RAD18* pathway has an essential role in the CLUV response when NER is actively eliminating ultraviolet-induced lesions.

RAD6–RAD18 damage tolerance consists of two highly conserved mechanisms (Supplementary Table 1)^{3,4,13} that allow lesion bypass by replication without lesion removal. The first, translesion DNA synthesis (TLS), requires Rad18-dependent monoubiquitination of Lys 164 of proliferating cell nuclear antigen (PCNA) and involves error-prone DNA polymerases^{14,15}. The second is error-free PRR; this is coordinated by Rad18- and Rad5-dependent polyubiquitination of PCNA Lys 164, and probably acts by means of transient template-strand switching^{14,16,17}. Consistently, a PCNA mutant lacking the ubiquitin attachment site (*pol30(K164R)*) was sensitive to CLUV exposure (Fig. 1d). A TLS-deficient strain (*tlsΔ*, a *rad30Δ rev3Δ rev1Δ* triple mutant) did not show detectable CLUV sensitivity, whereas *rad5Δ* and ATPase-deficient *rad5(K538A)* mutants showed CLUV hypersensitivity equivalent to *rad18Δ* and *rad6Δ* mutants (Fig. 1d). These indicate that error-free PRR is important for CLUV survival. Previous studies demonstrate that *rad5Δ* and *pol30(K164R)* are

slightly less sensitive to acute ultraviolet light than *rad18Δ*¹⁴. The same behaviour was observed for CLUV sensitivity when cells were exposed to a much lower ultraviolet dose ($<0.1 \text{ J m}^{-2} \text{ min}^{-1}$; Supplementary Fig. 3).

To analyse the role of PRR in CLUV tolerance, asynchronous wild-type, *rad18Δ* and *rad5Δ* cultures were treated with CLUV for 6 h and assayed by fluorescence-activated cell sorting. Cell cycle progression of wild-type cells was not significantly affected by CLUV exposure (Fig. 2a). However, most *rad18Δ* and *rad5Δ* cells arrested with 2C DNA content (Fig. 2a). More than 70% arrested as large-budded cells with one nucleus at the bud neck and a short mitotic spindle (Fig. 2b, c). Cdc45 and Mcm7 showed markedly reduced chromatin association in CLUV-exposed *rad18Δ* cells compared to wild-type cells (Supplementary Fig. 4). These replication proteins only bind chromatin during the S and G1–S phase, respectively, but not during the G2 phase¹⁸. Thus, *RAD6* error-free-PRR-deficient cells are arrested in the G2 phase under CLUV irradiation.

Next, cells were synchronized in G1 with α -factor and released into CLUV-exposure conditions. Most wild-type, *rad18Δ* and *rad5Δ* cells entered and completed S phase within 60 min. However, whereas

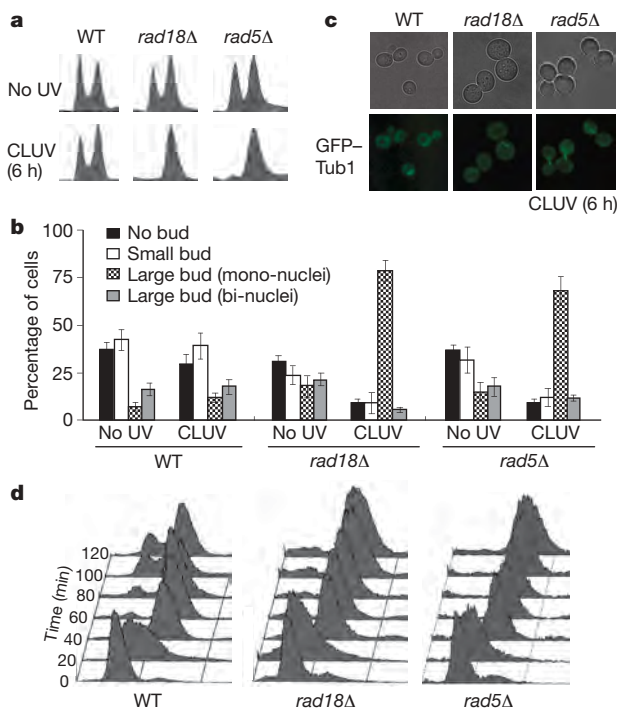


Figure 2 | CLUV-induced G2 arrest in *rad18Δ* cells. **a**, Flow cytometry of wild-type, *rad18Δ* and *rad5Δ* cells exposed to CLUV for 6 h. **b**, Cells from **a** were stained with 4,6-diamidino-2-phenylindole (DAPI) to evaluate nuclear and cellular morphology. Error bars indicate s.d. ($n = 3$). **c**, Cells expressing GFP-Tub1 were treated as in **a** and spindles were visualized by fluorescence microscopy. **d**, Flow cytometry of synchronized wild-type, *rad18Δ* and *rad5Δ* cells under CLUV irradiation. Cells were synchronized with α -factor, transferred to fresh medium and exposed to CLUV for the indicated time.

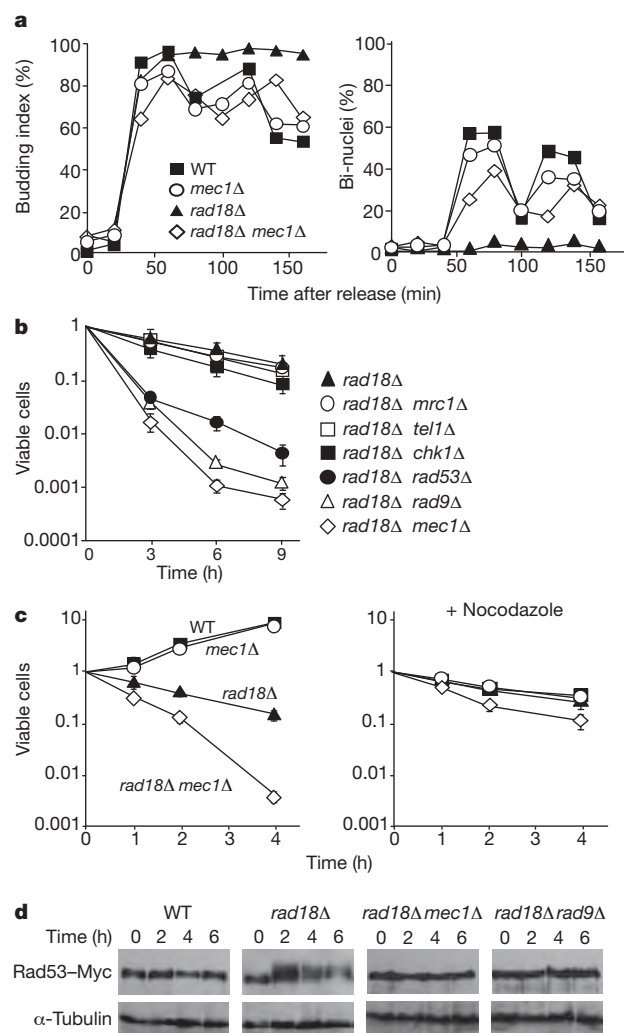


Figure 3 | DNA damage checkpoint activation in CLUV-exposed *rad18Δ* cells. **a**, Synchronized cells were released into CLUV exposure conditions for the indicated time and analysed microscopically for the nuclear and cellular morphology. **b**, The plating efficiency was determined as in Fig. 1a. **c**, Cells synchronized in G2/M with nocodazole were exposed to CLUV for the indicated time in the presence or absence of nocodazole. The error bars in **b** and **c** indicate s.d. ($n \geq 3$). **d**, Protein extracts from cells exposed to CLUV for the indicated time were prepared and analysed by western blotting with anti-Myc (9E10) antibody. α -Tubulin was used as a loading control.

wild-type cells continued through G2/M, *rad18Δ* and *rad5Δ* cells arrested with 2C DNA content before mitosis (Fig. 2d). Because *rad18Δ* and *rad5Δ* cells remain viable during CLUV exposure and they can resume cell cycle progression after cessation of the exposure (Fig. 1a and Supplementary Fig. 5a), we analysed *rad18Δ mec1Δ* and *rad5Δ mec1Δ* double mutants to establish whether G2 arrest contributed to viability. CLUV-exposed *rad18Δ mec1Δ* and *rad5Δ mec1Δ* cells did not arrest after release from G1 into CLUV (Fig. 3a and Supplementary Fig. 5b) and failed to form colonies (Fig. 3b and Supplementary Fig. 5a). To confirm that viability required G2 arrest, the double mutant and appropriate controls were arrested in G2 using nocodazole during CLUV exposure (Fig. 3c). Most *rad18Δ mec1Δ* cells remained viable, confirming a critical role for G2 arrest.

Because DNA-damage-checkpoint-mediated arrest is accomplished by a complex signal transduction network (ref. 19, see also Supplementary Table 2), we tested various checkpoint mutants. Neither *tel1Δ*, *mrc1Δ* nor *chk1Δ* affected viability of CLUV-exposed *rad18Δ* cells (Fig. 3b). In contrast, *rad18Δ rad53Δ* and *rad18Δ rad9Δ*, like *rad18Δ mec1Δ*, reduced viability (Fig. 3b), indicating that the Mec1-, Rad9- and Rad53-dependent damage checkpoint is activated. Similar behaviour was also observed in *rad5Δ* derivatives (Supplementary Fig. 5a). We next analysed Rad53 phosphorylation (Fig. 3d). Hyperphosphorylated Rad53 was not detected in wild-type cells after 6 h of CLUV exposure. In *rad18Δ* mutants, Mec1- and Rad9-dependent hyperphosphorylated Rad53 was evident after 2 h of CLUV exposure and accumulated with exposure time (Fig. 3d). Ddc2 (also known as Lcd2) is the Mec1 binding partner that recognizes RPA-coated single-stranded DNA (ssDNA)²⁰. We observed a notable increase in Ddc2 foci after CLUV exposure of *rad18Δ* and *rad5Δ* cells (Supplementary Fig. 6)²¹. Thus, our results clearly indicate that the Mec1-Rad9-Rad53-dependent DNA damage checkpoint is activated by CLUV exposure in cells defective for the RAD6 error-free PRR pathway. Rad9 functions predominantly in the G1/S and G2/M checkpoints, having only a minor role in the DNA replication checkpoint²². This, and the lack of increased sensitivity on *MRC1* deletion, supports the importance of G2 checkpoint arrest during CLUV exposure of error-free-PRR-deficient cells.

Acute high-dose ultraviolet treatments result in accumulation of ssDNA gaps when cells initiate replication^{23–25}. We examined the subcellular localization of RPA-YFP⁵ during CLUV exposure. Few RPA-YFP foci were observed in untreated wild-type, *rad18Δ* or *rad5Δ* cells. After 3 h of CLUV exposure, RPA-YFP foci appeared in >80% of *rad18Δ* and *rad5Δ* cells but only ~10% of wild-type cells (Supplementary Fig. 7). After release from G1 into CLUV conditions, *rad18Δ*, but not wild-type, cells rapidly accumulated RPA-YFP foci and arrested with budded morphology (Fig. 4a). Thus, ssDNA gaps accumulate in CLUV-exposed *rad18Δ* cells, probably resulting in G2 arrest.

RPA-coated ssDNA gaps at stalled replication forks are competent for, and required for, homologous recombination^{26,27}. We analysed subcellular localizations of the key homologous recombination protein Rad52. Rad52 foci were significantly increased in CLUV-exposed *rad18Δ* and *rad5Δ* cells compared to the wild type (Supplementary Fig. 8), implying homologous recombination activation. *RAD52* deletion caused viability loss in CLUV-exposed *rad18Δ* cells, although *rad52Δ rad18Δ* double mutant cells were competent for CLUV-induced G2 arrest (Fig. 4b, c and Supplementary Fig. 9). Interestingly, unlike *rad18Δ* single mutant cells, *rad18Δ rad52Δ* double mutant cells could not resume cell cycle progression after cessation of CLUV treatment (Fig. 4d and Supplementary Fig. 10). These results demonstrate that *rad18Δ rad52Δ* cells are not checkpoint-defective, but cannot recover from CLUV-induced G2 arrest. Thus, Rad52 has a critical role in CLUV tolerance that is required for reversible G2 arrest in the absence of RAD6 error-free PRR.

The results presented here are summarized in Fig. 4e. Under CLUV conditions, most ultraviolet lesions are repaired by NER, but lesions remaining at the onset of S phase block replication fork progression. The RAD6 error-free PRR pathway promotes replication across the damaged template, probably by using the newly synthesized sister chromatid as a template. This enables cells to complete replication without ssDNA gap accumulation and to continue growth under CLUV irradiation. In error-free-PRR-deficient cells, DNA replication of the damaged template is still completed by other replication-bypass mechanisms, possibly involving re-priming downstream of the damage^{25,28}. This generates ssDNA gaps spanning the fork-blocking

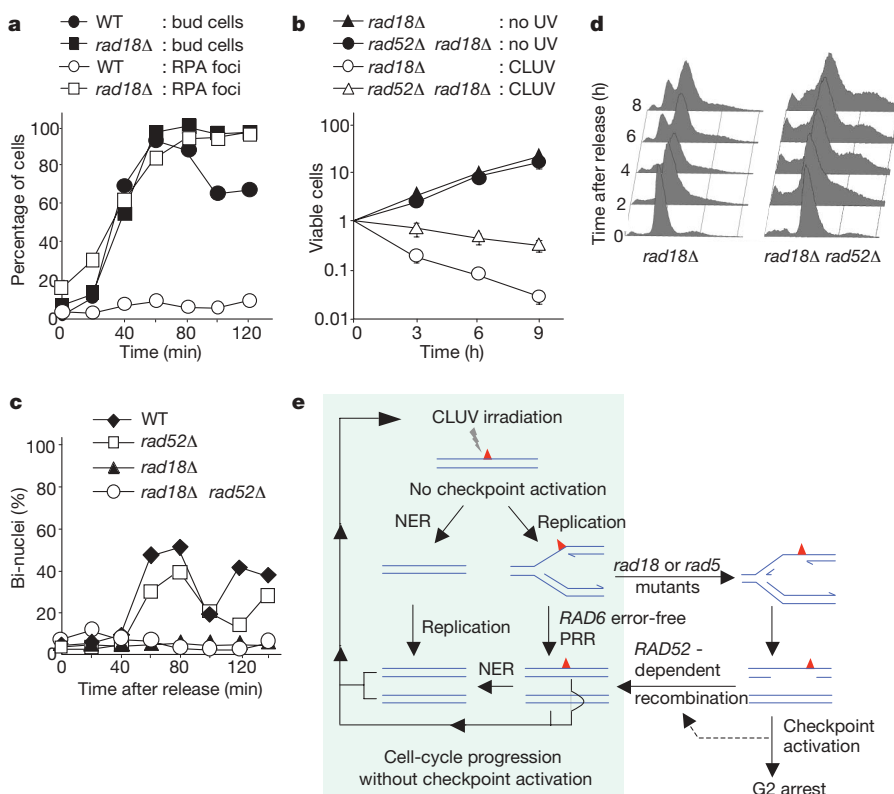


Figure 4 | CLUV-induced DNA damage in RAD6 error-free-PRR-deficient cells. **a**, Cell cycle distribution of CLUV-induced RPA foci. Synchronized wild-type and *rad18Δ* cells were released into CLUV exposure conditions and analysed microscopically for the presence of budded and RPA-focus-containing cells. **b**, Plating efficiency of *rad52Δ rad18Δ* cells exposed to CLUV. Error bars represent s.d. ($n = 3$). **c**, Cell cycle progression of *rad52Δ rad18Δ* cells. **d**, Flow cytometry of *rad18Δ* and *rad18Δ rad52Δ* cells after release from CLUV exposure for 3 h. Samples were taken every 2 h after terminating CLUV. **e**, A summary model for the CLUV damage tolerance in yeast. Triangles represent the ultraviolet lesions.

lesion that activate the DNA damage checkpoint and are subsequently repaired by *RAD52*-dependent mechanisms during the CLUV-induced cell cycle delay.

The DNA damage checkpoints are critical for genome stability, allowing time for accurate DNA repair and induction of apoptosis in multicellular organisms. However, such a strategy is probably counter-productive during exposure to extremely low levels of DNA damage. Our study provides robust evidence that error-free PRR prevents disadvantageous checkpoint activation during low-dose ultraviolet light. Further studies on the biological implications of *RAD6* pathway during chronic low dose damage exposure in other species will be of great interest.

METHODS SUMMARY

Standard methods were used to construct strains carrying deletion alleles or epitope-tagged proteins. To synchronize cells in G1 and G2, α -factor ($10 \mu\text{g ml}^{-1}$, Sigma) and nocodazole ($15 \mu\text{g ml}^{-1}$, Sigma) were added to cells in mid-log phase ($\sim 5 \times 10^6 \text{ cells ml}^{-1}$), respectively, and followed by incubation for 2 h at 30°C . For CLUV irradiation, cell cultures were incubated with horizontal shaking at 30°C under continuous exposure to $0.18 \text{ J m}^{-2} \text{ min}^{-1}$. Dot blot analysis for genomic DNA with CPDs was performed as described previously¹². Flow cytometry, western blotting and microscopic analysis were performed as described previously²⁹.

Full Methods and any associated references are available in the online version of the paper at www.nature.com/nature.

Received 26 March; accepted 24 October 2008.

Published online 14 December 2008.

- Shuck, S. C., Short, E. A. & Turchi, J. J. Eukaryotic nucleotide excision repair: from understanding mechanisms to influencing biology. *Cell Res.* **18**, 64–72 (2008).
- Kastan, M. B. & Bartek, J. Cell-cycle checkpoints and cancer. *Nature* **432**, 316–323 (2004).
- Ulrich, H. D. The *RAD6* pathway: control of DNA damage bypass and mutagenesis by ubiquitin and SUMO. *ChemBioChem* **6**, 1735–1743 (2005).
- Andersen, P. L., Xu, F. & Xiao, W. Eukaryotic DNA damage tolerance and translesion synthesis through covalent modifications of PCNA. *Cell Res.* **18**, 162–173 (2008).
- Lisby, M., Barlow, J. H., Burgess, R. C. & Rothstein, R. Choreography of the DNA damage response: spatiotemporal relationships among checkpoint and repair proteins. *Cell* **118**, 699–713 (2004).
- Friedberg, E. C. How nucleotide excision repair protects against cancer. *Nature Rev. Cancer* **1**, 22–33 (2001).
- Prakash, S., Sung, P. & Prakash, L. DNA repair genes and proteins of *Saccharomyces cerevisiae*. *Annu. Rev. Genet.* **27**, 33–70 (1993).
- Harm, W. Biological determination of the germicidal activity of sunlight. *Radiat. Res.* **40**, 63–69 (1969).
- Callegari, A. J. & Kelly, T. J. UV irradiation induces a postreplication DNA damage checkpoint. *Proc. Natl Acad. Sci. USA* **103**, 15877–15882 (2006).
- Hoeijmakers, J. H. Genome maintenance mechanisms for preventing cancer. *Nature* **411**, 366–374 (2001).
- Friedberg, E. C. *et al.* DNA repair: from molecular mechanism to human disease. *DNA Repair (Amst.)* **5**, 986–996 (2006).
- Giavara, S. *et al.* Yeast Nhp6A/B and mammalian Hmgb1 facilitate the maintenance of genome stability. *Curr. Biol.* **15**, 68–72 (2005).
- Prakash, S., Johnson, R. E. & Prakash, L. Eukaryotic translesion synthesis DNA polymerases: specificity of structure and function. *Annu. Rev. Biochem.* **74**, 317–353 (2005).
- Hoege, C., Pfander, B., Moldovan, G. L., Pyrowolakis, G. & Jentsch, S. *RAD6*-dependent DNA repair is linked to modification of PCNA by ubiquitin and SUMO. *Nature* **419**, 135–141 (2002).
- Stelter, P. & Ulrich, H. D. Control of spontaneous and damage-induced mutagenesis by SUMO and ubiquitin conjugation. *Nature* **425**, 188–191 (2003).
- Zhang, H. & Lawrence, C. W. The error-free component of the *RAD6/RAD18* DNA damage tolerance pathway of budding yeast employs sister-strand recombination. *Proc. Natl Acad. Sci. USA* **102**, 15954–15959 (2005).
- Blastyak, A. *et al.* Yeast Rad5 protein required for postreplication repair has a DNA helicase activity specific for replication fork regression. *Mol. Cell* **28**, 167–175 (2007).
- Zou, L. & Stillman, B. Formation of a preinitiation complex by S-phase cyclin CDK-dependent loading of Cdc45p onto chromatin. *Science* **280**, 593–596 (1998).
- Foiani, M. *et al.* DNA damage checkpoints and DNA replication controls in *Saccharomyces cerevisiae*. *Mutat. Res.* **451**, 187–196 (2000).
- Zou, L. & Elledge, S. J. Sensing DNA damage through ATRIP recognition of RPA-ssDNA complexes. *Science* **300**, 1542–1548 (2003).
- Paciotti, V., Clerici, M., Lucchini, G. & Longhese, M. P. The checkpoint protein Ddc2, functionally related to *S. pombe* Rad26, interacts with Mec1 and is regulated by Mec1-dependent phosphorylation in budding yeast. *Genes Dev.* **14**, 2046–2059 (2000).
- Sun, Z., Hsiao, J., Fay, D. S. & Stern, D. F. Rad53 FHA domain associated with phosphorylated Rad9 in the DNA damage checkpoint. *Science* **281**, 272–274 (1998).
- Rupp, W. D. & Howard-Flanders, P. Discontinuities in the DNA synthesized in an excision-defective strain of *Escherichia coli* following ultraviolet irradiation. *J. Mol. Biol.* **31**, 291–304 (1968).
- Prakash, L. Characterization of postreplication repair in *Saccharomyces cerevisiae* and effects of *rad6*, *rad18*, *rev3* and *rad52* mutations. *Mol. Gen. Genet.* **184**, 471–478 (1981).
- Lopes, M., Foiani, M. & Sogo, J. M. Multiple mechanisms control chromosome integrity after replication fork uncoupling and restart at irreparable UV lesions. *Mol. Cell* **21**, 15–27 (2006).
- Fanning, E., Klimovich, V. & Nager, A. R. A dynamic model for replication protein A (RPA) function in DNA processing pathways. *Nucleic Acids Res.* **34**, 4126–4137 (2006).
- Gangavarapu, V., Prakash, S. & Prakash, L. Requirement of *RAD52* group genes for postreplication repair of UV-damaged DNA in *Saccharomyces cerevisiae*. *Mol. Cell. Biol.* **27**, 7758–7764 (2007).
- Heller, R. C. & Marians, K. J. Replisome assembly and the direct restart of stalled replication forks. *Nature Rev. Mol. Cell Biol.* **7**, 932–943 (2006).
- Hishida, T., Ohno, T., Iwasaki, H. & Shinagawa, H. *Saccharomyces cerevisiae* *MGS1* is essential in strains deficient in the *RAD6*-dependent DNA damage tolerance pathway. *EMBO J.* **21**, 2019–2029 (2002).

Supplementary Information is linked to the online version of the paper at www.nature.com/nature.

Acknowledgements We thank R. Rothstein and H. Araki for strains; T. Matsunaga for anti-thymine dimer monoclonal antibody (designated TDM2 antibody); and T. Ohya for technical assistance. This work was supported by the Sumitomo foundation, by Grants-in-Aid for Scientific Research from the Ministry of Education, Culture, Sports, Science and Technology of Japan, and by the MRC (UK) grant G0600233.

Author Contributions T.H. designed the study. T.H. and Y.K. performed the experiments. H.I. coordinated the study. T.H., H.I. and A.M.C. analysed data and wrote the paper.

Author Information Reprints and permissions information is available at www.nature.com/reprints. Correspondence and requests for materials should be addressed to T.H. (hishida@biken.osaka-u.ac.jp).

METHODS

Strains. BY4741 and its derivatives (KanMX disruptants), *rad6Δ*, *rad18Δ*, *rad5Δ*, *rev1Δ*, *rad30Δ*, *rev3Δ*, *rad52Δ*, *rad14Δ*, *rad9Δ*, *chk1Δ*, *mrc1Δ* and *tel1Δ*, were obtained from Invitrogen. Other yeast strains used in this study are listed in Supplementary Table 2. The *RAD53-9myc* strain was constructed using a PCR-based method³⁰. The strains W3749-14C (*YFP-RAD52*), W3775-12C (*YFP-RFA1*) and W3849-15C (*DDC2-YFP*) were provided by R. Rothstein. A lysine-to-alanine substitution mutation was introduced into a conserved Walker A site in the *RAD5* gene by PCR-based mutagenesis combined with homologous recombination *in vivo*. The *pol30(K164R)* mutation was also introduced into the *POL30* gene as described previously³¹. All double or triple mutant strains were constructed by standard genetic crosses. Strain construction was confirmed by PCR analysis.

Media and growth conditions. Cells were grown in YPD media containing 0.01% adenine sulphate (YPAD) at 30 °C. To synchronize cells in G1, 10 µg ml⁻¹ α-factor (Sigma) was added to cells in mid-log phase (~5 × 10⁶ cells ml⁻¹), followed by incubation for 2.5 h at 30 °C. The cells were then washed with water and released into fresh media containing 100 µg ml⁻¹ pronase (Sigma). Nocodazole (Sigma) was used at a final concentration of 15 µg ml⁻¹.

Ultraviolet irradiation. CLUV exposure was carried out using the following conditions: cells were grown overnight, diluted to ~2 × 10⁶ cells ml⁻¹ and grown for several hours. Cultures (4 ml) were poured into plastic dishes (Sterilin; Bibby Sterilin Ltd) at a depth of less than 1.5 mm. Cells were incubated with horizontal shaking at 30 °C under continuous exposure to ultraviolet irradiation. Ultraviolet irradiation (254 nm) was attenuated at all times with an ultraviolet transparent cover on the dishes and cells were exposed to ultraviolet light at a dose of 0.18 J m⁻² per min. The source of ultraviolet irradiation was a GL-10 germicidal lamp (Toshiba). Ultraviolet irradiance was measured using a UVX radiometer with UVX-25 (Ultraviolet Products). For longer incubation periods, the surroundings of dishes were sealed to prevent evaporation of the media. Samples were taken at the indicated times, diluted and spread on YPD plates. Plates were incubated at 30 °C for 3 days in the dark without ultraviolet treatment. Relative cell survival was measured by preparing tenfold serial dilutions of cultures and spotting aliquots of the dilutions onto YPD plates. Plates were incubated with cells facing up at 30 °C for 2–3 days with continuous exposure to CLUV. All assays were repeated at least three times.

Dot blot analysis. Cells were grown in 5-ml aliquots, collected at the indicated time points, and DNA extracts were prepared as described previously¹². DNA was spotted onto a Duralon-UV membrane (Stratagene) using a dot-blot apparatus (Bio-Rad) in accordance with the manufacturer's instructions. The membrane

was dried at 80 °C for 2 h, incubated with 2.5% skimmed milk, and probed with a mouse monoclonal antibody against thymidine dimer (TDM2), which was kindly provided by T. Matsunaga. Detection was performed with HRP-conjugated secondary antibodies and advanced ECL (GE Healthcare).

Fluorescence microscopy. YFP signals were observed using a Zeiss Axioplan 2 microscope equipped with a Hamamatsu C4742-95 CCD camera. Images were visualized using Lumina Vision imaging software (Mitani Corporation). More than 150 individual cells were scored for each strain. Data were the average of three independent measurements.

Evaluation of cellular morphology. Cells were fixed in 70% ethanol, stained with DAPI and examined by fluorescence microscopy. At least 200 cells were counted per experimental condition. The result represents the average of three independent measurements.

Preparation of yeast extracts and western blotting. Protein extracts were prepared from 2 × 10⁷ logarithmically growing cells using the trichloroacetic acid (TCA) method, as described previously³². Proteins were analysed by SDS-PAGE, transferred to PVDF membrane, and probed with anti-Myc (9E10) monoclonal antibody (Roche). The *RAD53-13Myc* strains were constructed by integrating a carboxy-terminal 13-Myc tag into the endogenous *RAD53* locus.

Chromatin binding assay. Chromatin purification was performed as described previously^{33,34} with the following modifications. After spheroplasted cells were lysed by the addition of Triton X-100 to final a concentration of 1%, lysates were overlaid onto a 30% sucrose cushion and the chromatin-enriched fraction was isolated by high-speed centrifugation. The pellet was resuspended in lysis buffer and incubated for 15 min on ice with 15 U of Benzonase (Stratagene).

FACS analysis. Cells were fixed in 70% ethanol at 4 °C and processed as described previously²⁹.

30. Longtine, M. S. *et al.* Additional modules for versatile and economical PCR-based gene deletion and modification in *Saccharomyces cerevisiae*. *Yeast* **14**, 953–961 (1998).
31. Hishida, T., Ohya, T., Kubota, Y., Kamada, Y. & Shinagawa, H. Functional and physical interaction of yeast Mgs1 with PCNA: impact on *RAD6*-dependent DNA damage tolerance. *Mol. Cell. Biol.* **26**, 5509–5517 (2006).
32. Pellicioli, A. *et al.* Activation of Rad53 kinase in response to DNA damage and its effect in modulating phosphorylation of the lagging strand DNA polymerase. *EMBO J.* **18**, 6561–6572 (1999).
33. Schepers, A. & Diffley, J. F. Mutational analysis of conserved sequence motifs in the budding yeast Cdc6 protein. *J. Mol. Biol.* **308**, 597–608 (2001).
34. Kamimura, Y., Tak, Y. S., Sugino, A. & Araki, H. Sld3, which interacts with Cdc45 (Sld4), functions for chromosomal DNA replication in *Saccharomyces cerevisiae*. *EMBO J.* **20**, 2097–2107 (2001).

A spoonful of sugar

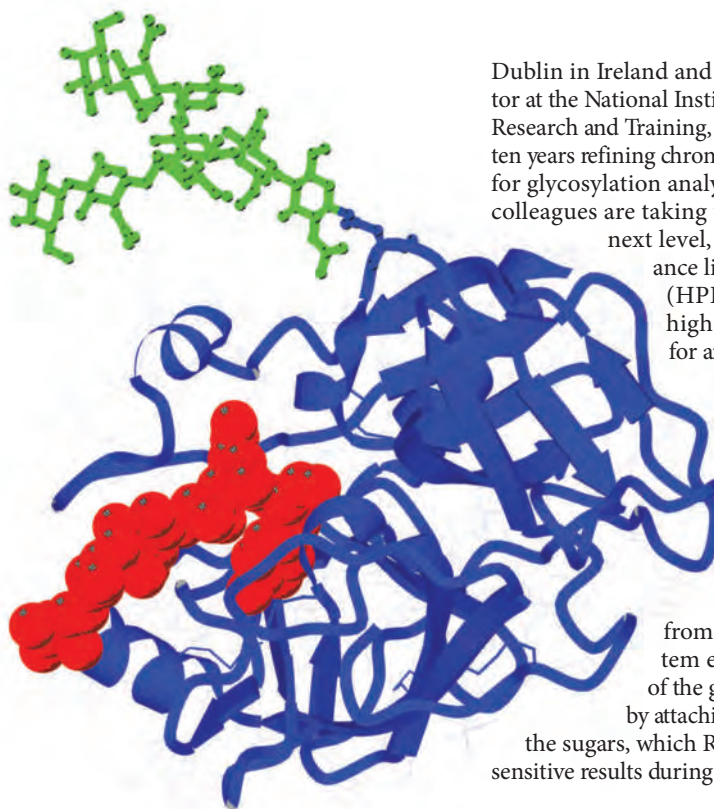
Carbohydrates are important in many biological processes, but the full extent of their distribution and function remains unclear. Advances in technology are now reveal those secrets. Nathan Blow reports.

Sugars occur in a variety of forms and locations throughout the human body. From those that are attached to proteins during glycosylation to the carbohydrates that decorate the surfaces of cells lining the lungs and digestive tract, the range of possible sugar conformations and glycoforms is tremendous. As a result, analysing carbohydrates is a tricky business for anyone interested in glycobiology.

The term glycobiology was coined in 1988 by biochemist Raymond Dwek at the University of Oxford, UK. Dwek used the phrase simply to emphasize the importance of relating sugars back to basic biology rather than just isolating and examining them outside of their biological context. Instead, he named a field that is thriving in its own right.

Today glycobiology is intertwined with fields such as immunology, virology, reproductive biology and drug discovery. "More people are starting to realize that sugars are not just there for protecting surfaces from proteolysis, but they have some functional role to play," says Ian Wilson, a structural biologist at the Scripps Research Institute in La Jolla, California.

But even as more researchers accept the importance of sugars in basic biology, many glycobiologists worry that the barrier to entry into their field remains too high, potentially delaying or hampering discovery and innovation. "The technical difficulty is so great now that many scientists are turned away," says Peter Seeberger, a chemist at the Swiss Federal Institute of Technology in Zurich. The solution, he adds, is to "lower the hurdle by providing access to technology more easily".



A molecular model of a prostate-specific antigen with tumour-associated glycosylation (in green).

To those ends, Seeberger is trying to develop user-friendly automated solutions for complicated procedures such as the synthesis of complex carbohydrates.

Seeberger is not alone. Pauline Rudd, a professor of glycobiology at University College

Dublin in Ireland and a principal investigator at the National Institute for Bioprocessing Research and Training, spent the better part of ten years refining chromatography approaches for glycosylation analysis. Now she and her colleagues are taking their approach to the next level, using high-performance liquid chromatography (HPLC) as the basis for a high-throughput pipeline for analysing glycans.

Glycoproteins featuring N-linked glycans are first immobilized either in gels or on membranes, and the glycans are then released using an enzyme that cleaves the sugars from the proteins. The system examines the patterns of the glycans on the proteins by attaching fluorescent labels to the sugars, which Rudd says offers highly sensitive results during chromatography.

Sweet analysis

The labelled sugars are run on a normal phase HPLC column and the resulting peaks are correlated to a pre-run dextran ladder, thereby assigning a 'glucose unit value' to each of the peaks. "We have a database that is automatically interrogated to give us a list of sugars that could have these particular glucose units," says Rudd. Using this information, a series of exoglycosidase digestions is performed and those data are fed back into the computer program to assign final structures.

The researchers recently installed an automated liquid-handling platform from Hamilton Robotics of Reno, Nevada, so that they could do their glycan analyses in 96-well plates. "One analysis will take about eight hours, so the aim is to get it done by the end of the shift," says Rudd.

Speed is important, Rudd notes, because the drug industry increasingly wants to monitor the glycosylation patterns of proteins. "When people want to achieve quality by design, they need to determine the optimal culture conditions and time for harvesting monoclonal antibodies," she says. "Therefore, they need to understand how the glycosylation changes over the course of production." Rudd says that her pipeline can test samples every hour, over a number of days or at different pH conditions to find those optimal points.



Pauline Rudd is advancing high-throughput glycan analysis.

M. WORMALD, P. RUDD

P. RUDD

Elizabeth Higgins, chief executive and founder of GlycoSolutions in Worcester, Massachusetts, feels that a different factor is driving the drug industry's interest in glycan analysis. GlycoSolutions offers glycomics services and analyses, and last year worked on 20 different glycosylation analysis projects for various pharmaceutical companies. Higgins says that the analyses were largely done to meet regulatory requirements. "Most companies we work with are driven by getting data for the Food and Drug Administration," she says.

Another company working on high-throughput tools for analysing glycosylation patterns to aid drug development is Procognia, in Ashdod, Israel. Because many different glycoforms can exist, an extensive knowledge of glycosylation patterns and how they change

during drug manufacturing is important for the development of biosimilar drugs, says Ilana Belzer, Procognia's vice-president of research and development. To tackle this issue, the firm has developed GlycoScope, a high-throughput workflow for glycosylation analysis platform that uses lectin (carbohydrate-binding protein) arrays and informatics tools to provide glycosylation fingerprints and glycan structures for glycoproteins.

By providing values of molecular weight that can be used to deduce initial structures, mass spectrometry (MS) is yet another approach to glycan analysis. "MS is very good at defining the sugar profiles of cell surfaces," says James Paulson, a glycobiologist at the Scripps Research Institute who studies glycan binding proteins that mediate cellular communica-

tion in the immune system. With additional isolation and fragmentation using either matrix-assisted laser desorption/ionization or electrospray ionization followed by tandem MS (MS/MS), researchers can deconvolute the configuration of sugars, a process very similar to protein sequencing.

The past few years have seen the arrival of many commercial programs and algorithms that assign glycan structures based on MS spectra. PREMIER Biosoft based in Palo Alto, California, sells SimGlycan, which uses MS/MS data to query a database of more than 8,000 theoretical glycan fragmentation patterns to generate a list of probable structures. Developers at the Palo Alto Research Center have designed new software packages that identify and annotate glycopeptides from a combina-

SURFACE SENSING

In recent years, glycan arrays have been used to identify the cell-surface sugars bound to by pathogens such as the flu virus. In parallel, companies such as CombiMatrix in Mukilteo, Washington, have developed specialized diagnostic instruments to identify pathogens, including tools to differentiate flu strains. Now researchers at the MITRE Corporation in Bedford, Massachusetts, and the University of California, San Diego (UCSD), have developed a method that could blur the line between these two types of tool.

The device was described in the December issue of *IEEE Sensors Journal* by MITRE researchers Grace Hwang and Elaine Mullen and UCSD researchers Lin Pang and Y. Shaya Fainman⁴. It features an array developed at the UCSD with a gold surface that is perforated with nanometre-wide holes. A glycoprotein is attached to the gold surface inside the hole and the pathogen or carbohydrate-binding lectin is added. The instrument detects binding events through surface plasmon resonance (SPR), measuring fluctuations in electron density at the boundary between the metal and a dielectric surface.

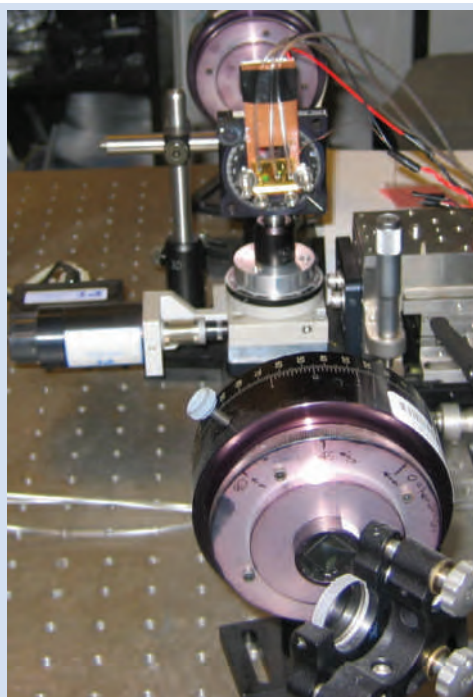
Hwang and Mullen use microfluidic delivery channels to place the glycoproteins on the gold surface. When the proteins attach to the gold there is a detectable change in plasmon resonance. Once this reaches equilibrium, the pathogen or lectin is introduced using the delivery channel and any binding that takes place further

changes the plasmon resonance. The device is reusable as acids can be used to break the glycan-lectin bonds and clean the array.

"The reason we wanted to use a plasmonic device was because plasmons are very sensitive to perturbations at the metal-dielectric interface," says Hwang. For studying pathogens such as the flu virus, sensitivity can be an issue. The binding of the virus to different oligosaccharides occurs in the low millimolar range says Ian Wilson, a structural biologist at the Scripps Research Institute in La Jolla, California. As a result, he notes, glycan arrays often need to amplify the fluorescence signal, which requires additional antibodies.

Hwang and Mullen's system avoids this problem, as plasmon detection does not require fluorescence to measure binding interactions — potentially opening the instrument up to a wide range of sensitive interactions. At the moment, however, the researchers are still working to improve the device's sensitivity for detecting flu viruses — their calculations suggest that it should be possible to identify up to one million influenza particles per millilitre.

Unlike other glycan arrays, the SPR system doesn't need printing or linkers to attach sugar targets to the gold surface. "The disulphide



Surface plasmon resonance provides label-free methods to look at carbohydrate interactions.

bonds in the glycoproteins will typically break and then bind to gold spontaneously," says Mullen. This is helpful because when the sulphide bonds form with the gold surface, the oligosaccharides of the glycoproteins are oriented properly with their bioactive sugars projecting towards the medium.

Nevertheless, using glycoproteins in this way means that Hwang and Mullen have to choose carefully and be confident in the glycosylation patterns of the glycoproteins they use as their target. To help them, Mullen and her colleagues built a database

called SugarBindDB (<http://sugarbinddb.mitre.org>). "We know which glycoproteins to choose by looking at our own database of pathogens and their specific sugar sequences," says Mullen. "Then we go to the GlycoSuite, a database of oligosaccharides, to determine which glycoprotein it was attached to when it was isolated and what organisms it came from."

Hwang acknowledges that it is challenging to identify potential glycoproteins that present only the sugars required for selective pathogen sensing. If the glycoprotein displays a mixture of sugars, then it could bind to non-pathogens. It is even more difficult to identify potential pathogen targets

displayed on glycoproteins in human tissue, but she and Mullen think this is a challenge not just for their device, but for glycobiologists in general.

"I realized from discussions with other researchers that predictive tools to compute binding affinities between sugars and lectins do not exist today," Hwang says, noting that this is a gap in glycan research tools that does not exist for nucleic acids and proteins. But she thinks in time, as more biophysical information is gained about glycan structures and properties, glycan arrays will catch up.

N.B.

tion of single and tandem MS data.

MS analysis works well early on, says Higgins, but can be dangerous when it comes to working out the exact sugar structure because researchers often make assumptions based on mass alone. But the main challenge in using mass spectrometry for glycan analysis is figuring out the linkages between sugars. This is complex because the system needs consistently to fragment the sugars at the correct point to show one sugar is linked to a certain position on another sugar, says Paulson. He adds that such consistency remains an issue.

Rudd says that the HPLC approach along with enzyme digests can identify specific sugar linkages. HPLC columns can resolve the sugars on the basis of their conformations, and each monosaccharide contributes a specific incremental value to the retention time of an oligosaccharide. The pools of released sugars are treated with enzyme arrays in which each enzyme is highly specific for a particular monosaccharide in a particular linkage. The sequence and the linkage between sugars can be determined simultaneously for all the sugars in the pool. To help researchers interested in using this approach, Rudd's group recently made available the database GlycoBase and the analytical tool AutoGU to aid in the assignment of provisional structures based on HPLC profiles¹.

Glycan arrays and bird flu

The hunt for specific binding partners to various branched sugars or sugar-binding proteins called lectins requires a higher-throughput system. This can be achieved using glycan arrays. First described in 2002, these arrays feature different oligosaccharides or polysaccharides printed on slides or held in wells on a plate. "I think that glycan arrays have been a spectacular success over the past few years," says Paulson.

Initially, the arrays contained relatively small

numbers of glycans and were designed mainly to study the specificity of antibodies and carbohydrate-binding proteins. But Wilson is one of a number of researchers who realized that some of these arrays would prove useful for diverse applications relevant to their own research. He uses glycan arrays for studying how the influenza virus binds to cells.

Some viruses, such as flu and HIV, attach themselves to host cells during the early stages of infection by binding to sugars on the cells' surface. Paulson, in fact, discovered in the 1980s that avian flu viruses recognize different sugar receptors from their human virus counterparts. For Wilson, glycan arrays offered a way to look in detail at the specificity of different flu strains for various sugars, especially the H5N1 strain of bird flu that emerged in 1997 as a worldwide health concern, as well as the strain that caused the human pandemic in 1918. "We have analysed 50 to 60 or maybe even more influenza haemagglutinin mutants on the array to look for how the 1918 and H5N1 influenza strains can convert from human-to-avian or avian-to-human receptor specificity," says Wilson. Work has gone far in explaining how mutations can change the sugars to which influenza strains bind, thereby interconverting the receptor-binding characteristics of avian strains and human strains.

Wilson thinks that glycobiology is



THERMOFISHER SCIENTIFIC

Advances in mass spectrometry are improving analyses of sugar composition.

brought to the attention of a much wider audience when researchers use tools such as glycan arrays to work on well-known microorganisms such as the flu virus (see 'Surface sensing'). "There are a lot of other uses for these arrays, but everyone understands flu and the risks of bird flu," he says.

The Consortium for Functional Glycomics (CFG), an effort funded by the US National Institute of General Medical Sciences, aims to provide unique resources for glycobiology research. Headed by Paulson, the consortium has expanded the number of glycans available for arrays. "There are now 480 glycans in the consortium library," says Paulson, "and they all have amino-terminal linkers that allow them to be printed on slides using standard robotics." The ease of generating and analysing these arrays is opening the field to ever more researchers who can now submit samples to the CFG for rapid analysis.

Commercial developers also make high-content arrays with both glycans and carbohydrate-binding lectins attached to the surface. Robotic Labware Designs in Encinitas, California, offers printing services for glycan arrays as well as a series of preprinted glycan arrays. QIAGEN, headquartered in Hilden, Germany, provides the Qproteome GlycoArray kit for glycosylation analysis. This array and analysis software, developed by Procognia, contains a series of specific lectins that bind different monosaccharides, which allows researchers to determine the pattern and relative abundance of specific glycosylation epitopes in a glycoprotein.

Although 480 glycans on one array might not seem impressive compared with DNA microarrays, which can contain over a million features, Paulson is unperturbed. For carbohydrate-binding proteins, which usually recognize and interact with the tips of glycans, 480 represents a reasonable approximation of the options.



ETH-ZÜRICH

Automated carbohydrate synthesis could speed glycobiology research efforts.

P. RUDD



Robotics are proving crucial in several high-throughput glycosylation analysis approaches.

"If you only consider the tips, or the last six or seven sugars, then it is a very finite number of structures, in the order of 500," he says.

The problem for glycobiochemists is how quickly carbohydrate diversity can grow when those 500 structures are attached to different branches on a single N-linked glycan. "If you allow any one of those structures to occur on any one of the four branches, you have this huge number of structures that could theoretically exist," says Paulson. And this is where glycan arrays run into a wall — researchers want this level of diversity on their arrays to help them understand how proteins and pathogens bind sugars, but generating such a diversity of glycans can be difficult.

Although many groups still try to isolate sugars from natural sources to use in their research, most agree that improving synthesis methods and technology is essential to obtaining large quantities of diverse carbohydrates.

"I think that up to now, carbohydrate synthesis has been restricted to a relatively small group of experts who bring considerable technical knowledge to the table," says Seeberger. Even for experts, such synthesis can take a long time — weeks or even years when it comes to making complex carbohydrates or glycoconjugates. Seeberger and his group, along with a handful of other labs around the world, have been working to improve carbohydrate synthesis methods. Ultimately they hope to develop automated instruments that can synthesize carbohydrates much like DNA synthesizers currently produce nucleic acids.

There are currently two main approaches to carbohydrate synthesis: solid-phase or one-pot synthesis. In 2001, Seeberger and his colleagues

described an automated system that uses solid-phase synthesis for carbohydrates². A programmable one-pot synthesis approach, meanwhile, has been advanced by Chi-Huey Wong, from the Scripps Research Institute and Academia Sinica in Taipei, Taiwan, and his colleagues.

Cooking up sugars

In solid-phase synthesis, sugar building blocks are attached to a surface or a bead, which can be moved during the synthesis process to allow other monosaccharides to be added. The one-pot approach uses a computer program to determine which monosaccharides to place in a flask; the next reagent is added and the mixture stirred. This process is repeated until an oligosaccharide is obtained. "What you save is the different work-up steps that often take much more time to achieve than the actual synthesis," says Seeberger of the one-pot approach. He adds that in this sense, both approaches cut down on the purification and separation steps in carbohydrate synthesis.



Peter Seeberger is working on fresh approaches to carbohydrate synthesis.

Seeberger sees the building blocks as a big issue for both approaches. Unlike DNA, which has four nucleotide bases, or the 20 amino acids that comprise peptides, there are 10 common monosaccharides in humans and many more in bacterial systems. Even more vexing when it comes to synthesis is the potential for branching of sugars. For example, glucose can link to another sugar at two points in its structure — a 1–6 linkage or a 1–4 linkage. This means that two different building blocks must be available for synthesis, which adds another level of complexity. The synthesis of monosaccharide building blocks was advanced recently when Shang-Cheng Hung in Taiwan

and his colleagues reported a selective one-pot synthesis approach for the synthesis of highly functionalized, differentially protected monosaccharides³.

Some commercial companies are producing monosaccharide building blocks for chemical syntheses. Dextra Laboratories in Reading, UK, offers monosaccharides as well as various glycoconjugates and more complex N-linked oligosaccharides. And other companies such as Omicron Biochemicals of South Bend, Indiana, and GLYCOTEAM in Hamburg, Germany, offer carbohydrate chemical synthesis services.

Chemical synthesis is not the only route to obtaining synthetic carbohydrates — researchers can also take advantage of nature's methods. "Enzymatic synthesis is one approach the CFG uses and that has enormously accelerated the rate at which you can synthesize complex natural sugars," says Paulson. But the approach is limited by the number of glycosyltransferase enzymes needed to synthesize all the carbohydrates researchers may be interested in. The number of glycosyltransferases needed for synthesis can be almost as daunting as the number of monosaccharide building blocks in chemical approaches. For example, GlycoGene, a company based in Ibaraki, Japan, offers enzymatic synthesis services to researchers through the use of more than 180 different glycosyltransferases. For this reason, the CFG has merged enzymology and chemistry in the production of many of the sugars on its glycan array.

Although he is keen to see automated chemical synthesis up and running, Paulson sees gaps when it comes to the carbohydrates that can be synthesized with existing methods. "You cannot make everything you want now, although you can make some carbohydrates quickly and easily," he says. "The gaps are the key things and these might be what people are really interested in looking at."

Despite this, Seeberger still sees access to tools as the greatest challenge in glycobiochemistry at the moment. "When you think about genomics and proteomics, you can sequence and you can synthesize," he says. "But those two things are still not generally possible in glycobiochemistry."

The field of glycobiochemistry is still finding its way 20 years after the word was first printed. Although advances in the analysis and synthesis of carbohydrates are leading to fresh insights, much remains to be discovered. But Dwek can sit back and take comfort in the knowledge that his word has blossomed into a field that continues to grow. "I think the future of glycobiochemistry is very exciting," he says. ■

Nathan Blow is the technology editor for *Nature* and *Nature Methods*.

1. Campbell, M. P., Royle, L., Radcliffe, C. M., Dwek, R. A. & Rudd, P. M. *Bioinformatics* **24**, 1214–1216 (2008).
2. Plante, O. J., Palmacci, E. R. & Seeberger, P. H. *Science* **291**, 1523–1527 (2001).
3. Wang, C.-C. et al. *Nature* **446**, 896–899 (2007).
4. Hwang, G. M., Pang, L., Mullen, E. H. & Fainman, Y. *IEEE Sens. J.* **8**, 2074–2079 (2008).

ETH-ZÜRICH

COMPANY	PRODUCTS/ACTIVITY	LOCATION	URL
Glycobiology companies			
Dextra Laboratories	Monosaccharides, glycoconjugates and N-linked oligosaccharides	Reading, UK	www.dextra-labs.co.uk
GlycoFi	Engineered yeast strains for specific human glycosylation; optimization of therapeutic proteins	Lebanon, New Hampshire	www.glycofi.com
GlycoGene	Carbohydrate synthesis using enzymatic approaches; biomarker screening; glyco-engineering with human glycosyltransferases	Ibaraki, Japan	www.glycogene.co.jp
Glycominds	Discovery and development of glycan biomarkers for medical diagnostics	Redwood City, California	www.glycominds.com
Glycorex Fine Chemicals	Building blocks for carbohydrate synthesis; glycosides; carbohydrates for affinity chromatography	Lund, Sweden	www.finechem.glycorex.com
Glycoseparations	Natural oligosaccharides	Moscow, Russia	www.glycoseparations.com
GlycoSolutions	Glycan analysis service including chromatography and mass spectrometry	Worcester, Massachusetts	www.glycosolutions.com
Glycoteam	Carbohydrate synthesis services and analysis; combinatorial chemistry	Hamburg, Germany	www.glycoteam.com
GlycoTech	Selectins, carbohydrate polymers, carbohydrate antibodies, cell-adhesion apparatus and accessories	Gaithersburg, Maryland	www.glycotech.com
GlycoThera	Development of glycoprotein products and contract analytical services	Hannover, Germany	www.glycothera.de
Glycosynth	Enzyme substrates; fluorogenic substrates; chromogenic substrates	Warrington, England	www.glycosynth.co.uk
IsoSep	Organic synthesis of carbohydrates	Uppsala, Sweden	www.isosep.com
Lectinity	Glycoconjugates and lectins; custom synthesis services	Moscow, Russia	www.lectinity.com
Omicron Biochemicals	Carbohydrate synthesis services	South Bend, Indiana	www.omicronbio.com
Procognia	High-throughput glycan analysis for pharmaceutical companies and life-science researchers	Ashdod, Israel	www.procognia.com
Qiagen	Qproteome Glycoarray kit for glycosylation analysis; molecular- and cell-biology kits and reagents	Hilden, Germany	www.qiagen.com
Robotic Labware Designs	Glycan arrays and printing services for glycan arrays	Encinitas, California	rldarrays.com
Sussex Research	Design, synthesis and manufacturing of carbohydrate-based molecules and building blocks	Ontario, Canada	www.sussex-research.com
Chromatography			
Advanced Separation Technologies	Analytical and preparative chromatography products; HPLC and chiral chromatography	Bellefonte, Pennsylvania	www.astecusa.com
Alcott Chromatography	HPLC equipment and software, ion chromatography, hydrochromatic chromatographs	Hamilton Square, New Jersey	www.alcottchromatography.com
Biotage	Chromatography columns and accessories; FLASH chromatography systems	Uppsala, Sweden	www.biotage.com
Capital HPLC	HPLC and CE columns and accessories	Broxburn, Scotland	www.capital-hplc.co.uk
Cecil Instruments	Modular HPLC instruments, ion chromatography, UV/visible spectrophotometers	Cambridge, UK	www.cecilinstruments.com
DataApex	Chromatography software	Prague, Czech Republic	www.dataapex.com
GE Healthcare	AKTExpress automated liquid-chromatography platform	Little Chalfont, UK	www.gehealthcare.com
Gilson	Solid-phase extraction systems, liquid chromatography	Middleton, Wisconsin	www.gilson.com
Hamilton	Automated solid-phase extraction systems	Reno, Nevada	www.hamiltoncompany.com
Phenomenex	Chromatography columns and accessories	Torrence, California	www.phenomenex.com
Mass spectrometers			
Agilent Technologies	Mass-spectrometry instruments, sample preparation and software	Santa Clara, California	www.agilent.com
Applied Biosystems	Mass-spectrometry instruments, reagents and software; ion sources	Foster City, California	www.appliedbiosystems.com
Bruker Daltonics	Mass spectrometers for different applications	Bremen, Germany	www.bdal.de
Hitachi High Technologies	Liquid-chromatography and mass spectrometers systems	Tokyo, Japan	www.hitachi-hitec.com
LECO	Mass-spectrometry instrumentation and analysis tools	St Joseph, Michigan	www.leco.com
Shimadzu	Laboratory instruments including mass spectrometers and data-management systems	Kyoto, Japan	www.shimadzu.com
Thermo Scientific	High-end analytical instruments, including mass spectrometers, as well as laboratory equipment, software, services, consumables and reagents	Waltham, Massachusetts	www.thermo.com

COMPANY	PRODUCTS/ACTIVITY	LOCATION	URL
Varian	Analytical instruments including NMR and magnetic-resonance imaging systems, mass-spectrometry instruments, Fourier Transform-infrared and X-ray crystallography	Palo Alto, California	www.varianinc.com
Waters	Liquid-chromatography systems; chromatography columns and chemistry products; mass-spectrometry systems; laboratory-informatics solutions	Milford, Massachusetts	www.waters.com
General			
Alexis Biochemicals	Reagents for molecular- and cell-biology research	Lausanne, Switzerland	www.alexis-corp.com
Attagene	Transcription-factor profiling system; software	Research Triangle Park, North Carolina	www.attagene.com
BD Biosciences	Research reagents, bioimaging systems, instrumentation	San Diego, California	www.bd.com
Biomol	Services for chemical synthesis, cell culture and antibody production	Hamburg, Germany	www.biomol.de
Bio-Rad	Products, instruments and software for life-sciences research	Hercules, California	www.bio-rad.com
BMG Labtech	Microplate and array readers, and handling systems	Offenburg, Germany	www.bmglabtech.com
Cambrex	Products for molecular- and cell-biology research	East Rutherford, New Jersey	www.cambrex.com
CombiMatrix	Influenza detection systems and microarrays	Mukilteo, Washington	www.combimatrix.com
Cole-Parmer	Instruments and reagents	Vernon Hills, Illinois	www.coleparmer.com
EMD Biosciences	Calbiochem, Novabiochem and Novagen product lines	San Diego, California	www.emdbiosciences.com
Enzo Life Sciences	Consumables and assays for molecular biology, gene expression and genomic analysis	New York, New York	www.enzo.com
Geneservice	Genomic and proteomic resources; contract services for DNA sequencing, microarray analysis and SNP genotyping	Cambridge, UK	www.geneservice.co.uk
Hamilton Robotics	Automated liquid-handling solutions, automated robotic platforms	Reno, Nevada	www.hamiltonrobotics.com
Harvard Apparatus	Instruments and equipment for electrophysiology and cell biology	Holliston, Massachusetts	www.harvardapparatus.com
Horiba Jobin Yvon	Spectroscopy systems and accessories including Raman, atomic-emission and UV spectroscopy	Edison, New Jersey	www.jobinyvon.com
Integra Biosciences	Equipment for sterilization, liquid handling, cell culture and sample storage	Baar, Switzerland	www.integra-biosciences.com
Irvine Scientific	Defined media for cell-culture applications; custom media services	Santa Ana, California	www.irvinesci.com
Lonza	Molecular-biology reagents and systems; advanced chemical synthesis	Basel, Switzerland	www.lonza.com
Merck	Chemicals, kits and reagents for chemistry, molecular- and cell-biology-related research	Darmstadt, Germany	www.merck.de
Metrohm	Laboratory instruments; consumables	Westbury, New York	www.metrohmusa.com
Molecular Devices	Liquid handling and microplate processing equipment; imaging instruments	Sunnyvale, California	www.moleculardevices.com
MP Biomedicals	Reagents and chemicals for research	Aurora, Ohio	www.mpbio.com
New England Biolabs	Molecular-biology-related reagents, kits and enzymes	Ipswich, Massachusetts	www.neb.com
Nalge Nunc International	Labware	Rochester, New York	www.nalgenunc.com
Palo Alto Research Center	Software for the analysis of glycan mass spectrometry data sets	Palo Alto, California	www.parc.com
PerkinElmer Life Sciences	Instruments, reagents and kits for life sciences	Waltham, Massachusetts	las.perkinelmer.com
Pierce Chemical	Protein assays, purification, Western blotting	Rockford, Illinois	www.piercenet.com
Promega	Chemicals for mass spectrometry analysis	Madison, Wisconsin	www.promega.com
Premier Biosoft	Software for life-sciences research; SimGlycan analysis tool	Palo Alto, California	www.premierbiosoft.com
Princeton Separations	DNA purification columns and reagents, fluorescent-protein labelling kits,	Adelphia, New Jersey	www.prinsep.com
Stratagene	Tools and reagents for molecular biology, genomics and proteomics	La Jolla, California	www.stratagene.com
Takara Bio	Reagents, kits and consumables for molecular biology	Shiga, Japan	www.takara-bio.com
Tocris Bioscience	Chemicals for life-science research; contract research services	Bristol, UK	www.tocris.com
Wako USA	Speciality chemicals; clinical diagnostic reagents	Richmond, Virginia	www.wakousa.com
USB	Chemicals and reagents for molecular biology	Cleveland, Ohio	www.usbweb.com

● see advertisement

naturejobs

**THE CAREERS
MAGAZINE FOR
SCIENTISTS**

With one phrase in his inaugural address, US President Barack Obama raised hopes for a significant increase in federal science funding. Obama pledged “to restore science to its rightful place”.

This phrase could have been a rebuke to former president George W. Bush, for his stance against embryonic stem-cell research and reluctance to act on global warming. But Obama’s words could also be heard as a promise to counteract several years of relatively flat funding for agencies such as the National Institutes of Health (NIH) and the National Science Foundation (NSF).

The speech comes a week after the US House of Representatives’ appropriations committee announced that it was including science funding hikes as part of an economic stimulus package. Under the plan, the NIH stands to receive a bump of \$3.5 billion over two years and the NSF \$3 billion (see *Nature* **457**, 364–365; 2009). Of course, even if the money materializes in an anticipated February vote, it is unclear exactly how the cash infusion will benefit individual scientists. After the NIH’s budget doubled from 1999 to 2003, to more than \$28 billion a year, not everyone gained. Halfway through that five-year cycle, some grant-seekers found less success than they had hoped, because much of the money had already been committed. The increase also covered major collaborations, large-scale science initiatives and a shift from basic to applied science. And after the terrorist attacks of 11 September 2001, NIH cash was funnelled to biodefence research rather than basic research — \$1.5 billion in 2003. The success rate for NIH grant applicants fell from 33% in 2001 to 20% in 2006, and entry-level postdoc stipends flattened.

The appropriations committee has said that money invested in grants creates other jobs — a major goal of the economic stimulus package. But many questions remain. One is, how much of the money will actually go to individual grants and fellowship programmes? Perhaps the most important question should be, not whether this investment will have a positive effect on both science and the economy, but rather how this windfall can sustain research in the long term.

Paul Smaglik moderates the Naturejobs Nature Network career-advice forum.

CONTACTS

Editor: Gene Russo

Assistant editor: Karen Kaplan
e-mail: naturejobseditor@nature.com

European Head Office, London
The Macmillan Building,
4 Crinan Street, London N1 9XW, UK
Tel: +44 (0) 20 7843 4961
Fax: +44 (0) 20 7843 4996
e-mail: naturejobs@nature.com

European Sales Manager:
Dan Churchward (4966)
e-mail: d.churchward@nature.com
Assistant European Manager:
Nils Moeller (4953)

Natureevents:
Ghizlaine Ababou (+44 (0) 20 7014 4015)
e-mail: g.ababou@nature.com

Southwest UK/RoW:
Alexander Ranken (4944)

Northeast UK/Ireland:
Matthew Ward (+44 (0) 20 7014 4059)

France/Switzerland/Belgium:
Muriel Lestringuez (4994)

Scandinavia/Spain/Portugal/Italy:
Evelina Rubio-Hakansson (4973)

North Germany/The Netherlands/Eastern Europe: Kerstin Vincze (4970)

South Germany/Austria:
Hildi Rowland (+44 (0) 20 7014 4084)

Advertising Production Manager:
Stephen Russell
To send materials use London address above.
Tel: +44 (0) 20 7843 4816
Fax: +44 (0) 20 7843 4996
e-mail: naturejobs@nature.com

Naturejobs web development: Tom Hancock
Naturejobs online production: Dennis Chu

US Head Office, New York
75 Varick Street, 9th Floor,
New York, NY 10013-1917

Tel: +1 800 989 7718
Fax: +1 800 989 7103
e-mail: naturejobs@nature.com
US Sales Manager: Ken Finnegan

India
Vikas Chawla (+91 1242881057)
e-mail: v.chawla@nature.com

Japan Head Office, Tokyo
Chiyoda Building, 2-37 Ichigayatamachi,
Shinjuku-ku, Tokyo 162-0843
Tel: +81 3 3267 8751
Fax: +81 3 3267 8746

Asia-Pacific Sales Manager:
Ayako Watanabe (+81 3 3267 8765)
e-mail: a.watanabe@natureasia.com
Business Development Manager, Greater China/Singapore:
Gloria To (+852 2811 7191)
e-mail: g.to@natureasia.com



SHOW US THE MONEY

The results of last year's UK Research Assessment Exercise (RAE) have left the country's universities and colleges with mixed feelings. Some are elated about their performance in this extensive audit of UK research quality, last undertaken in 2001. They anticipate boosting the number of research staff with the government funding they are likely to receive on the basis of the rankings. Some institutions are dismayed by the results, which they feel did not reflect the value of their work. Others are waiting to see what effect their ranking will have on their funding.

Administered on behalf of the four UK higher-education funding councils, the RAE classifies the quality of research submitted by participating colleges and universities. Work submitted by the 159 institutions that took part was judged by peer review, using experts from many countries to compare the research with the rest of the world's. The funding councils will use the results, released on 18 December (see *Nature* 457, 13; 2009), to determine how to allocate research funding to those institutions. Some £1.5 billion (US\$2.1 billion) will be distributed for 2009–10.

But although the rankings may hint at the government's intentions, institutions won't learn for sure until March or April exactly how much they will receive. The Higher Education Funding Council of England announces its results on 5 March; the Higher Education Funding Council for Wales on 16 March; Northern Ireland's Department for Employment and Learning at the end of March or the beginning of April, and the Scottish Funding Council on 2 April.

The government's assessment of UK colleges and universities sets up a waiting game for new funds and recruitment. Karen Kaplan reports.

Research submissions were ranked as world-leading (four-star), internationally excellent (three-star), internationally recognized (two-star) or nationally recognized (one-star). Submissions from each institution were grouped in each category according to the percentage of work earning that rating (see chart.)

World-class people

The results have given some participants grounds for optimism about funding. "We feel confident that we can make plans for strategic investments," says Alan Gilbert, president and vice-chancellor of the University of Manchester. Gilbert hopes Manchester's performance in several areas, among them nuclear energy R&D, cancer studies and systems biology, will merit a healthy funding stream, which in turn will allow it to carry on with high-calibre recruitment.

"We want to continue investing in world-class people and concentrate on areas where we have a chance of making a difference," he says, adding that the university seeks to also build expertise in aerospace engineering and areas in biology. "We've actually found that making very ambitious and high-profile appointments is revenue positive," Gilbert says. Hiring prominent researchers tends to attract more students and can boost the quality of research, he says. This in turn facilitates earning more grants.

The University of Exeter also likes its rankings results, according to its deputy vice-chancellor for research, Roger Kain. He says Exeter hopes to take on additional research staff, most likely in biological sciences and geography. "From our estimate, it looks

N. HAMID

STARS OF SCIENCE

	Chemistry	Physics	Chemical engineering	Geography & environmental studies	Biological sciences	Preclinical and human biological sciences	Earth systems	Epidemiology	Infection & immunology	Cancer studies
University of Cambridge	40	25	30	30	20	X	40	40	35	35
University of Oxford	30	20	X	30	25 (plant) 15 (zoology) 35 (biochem.)	30	35	40	45	25
Imperial College London	20	20	30	X	20	X	X	40	30	15
University of Nottingham	30	25	X	20	10	5	X	5	0	X
University College London	15	20	15	25	15*	35	25*	25	20	25
University of Manchester	20	20	25	15	25	20	20	15	X	30
University of Edinburgh	30**	20	X	20	15	X	15	X	X	X
University of Bristol	25	20	X	30	10 (biol. sci.) 20 (biochem.)	15	25	35	5	X
University of Durham	20	20	X	30	10	X	15	X	X	X
University of Reading	0	X	X	10	5	X	30	X	X	X
Queen Mary, University of London	X	15	X	25	5	20	X	30	X	15

These 11 universities (along with two specialists: the London School of Hygiene & Tropical Medicine and the Institute of Cancer Research) received the highest percentage of four-star ratings in natural sciences in the Research Assessment Exercise. Numbers are the percentage of four-star ratings earned in each category. X indicates no submissions in the category. Joint submissions: *with Birkbeck College; **with the University of St Andrew's. Source: RAE.

as if we are going to benefit very nicely from the funding,” he says.

At the University of Leeds, John Fisher, deputy vice-chancellor, says he expects the university will be able to hire more researchers as well. The university hopes to boost research staff in biomedicine and health, food security and sustainable agriculture, among other areas. Its rankings performance “meets our highest expectations”, says Fisher, adding that it achieved higher rankings this time around than in the previous RAE. “Getting a good outcome in the RAE moves us closer to [our goal] in terms of research quality.”

Other notable institutions suggested the rankings will have little effect on hiring. “We’d like to think we’ve improved our comparative position in the RAE,” says Nigel Brown, vice-principal and head of the University of Edinburgh’s College of Science and Engineering. “But it won’t translate into positions won or lost. What it will do is help in our recruitment.”

At University College London (UCL), it’s uncertain how, or whether, the rankings might translate into payroll changes. “We don’t have strategic plans to greatly increase our staffing,” says UCL’s vice-provost for research, David Price. “However, we do not anticipate significant — or any — reductions, either.”

Ian Leslie, pro-vice chancellor for research at the University of Cambridge, says that the university’s winning performance presented no surprises. “We’re still at the top,” he says. “The major thing is that in reputational terms, at an institutional level, not a great deal has changed for us since 2001. How that turns into money, we’ll know in March.”

Several institutions declined to ruminate about the ramifications for funding allocation. “It’s difficult to say,” says Ian Postlethwaite, pro-vice chancellor for research at the University of Leicester. “I think we’re all just hanging on to see what money we get.” Spokespeople from the University of Newcastle and

the University of Glamorgan in Pontypridd, Wales, likewise balked at speculating on the implications of the rankings.

Green developments overlooked

Could valuable work be put at risk by poor rankings? Trevor Newsom, director of research and regional services for Queen’s University Belfast, says that years of research and infrastructure investments have gone unnoticed. Queen’s has spent considerable time and money on improving its programmes in areas such as biomedicine and chemistry, he says. In 2004, it invested £25 million in a centre for cancer research. “In terms of its current research output, and the esteem and the nature of the contracts, it is already beginning to show great potential,” he says.

Queen’s also reconfigured its chemistry programme a decade ago to focus on reducing or eliminating pollution. It opened a new ‘green chemistry’ lab last year, for example, to work on a £5.25-million contract for Petronas, the Malaysian government’s oil and gas corporation. The university had expected its submissions in this field to receive higher ratings.

The new Research Excellence Framework (REF), which will replace the RAE and for which preliminary research evaluations begin this year, is expected to rely more heavily on bibliometrics, such as publication citations, to judge research quality (see *Nature* 457, 7–8; 2009). Other evaluation criteria and benchmarks are still being developed. The first REF rankings will be released in 2013, with funding allocations in 2014.

Newsom says Queen’s will be sure to adjust its portfolio accordingly. “We don’t want to be driven by a process,” he says. “But the funding that comes through the evaluation exercise is a fundamental and very important part of the university’s income.” Queen’s, he says, cannot afford to simply ignore the ratings. ■

Karen Kaplan is the assistant editor of *Naturejobs*.



Waiting: Alan Gilbert (top) and Ian Postlethwaite.

MOVERS

Alan Lewis, president and chief executive, Juvenile Diabetes Research Foundation, New York



2006-08: President and chief executive, Novocell, San Diego, California

2000-06: President, Signal division of Celgene, San Diego, California

1994-2000: President and chief executive, Signal Pharmaceuticals, San Diego, California

Alan Lewis's enthusiasm for drug hunting and a desire to work at the forefront of science have seen him chart a 36-year career in the drug industry. As the next head of the Juvenile Diabetes Research Foundation (JDRF) in New York, he plans to use his industry ties to help bring novel treatments for type 1 diabetes to market quickly.

Lewis, whose father was a pharmacist in Wales, studied biochemistry and physiology at the University of Southampton, UK, but was most excited by his pharmacology course. He did a PhD in pharmacology at the University of Wales Institute in Cardiff, and then studied as a postdoc at the University of Guelph in Ontario, Canada, where he worked on animal models of asthma.

It was visa troubles rather than science that proved pivotal in Lewis's next career move. His wife's visa problems cut short his stay as a research associate at Yale University, but led to new opportunities. Lewis decided to join industry, first at Netherlands-based drug maker Organon Laboratories, where he designed drugs to suppress or augment the immune system. "I really loved the focus and directed-goal orientation of drug hunting," he says.

Lewis then joined Wyeth Pharmaceuticals in Princeton, New Jersey, where as vice-president of research he helped develop the antidepressant Effexor, an immunosuppressant used in transplant therapy. Buoyed by the potential of the biotechnology industry, Lewis moved to Signal Pharmaceuticals, a small company in San Diego, California, that he helped grow from 9 to 90 people. Still energized with entrepreneurial zeal, Lewis joined Novocell, also in San Diego, which develops insulin-producing cells from embryonic stem cells to treat diabetes.

Leading the nonprofit JDRF is part of a natural career progression, says Lewis. "Passion drives what we do at industry — and at non-profits," he says. Steven Gilman, chief scientific of Cubist Pharmaceuticals in Lexington, Massachusetts, was initially surprised that Lewis was leaving industry, but says it makes sense given his drive to develop treatments. "Alan's passion for making an impact on patients' lives is evident to all who know him, and he'll use that to help the JDRF work towards new treatments," says Gilman.

And with the industry exploring ways to develop an artificial pancreas that can control blood glucose levels, Lewis is optimistic that better treatments for type 1 diabetes are not far away.

Virginia Gewin

NETWORKS & SUPPORT

Age versus talent in India

Indian prime minister Manmohan Singh is looking for talented young scientists. He told 4,000 scientists at the annual Science Congress in Shillong, Meghalaya, on 3 January that Indian science needed "a new generation of role models and leaders".

Despite government efforts, he said, Indian science is lagging behind not just developed nations, but also newly industrialized states such as China.

A bias towards seniority is the norm in India, says Jayaraman Gowrishankar, director of the Centre for DNA Fingerprinting and Diagnostics in Hyderabad. Finding young leaders is not easy, as the average age of scientists in national laboratories is close to 50. However, says Thirumalachari Ramasamy, president of the Science Congress, "identifying younger talent is possible if selection committees heed Singh's advice".

Gifted students are increasingly seeking better-paying fields outside science, exacerbating a brain drain to the West that has continued since the 1970s. This has created a vacuum in mid-career positions, says C. N. R. Rao, science adviser to Singh.

But this may be about to change. India's education and science ministries have increased fellowship money by 50%. Last month, Singh launched a five-year, 21-billion-

rupee (US\$427-million) scholarship programme for a million 10-15-year-olds, whose funding can continue through graduate school as long as they continue with science. And a new programme called INSPIRE (innovation in science pursuit for inspired research) is to give selected new PhDs five-year government or university research positions.

Still, it will take time for a new crop of scientists to emerge, says Govindarajan Padmanaban, former director of the Indian Institute of Science (IISc) in Bangalore. The immediate challenge, he says, is to find thousands of new faculty members. He suggests that rules could be relaxed to recruit fresh PhDs and the retirement age be raised from 60 to 65.

A Global Indian Network of Knowledge initiative, announced on 8 January, will let expatriates who have given up Indian citizenship return more easily by acquiring an Overseas Citizenship of India card. The government has so far issued nearly 350,000 cards.

This, however, is unlikely to affect top institutions such as the IISc that already attract expatriates. "I do not believe we have enough committed Indians abroad wanting to return," says Padmanaban.

K. S. Jayaraman

POSTDOC JOURNAL

Zen science

The stark reality of balancing motherhood and a postdoc is about to hit me like an out-of-control truck. It was all planned. I would leave my toddler at home with his dad while I went on a workshop to discuss climate change and biodiversity. But just as I had successfully worked through the guilt of leaving my child, my partner was offered work in Papua New Guinea, at Aus\$700 (US\$460) a day for a month. We are both looking for new postdocs next year. He needs the work experience and we need the money. Now my first real academic outing in two-and-a-half-years includes an entourage: my toddler and my mother-in-law.

I expect that the next year, and future years, will include similar challenges if I wish to continue down the academic path. So far, I have been lucky. For the past three years, my postdoc has been part-time; I have three days a week to play Earth Mother and be a good influence on my son. My success is questionable, however; I have a child that looks like a cherub but swears like a sailor.

I doubt if this can continue. Part-time postdocs are rather rare. Over the next 12 months I have to find another postdoc, or (gulp), a real job. Or, I need to consider the alternative: more child-friendly career options. I aim to take a Zen approach to 2009, accepting each challenge as an opportunity to grow, while I strive for a happy work-family balance.

Joanne Isaac is a postdoc in climate-change effects on biodiversity at James Cook University in Townsville, Australia.

One less concern

The improbable dream.

Victor Thijssen

When Peter looked outside, rain was still pouring down. They should have called it global soaking instead of global warming, he thought. He finished his coffee and considered his options: take the old-fashioned way and get soaked, or use the modern and dry way of travelling.

"Would you like a refill sir?" the waitress asked, holding a coffee pot with coffee strong enough to make the glass crack. Peter turned his head and looked at her name tag.

"No thanks, Andrea, I'm already late. Could you bring me the check please?"

Andrea nodded, a bit disappointed, and Peter noticed that she took a glance at his ring before she walked back to her colleague. He looked at his finger and couldn't blame her, it truly was a beautiful piece of craftsmanship, a titanium ring inlaid with two drops of crude oil shaped as the yin and yang sign, captured in a small circle of 18-carat gold. Once a precious gift and sign of recognition: now worth just as little as his empty coffee mug.

Peter averted his eyes from the ring and looked back to the building on the other side of the square. The raindrops on the window almost made it appear as if Gaudí and Escher had teamed up to design a magnificent, but at the same time impossible, edifice. It struck him that this was actually the first time that he'd looked at the main entrance of the building in which he spent almost half his life. He'd seen it before — obviously — but he never paid much attention to the architectural details. The longer Peter stared at the pompous façade, the more it seemed that the building gazed back at him; a huge slick face with the big granite 'ConCERN' characters as an odious grin. A shiver ran down his spine and he quickly looked away and focused on the sculpture in the centre of the square. It was the same emblem as on his own ring, lying on its side in a shallow pond. It was just as if Goliath himself had carefully put it there to protect it from his upcoming battle with David. The rain splashing in the pond created a sense of movement, and, for a short moment Peter was convinced he could see the gigantic ring sinking slowly into the depths.

Apart from their size, the only difference between both

rings was the inscription on the inside of the statue. Peter could not read it from this distance but he knew the words by heart:

If an event with a desirable but unlikely outcome is repeated indefinitely, and each time there is a probability of success, then sooner or later the desired outcome will occur.

Nowadays, it was referred to as Murphy's reverse law, but it was actually postulated by Peter, seemingly centuries ago. The inscription in Peter's ring only mentioned the word CERN and a date; the day when the sculpture was unveiled. On that day, the ring was presented to him as a memento of his discovery of the probability particle, or proson. It was the reward for the decade of hard work that it had taken to prove the existence of this novel elementary particle. Even more, it had been the incentive for another 15-year-long expedition to find applications for their discovery, which eventually resulted in the first teleportation device.

Peter closed his eyes and smiled when he boarded his personal time-machine and travelled back to those days of glory. He remembered the excitement when one of his PhD students discovered a method to generate multiple prosons simultaneously

in the LHC-II. He could almost taste the champagne that appeared out of nothingness to celebrate the teleportation of a marble to the other side of the lab. He saw Steven burst into tears when they successfully teleported the first living organisms, albeit only a colony of bacteria. They were at the frontiers of teleportation science, the invincible probability warriors who were on a quest to tame chance and change the world forever. It was a time when scientists at CERN were still doing science, and long, long before CERN turned into ConCERN, the multinational with a larger annual turnover than Microsoft and a budget that made the losses due to the mortgage crisis early in the century look like small change.

"Professor Vangow ... Professor Vangow?"

Peter snapped out of his dream and for a moment he was surprised to see Andrea instead of a crying Steven.

"Your check, Professor Vangow," the waitress said, a little embarrassed when she realized that she had woken him. Peter wondered how she knew his name and it took his sleepy brain a few seconds to realize that they probably had portraits of all CERN's Nobel laureates pinned to a wall in a dark corner of the restaurant. Their own scientific hall of fame. He managed to produce a smile and handed her a 5-euro note.

"Keep the change. Do you have a probilivator?"

Andrea nodded, "It's in the back sir, next to the rest rooms. Bonne chance."

"Thanks."

Peter put on his wet coat and took his briefcase. Still a bit disorientated, he manoeuvred between the tables to the back of the diner. He took his ConCERN travel card from the inside pocket and pushed on the card's short-key to select his home address. He held it in front of the card-reader and when the glass doors opened he could vaguely hear the humming noise of the circulating prosons. At least we don't have to get wet anymore. That's one less concern, he thought, and stepped into the bluish light. ■

Victor Thijssen is a Dutch research scientist in the area of tumour angiogenesis. The publication of this short story is the first proof of Murphy's reverse law.



JACEY